One, Two, Many Modes

Development & Application of High-dimensional Systems for Quantum Information Science

Der Naturwissenschaftlichen Fakultät
der Universität Paderborn
zur
Erlangung des Doktorgrades Dr. rer. nat.
vorgelegt von

REGINA KRUSE

Table of Contents

Abstract

In recent years, one of the main quests in quantum optics has been to finally show that quantum-enhanced applications surpass their classical counterparts. In communication, computation and metrology, this aim necessitates the implementation of large Hilbert spaces. Therefore in quantum optics, the challenge is to push existing technology and develop compact architectures that implement large quantum networks with many photons for large Hilbert spaces.

In this thesis, we present new techniques and applications aiming towards this goal. We start with the implementation of a dual-path waveguide source of quantum light, where we exploit the underlying waveguide architecture to specifically tailor a parametric down-conversion process and produce post-selection free two-photon N00N states. Next, we investigate this source in the few photon regime by means of quasi-photon-number-resolved detection. To this aim, we consider the fundamental limits of time-multiplexed photon counting detectors and experimentally calibrate a state-of-the-art implementation of such a detector. With this detector and our dual-path source, we simulate the effects of atmospheric turbulence on the non-classicality of a transmitted quantum signal. Extending the concept of the dual-path source, we discuss large, non-linear waveguide arrays. Based on this system, we develop the theoretical concept of driven quantum walks that allows us to probe fundamentally different dynamics compared to passive systems. Furthermore, we show how to use this *intrinsically non-linear* waveguide array to implement the *intrinsically linear* computational problem of BosonSampling. Finally, we develop the protocol of Gaussian BosonSampling with squeezed states as a classically hard-to-solve computation problem and can therefore answer the last open question of BosonSampling, whether sampling problems with Gaussian states are hard, in the affirmative.

In the beginning
there was the cold and the night
Prophets and angels
gave us the fire and the light
Man was triumphant
armed with the faith and the will
even the darkest ages couldn't kill

Billy Joel - 2000 Years

1

High-dimensional Quantum Optics

Hilbert space is a big place! This sentence from Carlton M. Caves summarises the advantages of quantum mechanics in general, and quantum optics specifically, quite nicely. To motivate why large Hilbert spaces are advantageous for quantum information science, let us first consider the example of a classical bit [1], e.g. the ball in a hallway as in figure 1.1. This ball has only two possibilities, either it goes to the left state 0 or it goes to the right state 1, so

$$\text{ball} = 0 \quad \text{or} \quad \text{ball} = 1\,. \tag{1.1}$$

As the ball has only two states that it can occupy, a single digit (0 or 1) is enough to store the complete information.

Now, consider an equivalent quantum particle, or a qubit [1]. Imagine you have one photon, a single energy quantum of the light field [2]. Due to its nature as an electric field, it possesses the polarisation degree of freedom, which we can use to encode information. Contrary to the described classical situation, we use *superpositions* in the context of quantum mechanics [1, 2], which means that the photon can be both in horizontal and vertical polarisation at the same time[1] with different weights

$$|\text{photon}\rangle = \alpha\,|0\rangle + \beta\,|1\rangle\ . \tag{1.2}$$

In our example with the hallway in figure 1.1, this means that the probability to find the photon either in the left or right side splits according to the weights $\alpha, \beta \in [0,1] \times i[0,1]$, with $|\alpha|^2 + |\beta|^2 = 1$ as the normalisation [1]. As such, we have infinitely many possibilities for a qubit state, since α and β are continuous. For a single qubit, the corresponding Hilbert space is then two-dimensional [1], as it is spanned by the two orthogonal basis vectors $|0\rangle$ and $|1\rangle$. As α

[1] However, we are not restricted to choose horizontal and vertical polarisation as basis states. A choice of diagonal and anti-diagonal polarisation is equivalent. While the superposition of orthogonal polarisation states is well-known from classical optics, the quantum exclusive bit is that we consider only a single energy quantum of the field.

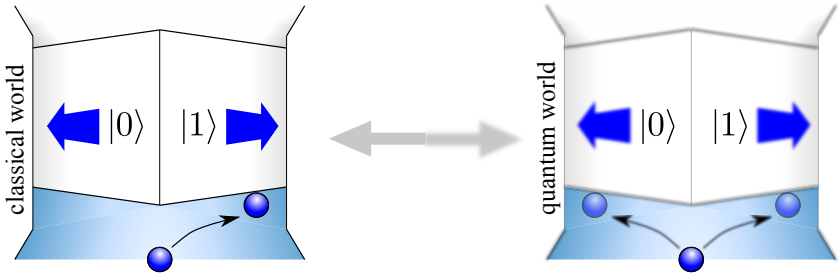

Figure 1.1 – Weird quantum world. A classical particle has to go either left *or* right, while a quantum particle can go left *and* right in the quantum world.

and β are both complex, we now have to store two complex numbers to represent the encoded information.

Let us now compare the same situation, but for two particles. In the classical case, we copy the example with the ball and retain four possible combinations between the ball going left or right

$$\begin{aligned} 2\text{ balls} = 0_A 0_B \quad &\text{or} \quad 2\text{ balls} = 0_A 1_B \\ \text{or} \quad 2\text{ balls} = 1_A 0_B \quad &\text{or} \quad 2\text{ balls} = 1_A 1_B\,, \end{aligned} \tag{1.3}$$

where the subscripts A, B denote the possibilities of ball A and ball B going left or right, respectively. This situation is sketched in figure 1.2(a). We can only combine two discrete possibilities, as indicated by the isolated levels, therefore two binary numbers are enough to store the full information about two classical particles. Generalising this to N balls, or N bits, we can store all the information that they contain in a string comprising N single binary digits.

As before with the single qubit, the situation differs drastically for the quantum particle. Again, we allow for superpositions between the different basis states, however we now have to consider four allowed basis vectors that span the Hilbert space for the two qubits. The corresponding Hilbert space $\mathcal{H}$ therefore has the dimension $\dim(\mathcal{H}) = 2^2 = 4$. As with the single qubit case, we have infinitely many possibilities for a qubit state, where the most general case for two qubits is then given by

$$|2\,\text{photons}\rangle = \alpha\,|0\rangle_A \otimes |0\rangle_B + \beta\,|0\rangle_A \otimes |1\rangle_B + \gamma\,|1\rangle_A \otimes |0\rangle_B + \delta\,|1\rangle_A \otimes |1\rangle_B\,, \tag{1.4}$$

where $\otimes$ is the tensor product and superpositions between the different basis states give rise to unintuitive, quantum-exclusive features like entanglement [1, 2]. As we observe from equation (1.4), we now have to store four complex variables to encode the full information of the quantum state. In figure 1.2(b), we illustrate this situation by considering two qubits and represent the necessary basis states to span the full Hilbert space in equation (1.4) by connecting arrows between the levels of the separate qubits. As such, if we consider N qubits, we find 2^N orthogonal basis states and need a string comprising 2^N complex numbers to store the complete information on the system. On the other hand this means that we can encode much more information in the 2^N complex numbers of the quantum system, than in the N bits of the classical one. This

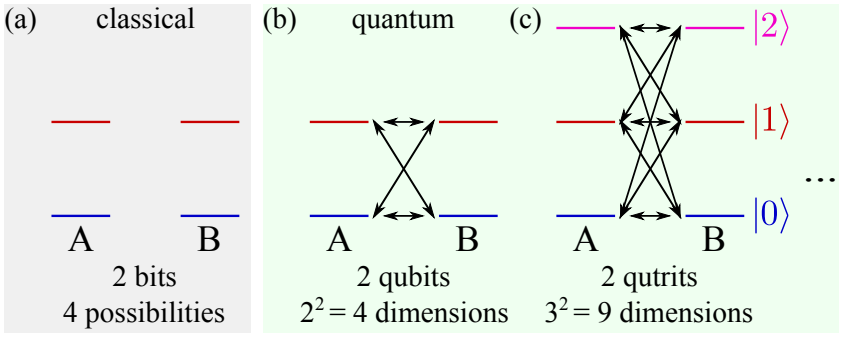

Figure 1.2 – Dimensionality of two classical bits (a), two qubits (b) and two qutrits (c). While the two classical bits in (a) only have four possible combinations, the two qubits in (b) form a four-dimensional continuous Hilbert space due to the superposition principle. We illustrated the needed combinations of the basis states by the arrows. The two qutrits in (c) already form a nine-dimensional Hilbert space, as 3^2 combinations of the single qutrit basis states are needed to span the full space.

exponential dependence for the quantum system presents such an enormous advantage that the sentence from Carlton M. Caves, that we used to open this thesis, becomes understandable.

And this is only the beginning. For the particle with the next higher amount of states, i.e. a single qutrit which is a three-level system with $|0\rangle$, $|1\rangle$ and $|2\rangle$, the single-particle Hilbert space is three-dimensional and we need three variables per qutrit to store the full information of the state. We illustrate the dimensionality of a two qutrit state in figure 1.2(c). As in the case of the two qubits, we denote the necessary basis vectors with the connecting arrows between the single qutrit levels. As such, we find that we need 3^2 basis states to span the full Hilbert space. Following our considerations on the combination of N qubits, a combination of N qutrits then needs 3^N complex variables to store all the information in the system.

For even higher-dimensional systems of dimension m this generalises to m^N complex numbers to store the full information of the composite quantum system [1]. Therefore, while the qubit already possesses a lot of advantages for quantum information science, it is even more desirable to encode information in higher-dimensional Hilbert spaces.

However, the situation is not as easy as we described above. The problem with the infinitely many possible superpositions is to extract the precise information of the internal state (i.e. α, β...) from the photons. A measurement, for example on a single qubit, always projects onto a basis state with a probability of $|\alpha|^2$ and $|\beta|^2$, and this even only if we use the correct encoding for $|0\rangle$ and $|1\rangle$ [1]. As such, we have to perform measurements on infinitely many copies of the same state in order to precisely reconstruct the information.

Nevertheless, we can use the encoded information to, for example, secure a quantum communication channel [1, 3, 4] or perform quantum computing operations [1, 5, 6]. The reason why the inability to measure the full state of the qubit does not impact quantum information science severely is that the internal state of the photons is oftentimes *not relevant*.

As such, the advantages of superpositions for quantum information science hold true and

can be exploited. This can be observed from the fact that many everyday applications have acquired a "Quantum" for their names since the development of Quantum Mechanics in the first half of the 20*th* century. Quantum computing [1, 5–7], quantum communication [1, 3, 4], quantum metrology [8–10] and quantum simulation [11–14] profit from the use of qubits or higher-dimensional systems. All of them exploit quantum advantages to become better than their classical counterpart. This ambition has coined the keyword *Quantum Supremacy*, which is used to summarise all types of quantum-over-classical advantages. All those applications promise something that the classical world cannot offer: extreme computing speed gain with the same resources for quantum computing, unbreakable security for quantum communication, better-than-classical resolution limits in quantum metrology, and so on and so forth. But how would we implement something along those lines?

The space of degrees of freedom that we might use for such applications is almost as big as the high-dimensional systems that we aim to implement. We can use space [15–24], time [25–33], frequency [34–37], photon number [8–10], momenta in all variants [38–42], frequency comb structures [43–46], spins of coupled atoms [47–52] etc. All these degrees of freedom implement a large, and many of them even an infinite-dimensional, Hilbert space at least in theory.

This introductory chapter comprises the two following sections: In the next section, we introduce some of the core concepts of quantum optics and quantum information science. If you are familiar with these fields, you may want to skip the next section completely or skim it to get an idea about the notation that we employ here. After this conceptual introduction, we explain the road-map for this thesis that connects the different chapters of this work.

Basic concepts of quantum optics

Quantum optics is the part of quantum mechanics that deals with the quantised electric field [2]. Due to this fact, the notation in this field inherits the notation of standard quantum mechanics. In general, we describe the states of our fields in terms of vectors $|\psi\rangle$ which live in a Hilbert space $\mathcal{H}$. They retain all properties that we expect from a quantum mechanical state [1], such as

$$\begin{aligned}
\text{scalar product} &: \langle\varphi|\,\psi\rangle \\
\text{norm} &: \sqrt{\langle\psi|\,\psi\rangle} = 1 \\
\text{orthonormality} &: \langle i|\,j\rangle = \delta_{ij} \\
\text{completeness relation} &: \sum_i |i\rangle\langle i| = \mathbb{I} \\
\text{outer product e.g. for density matrices} &: \rho = |\psi\rangle\langle\psi| \\
\text{and the time evolution} &: |\psi(t)\rangle = \exp\left(-\frac{i}{\hbar}\int_{t_0}^{t}\hat{H}(t')\mathrm{d}t'\right)|\psi(t_0)\rangle\ ,
\end{aligned} \tag{1.5}$$

with $\hat{H}(t)$ as the Hamiltonian of the governing system. In this thesis, we deal with high-dimensional composite systems. The overall Hilbert space of such systems is described by composite Hilbert spaces $\mathcal{H}_{\mathrm{comp}}$ that are constructed by the tensor product of the isolated sys-

tem's Hilbert spaces $\mathcal{H}_i$ [1]

$$\mathcal{H}_{\text{comp}} = \mathcal{H}_1 \otimes \mathcal{H}_2 \,. \tag{1.6}$$

Analogously, the basis vectors that span such a Hilbert space (here, again the example for two qubits) are also given by tensor products

$$|0\rangle_1 \otimes |0\rangle_2 \,, \quad |0\rangle_1 \otimes |1\rangle_2 \,, \quad |1\rangle_1 \otimes |0\rangle_2 \,, \quad |1\rangle_1 \otimes |1\rangle_2 \,. \tag{1.7}$$

A difference to quantum mechanics is the type of particles and the degrees of freedom that we deal with in quantum optics. The intangible quantity that we work with in quantum optics is the *photon*. This little beast is responsible for things like the photo-electric effect [53], the Boltzmann distribution [54] and some other effects that puzzled physicists until about 100 years ago, when Planck and Einstein postulated the existence of this energy quantum of the electromagnetic field.

In practice, the photon is a rather benign quantity. From the field quantisation [2], we find that the energy quanta of the electric field behave like the excitations in a quantum harmonic oscillator. As such, we can treat photons with creation and annihilation operators, $\hat{a}^\dagger$ and $\hat{a}$ that obey the following rules [2]

$$\begin{aligned} \hat{a}\,|n\rangle &= \sqrt{n}\,|n-1\rangle \\ \hat{a}^\dagger\,|n\rangle &= \sqrt{n+1}\,|n+1\rangle \\ \hat{a}\,|0\rangle &= 0 \\ |n\rangle &= \frac{1}{\sqrt{n!}}\hat{a}^{\dagger n}\,|0\rangle \\ \left[\hat{a}, \hat{a}^\dagger\right] &= 1 \,. \end{aligned} \tag{1.8}$$

Note, that the quantity n in the ket-notation is the number of photons and does not denote an encoding[2], as for example in equation (1.7). The commutation relation gives rise to the well-known Heisenberg uncertainty relation [55]

$$\Delta\hat{x}\Delta\hat{p} = \Delta(\hat{a}^\dagger + \hat{a})\Delta(\hat{a}^\dagger - \hat{a}) \geq \hbar \,. \tag{1.9}$$

In these definitions, we did not consider that a photon may live on different degrees of freedom. If we now include these properties, especially the commutation relation for the creation and annihilation operators is modified

$$\left[\hat{a}_\sigma(\omega, k), \hat{a}^\dagger_{\sigma'}(\omega', k')\right] = \delta_{\sigma,\sigma'}\delta(\omega - \omega')\delta(k - k') \,. \tag{1.10}$$

The dependencies of the creation and annihilation operators, here on the frequency and momentum ω and k, as well as the polarisation σ, denote *modes* in the quantum optics language.

In quantum optics, we define a "mode" as a degree of freedom of the electric field that photons can live on. In general, a photon will not only live on a single mode, but on a combination of all possible degrees of freedom in the electric fields. However, it is not always necessary to consider

[2] In the case, where both the encoding and the photon number are considered, one writes something like $|\omega_1; \omega_2\rangle$ for two photons with frequencies ω_1 and ω_2.

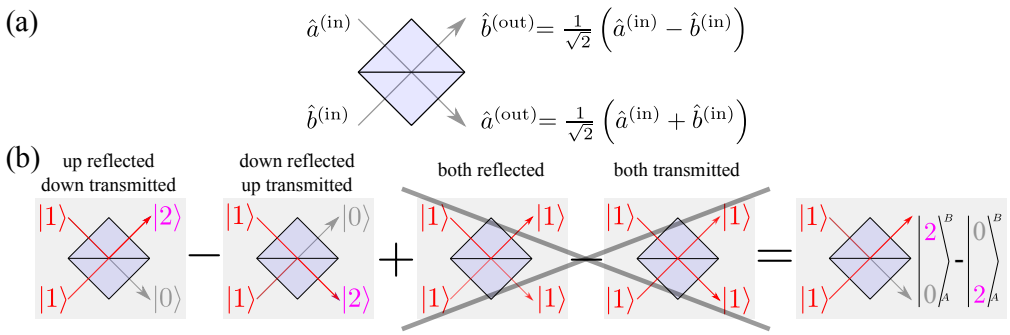

Figure 1.3 – Mode notation of a beam splitter in (a) and Hong-Ou-Mandel interference (b). The Hong-Ou-Mandel effect, sketched in (b) is a path interference of two incoming indistinguishable, single photons $|1\rangle_A \otimes |1\rangle_B$. We depict all possible paths that two photons can take through the beam splitter. However, as the last two paths acquire different signs from the unitarity of the beam splitter, they cancel out.

all modes for a specific experiment. Due to this definition, a mode can be basically anything. A popular "mode" is, for example, the polarisation of a photon, as for our example with the qubit in the beginning. However, also the frequency of a photon can be a mode [56], the momentum of a photon [57] or even the spatial mode of a waveguide [58] can be a mode for a photon. In the following section, we clarify this concept with the example of a beam splitter, which is the simplest mode-mixing device in quantum optics [1].

Passive Quantum Optics

Since quantum optics is a sub-field of general quantum mechanics, the evolution of a photon is described by a unitary transformation. Unitary transformations U are mainly characterised by the fact that they preserve the scalar product and the norm of a quantum state. The main task of *passive* unitaries, i.e. photon number preserving unitaries that we consider here, is to couple different modes with each other. The dimension of the unitary transformation is given by the number of modes that they can mix [1][3].

A beam splitter is the simplest unit to mix different modes, see figure 1.3(a). Two input modes $\hat{a}^{(\mathrm{in})}$ and $\hat{b}^{(\mathrm{in})}$ are impinging on the device and mapped to two output modes via [2]

$$\begin{pmatrix} \hat{a}^{(\mathrm{out})} \\ \hat{b}^{(\mathrm{out})} \end{pmatrix} = U_{\mathrm{BS}} \begin{pmatrix} \hat{a}^{(\mathrm{in})} \\ \hat{b}^{(\mathrm{in})} \end{pmatrix} = \frac{1}{\sqrt{2}} \begin{pmatrix} 1 & 1 \\ 1 & -1 \end{pmatrix} \begin{pmatrix} \hat{a}^{(\mathrm{in})} \\ \hat{b}^{(\mathrm{in})} \end{pmatrix} \tag{1.11}$$

Here, we use the Heisenberg picture of quantum mechanics [1, 2], as we apply the transformation on the operators and not on the quantum states themselves. Throughout this thesis, we use it in several cases, since this description offers more intuition on the physics and simplifies the

[3] In a more technical phrasing, it is given by the dimension of the Hilbert space they live on. But since the Hilbert space is spanned by the number of independent modes (as basis states), the two formulations are equivalent.

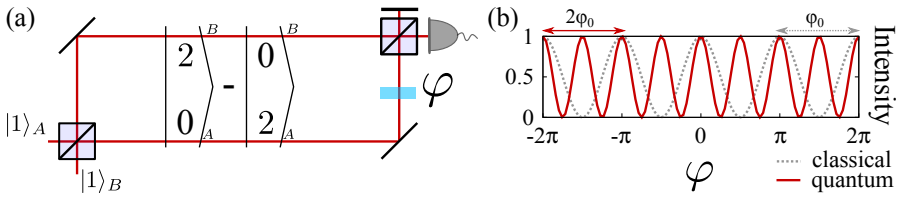

Figure 1.4 – Mach-Zehnder interferometer with two single-photon inputs and resulting interference compared to a classical reference.

calculations. The minus sign in the last entry of the matrix is needed to make the beam splitter transformation U_{BS} unitary. The beam splitter is the smallest mode mixing device with

$$\dim\left(U_{\mathrm{BS}}\right) = 2\,, \tag{1.12}$$

as it couples only two modes to each other.

However, already with such simple mode mixing devices, we are able to observe genuine quantum effects, such as the Hong-Ou-Mandel interference [59]. Here, two single, indistinguishable photons impinge on different sides on a beam splitter, one in mode A $|1\rangle_A$ and one in mode B $|1\rangle_B$, compare figure 1.3(b). Then, we have the input state

$$|\psi\rangle_{\mathrm{in}} = \hat{a}^{(\mathrm{in})^\dagger}\hat{b}^{(\mathrm{in})^\dagger}\,|0\rangle = |1\rangle_A \otimes |1\rangle_B\,. \tag{1.13}$$

If we consider all paths that the two photons may take through the beam splitter, as sketched in figure 1.3(b), we find that only the first two paths survive. This is because we cannot distinguish the cases, where both photons are either transmitted or reflected. Due to the unitarity of the beam splitter, one of them acquires a different sign and the two *paths* interfere destructively. As such, we only retain both photons either in the upper or in the lower output mode of the beam splitter and obtain the output state

$$|\psi\rangle_{\mathrm{out}} = \frac{1}{\sqrt{2}}\left(|2\rangle_A \otimes |0\rangle_B - |0\rangle_A \otimes |2\rangle_B\right)\,. \tag{1.14}$$

This result, the Hong-Ou-Mandel effect, is considered a genuine quantum interference, as the paths of the *photons* interfere and not the *amplitudes* of the involved electric fields, as in the classical case. In practice, the situation is not as simple. If the two photons differ in any other degree of freedom (i.e. frequency or polarisation), they inhabit different modes during the interference and we are able to distinguish the two cases where both photons were transmitted or reflected. Then, the last two paths in figure 1.3(b) do not cancel anymore and the Hong-Ou-Mandel effect vanishes.

The Hong-Ou-Mandel effect is a good example for the unintuitive ways that quantum optics may surprise us. The resulting state on the other hand is also the starting point for the field of quantum metrology [8]. The reason for this statement is depicted in figure 1.4. Figure 1.4(a) shows a typical Mach-Zehnder setup with two single photons in the input ports of the first beam

splitter. As we have seen in equation (1.14), the two input photons always exit the beam splitter together, leaving vacuum in the other output. Then, we put a phase-plate φ into one arm of the interferometer and record the interference pattern at one output of the second beam splitter.

The resulting interference pattern in this setup is shown in figure 1.4(b). While the interference behaviour of a classical, coherent-state reference is shown in grey, the observed two-photon interference shows a doubled fringing frequency. The reason for this behaviour is that each single photon acquires the phase φ from the phase-plate. If two photons pass the plate then

$$U_{\mathrm{PS}}(\varphi)\,|2\rangle = e^{2i\varphi}\,|2\rangle \tag{1.15}$$

each of the photons acquires a phase φ and the interference at the beam splitter exhibits twice the classical fringing frequency. This effect can be generalised to N photons, the N00N states [8]. They are defined analogously to equation (1.14)

$$|N00N\rangle = \frac{1}{\sqrt{2}}\left(|N\rangle_A\,|0\rangle_B + e^{i\vartheta}\,|0\rangle_A\,|N\rangle_B\right)\,, \tag{1.16}$$

where ϑ is an arbitrary phase-factor. In equation (1.14), we found $\vartheta = \pi$ as a special case, due to the unitarity of the beam splitter. In the interference of N00N states, again each photon acquires a phase of φ and the fringing frequency increases by a factor of N, proportional to the photon number.

The reason why this is useful for quantum metrology applications lies in the increased phase sensitivity. Compared to a classical reference, N00N states perform N times better than a classical reference of the same wavelength. This potentially allows for smaller structures in lithography applications, better phase sensitivity for sensing applications, etc. However, the practical use of this type of states is rather limited [8]. First, they are notoriously difficult to produce [9], second, to obtain a practical use in lithographic applications special types of photo-resist would be needed that work with multi-photon absorption and third, they are over-sensitive to loss and lose their enhanced phase-sensitivity already for small loss values.

As a side remark, not only many photons in few modes, as for N00N states, is an interesting application in passive quantum optics. Also rather few photons in many modes is an interesting problem, as it is difficult to compute the output probabilities after a high-dimensional coupling matrix [7, 60]. This is due to the fact that photons perform Hong-Ou-Mandel interference and we have to count all different paths that the particles might have taken. To keep track of this behaviour is difficult and led to the quantum computational problem of BosonSampling [7]. This is a problem that we will introduce in detail in section 4.3. For the moment, the take-home message is that already passive quantum optical systems show a rich multitude of complex quantum phenomena.

State Description in Phase-Space

In the previous section, we discussed the passive evolution of quantum states. Now, we introduce a state description technique that is motivated by the classical phase-space description.

The classical phase-space describes the position x and momentum p of a single particle. The time evolution of the particle is then described as trajectories through this phase-space. This

situation is sketched in figure 1.5.

Contrary to the classical particle, a quantum state cannot be described by a single point in phase-space and we cannot describe the time evolution by a defined trajectory [61]. The Heisenberg uncertainty principle [55] $\Delta x \cdot \Delta p \geq \hbar$ prohibits to determine a single point in space and assign a single momentum. Already for the coherent state, which is often considered as classical because it has a description consistent with classical theory, this is not possible. Hence, we have to find new mathematical ways to describe quantum states to obtain a phase-space representation.

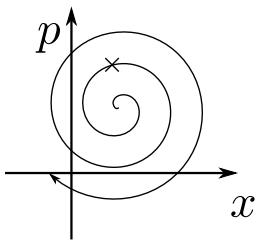

Figure 1.5 – A classical particle in phase-space.

While it may sound trivial to extend a classical phase-space description to the quantum domain by just adding some uncertainty in the position and momentum space, it is anything but easy. First, we have to find a good substitution for the two phase-space variables $\hat{x}$ and $\hat{p}$ in the quantum optics domain. Considering that light may be described by a quantum harmonic oscillator, position and momentum can be expressed by creation and annihilation operators. Then, the coherent states $|\alpha\rangle$ seem to be a prime candidate to build a phase-space[4].

As such, it is our task to develop the quantum states in question in the coherent state basis. Although this basis is not orthonormal [2, 61], it has a completeness relation

$$\mathbb{I} = \frac{1}{\pi} \int \mathrm{d}\alpha \mathrm{d}\alpha^* \, |\alpha\rangle \langle\alpha| \, , \tag{1.17}$$

where the prefactor $\frac{1}{\pi}$ compensates for the fact that coherent states are overcomplete.

Using the fact that coherent states are the left- and right-hand eigenvectors for the creation and annihilation operators, we can develop any quantum state density matrix $\hat{\rho}$ into a diagonal matrix of coherent states [61]

$$\hat{\rho} = |\psi\rangle \langle\psi| = \int \mathrm{d}^2\alpha P(\alpha) \, |\alpha\rangle \langle\alpha| \, . \tag{1.18}$$

Here, we have used the short hand $\mathrm{d}^2\alpha = \mathrm{d}\alpha \mathrm{d}\alpha^*$. The function $P(\alpha)$ [62, 63] is already one solution to our problem. It is a quasi-probability distribution that describes the properties of the quantum state in a phase-space representation. However, it is generally not very well-behaved. Already for a single coherent state $|\alpha_0\rangle$, we find that the P-function does not behave like a proper probability distribution, as it is singular

$$P(\alpha) = \delta(\alpha - \alpha_0) \, . \tag{1.19}$$

For Fock states, the situation becomes even more complicated, as the corresponding P-function becomes even more singular than a δ-distribution, it introduces its n-th derivative for an n-

[4] Coherent states are left- and right-hand eigenstates to the creation and annihilation operators, i.e. $\langle\alpha| \, \hat{a}^\dagger = \langle\alpha| \, \alpha^*$ and $\hat{a} \, |\alpha\rangle = \alpha \, |\alpha\rangle$. It reduces the operators $\hat{a}$ and $\hat{a}^\dagger$ to complex numbers α and α^*. From this, we infer $\alpha = \frac{1}{\sqrt{2}}(\hat{x} + i\hat{p})$ For a derivation of the phase-space representation with coherent states, see [2, 61].

photon Fock state [61].

Therefore, it can be useful to try a different phase-space representation. Another way to represent the density matrix $\hat{\rho}$ in terms of coherent states is to calculate its expectation value with coherent states

$$Q(\alpha) = \frac{1}{\pi} \langle \alpha | \hat{\rho} | \alpha \rangle \tag{1.20}$$

and receive the Q-function [64]. The Q-function is a completely equivalent description of the quantum state $\hat{\rho}$ in phase-space [61]. However, it is usually much better behaved than the P-function and is much closer to the properties of a classical probability distribution, i.e.

$$0 \leq Q(\alpha) \leq 1$$
$$\int \mathrm{d}^2\alpha Q(\alpha) = 1 \,.$$

The important take-home message for P- and Q-functions is that we can use them to calculate expectation values. In general, quantum mechanical expectation values can be evaluated by tracing over the operator in question multiplied by the quantum state, i.e.

$$\langle \hat{O} \rangle = \mathrm{tr}(\hat{O}\hat{\rho}) \,. \tag{1.21}$$

In phase-space, we transfer this expression to the P- and Q-functions, such that

$$\langle \hat{O} \rangle = \int \mathrm{d}^2\alpha P_{\hat{O}}(\alpha) Q_{\hat{\rho}}(\alpha) = \int \mathrm{d}^2\alpha P_{\hat{\rho}}(\alpha) Q_{\hat{O}}(\alpha) \,. \tag{1.22}$$

This means that either the operator of interest is expressed in terms of the P-function and the state via the Q-function or vice versa. For a full derivation of this expression, see [61]. The main message of this equation however is that P- and Q-functions are complementary and we can calculate expectation values with phase-space methods.

State description with Photon Number Statistics

Another popular method to describe or illustrate these different classes of states are their photon number statistics [2]. As the Fock states [equation (1.8)]

$$|n\rangle = \frac{1}{\sqrt{n!}} \hat{a}^{\dagger^n} |0\rangle \tag{1.23}$$

form an infinite dimensional, orthonormal [2] basis, we can expand any quantum state into this basis. It is therefore the perfect candidate to play around with high-dimensional spaces. However, this is not the property that we want to consider at this point and will intensify our relationship with the photon number basis at a later point in this thesis.

Due to the property that the Fock, or photon number states $|n\rangle$ form an orthonormal basis, we can write any state $|\psi\rangle$ as

$$|\psi\rangle = \sum_n \psi_n |n\rangle \,. \tag{1.24}$$

Compared to the phase space description, the photon number representation is a fully equivalent way of thinking about quantum states. The advantage of this method is that we are able to directly measure the photon number properties of a state by means of the photon number statistics.

The photon number statistics give the probability of finding a fixed number of photons n_0 in the state $|\psi\rangle$, i.e.

$$\mathrm{P}(n_0) = |\langle\psi|\, n_0\rangle|^2 \,. \tag{1.25}$$

The calculation of the photon number statistics from quantum states in the Fock representation is straightforward. We exploit the orthonormality of the Fock basis and find that the probability $\mathrm{P}(n_0)$ is given by the coefficients ψ_n

$$\mathrm{P}(n_0) = |\psi_{n_0}|^2 \,. \tag{1.26}$$

In the scope of this thesis, we will consider the measurements of photon number statistics in chapter 3 and show its applications for quantum information.

State Generation 101

In this section, we want to apply the state description techniques that we discussed in the previous section to three different classes of quantum states: coherent, single-mode and two-mode squeezed states. Additionally to their description, we consider the mathematical representation and the generation of the state in the laboratory.

Coherent States

Coherent states are typically considered the most classical of quantum states [2], as they describe the light that is produced by a laser. Another reason for this statement is their representation in phase space. In 1.6(a), we depicted the representation of a coherent state. Its description is, as we will see later, the most similar phase space function compared to a classical particle (a point). It is a filled ball at a distance $|\alpha|$ from the origin, as it has to obey the Heisenberg uncertainty principle [2]. The ball runs with the speed of $e^{i\omega t}$ around the origin in the free time evolution, if ω is the frequency of the light field.

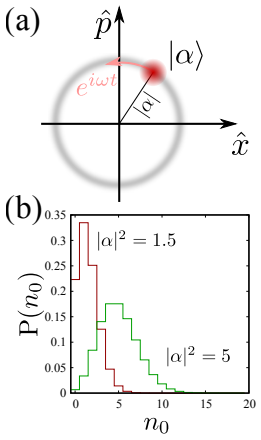

Figure 1.6 – Phase-space (a) and photon-number representation (b) of a coherent state.

In this thesis, we call the governing Hamiltonian for the generation of coherent states *lasing* Hamiltonian[5]. It can be defined by [65]

$$\hat{H}_{\text{lasing}} = i\hbar(\alpha\hat{a}^\dagger - \alpha^*\hat{a}) \,. \tag{1.27}$$

[5] Our definition of this lasing Hamiltonian is inspired by the Schrödinger picture.

From this Hamiltonian, we obtain the *coherent-state displacement operator*

$$\hat{D}(\alpha) = \exp\left(-\frac{i}{\hbar}\hat{H}_{\text{lasing}}\right) = \exp(\alpha\hat{a}^\dagger - \alpha^*\hat{a})\,, \tag{1.28}$$

which, applied on vacuum creates a coherent state $|\alpha\rangle$. This operator is decidedly *non-passive* in the sense that it does not preserve the photon number[6] when it is applied to a state. Therefore we call it an *active* transformation. This is most obvious when we apply it to the vacuum state $\hat{D}(\alpha)\,|0\rangle = |\alpha\rangle$ and calculate its mean photon number $\langle n\rangle = |\alpha|^2 > 0$. To describe the state in terms of photon number statistics, we have to develop it into the photon number basis. Then, the coherent state reads as a superposition of different Fock states $|n\rangle$

$$|\alpha\rangle = \exp\left(-\frac{1}{2}|\alpha|^2\right)\sum_{n=0}^{\infty}\frac{\alpha^n}{\sqrt{n!}}\,|n\rangle\ . \tag{1.29}$$

We depict the photon number statistics of two coherent states with amplitudes $|\alpha|^2 = 1.5$ and $|\alpha|^2 = 5$ in figure 1.6(b). As we expect from classical optics, the coherent state has Poissonian statistics [2].

Squeezed States

Now let us go really quantum. The class of states that we use in this thesis are squeezed vacuum states [2], where we have to differentiate between single-mode and two-mode squeezing. Consider single-mode squeezed states first. In the phase-space representation, plotted in figure 1.7(a), it becomes clear, why this state is called "squeezed". It is an ellipse, where the variance of the state in one direction has been reduced at the cost of increasing the other [2]. The time evolution is given as in the coherent state case, it rotates at a speed of $e^{i\omega t}$ around its centre.

The generation process of single-mode squeezed states is governed by the *squeezing* Hamiltonian [65]

$$\hat{H}_{\text{SM squeezing}} = \frac{i\hbar}{2}\left(\zeta^*\hat{a}^2 - \zeta\hat{a}^{\dagger 2}\right)\ . \tag{1.30}$$

The resulting *quadrature-squeezed operator* [2] for the single-mode case is then given by

$$\hat{S}_{\text{SM}}(\zeta) = \exp\left(-\frac{i}{\hbar}\hat{H}_{\text{SM squeezing}}\right) = \exp\left(\frac{1}{2}\zeta^*\hat{a}^2 - \frac{1}{2}\zeta\hat{a}^{\dagger 2}\right) \tag{1.31}$$

This operator is also active as it does not preserve the photon number $\langle n\rangle = \sinh^2(r) > 0$. Here, $r = |\zeta|$ is the absolute value

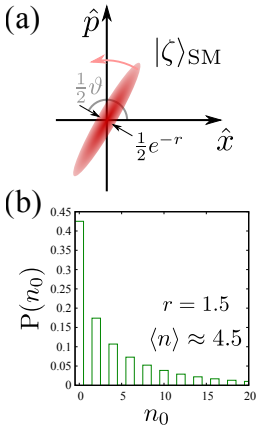

Figure 1.7 – Phase-space (a) and photon-number representation (b) of a single-mode squeezed state.

[6] It is however unitary $\hat{D}(\alpha)\hat{D}^\dagger(\alpha) = \hat{D}^\dagger(\alpha)\hat{D}(\alpha) = 1$.

of the complex squeezing parameter $\zeta = re^{i\vartheta}$. As with the coherent state, we develop the single-mode squeezed state in the Fock basis and obtain [2]

$$|\zeta\rangle_{\mathrm{SM}} = \frac{1}{\sqrt{\cosh(r)}} \sum_{n=0}^{\infty} \frac{\sqrt{(2n)!}}{n!} \left[-\frac{1}{2} e^{i\vartheta} \tanh(r) \right]^n |2n\rangle \ . \tag{1.32}$$

Both from the operator representation and the Fock basis representation we observe that a single-mode squeezed vacuum state only contains even photon numbers. This propagates through to the photon number statistics, illustrated in figure 1.7(b), which show that the probability to measure uneven photon numbers is zero.

For the two-mode squeezed vacuum state the situation is slightly different. Instead of one mode in the single-mode squeezing case, now two modes (i.e. $\hat{a}$ and $\hat{b}$) are affected by the squeezing operation. For the governing Hamiltonian of the state generation this means

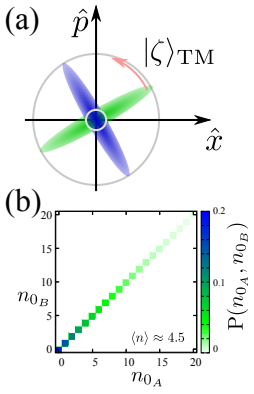

Figure 1.8 – Phase-space (a) and photon-number representation (b) of a two-mode squeezed state.

$$\hat{H}_{\mathrm{TM\,squeezing}} = \frac{i\hbar}{2} \left(\zeta^* \hat{a}\hat{b} - \zeta \hat{a}^\dagger \hat{b}^\dagger \right) \ . \tag{1.33}$$

In the phase space representation in 1.8(a), this can be imagined by having two ellipses that are tilted by 90°. The small circle describes the uncertainty for one variable, e.g. $\hat{x}$ after a measurement in the other mode, while the large circle describes the uncertainty in the conjugate mode. As for the other cases, they rotate around their centre with the speed $e^{i\omega t}$. The corresponding two-mode squeezing operator is given by

$$\hat{S}_{\mathrm{TM}}(\zeta) = \exp\left(\frac{1}{2} \zeta^* \hat{a}\hat{b} - \frac{1}{2} \zeta \hat{a}^\dagger \hat{b}^\dagger \right) \ , \tag{1.34}$$

which depends on the same squeezing parameter ζ as the single-mode squeezed state. The Fock expansion of the two-mode squeezed state reads

$$|\zeta\rangle_{\mathrm{TM}} = \frac{1}{\cosh(r)} \sum_{n=0}^{\infty} \left[e^{i\vartheta} \tanh(r) \right]^n |n\rangle_A \otimes |n\rangle_B \ . \tag{1.35}$$

The two-mode squeezed state yields *perfect photon number correlation*, i.e. same number of photons, between the two affected modes A and B. We calculate the photon number statistics of a two-mode squeezed state and plot them in figure 1.8(b). As we have to consider the photon numbers for two modes A and B[7], the corresponding plot is two-dimensional. From this figure, we can directly observe the perfect photon number correlations between modes A and B, which can be used for detector calibration [66].

[7] As two-mode squeezing populates two modes with n photons $|n\rangle_A \otimes |n\rangle_B$, we obtain a two-dimensional probability distribution $\mathrm{P}(n_{0_A}, n_{0_B}) = |\langle \psi | \, n_{0_A} \otimes n_{0_B} \rangle|^2$ for the photon number statistics.

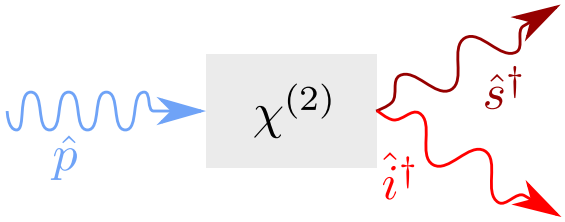

Figure 1.9 – Schematic of a down-conversion process. A high-energy pump photon $\hat{p}$ decays probabilistically into two daughter photons, signal $\hat{s}^\dagger$ and idler $\hat{i}^\dagger$.

Squeezed State Generation via Down-conversion

The remaining question that we have to answer is how to generate these states in the laboratory. Implementing a coherent state is relatively easy, as it is the state that is produced by a laser [2]. The generation of a squeezed state is a bit more tricky. In this thesis, we employ the process of parametric down-conversion [67, 68], as schematically depicted in figure 1.9. Here, a photon from a high-energy, classical pump field decays probabilistically into two daughter photons, usually labelled signal and idler, or signal and herald. In the following chapters, we will go into the details of parametric down-conversion, however at this point we only want to roughly sketch why such a process may be used to generate squeezed states. Encoding the corresponding decay process in the second quantisation formalism yields [69]

$$\hat{H}_{\mathrm{PDC}} \propto \hat{p}\hat{s}^\dagger\hat{i}^\dagger + \mathrm{h.c.}\,, \tag{1.36}$$

where we use the hermitian conjugate to construct a hermitian operator. Here, $\hat{p}$ denotes the decayed pump photon, $\hat{s}^\dagger$ the created signal and $\hat{i}^\dagger$ the created idler photon. Naturally, this "derivation" is neither complete or an ironclad argument, however it is enough to motivate why a decay process such as parametric down-conversion implements a squeezing Hamiltionan, as it looks very similar to equations (1.30) and (1.33). With this argument, we can identify the two generated photons of signal and idler as the two creation operators in the squeezing Hamiltonian.

However, in equation (1.36), we find an additional annihilation operator for a pump photon, which is not contained in the squeezing Hamiltonian. This discrepancy may be resolved with the information that the down-conversion process is very inefficient and we use a strong, classical pump field to generate the photon pairs. Then, we approximate the annihilation operator in equation (1.36) by a classical field amplitude.

Depending on the modes that the signal and idler photons are created in, we distinguish between different types of parametric down-conversion. If they are created in the same mode, we implement

$$\hat{H}_{\mathrm{PDC\,1}} = \alpha_p\hat{a}^\dagger\hat{a}^\dagger + \mathrm{h.c.}\,, \tag{1.37}$$

which is a single-mode squeezed state. As the photos are created in the same mode and described by the same creation operator, the photons are *fundamentally indistinguishable* [2]. In practice, this means that the two photons are generated into the same polarisation mode and the process

is classified as either *type-0* or *type-I* [69].

However, we can also create the signal and idler photons in different modes. Then, we implement a two-mode squeezer with our down-conversion process with the governing Hamiltonian

$$\hat{H}_{\mathrm{PDC}\,2} = \alpha_p \hat{a}^\dagger \hat{b}^\dagger + \mathrm{h.c.}\,. \tag{1.38}$$

In the experiment, this means that we generate our two photons in orthogonal polarisation modes. Such a down-conversion process is classified as *type-II* [69].

State Detection

The simplest measurement operator in quantum optics is the projector $\hat{\mathcal{P}}_m$ [1]. It projects the incoming state $|\psi\rangle$ onto its subspace $|m\rangle$ and yields the probability $|p_m|^2$ that $|\psi\rangle$ has been in this subspace

$$\hat{\mathcal{P}}_m |\psi\rangle = p_m |m\rangle \ . \tag{1.39}$$

However, for many applications this formalism is too narrow. Especially in the case, where we are only interested in the measurement *probabilities* $|p_m|^2$ the use of projectors is not always the method of choice. Then, usually POVMs (or Positive Operator-Valued Measures) are used [1]. Consider a measurement M which has different outcomes m. Then $\hat{M}_m$ is a corresponding measurement operator, whose shape is not of particular interest here. As before, we want to measure a quantum state $|\psi\rangle$. The probability to measure the result m is given by

$$|p_m|^2 = \langle\psi| \hat{M}_m^\dagger \hat{M}_m |\psi\rangle \ . \tag{1.40}$$

Note, that this expression does not consider the final state after the measurement, as it is not of interest. We can further combine the two operators $\hat{\pi}_M = \hat{M}_m^\dagger \hat{M}_m$, where $\hat{\pi}_m$ is a positive operator[8] with

$$\begin{aligned} \sum_m \hat{\pi}_m &= \mathbb{I} \\ |p_m|^2 &= \langle\psi| \hat{\pi}_m |\psi\rangle \ . \end{aligned} \tag{1.41}$$

The operators $\hat{\pi}_m$ are called the POVM elements of the measurement M and the set of $\{\hat{\pi}_m\}$ is the associated POVM [1]. For this thesis, the only important thing to know about POVMs is that they describe a specific measurement or detection setup completely. We will use this later for the characterisation of a detector system.

Structure of this Work

In this work, we present and discuss new techniques and applications of high-dimensional quantum optics. This field is a vast playground of degrees of freedom, so we have taken a perhaps slightly unusual approach for this thesis. We proceed concept by concept, as we consider many different aspects of high-dimensionality in this thesis and therefore discuss different concepts in

[8] Which means that its eigenspectrum only has positive-semidefinite eigenvalues.

the different chapters and distribute the corresponding state of the art and the theoretical concepts accordingly.

This thesis is divided into three main chapters. In chapter 2, we develop a novel type of down-conversion source, which uses coupled waveguides to produce two-photon N00N states. We review the theory of coupled waveguides and apply it to the process of parametric down-conversion. With this approach, we develop a genuinely novel type of quantum state source and experimentally show that we can produce and verify the expected two-photon N00N state.

In chapter 3 we apply the newly developed quantum state source with its higher photon number contributions to investigate transmission of non-classicality in atmospheric channels. As we consider higher photon number contributions, we review a method for photon number resolved detection by means of time-multiplexing and explore its limits for the resolution of high photon number states in section 3.1. Afterwards, we develop a detector calibration technique in section 3.2, based on the time-multiplexing technique to probe detector properties with minimal experimental and computational overhead. Finally, in section 3.3, we combine our results from chapters 2 and 3 to probe the resilience of non-classical light under atmospheric turbulences. This is a particularly interesting question in the field of quantum communication, as the non-classicality of the light may be destroyed on, e.g. the way from a satellite to the ground station. Here, both our developed down-conversion source and the time-multiplexed technique find their application to identify regimes where quantum secure communication is preserved.

Chapter 4 is inspired by a down-conversion source with many coupled waveguides, which we review in section 4.1. From this idea, we develop several theoretical core concepts that find their application in quantum computation. First, we present a new type of quantum walk scenario in section 4.2, where we introduce fundamentally new quantum dynamics by introducing a driving force, either by a lasing or a squeezing Hamiltonian. The last two sections of this work address the concept of BosonSampling. We introduce this computational model in depth in section 4.3, before we map it to the high-dimensional coupled waveguide system from section 4.1. Finally, we present the concept of *Gaussian* BosonSampling, which uses genuine Gaussian states, i.e. single-mode squeezed states, to formulate a problem that is hard to solve with classical resources and probe the possibilities of quantum vs. classical computation power.

Finally, we summarise our work and give a conclusion in chapter 5.

Vielleicht fall ich auf die Fresse,
aber lest mir keine Messe!
Egal was auch passiert:
Ich hab's wenigstens probiert!

Wise Guys - Jetzt erst recht

2

Dual-rail down-conversion source for two-photon N00N states

Contents

Before discussing *high*-dimensional quantum systems, we begin with a small, manageable system to understand the basics. To this aim, we focus on the implementation of a dual-path integrated parametric down-conversion source and discuss how it is able to produce post-selection free two-photon N00N states [70].

We already learned about the existence of two-photon N00N states and their application for quantum metrology in chapter 1 in the context of Hong-Ou-Mandel interference [8, 59]. Yet, the generation of N00N states in the Hong-Ou-Mandel experiment was a rather accidental aspect and therefore has not been recognised at that time.

Originally, N00N states were introduced in 1989 by Barry Sanders [71], who was interested in the dynamical properties of the nonlinear rotator. Even with the Hong-Ou-Mandel experiment two years earlier [59], it took until the year 2000, when the group of Jonathan Dowling recognised the potential of N00N states for quantum metrology [8]. They found that a state of the form

$$|N00N\rangle = \frac{1}{\sqrt{2}}(|N0\rangle + e^{i\varphi}\,|0N\rangle) \tag{2.1}$$

exhibits an N-fold enhanced sensitivity to phase changes in an optical interferometer, compared to a coherent state reference. Due to this potential quantum advantage and the fact that with large N, we obtain a macroscopic entangled state that may probe the quantum-classical border, many experiments have been performed to generate these states.

The simplest generation technique for two-photon N00N states is the bulk Hong-Ou-Mandel

experiment [59], which we discussed in chapter 1. We take two indistinguishable photons, however they have been produced, and interfere them on a beam splitter to obtain the desired N00N state. However, $N = 2$ is the largest N00N state that we can directly generate with a beam splitter. Consider the N-photon component of a two-mode squeezed input state $|N\rangle |N\rangle$ and interfere the two modes on a beam splitter. This leads to a generalised Hong-Ou-Mandel interference

$$\begin{aligned} & U_{\mathrm{BS}} |N\rangle |N\rangle \\ & \quad \propto c_N |N\rangle |0\rangle + c_{N-2} |N-2\rangle |2\rangle + ... + c_{N/2} |N/2\rangle |N/2\rangle \\ & \qquad + ... + c_{N-2} |2\rangle |N-2\rangle + c_N |0\rangle |N\rangle \ , \end{aligned} \tag{2.2}$$

which definitely does not produce a N00N state [9]. While this state is still interesting for quantum metrology, as it surpasses the classical resolution limit, it does not perform as optimal as the pure N00N states [72].

As such, one challenge is to generate higher order N00N states in an experiment. As the generalised Hong-Ou-Mandel interference does not produce N00N states, several other protocols based on effective nonlinearities from detection processes (heralding or post-selection) have been proposed [73–77]. Using these techniques, the first $N > 2$ experiments could be performed in 2004 by the groups of A. Steinberg ($N = 3$) [78] and A. Zeilinger ($N = 4$) [79], with fringing visibilities[1] of $\mathcal{V}_{\text{Stein}} = 42\,\%$ and $\mathcal{V}_{\text{Zeil}} = 61\,\%$, respectively. Three years later, in 2007, N00N-like superresolution with $N = 6$ was demonstrated by the group of A. White [80] using only coherent states. This is a surprising result, as coherent states should follow the classical behaviour that we discussed in chapter 1. However, the superresolution that was demonstrated in this experiment does not contradict the classical expectations. While the fringing period of the interference signal was enhanced by a factor of $N = 6$, the sensitivity of the state to phase changes (as given by the slope of the interference curve) did not exceed the classical limit due to the low visibility of the interference signal. Indeed, this problem with superresolution was pointed out already in 2004 [79] and expected by the authors [80]. Only later in 2007, the first experiment to achieve good enough visibility to both verify superresolution and supersensitivity was demonstrated [81] with $N = 4$ N00N states and a fringing visibility of $\mathcal{V} = 91\,\%$. As it is, the record number for "real" N00N states is $N = 5$, as demonstrated by the group of Y. Silberberg in 2010 [82]. Since then, many N00N state experiments have been performed in various platforms [83–92]. However it still remains a challenge to reliably detect N00N states with a good fidelity, as they are not only supersensitive with respect to phase changes, but also to loss [8]. As such, different classes of states have been investigated that promise more robustness for real-life quantum metrology [93–95].

In this thesis, it is not our aim to push the high N00N state production further, but we want to investigate another challenge in the generation of N00N states, the transfer to an integrated platform. While the task to integrate the Hong-Ou-Mandel experiment on a single chip may sound straightforward, it is anything but easy. In an integrated platform, we use waveguided parametric down-conversion processes, where the generated photons are usually created in the same spa-

[1] The visibility describes the contrast between minima and maxima of the interference curve. It is usually defined by $\mathcal{V} = \frac{\text{Max}-\text{Min}}{\text{Max}+\text{Min}}$.

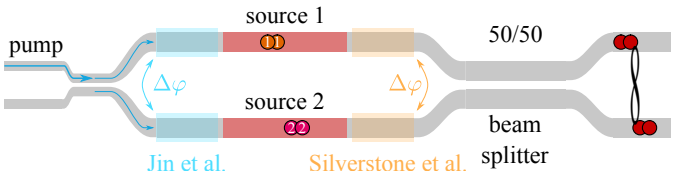

Figure 2.1 – Two-photon N00N state generation scheme adapted from [96, 97]. Two separate down-conversion sources are interfered on a 50/50 beam splitter to erase the information in which source the photon pair has been created. Both schemes need additional integrated phase-shifters ($\Delta\varphi$) to control the N00N state generation and narrowband filtering after the chip (not shown) to enable the indistinguishability of the two sources.

tial mode of the same waveguide [98]. As such, it is difficult to separate the generated photons (for type-II down-conversion with a polarising beam splitter) and interfere them later on (as the speed of the photons on the two polarisation axes has to be compensated). For a type-I process, it is even impossible to separate them deterministically, as the photons are indistinguishable.

As such, only recently two experiments by Silverstone et al. [96] and Jin et al. [97] demonstrated the generation of two-photon N00N states in an integrated platform. Both schemes comprise two separately pumped down-conversion sources ([96] uses silica as support material, while [97] uses lithium niobate) which are then interfered on an integrated beam splitter to erase the information which source created the photon pair, see figure 2.1. While this two-source solution fulfils the aim to generate the desired two-photon N00N states, it does not present a single integrated device, but relies on a full integrated circuit comprising one phase-shifter ($\Delta\varphi$), two separate sources and two integrated beam splitters. Furthermore, this approach needs to use additional resources, such as post-selection and has to apply narrow-band filtering to ensure the indistinguishability of the two down-conversion sources.

Our aim in this chapter of the thesis is to develop a single non-linear integrated component which produces post-selection free two-photon N00N states. We use a non-linear waveguide coupler that comprises two parallel, weakly coupled waveguides at a distance of several μm which are periodically poled [99, 100], see figure 2.2. Our approach to utilise the underlying linear waveguide geometry [101–104] to engineer the state generation via parametric down-conversion (PDC) [67, 68, 98] is a novel physical concept that intrinsically introduces the path degree of freedom to photonic state generation in waveguide based technology. As such, we further increase the integration density by developing a single integrated device that produces two-photon N00N states.

This chapter is structured as follows: we lay down the foundations of the linear coupling model for weakly coupled waveguides in section 2.1, before we explain the impact on the photon generation via PDC in section 2.2. From the experimental side, we first characterise the linear properties of the used sample[2], i.e. loss and coupling strength in section 2.3. Afterwards,

[2]Courtesy of S. Brauner, who characterised the samples during his time as a student helper in our group.

we focus on the main result, the verification that a non-linear two-coupled waveguide device produces post-selection free two-photon N00N states in section 2.4. To do this, we first directly record the spatially resolved two-photon click events (coincidences) as a necessary condition for N00N states and in a second step show the expected double-frequency interference pattern as the sufficient condition. Finally, we discuss the properties of the higher photon number contributions of this coupled waveguide source in section 2.5.

2.1 Model for the Weak Coupling Regime

To understand the impact of coupled waveguides on the photon generation process, we review the linear properties of coupled two-waveguide structures in this section. An example system is sketched in figure 2.2(a). It consists of two parallel waveguide channels that are close enough to each other that an incoupled field E_{in} can traverse to the adjacent channel. In our case, we assume the waveguides to be weakly coupled, which implies two assumptions [104][3]. Firstly, the solution of the coupled system is given by a linear combination of the undisturbed waveguide solutions [105], i.e. the spatial field distribution inside a single waveguide is not modified by the coupling and only the field amplitudes change over time. Secondly, the coupling strength C is proportional to the overlap between the electric fields in waveguide 1 and waveguide 2 [106].

Then, the evolution of the electric fields in the coupled waveguide structure along the propagation direction z is given by the following differential equations [104]

$$\begin{aligned} \frac{d}{dz}e_1(z)E_1(x,y) &= i\beta(\omega)e_1(z)E_1(x,y) - iCe_2(z)E_2(x,y) \\ \frac{d}{dz}e_2(z)E_2(x,y) &= i\beta(\omega)e_2(z)E_2(x,y) - iCe_1(z)E_1(x,y)\,, \end{aligned} \tag{2.3}$$

where $E_i(x,y)$ denotes the spatial mode profiles of the uncoupled waveguides in the x,y-plane, perpendicular to z and $\beta(\omega) = n_{\mathrm{eff}}(\omega)\omega/c$ is the propagation constant for an electric field of frequency ω that propagates in a waveguide with effective refractive index $n_{\mathrm{eff}}(\omega)$. Here, we incorporated the assumption that the spatial mode profiles remain unmodified by separating the propagating excitation amplitudes $e_i(z)$ along the z-axis from the mode profiles $E_i(x,y)$. Focusing only on the excitation amplitudes and using a matrix representation, equation (2.3) reads

$$\frac{d}{dz}\begin{pmatrix} e_1(z) \\ e_2(z) \end{pmatrix} = i\begin{pmatrix} \beta(\omega) & -C \\ -C & \beta(\omega) \end{pmatrix}\begin{pmatrix} e_1(z) \\ e_2(z) \end{pmatrix}. \tag{2.4}$$

Solving equation (2.4) yields the eigenmode description of the coupled waveguide system. The so-called anti-symmetric eigensolution is given by

$$\begin{aligned} \beta_A(\omega) &= i[\beta(\omega) + C] \\ E_A &= \frac{1}{\sqrt{2}}\begin{pmatrix} 1 \\ -1 \end{pmatrix} \end{aligned} \tag{2.5}$$

[3]The large separation of the two waveguides in the experimental implementation justifies this pertubative approach.

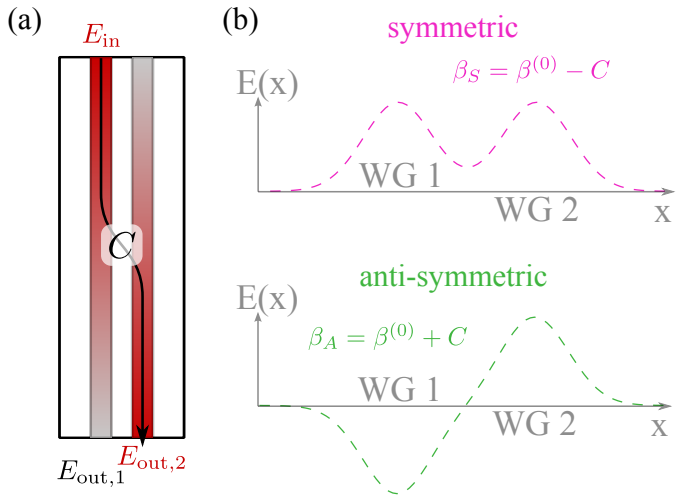

Figure 2.2 – Sketch of the linear part of the sample and eigenmode description. Figure (a) shows the linear part of our structure that consists of two parallel, weakly coupled waveguides. The overlap of the electric fields between the two waveguides directly determines the coupling parameter C. In (b), we have depicted the eigenmode solution to the system. In the weak coupling regime, the two eigenmodes are given by a linear combination of the single waveguide modes, i.e. the symmetric (pink) and anti-symmetric (green) combination.

and the symmetric solution by

$$\begin{aligned} \beta_S(\omega) &= i[\beta(\omega) - C] \\ E_S &= \frac{1}{\sqrt{2}} \begin{pmatrix} 1 \\ 1 \end{pmatrix} . \end{aligned} \tag{2.6}$$

The eigensolutions are characterised by the fact that they are position-independent and $\beta_j(\omega)$ denotes the modified propagation constant of the j-th eigenmode. If we re-insert the spatial mode profiles of the undisturbed waveguide $E = e_i(z)E_i(x, y)$, where $e_i(z)$ is in the eigenmode description and position-independent, equations (2.5) and (2.6) read

$$E_A = \frac{1}{\sqrt{2}} \begin{pmatrix} E_1(x, y) \\ -E_2(x, y) \end{pmatrix} \quad \text{and} \quad E_S = \frac{1}{\sqrt{2}} \begin{pmatrix} E_1(x, y) \\ E_2(x, y) \end{pmatrix} . \tag{2.7}$$

We plot two eigenmodes of a coupler system in figure 2.2(b). Finally, the position-dependent electric field in the waveguides 1 and 2 is given by linear combinations of the eigenmodes [104]

$$\begin{aligned} E_1(x, y, z) &= \frac{1}{\sqrt{2}} \left[e^{-i\beta_S(\omega)z} + e^{-i\beta_A(\omega)z} \right] E_1(x, y) \\ E_2(x, y, z) &= \frac{1}{\sqrt{2}} \left[e^{-i\beta_S(\omega)z} - e^{-i\beta_A(\omega)z} \right] E_2(x, y) . \end{aligned} \tag{2.8}$$

This general solution to the coupled differential equation system of equation (2.3) describes the field coupling between the two waveguides as an interference of the two eigenmodes. As the eigenmodes themselves are position-independent with different propagation constants, they will interfere constructively in waveguide 1 at[4] $z = 0$. However, at this position, they will interfere destructively in waveguide 2 and the overall field strength is concentrated in waveguide 1. This situation is reversed at $z = \frac{\pi}{\beta_S(\omega) - \beta_A(\omega)}$.

2.2 Impact on the Photon Pair Generation

In the previous section, we have considered the effect of the weak coupling between two waveguides on the electric fields. Now, we discuss the non-linear PDC process and analyse how the modification by the coupling influences the properties of the photon generation. However, firstly we briefly recapitulate the properties of a simple PDC process, either for bulk or single waveguides. For a more in-depth discussion of PDC processes, along with a mathematical derivation of the governing Hamiltonian, we recommend [69, 107, 108] as independent reading.

During the PDC process, a high-energy pump photon with frequency ω_p spontaneously decays inside a crystal of length L into two low energy photons, signal with ω_s and idler with ω_i, compare figure 2.3(a). The pump, signal and idler fields are coupled via a $\chi^{(2)}$ non-linearity and the full process is governed by [109]

$$\hat{H}_{\mathrm{int}} \propto \chi^{(2)} \int\limits_V \mathcal{E}_p^{(+)}(\vec{r}, t)\, \hat{E}^{(-)}(\vec{r}, t)\, \hat{E}^{(-)}(\vec{r}, t) + \mathrm{h.c.}\, d^3 r\,, \tag{2.9}$$

where $\mathcal{E}_p$ is the classical pump and $\hat{E}$ are the generated quantum field amplitudes. In the scope of this thesis we only consider type-I processes where the two quantum fields are generated in the same polarisation mode[5]. Therefore, we have omitted the labels for signal and idler for the quantum field amplitudes. Then, the generated photons are fundamentally indistinguishable [2], which guarantees perfect interference properties [59] between them.

Solving the Hamiltonian is a straightforward calculation and results in the output state[6]

$$|\Psi_{\mathrm{out}}\rangle = \exp\left\{ -\frac{i}{\hbar} \int\limits_{-\infty}^{\infty} d\omega_s \int\limits_{-\infty}^{\infty} d\omega_i, \alpha(\omega_s + \omega_i) \right. \\ \left. \times\ \mathrm{sinc}\left[\Delta\beta(\omega_s, \omega_i) \frac{L}{2} \right] e^{-i\Delta\beta(\omega_s,\omega_i)\frac{L}{2}} \hat{a}^\dagger(\omega_s) \hat{a}^\dagger(\omega_i) + \mathrm{h.c.} \right\} |0\rangle\ , \tag{2.10}$$

where $\alpha(\omega_s + \omega_i)$ contains the spectral shape of the pump field as well as the energy conservation

[4] This corresponds to an excitation of waveguide 1 at $z = 0$. Other initial conditions may be encoded by introducing a $z - z_0$ variable, with $e_1(z_0) = 1$.

[5] As opposed to a type-II process where the photons are generated into orthogonal polarisations. Speaking in quantum states, a type-I process generates a single-mode squeezed state, while a type-II process generates a two-mode squeezed state.

[6] Neglecting time-ordering effects [110], which is justified at our power levels.

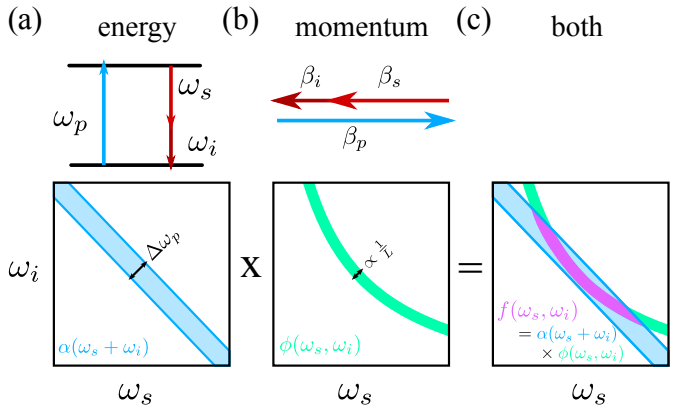

Figure 2.3 – Interpretation of the governing functions in the PDC process. Figure (a) represents the energy conservation with the frequencies of the involved fields. The corresponding characteristic function is the pump distribution $\alpha(\omega_s+\omega_i)$, its width is directly given by the pump spectrum. Figure (b) illustrates the momentum conservation for the propagation vectors. Contrary to the energy conservation, the width of the characteristic phase-matching function is mostly determined by the length of the crystal. In (c) both are combined to the joint-spectral-amplitude function, that completely determines the spectral properties of the PDC process.

condition $[\omega_p = \omega_s + \omega_i]$. The sinc-function represents momentum conservation that is given by the propagation constants of the three light fields $[\Delta\beta = \beta(\omega_p) - (\beta(\omega_s) + \beta(\omega_i)) - \frac{2\pi}{\Lambda}]$[7]. The additional $\frac{2\pi}{\Lambda}$ comes from a periodic sign-inversion of the $\chi^{(2)}$ non-linearity, the periodic poling [99, 100]. This sign-inversion with period Λ introduces an additional momentum contribution, which allows us to shift the phase-matching condition to the desired wavelength combinations.

A graphical interpretation of the output state in equation (2.10) is given in figure 2.3. We consider the energy conservation condition in 2.3(a). The top part depicts this condition for the frequencies and the bottom part shows the pump spectrum dependent on the signal and idler wavelengths. As we have to fulfil $\omega_p = \omega_s + \omega_i$, α is oriented along the $-45°$-diagonal. The width of this function is solely given by the width of the pump spectrum $\Delta\omega_p$. Correspondingly, the top part of figure 2.3(b) represents the momentum conservation condition. Depicting the momentum conservation condition depending on the signal and idler frequencies also gives a curve oriented along the $-45°$-axis, however the width of this phase-matching function ϕ is determined by the finite width of the crystal and the curvature by the dispersion of the material. Combining pump spectrum and phase-matching, as shown in (c), yields the joint-spectral-amplitude f (shown in pink) that fully determines the spectral properties of the generated PDC state. Note that the pump spectrum cuts only a finite part of the phase-matching. This will enable us to excite specific spatial properties in the generated PDC states by tuning the pump spectrum.

[7] Usually, the output state also contains a phase-term that originates from the free propagation of the field inside the crystal [111]. It is however not important for the interpretation of the state given in (2.10) and will be omitted at this point of the discussion.

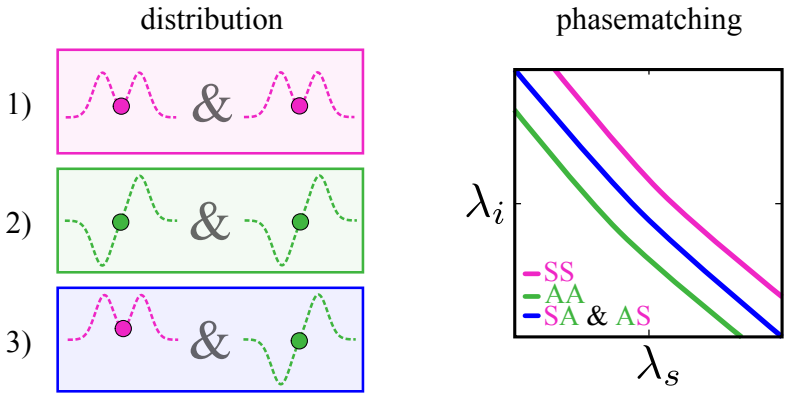

Figure 2.4 – Effect of the eigenmode combinations on the phase-matching function of the PDC process. During PDC photons are always created pairwise. This means, that we have three different possibilities to distribute the photons of one pair across the eigenmodes of the coupler structure. Possibility 1) considers that both photons are generated into the symmetric eigenmode and the corresponding phase-matching curve is given in pink. For 2), both are generated into the anti-symmetric eigenmode and the phase-matching curve is shifted, as drawn in green. The third possibility, one photon in each eigenmode is shifted to the middle and sketched in blue.

The impact of the coupler structure on the PDC process is encoded in the phase-matching condition $\Delta\beta \stackrel{!}{=} 0$. As we have seen in the previous section, the coupler structure introduces two, non-degenerate eigenvalues for the propagation vector. This means that we have to consider the impact of different eigenmode combinations on the phase-matching condition. We have sketched this influence on the phase-matching function in figure 2.4. During the PDC process, photons are always created in pairs [69]. This gives us the freedom to distribute two photons in combinations of two eigenmodes, as shown in the left-hand part of the figure. We have three distinct possibilities with propagation vectors accordingly modified

1) both photons symmetric: $\Delta\beta = \beta(\omega_p) - [\beta_S(\omega_s) + \beta_S(\omega_i)]$,

2) both photons anti-symmetric: $\Delta\beta = \beta(\omega_p) - [\beta_A(\omega_s) + \beta_A(\omega_i)]$ and

3) one photon in each: $\Delta\beta = \beta(\omega_p) - [\beta_S(\omega_s) + \beta_A(\omega_i)]$.

Due to the non-degeneracy of the coupler-eigenvalues $\beta_{S/A}(\omega)$, we get three different, spectrally distinct phase-matching functions [70], as shown on the right side of figure 2.4. For better comparability to the measured data in following sections, we have changed the axes from frequency to wavelength scale. Possibility 1) gives a phase-mismatch $\Delta\beta_{SS} = \Delta\beta^{(0)} + 2C$, which shifts the phase-matching curve (pink) to higher wavelengths (or smaller frequencies). The fully anti-symmetric possibility 2) gains the negative phase-mismatch from the coupler structure $\Delta\beta_{AA} = \Delta\beta^{(0)} - 2C$ and is accordingly shifted to lower wavelengths (or higher frequencies) (green). For the third combination, the contributions from symmetric and anti-symmetric eigen-

value cancel out and we remain with $\Delta\beta_{SA,AS} = \Delta\beta^{(0)}$ (blue). It is accordingly not shifted and lies on the phase-matching curve of the undisturbed system.

For the full PDC output state of the coupler structure in the two-photon picture, i.e. taking only the first order Taylor-expansion of equation (2.10), we have to add all possible phase-matching conditions. The output state then reads [70]

$$\begin{aligned}|\Psi\rangle^{\mathrm{eig}} = \frac{1}{\mathcal{N}} \int_{-\infty}^{\infty} d\omega_s \int_{-\infty}^{\infty} d\omega_i \, \alpha(\omega_s+\omega_i) \, \Big[\gamma \,\mathrm{sinc}\left(\Delta\beta_{S,S}\frac{L}{2}\right) e^{-i\Delta\beta_{S,S}\frac{L}{2}} \hat{a}_S^\dagger(\omega_s)\hat{a}_S^\dagger(\omega_i) \\ +\delta \,\mathrm{sinc}\left(\Delta\beta_{S,A}\frac{L}{2}\right) e^{-i\Delta\beta_{S,A}\frac{L}{2}} \hat{a}_S^\dagger(\omega_s)\hat{a}_A^\dagger(\omega_i) + \delta \,\mathrm{sinc}\left(\Delta\beta_{A,S}\frac{L}{2}\right) e^{-i\Delta\beta_{A,S}\frac{L}{2}} \hat{a}_A^\dagger(\omega_s)\hat{a}_S^\dagger(\omega_i) \\ + \gamma \,\mathrm{sinc}\left(\Delta\beta_{A,A}\frac{L}{2}\right) e^{-i\Delta\beta_{A,A}\frac{L}{2}} \hat{a}_A^\dagger(\omega_s)\hat{a}_A^\dagger(\omega_i)\Big] \, |0\rangle \ ,\end{aligned} \tag{2.11}$$

in the eigenmode basis of the coupler, where γ and δ are the excitation amplitudes for the pump in the symmetric and anti-symmetric eigenmode, respectively and $\mathcal{N}$ is the normalisation constant of our state. The additional phase-terms $e^{-i\Delta\beta_{i,j}\frac{L}{2}}$ in the coupler state stem from the linear propagation inside the sample [111]. While they, in general, can be ignored, the use of a basis transformation in the spatial domain is sensitive to additional phases. Omitting them from the calculation yields incorrect results. For a complete mathematical derivation of the coupler state, see appendix B.

To transform this description back to the waveguide basis of the experiment, we have to apply the time-independent basis transformation of equation (2.8)

$$E_1 = \frac{1}{\sqrt{2}}(E_S + E_A) \qquad E_2 = \frac{1}{\sqrt{2}}(E_S - E_A)\,. \tag{2.12}$$

This yields [70]

$$\begin{aligned}|\Psi\rangle^{\mathrm{WG}} = \frac{1}{2\sqrt{\mathcal{N}}} \int_{-\infty}^{\infty} d\omega_s \int_{-\infty}^{\infty} d\omega_i \, \alpha(\omega_s+\omega_i) \\ \Bigg[\Bigg(\gamma \left\{\mathrm{sinc}\left(\Delta\beta_{S,S}\frac{L}{2}\right) e^{-i\Delta\beta_{S,S}\frac{L}{2}} + \mathrm{sinc}\left(\Delta\beta_{A,A}\frac{L}{2}\right) e^{-i\Delta\beta_{A,A}\frac{L}{2}}\right\} \\ + \delta \left\{\mathrm{sinc}\left(\Delta\beta_{S,A}\frac{L}{2}\right) e^{-i\Delta\beta_{S,A}\frac{L}{2}} + \mathrm{sinc}\left(\Delta\beta_{A,S}\frac{L}{2}\right) e^{-i\Delta\beta_{A,S}\frac{L}{2}}\right\}\Bigg) \hat{a}_1^\dagger(\omega_s)\hat{a}_1^\dagger(\omega_i) \\ + \Bigg(\gamma \left\{\mathrm{sinc}\left(\Delta\beta_{S,S}\frac{L}{2}\right) e^{-i\Delta\beta_{S,S}\frac{L}{2}} - \mathrm{sinc}\left(\Delta\beta_{A,A}\frac{L}{2}\right) e^{-i\Delta\beta_{A,A}\frac{L}{2}}\right\} \\ - \delta \underbrace{\left\{\mathrm{sinc}\left(\Delta\beta_{S,A}\frac{L}{2}\right) e^{-i\Delta\beta_{S,A}\frac{L}{2}} - \mathrm{sinc}\left(\Delta\beta_{A,S}\frac{L}{2}\right) e^{-i\Delta\beta_{A,S}\frac{L}{2}}\right\}}_{=0}\Bigg) \hat{a}_1^\dagger(\omega_s)\hat{a}_2^\dagger(\omega_i)\end{aligned} \tag{2.13}$$

$$
\begin{aligned}
&+\Bigg(\gamma\left\{\operatorname{sinc}\left(\Delta\beta_{S,S}\frac{L}{2}\right)e^{-i\Delta\beta_{S,S}\frac{L}{2}}-\operatorname{sinc}\left(\Delta\beta_{A,A}\frac{L}{2}\right)e^{-i\Delta\beta_{A,A}\frac{L}{2}}\right\}\\
&\quad+\delta\underbrace{\left\{\operatorname{sinc}\left(\Delta\beta_{S,A}\frac{L}{2}\right)e^{-i\Delta\beta_{S,A}\frac{L}{2}}-\operatorname{sinc}\left(\Delta\beta_{A,S}\frac{L}{2}\right)e^{-i\Delta\beta_{A,S}\frac{L}{2}}\right\}}_{=0}\Bigg)\hat{a}_2^\dagger(\omega_s)\hat{a}_1^\dagger(\omega_i)\\
&+\Bigg(\gamma\left\{\operatorname{sinc}\left(\Delta\beta_{S,S}\frac{L}{2}\right)e^{-i\Delta\beta_{S,S}\frac{L}{2}}+\operatorname{sinc}\left(\Delta\beta_{A,A}\frac{L}{2}\right)e^{-i\Delta\beta_{A,A}\frac{L}{2}}\right\}\\
&\quad-\delta\left\{\operatorname{sinc}\left(\Delta\beta_{S,A}\frac{L}{2}\right)e^{-i\Delta\beta_{S,A}\frac{L}{2}}+\operatorname{sinc}\left(\Delta\beta_{A,S}\frac{L}{2}\right)e^{-i\Delta\beta_{A,S}\frac{L}{2}}\right\}\Bigg)\hat{a}_2^\dagger(\omega_s)\hat{a}_2^\dagger(\omega_i)\Bigg]|0\rangle\ .
\end{aligned}
$$

To simplify this equation, we can exploit the fact that we use a type-I PDC process (details in section 2.4), where the two generated photons are fundamentally indistinguishable [2]. This means that the marked terms in the $|1,1\rangle$-part of the state cancel each other.

We can interpret this behaviour as Hong-Ou-Mandel interference [59] that happens during the basis transformation. The AS- and SA-terms correspond to generating a photon in each of the eigenmodes and the basis transformation is mathematically equivalent to a beam splitter. As such, the two generated photons interfere equivalently to Hong-Ou-Mandel interference, but without a beam splitter.

As the three phase-matching conditions are spectrally distinct, we can use the pump wavelength to excite either the SS, AA or the SA, AS phase-matching condition. This yields three different states with different spatial properties[8]

$\Delta\beta_{SS}$: $|\Psi\rangle^{\mathrm{WG}} = \frac{\kappa(\Delta\beta_{SS})}{2\sqrt{\mathcal{N}}}[|2,0\rangle + 2\,|1,1\rangle + |0,2\rangle] = \frac{\kappa(\Delta\beta_{SS})}{2\sqrt{\mathcal{N}}}(|1,0\rangle + |0,1\rangle)^2$. This state is equivalent to the generated output when two indistinguishable photons enter a beam splitter from the same side.

$\Delta\beta_{AA}$: $|\Psi\rangle^{\mathrm{WG}} = \frac{\kappa(\Delta\beta_{AA})}{2\sqrt{\mathcal{N}}}[|2,0\rangle + 2\,|1,1\rangle + |0,2\rangle] = \frac{\kappa(\Delta\beta_{AA})}{2\sqrt{\mathcal{N}}}(|1,0\rangle + |0,1\rangle)^2$. This is again the state that is created when two photons enter a beam splitter from the same side.

$\Delta\beta_{AS}$: $|\Psi\rangle^{\mathrm{WG}} = \frac{\kappa(\Delta\beta_{AS})}{2\sqrt{\mathcal{N}}}[|2,0\rangle - |0,2\rangle]$. This is the state that is generated, when the photons enter the beam splitter from opposite sides (i.e. Hong-Ou-Mandel interference) and a genuine, post-selection free two-photon N00N state.

Hence, to generate the two-photon N00N state, which is the overall aim of this chapter, we have to match the pump wavelength to the $\Delta\beta_{AS}$ phase-matching condition, where we generated post-selection free N00N states. In the following, our aim will be to implement such a source and demonstrate the two-photon N00N state generation.

[8] Using also the spatial degree of freedom gives of course more flexibility in the state generation. Here, we have restricted ourselves to a single waveguide pump for the sake of experimental stability and simplification. State generation with use of the full spatial domain was demonstrated in [112].

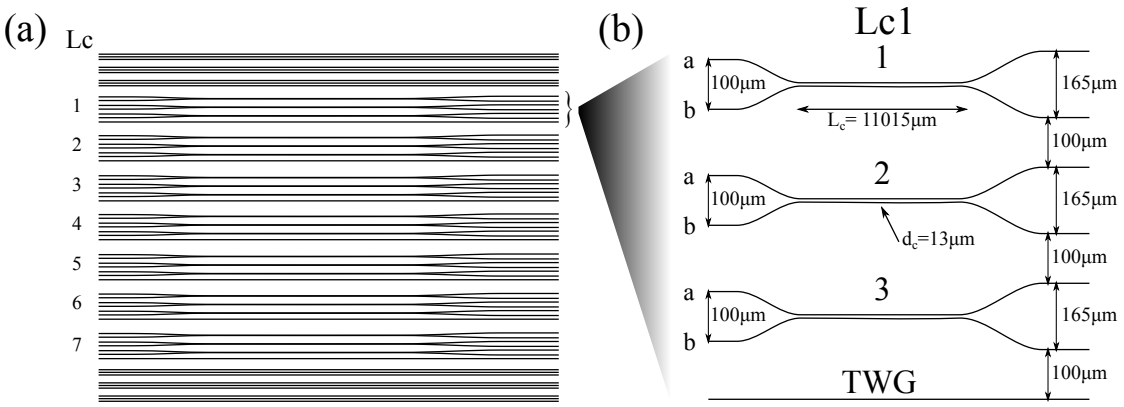

Figure 2.5 – The underlying waveguide structure of the implemented N00N state source. The overall sample, as shown in (a), consists of two times three test channels at the edges of the sample and seven coupler groups of varying stem length L_{stem}. A single group is shown in (b). It comprises three identical coupler structures, in particular for Lc1 with a stem length $L_{\mathrm{stem}} = 11015\,\mu$m and an uncoupled test waveguide (TWG). The distance between the waveguides in the coupling region is fixed throughout the sample with $d_c = 13\,\mu$m.

2.3 Device Characterisation

Before we are able to implement the PDC process for the quantum measurements, we have to characterise the produced sample classically to evaluate parameters such as the coupling strength or the phase-matching condition and to estimate the influence of fabrication imperfections, such as waveguide losses and residual coupling outside the periodically poled region. The linear characterisation, i.e. loss estimation and the measurement of the coupling properties were done with S. Brauner during his time as a student helper.

First, we describe the sample layout and the fabrication parameters for the utilised sample L224za. Afterwards, we describe the loss measurement technique that is used in our group and summarise the results for our waveguide sample. Then, we experimentally determine the coupling strength in the fabricated waveguide couplers and finally characterise the non-linear response of the single waveguides and coupler structures.

2.3.1 Sample Layout and Fabrication Parameters

Our sample for the N00N state source was fabricated from lithium niobate ($LiNbO_3$, LN) by R. Ricken. He produced waveguides according to the sample layout, sketched in figure 2.5(a). This layout consists of three control groups consisting of three waveguides each at both edges of the sample, which frame seven coupler groups (Lc 1-7) of different coupler stem lengths L_{stem}. The coupler group Lc1 that we are using in the experiment is magnified in figure 2.5(b). It comprises a test waveguide (TWG) and three identical coupler structures with a nominal coupler stem length of $L_{\mathrm{stem,\,Lc1}} = 11015\,\mu$m, which is the length where the waveguides run parallel at a

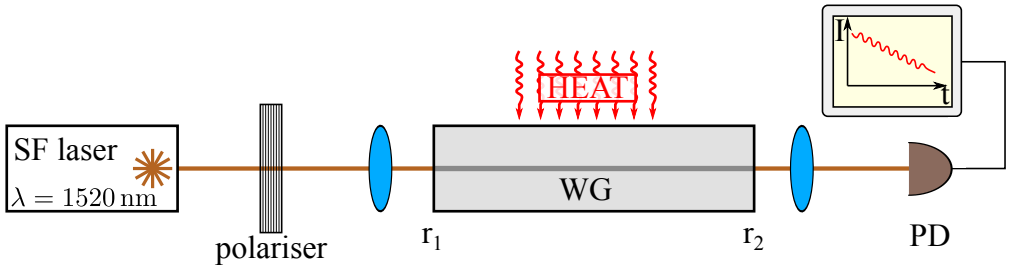

Figure 2.6 – Schematic of the loss characterisation setup [113]. The two end-facets of the LN crystal form a low-finesse cavity with a certain loss α. We scan the cavity resonances by heating the crystal and monitor the transmission of a polarised single-frequency continuous wave laser. With known end-facet reflectivities, the contrast of the cavity transmission signal is solely determined by the loss inside the cavity, i.e. the loss of the waveguide.

short distance, see 2.5(b). To both sides, the coupler stem is enclosed with a bending area that bridges the distance of the waveguides at the end facets of $\approx 100\,\mu$m to the coupler separation of $d_c = 13\,\mu$m. As the waveguide distance close to the coupler stem length is still small, we expect residual overcoupling of the light fields that has to be evaluated in the optical characterisation later.

The waveguides were produced via titanium indiffusion [104][9], where a titanium strip of defined width and height is deposited on the sample and heated to 1060°C for 8.5 hours. This causes an exchange of lithium atoms for titanium atoms in the crystal lattice, which increases the refractive index of the material for both TE and TM polarisation. In our case, the stripes had a measured width of $w = 6.9\,\mu$m and a measured height of $h = 79\,$nm.

As a final step, the sample was periodically poled [99, 100] at the position of the Lc1 coupler stem length. We only use a local periodic poling across the Lc1 coupler stem length to avoid spurious down-conversion processes in the uncoupled regions. As we did not use a defined mask for this process, the exact length of the poled region has to be determined in the non-linear measurements. The used grating period of $\Lambda = 16.6\,\mu$m should lead to a type-I quasi-phase-matching condition[10] in the telecom regime at room temperature, which has to be evaluated by a non-linear second harmonic measurement.

2.3.2 Losses

As the standard loss characterisation method in our group, we use the proposal by Regener and Sohler [113]. To quickly summarise this technique, we consider the schematic characterisation setup in figure 2.6. Due to the refractive index change at the two end-facets at the crystal, it

[9] This reference also contains a comprehensive overview for several fabrication techniques. Naturally, they do not describe the exact process used by R. Ricken, as our group has optimised the manufacturing parameters. Nevertheless, the overall procedure is very similar and should give an idea of the fabrication process.

[10] pump: extraordinary (TM) → signal: extraordinary (TM), idler: extraordinary (TM)

forms a low-finesse cavity. The two mirror reflectivities of the end-facets are directly determined by the refractive index contrast between the $LiNbO_3$ and the surrounding air. For the used TM polarisation in the telecom regime, the reflectivities are $r_1 = r_2 \approx \sqrt{0.13}$. We heat the sample, which scans the resonances of the low-finesse cavity via thermal expansion. We monitor this scan by a single frequency (SF), continuous wave laser at a wavelength of $\lambda = 1520\,\text{nm}$, which is polarisation-cleaned by a polariser. After passing the sample, we detect the transmitted cavity signal on a photo-diode (PD). Assuming, that the reflectivities of the end-facets remain unchanged by heating, the contrast K of the transmitted cavity signal is solely determined by the loss α inside the cavity [113]

$$\alpha \approx \frac{4.34}{L_{\text{sample}}}(\ln R + \ln 2 - \ln K)\,, \tag{2.14}$$

where $R = r_1^2$.

With this method, we have measured the loss parameters α in the test waveguides (marked TWG in figure 2.5(b)) of groups Lc 1-7. The measured sample length is $L_{\text{sample}} = 40.7\,\text{mm}$ and we measured at room temperature $T_0 = 21\,°\text{C}$. In table 2.1, we have summarised the loss values for TM-polarisation, as measured by S. Brauner. The relatively low losses of $\alpha = 0.2$ to $0.5\frac{\text{dB}}{\text{cm}}$ throughout the sample underline the good fabrication quality of our in-house production.

Lc	$\alpha_{\text{min.}}\ \left[\frac{\text{dB}}{\text{cm}}\right]$	$\alpha_{\text{est.}}\ \left[\frac{\text{dB}}{\text{cm}}\right]$	$\alpha_{\text{max.}}\ \left[\frac{\text{dB}}{\text{cm}}\right]$
1	0.44	0.49	0.56
2	0.11	0.2	0.31
3	0.27	0.3	0.32
4	0.2	0.24	0.29
5	0.25	0.29	0.33
6	0.35	0.43	0.5

Table 2.1 – Loss values in the test waveguides of groups Lc 1-6. $\alpha_{\text{est.}}$ is the estimated loss value of the waveguide, while $\alpha_{\text{min.}}$ and $\alpha_{\text{max.}}$ give the estimated error bars.

2.3.3 Coupling

Additionally to the loss characterisation of the waveguides, we have to characterise the coupling strength of the implemented coupler structures. In order to extract this parameter, we couple into one waveguide of the coupler structure and measure the output powers at the output waveguides separately, as sketched in figure 2.7.

With equation (2.8), we predict the expected behaviour of the coupler structures depending on the stem length L_c [104]

$$\begin{aligned} P_{||} &\propto |E_1(L_c)|^2 = \frac{1}{2} + \frac{1}{2}\cos(C \cdot L_c) \\ P_X &\propto |E_2(L_c)|^2 = \frac{1}{2} - \frac{1}{2}\cos(C \cdot L_c)\,, \end{aligned} \tag{2.15}$$

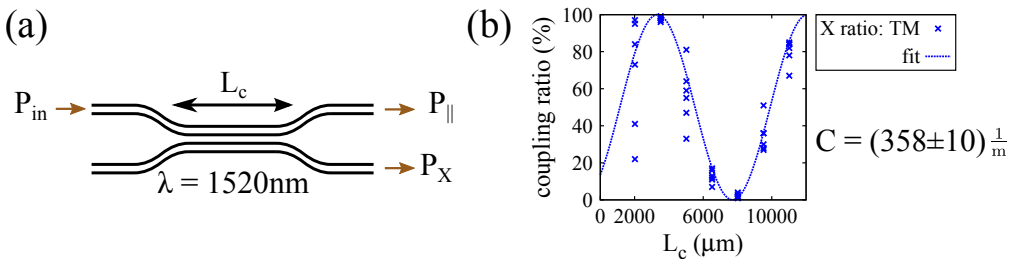

Figure 2.7 – Coupling parameter characterisation and results. To analyse the coupling strength of the implemented couplers, we launch infra-red light at $\lambda = 1520\,\mu$m into one input of the structure, as depicted in (a). We then measure the output power in both outputs and calculate the coupling ratio by normalising the cross-coupled power to the overall output power. Measuring for different stem lengths L_c gives a sinusoidal behaviour as shown in (b). By fitting the curve, we extract the coupling parameter $C = (358 \pm 10)\,\mathrm{m}^{-1}$ for our sample. Note, that for $L_c = 0\,\mu$m we still find a finite coupling ratio, which is an indication that residual coupling happens in the s-bends of the structure.

where $P_{||}$ is the power remaining in the input waveguide and P_X the coupled power to the neighbouring waveguide. The input amplitudes for the eigenmodes are assumed to be equal, as we launch light only into one input. To estimate the coupling strength, we measured the coupling ratio for the coupled power dependent on the coupler stem length in TM polarisation. We characterised all couplers from group Lc 1-6 twice by coupling into each input waveguide separately and recorded the output powers. The results, as taken by S. Brauner, are plotted in figure 2.7(b). While the trend roughly follows a sinusoidal behaviour, the strong scattering at short stem lengths prevents a perfect fit. The reason for this strong scattering is that the coupling strength is a sensitive parameter that reacts very strongly even to small variations in the fabrication process. Since we compare many different implementations of the same structure at different positions on the sample, the varying fabrication conditions over the width of the sample lead to the strong scattering in the results for the coupling strength. Nevertheless, we were able to extract the coupling parameter with $C = (358 \pm 10)\,\mathrm{m}^{-1}$. Finally, we would like to point out that for a stem length of $L_C = 0\,\mu$m, we find a finite y-intercept of roughly $15\,\%$. This hints to the fact that coupling of the electric fields does not only happen in the designed coupling region but also outside, which will affect the quality of our generated two-photon N00N state.

2.3.4 Second Harmonic Characterisation

After the in-depth characterisation of the waveguide structures in the linear regime, we evaluate the non-linear properties of the periodic poling. To this aim, we employ the process of second harmonic generation (SHG) [69], which is colloquially referred to as the inverse process of our desired PDC. Contrary to PDC, SHG is considered to be a fully classical effect, as it has a known solution from the an-harmonic mechanical oscillator. Consider figure 2.8(a). In the case of the harmonic potential (plotted in dashed lines as a reference), the time-dependent solution for a

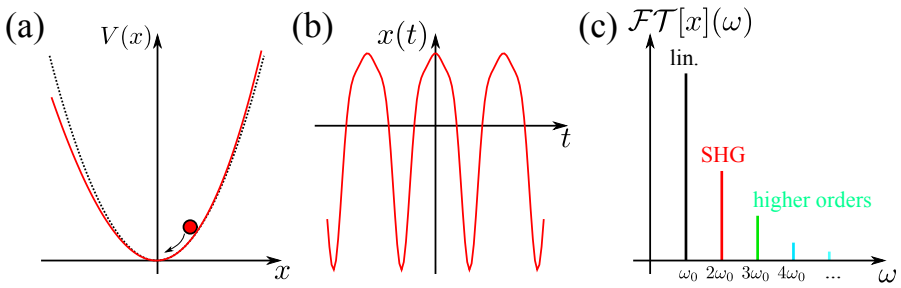

Figure 2.8 – Origin of second harmonic generation. Particles that move in an anharmonic potential (red curve in (a)) do not follow the harmonic solution after a certain excitation amplitude (b). In the Fourierspectrum in (c), the higher frequency components in the anharmonic solution become obvious.

particle moving inside this potential are the well-known harmonic sine and cosine functions. However, the approximation of an arbitrary potential by the harmonic oscillator breaks down at some point [69], e.g. a pendulum beyond Hooke's law. In this scenario, we have to consider anharmonic contributions (plotted in red) which disturb the harmonic solutions for a moving particle, i.e. an electron in the potential of a nucleus, as shown in figure 2.8(b). In Fourier space, as shown in figure 2.8(c), the anharmonic disturbances are revealed to be higher order frequency contributions, which can be identified as the second harmonic (SHG) or even higher order contributions [69].

In optics, the moving particles are electrons inside a crystal and the potential is the susceptibility (or χ-) tensor of the material. Usually, only the harmonic approximation is considered, which is the linear refractive index. However, when we drive the material system with high intensities, a whole zoo of non-linear effects appears. For a thourough review of non-linear effects, we recommend [69].

For our non-linear characterisation, we use the effect of second harmonic generation to probe the $\chi^{(2)}$-level of the full susceptibility tensor. To do so, we implemented a setup based on figure 2.9(a). We pump a single waveguide of our coupler structure hard enough with telecom light to generate measurable second harmonic power, divide the two colours on a dichroic mirror and record both the fundamental and second harmonic powers. In this configuration, we probe the phase-matching function along the $+45°$-axis as illustrated in figure 2.9(b) by tuning the wavelength of the fundamental field. For comparison, we perform this measurement also with the corresponding TWG of group Lc1.

The results for this characterisation are plotted in figure 2.9(c) for the uncoupled test waveguide. The x-axis gives the tuning of the fundamental wavelength plotted against an (uncorrected) conversion efficiency that computes via the recorded powers P

$$\eta_{\mathrm{SHG}} = \frac{P_{\mathrm{SHG}}}{P_{\mathrm{fund.}}^2 L^2} \,. \tag{2.16}$$

The efficiency η_{SHG} is normalised to the square of the fundamental power, as the fundamental

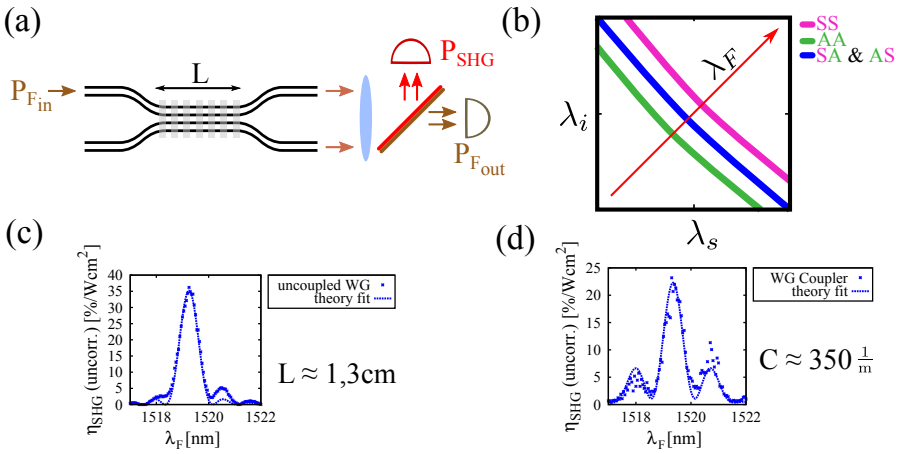

Figure 2.9 – Setup, working principle and results of second harmonic generation (SHG). To measure the non-linear SHG response of the periodic poling in (a), we couple light at the fundamental wavelength of $\lambda_F \approx 1520\,\mathrm{nm}$ in one waveguide of the coupler and divide the SHG from fundamental power at a dichroic mirror. We record fundamental and second harmonic power for both waveguides. This measurement corresponds to a scan along the $+45°$-axis of the phase-matching function, as shown in (b). In (c), we characterised the TWG of Lc 1 and could infer the length of the periodically poled region to $L \approx 1.3\,\mathrm{cm}$. Figure (d) shows the characterisation of a Lc 1 coupler. The splitting of the three phase-matching conditions corresponds to a coupling parameter of $C \approx 350\,\mathrm{m}^{-1}$, which confirms the results from the linear coupling characterisation. The error bars on these values are difficult to infer, as we have fitted the expected second harmonic signals to the measurement results by hand.

field enters into the conversion process twice. Furthermore, we have normalised the conversion efficiency to the poled length of the sample L. With this rather simple relation between conversion efficiency and the measurement parameters, we have ignored imperfect splitting of the colours in the dichroic mirror, different detection efficiencies for the power meters or wavelength dependent absorption in the transmissive optics, such as lenses. Therefore, we cannot scale the conversion efficiency η_{SHG} absolutely, but can only give a coarse (uncorrected for errors) estimate.

Nevertheless, we are able to extract the length of the periodically poled area by fitting the expected sinc^2-behaviour of the phase-matching function to the measured width of the second harmonic signal. In the case of our isolated waveguide, this length was estimated with $L \approx 1.3\,\mathrm{cm}$. It is not possible to estimate the error bars on this value as the automated fit did not converge properly and the SHG signal was fitted by hand.

Finally, we characterised the non-linear coupler structure in figure 2.9(d). Analogously to figure 2.9(c), we have plotted the conversion efficiency of the SHG process against the fundamental wavelength. The expected splitting of the phase-matching into three peaks due to the coupling is nicely observable. With the estimated length from the measurement of the uncoupled waveg-

uide, we can fit the coupling parameter from the distance of the main peak to the two side-peaks. For the measured couplers, we estimate a coupling parameter of $C \approx 350\,\mathrm{m}^{-1}$, which confirms the classical estimation of $C = (358 \pm 10)\,\mathrm{m}^{-1}$.

Comparing figures 2.9(c) and (d), an asymmetry in the phase-matching conditions becomes noticeable. This asymmetry is an artifact from inhomogeneities in the periodic poling and hints towards a chirp in the poled-unpoled duty cycle, which therefore leads to an asymmetric phase-matching condition. This behaviour is intrinsic in the source and will therefore also affect the following quantum measurements with the two-photon N00N states.

2.4 Quantum Experiments: Implementing the two-photon N00N State

After we have now fully characterised the sample and have extracted the defining parameters, we can move on to the quantum measurements, as we reported in [70], to verify the generation of genuine post-selection free two-photon N00N states in a single device.

The first step to verify the N00N state generation is to find the correct operation point of the implemented device. As we have elaborated in section 2.2, we have to cut out the $\Delta\beta_{A,S}$ phase-matching condition with the correct pump wavelength to generate the two-photon N00N state. To achieve this, we have implemented the setup in figure 2.10(a) and recorded the spatially resolved coincidence patterns dependent on the pump wavelength in order to find a hint for two-photon N00N state generation. We use $\sim 2.3\,\mathrm{ps}$ pulses[11] (autocorrelation) from a Ti:Sapphire laser (Coherent, Mira 900-D) with a pulse picker to generate a pulse train with a repetition rate of $R_{\mathrm{rep}} = 1\,\mathrm{MHz}$. The pulses at a wavelength around $\lambda_p \approx 760\,\mathrm{nm}$ pass through a power control, consisting of a half-wave-plate (HWP) and a polarising beam splitter (PBS), to achieve an input power of $P_{\mathrm{in}} = 0.05\,\mu\mathrm{W}$ (cw-equivalent) before the pulse polarisation is matched to the desired type-I PDC process with a HWP. Afterwards, the light is coupled to waveguide Lc1,3a in which the state generation takes place.

After the sample, we use a silicon slab (front: coated high-reflective around $800\,\mathrm{nm}$ and anti-reflective for telecom wavelengths, back: anti-reflection coating for telecom wavelengths) to filter out the remaining pump light with relatively low losses in the infrared of around $10\,\%$. We filter out undesired background light, i.e. from pump fluorescence or the other phase-matching conditions, in the telecom regime with an angle-tunable band-pass filter with a bandwidth of $\lambda_{\mathrm{BP}} = 50\,\mathrm{nm}$. Finally, we couple the generated photons to single-mode fibres in the telecom range (SMF28), where they are detected by time-gated InGaAs avalanche photo-diodes (APD, IdQuantique201) with a gating window of 2 ns and a detection efficiency of $\eta_{\mathrm{det}} = 20\,\%$.

To match the time delays between the two arms in our coincidence detection, we use an electrical trigger pulse from the MIRA system and feed it through a delay generator (Stanford Research DG645), which introduces a tunable time delay relative to the trigger pulse, see figure 2.11. We then use two channels of the delay generator to trigger the two APDs and optimise the delays separately to obtain maximum count rates. We then record the arrival times of the

[11] An absolute value of this number is not available, as the pulse duration depends on the daily operation of the laser and the length of the pulses was not monitored, due to equipment shortage.

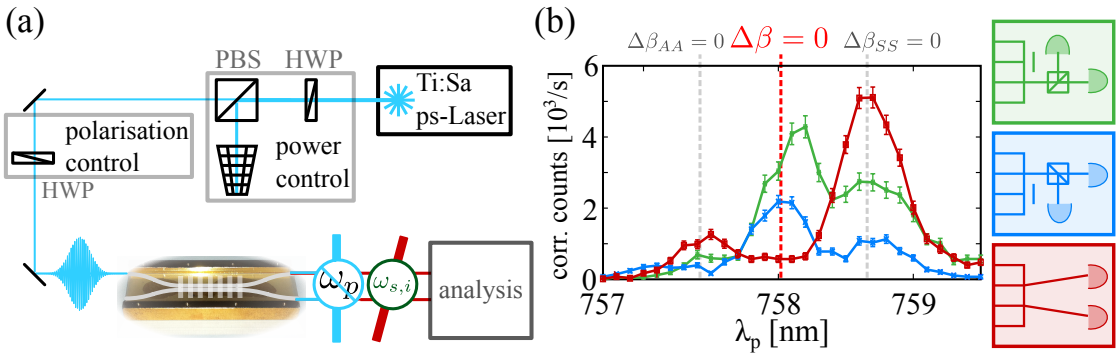

Figure 2.10 – Setup and results for the spatially resolved coincidence measurement as presented in [70]. The pulses of a Ti:Sapphire laser at $\lambda_p \approx 760\,\text{nm}$ and 1 MHz repetition rate (a) that pass trough a power and polarisation control consisting of half-wave plates (HWP) and polarising beam splitters (PBS). Afterwards, we couple the pulses into one waveguide of coupler Lc1,3a and clean the generated PDC photons from remaining pump light and undesired background in the telecom regime. Finally, we take the spatially resolved coincidences in (b) depending on the pump wavelength. In green, we show the coincidences in pumped waveguide, in blue the unpumped waveguide and in red the coincidences between waveguides. At a wavelength of $\lambda \approx 758\,\text{nm}$, the coincidences between waveguides almost vanish, which is a clear sign for the production of two-photon N00N states.

electric output pulses for the detection events by means of a time-to-digital converter (ACAM AM-GPX, resolution: 82ps) and extract the single (all detection events of a single APD) and coincidence (all detection events, where APD 1 and APD 2 record an event within the same gate window) counts.

To find the correct operating point for the two-photon N00N state generation, we scan the pump wavelength over all phase-matching conditions and record the spatially resolved coincidences, as shown in figure 2.10(b). In green, we depict the coincidence counts for the pumped waveguide, split by a fibre-coupled 50/50 beam splitter and normalised to the measured detection efficiency. We can clearly identify the peaks for the three phase-matching conditions: anti-symmetric, anti-symmetric ($\Delta\beta_{AA}$); symmetric, anti-symmetric ($\Delta\beta_{SA} = \Delta\beta = 0$) and symmetric, symmetric ($\Delta\beta_{SS}$) eigenmode. Blue represents the coincidence counts in the unpumped waveguide, while red shows the coincidences between the two waveguide modes. In the middle of the phase-matching curve, the coincidences between the two waveguides vanish, which is a strong indication for the generation of two-photon N00N states.

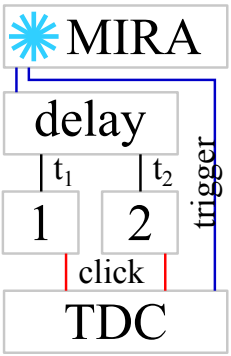

Figure 2.11 – Circuitry of the coincidence measurement.

From the normalised coincidence counts, we extract a maxi-

mum state fidelity at $\lambda_p = 758.1\,\mathrm{nm}$ via

$$\mathcal{F} = \frac{R_1 + R_2 - R_{12}}{R_1 + R_2 + R_{12}} = (84.2 \pm 2.6)\,\%\,, \tag{2.17}$$

where R_j are the normalised coincidences in waveguide j and R_{12} are the normalised coincidences between the waveguides. For details concerning the raw data, the setup characterisation and the normalisation of the coincidence rates in figure 2.10(b), see appendix C.

The measured fidelity is limited by two mechanisms. The first is a finite finite spectral overlap between the three phase-matching conditions due to the short stem length of the poled coupler as well as the finite coupling parameter. This mechanism restricts the theoretically achievable fidelity to $\mathcal{F}_{\mathrm{theo}} \approx 93\,\%$, which we obtained from numerical simulations for the source parameters. The other, experimental, mechanism is the overcoupling in the bendings that enclose the poled coupler region. As we have estimated in figure 2.7(b), we find a finite coupling ratio of $15\,\%$ for a coupler stem length of $L_{\mathrm{stem}} = 0\,\mu\mathrm{m}$. Considering that we have one bending in front of the coupled region and one behind, the generated quantum state is affected by a beam splitter with roughly 90:10 coupling ratio, which diminishes the theoretically estimated fidelity to roughly the measured value.

To optimise the measured fidelity, we recommend to use longer periodically poled couplers[12] to reduce the spectral overlap between the different phase-matching conditions. Another way to avoid this problem is, either, specific tailoring of the bending radii as well as the titanium layer thickness to minimise overcoupling or cutting away the bendings completely and only leaving the parallel coupling region, which however, might lead to interfacing problems with fibre networks.

Nevertheless, the spatially resolved coincidence measurement is only a hint that a genuine two-photon N00N state is generated. It remains to show the phase coherence between the two implemented paths of the waveguide chip. To verify this phase coherence, we implemented the interferometric setup shown in figure 2.12(a). We interfere the two waveguide outputs of the already implemented source of figure 2.10(a) on a 50:50 bulk beam splitter and change the relative phase between the two arms by tilting a thin glass plate. To ensure both spatial and temporal mode matching between the two paths, we used classical light from a femtosecond laser source at $\lambda_{\mathrm{ref}} = 1550\,\mathrm{nm}$ (OneFive, Origami) to align the interference and record the phase-dependent interference pattern with a power meter (Thorlabs). The result is shown in figure 2.12(b). In grey, we plot the interference pattern of the classical reference dependent on the implemented relative phase between the two arms. The measured visibility of $\mathcal{V}_{\mathrm{class}} = (95.4 \pm 0.4)\,\%$ is close to the achievable limit, as given by the unequal output powers of the two waveguides as well as the uneven splitting ratio of the bulk beam splitter.

After the classical reference measurement, we employed the PDC pumping scheme of figure 2.10(a) and tuned the pump wavelength to the phase-matching condition of the two-photon N00N state generation. We used a pump power of $P_{\mathrm{in}} = 0.25\,\mu\mathrm{W}$ for the state generation and coupled the two output ports of the beam splitter to two single mode fibres, which were again connected to APDs (this time with a detection efficiency of $\eta_{\mathrm{det}} = 15\,\%$) and measured the

[12] Such coupler structures were not available in our group at the time of this experiment.

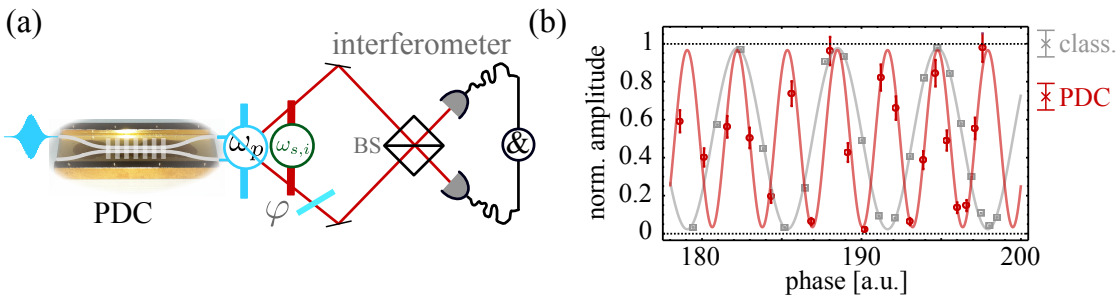

Figure 2.12 – Interferometric setup and interference fringes for the coherence proof as in [70]. We interfere the waveguide outputs on a bulk 50:50 beam splitter (a), change the phase φ between the two arms with a small glass plate and consequently record the coincidences in the beam splitter outputs. Figure (b) shows the results. Grey denotes the classical reference measurement with a femto-second pulsed laser (One-Five Origami), while red gives the interference pattern of the PDC signal. The expected double frequency of the fringing is clearly observable with high visibility of $\mathcal{V}_{\mathrm{PDC}} = (93.3 \pm 3.7)\,\%$.

phase-dependent coincidence counts between the two outputs of the beam splitter with the same coincidence logic as for the measurements in figure 2.10(b). The results for the quantum interference are plotted in red in figure 2.12(b). The expected double fringing for the two-photon N00N state is clearly observable also with a very high, measured visibility of $\mathcal{V}_{\mathrm{PDC}} = (93.3 \pm 3.7)\,\%$. This coincides with the classically measured visibility within the error bars, verifying both the phase coherence between the two paths of the generated state, as well as the high level of indistinguishability of the two waveguide outputs, as expected.

2.5 Higher-order Photon Number Contributions

Up to now, we restricted ourselves to the first order Taylor-expansion of equation (2.10) and have shown that we produce a post-selection free two-photon N00N state, as predicted by the two-photon picture. This has been a fair assumption, as our experiment only probed the photon generation at low pump powers, where the probability to generate higher photon number contributions is negligible.

However, in the next chapter, we want to probe quantum effects with photon-number resolved detection and need a well-calibrated source with higher photon-number contributions. To provide a theoretical framework for our coupled waveguide source, we investigate the higher order photon-number contributions in this section.

As in the case for the two-photon N00N state generation, the interesting physics happens when we select the symmetric-antisymmetric eigenmode combination for the photon-pair generation. To investigate the higher photon numbers, we accordingly restrict ourselves to this condition and

remind ourselves of the state in the two-photon picture

$$|\Psi_{A,S}\rangle^{1,2} = \int_{\omega_{\min}}^{\omega_{\max}} d\omega_s \int_{\omega_{\min}}^{\omega_{\max}} d\omega_i \left[f_{A,S}(\omega_s,\omega_i)\hat{a}_1^\dagger(\omega_s)\hat{a}_1^\dagger(\omega_i) - f_{A,S}(\omega_s,\omega_i)\hat{a}_2^\dagger(\omega_s)\hat{a}_2^\dagger(\omega_i)\right]|0\rangle \,, \tag{2.18}$$

where we have used the shorthand for the normalised joint-spectral amplitude $f_{A,S}(\omega_s,\omega_i) = \frac{2\delta}{\mathcal{N}'}\,\alpha(\omega_s+\omega_i)\,\mathrm{sinc}\left(\Delta\beta_{A,S}\frac{L}{2}\right)e^{-i\Delta\beta_{A,S}\frac{L}{2}}$ and a possible filter bandwidth $\Delta\omega_{\mathrm{Filter}} = \omega_{\max}$ to $\omega_{\min}$. Using the full generation unitary for the PDC process, we recall (2.10)

$$\hat{U}_{PDC}\,|0\rangle = \exp\left[-\frac{i}{\hbar}\int_{\omega_{\min}}^{\omega_{\max}} d\omega_s \int_{\omega_{\min}}^{\omega_{\max}} d\omega_i \left(f(\omega_s,\omega_i)\hat{a}_1^\dagger(\omega_s)\hat{a}_1^\dagger(\omega_i) - f(\omega_s,\omega_i)\hat{a}_2^\dagger(\omega_s)\hat{a}_2^\dagger(\omega_i)\right) + \mathrm{h.c.}\right]|0\rangle \,. \tag{2.19}$$

We can use the properties of operator-valued exponential functions to rewrite this equation to separate the components for the two waveguides

$$\begin{aligned}
\hat{U}_{PDC} = \exp\Bigg[&-\frac{i}{\hbar}\int_{\omega_{\min}}^{\omega_{\max}} d\omega_s \int_{\omega_{\min}}^{\omega_{\max}} d\omega_i \left(f(\omega_s,\omega_i)\hat{a}_1^\dagger(\omega_s)\hat{a}_1^\dagger(\omega_i) + \mathrm{h.c.}\right) \\
&+ \frac{i}{\hbar}\int_{\omega_{\min}}^{\omega_{\max}} d\omega_s \int_{\omega_{\min}}^{\omega_{\max}} d\omega_i \left(f(\omega_s,\omega_i)\hat{a}_2^\dagger(\omega_s)\hat{a}_2^\dagger(\omega_i) + \mathrm{h.c.}\right)\Bigg] \\
= \exp\Bigg[&-\frac{i}{\hbar}\int_{\omega_{\min}}^{\omega_{\max}} d\omega_s \int_{\omega_{\min}}^{\omega_{\max}} d\omega_i \left(f(\omega_s,\omega_i)\hat{a}_1^\dagger(\omega_s)\hat{a}_1^\dagger(\omega_i) + \mathrm{h.c.}\right)\Bigg] \\
&\otimes \exp\left[-\frac{i}{\hbar}\int_{\omega_{\min}}^{\omega_{\max}} d\omega_s \int_{\omega_{\min}}^{\omega_{\max}} d\omega_i \left(f(\omega_s,\omega_i)e^{i\pi}\hat{a}_2^\dagger(\omega_s)\hat{a}_2^\dagger(\omega_i) + \mathrm{h.c.}\right)\right] ,
\end{aligned} \tag{2.20}$$

where the joint-spectral amplitude for waveguide 2 acquired a π-phase-shift. With a little bit of rewriting, we identify that the two parts of the above equation represent two separate PDC processes for the two waveguides

$$\hat{U}_{PDC} = \hat{S}_{\mathrm{WG1}} \otimes \hat{S}_{\mathrm{WG2}} \,, \tag{2.21}$$

where $\hat{S}$ is the squeezing operator for a spectrally multi-mode process [114–116]. From the shape of this equation, i.e. its tensor-product form, we can tell that our source generates two spectrally identical, independent, phase-stable, broadband single-mode squeezed states in spatially separate output ports.

The fact that the dual-path source produces two independent squeezed states excludes the possibility to generate higher-order N00N states in the same way as for the two-photon component. N00N states are maximally entangled states in the path degree of freedom, however

the two squeezers are independent and therefore cannot be entangled. Nevertheless, the phase-stable generation of single-mode squeezed states may still be interesting for quantum metrology applications.

Summary

In summary, we developed a post-selection free two-photon N00N state source by using the underlying waveguide structure to engineer the spatial properties of the generated photons. We developed a theoretical description for this type of devices and presented the characterisation of our used sample. We furthermore verified the generation of the N00N state with a fidelity of $\mathcal{F} = (84.2 \pm 2.6)\,\%$ and double-fringing visibility of $\mathcal{V}_{\mathrm{PDC}} = (93.3 \pm 3.7)\,\%$. Finally, we gave an outlook to the behaviour of the higher photon number contributions and found that we generate two phase-stable single-mode squeezed states with our dual-path source.

Hello darkness, my old friend
I've come to talk with you again
Because a vision softly, creeping
Left its seeds while I was, sleeping
And the vision, that was planted in my brain... still remains
Within the sound of silence

Simon & Garfunkel - The Sound of Silence

3

Probing atmospheric quantum channels with photon number resolved detection

Contents

In this chapter, our main focus lies on the detection of (high-dimensional) photon number statistics, which we discussed with the aid of coherent and squeezed states in chapter 1. The final aim will be to exploit the higher order photon number contributions in the photon number statistics of our dual-path source from the previous chapter to probe the resilience of nonclassical light under the influence of atmospheric turbulence.

There are several methods to detect higher order photon number contributions to gain information about the photon number statistics. The most straightforward way is to build a truly photon number resolving detector. However straightforward this idea may sound, the optimisation of this type of detector is involved and only succeeded quite recently [117–120], compared to single-photon sensitive diodes, which have been around since the 1980s [121]. Furthermore, the realised transition-edge-sensors, which detect the photon absorption by means of an infinitesimal temperature shift only became recently available and are quite expensive and resource-demanding [122–126].

Due to these reasons, alternative approaches to photon counting have been investigated. In general, these approaches use conventional on-off detectors, i.e. detectors that give a "click" when any number of photons is present and "no-click" otherwise. An example for such an on-off detector are the readily available APDs that we used in the previous chapter (see section 2.4).

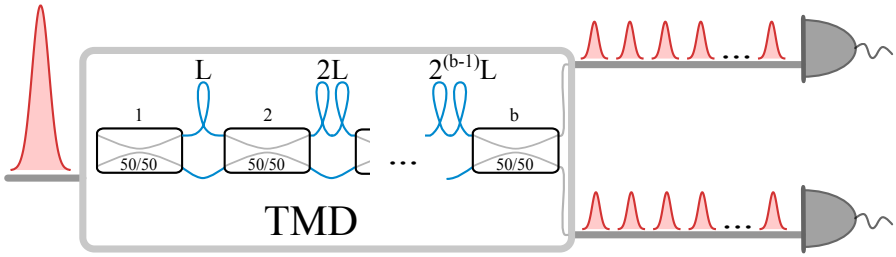

Figure 3.1 – Schematic of a time-multiplexed detector. A strong pulse at the input with higher order photon number contributions gets split at the 50/50 beam splitters and is partially delayed in different fibre lengths. At the end a pulse train, corresponding to different time bins arrives at on-off detectors. The time bins should then contain less than one photon on average.

Yet, a simple on-off detector is not able to give any amount of photon number resolution, it gives a "click" independently of the mean photon number (if $\langle n \rangle \gtrsim 1$) that arrives on the detector, because it will "click" every time. However, if we are able to weaken the impinging mean photon number on a single detector to $\langle n \rangle \ll 1$, we are not saturating the detector and the count rate will be proportional to the impinging mean photon number. As such, the aim will be to *multiplex* many on-off detectors, such that the mean photon number per detector fulfils this requirement.

The method that we consider in this thesis uses *time-multiplexing*, which has been independently developed in the groups of I. Walmsley [25, 28], M. Hamar [26] and J.D. Franson [27] and for the first time applied to measure the photon statistics of a down-conversion source by [29]. With the time-multiplexing method, we split the incoming photons probabilistically in different *time bins*, which we then feed consecutively on a single on-off detector. An example for such a scheme comprising different time delays and 50/50 beam splitters is depicted in figure 3.1, where usually fibre-integrated realisations of the device are used to implement the necessary time delays due to detector relaxation times[1]. Consider a strong input pulse with more than one photon that impinges on the time-multiplexed detector (TMD). Then, the pulse gets split at the first 50/50 beam splitter and one half gets delayed by a fibre of length L, compared to the other half. As such, we now have two pulses in two time bins that each contain half the original photon number. If we repeat this operation b times, we split up the strong input pulse in 2^b different pulses at different times containing a $\frac{1}{2^b}$-fraction of the original photon number. Thus, the TMD probabilistically splits up the higher order photon numbers such that, on average, less than one photon impinges on the on-off detector, as desired. As the TMD uses the same on-off detectors again and again, they are a cost-efficient, reliable and practical alternative to the demanding photon number resolved detectors.

This chapter contains three main concepts that lead up to the application of the photon number

[1] For example the dead time of an InGaAs APD, such as the one we used, which is around 1 μs corresponding to a delay line of $\approx$ 300 m length. For the superconducting detectors that we use in the latter part of this thesis the cool-down times are $\approx$ 100 ns, which still requires a delay line of $\approx$ 30 m length.

statistics from our dual-path waveguide source in the context of quantum communication in atmospheric channels. First, we probe the fundamental limits of the time-multiplexed photon counting technique. How many photons can we reliably detect with this method and what is the quality of the measured photon number statistics? We want to reliably detect higher photon numbers, but inevitable losses in the fibre network and the distribution of photons on a finite set of time bins will deteriorate the photon number statistics. We investigate this deterioration effects with Fock input states and quantify the deterioration of statistics in the time-multiplexed network. Secondly, we develop and perform a novel type of detector calibration for a photon number resolved detector with 8 time-bins in each of the two modes. This work was done in collaboration with M. Bohmann from the group of W. Vogel in Rostock, who provided the theory support to evaluate our experimental data. Finally, we use these results to probe the transmitted nonclassicality of the photon number statistics from the two-coupled waveguide source from chapter 2 in a quantum communication setting with atmospheric noise. To do this, we simulate the effect of atmospheric noise on the generated quantum state by a variable loss and mix the different loss levels according to different atmospheric models. This work was also done in collaboration with M. Bohmann from Rostock.

3.1 Limits on the Time-multiplexed Photon-counting Method

In this section, we consider the fundamental limits of detecting large photonic quantum states with the time-multiplexing technique, which we presented in [127]. While this technique is often called scalable and stable, up to this point a rigorous investigation of the scalablility has been missing. While Sperling et al. [128] have investigated the minimum size that is needed to get reliable data on large photonic quantum states, they considered loss-free networks which is not feasible in reality. Therefore, we consider, for the first time, the limits of a time-multiplexing network for photon counting that includes realistic imperfections such as loss or fibre dispersion.

First, we discuss the fundamental limits as imposed by the dispersion of the fibres itself and impose a hard limit that we cannot overcome. Afterwards, we comment on the effect that losses have on the photon number statistics in our network and discuss different figures of merit for our investigation. We define our model for the TMD based on the loss formula by [28] and the convolution description of [128]. With this model, we consider the ability to discriminate between different Fock states after the TMD and probe the deterioration of Fock states after the TMD for reconstruction purposes. With this information, we extract an optimal bin number for our figures of merit.

3.1.1 Limitation by Dispersion

The first effect that we have to consider for the limits of TMD measurements is the dispersion of the used fibres. In general, we use input *pulses* to measure the higher order photon numbers with a TMD[2]. Thus, the input light comprises of more than one wavelength and is therefore subject to dispersion. To investigate the effect of dispersion on our input pulses, we assume perfect

[2]We need a time information in the input state that we can split. In a continuous wave experiment a TMD does not work.

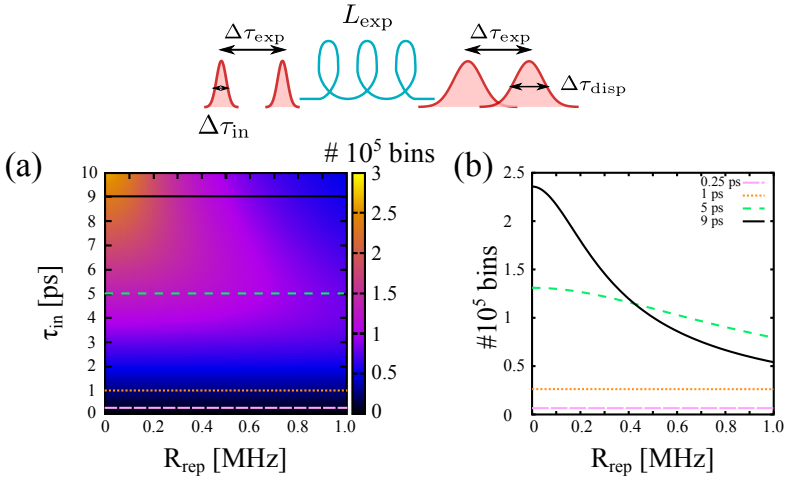

Figure 3.2 – Hard limit of the available time bins as determined by dispersion properties [127]. The limits of the dispersion depend both on the repetition rate of the experiment $R_{\mathrm{rep}} = \frac{1}{\Delta\tau_{\mathrm{exp}}}$ and on the input pulse duration which gets dispersed by a fibre length L_{exp} and overlap after the fibre. In (a), we plot the maximum number of available time bins as restricted by dispersion. The maximum number for long pulses and low repetition rates does not exceed $\approx 2.5 \cdot 10^5$ bins. For (b), we take different slices trough (a) and consider the behaviour for different repetition rates. We show 250 fs in pink, 1 ps in orange, 5 ps in green and 9 ps in black. As the dispersion does not play a strong role for long pulses, we observe an increase of maximum time bins for long repetition rates, while for short pulses this effect is cancelled out by dispersion in the longer fibres.

detectors, which means no loss and perfect timing resolution. Then, the maximal number of time bins is determined by the number of dispersed output pulses with an output width of $\Delta\tau_{\mathrm{disp}}$ that fit into the time between two experiments, i.e. two input pulses $\Delta\tau_{\mathrm{exp}}$, see system sketch in figure 3.2. If we express the time between two experiments in terms of the repetition rate R_{rep}, we can define the maximum number of time bins via [127]

$$N_{\mathrm{max,\,disp}} = \frac{\Delta\tau_{\mathrm{exp}}}{\Delta\tau_{\mathrm{disp}}} = (R_{\mathrm{rep}}\Delta\tau_{\mathrm{disp}})^{-1}\,. \tag{3.1}$$

We consider that $\Delta\tau_{\mathrm{disp}}$ is the full width at half maximum (FWHM) of the output pulses. The dispersion for standard single mode fibres is given by the group velocity dispersion, which is determined by [129]

$$\Delta\tau_{\mathrm{disp}} = \Delta\tau_{\mathrm{in}}\sqrt{1 + \left(\frac{4\ln(2)}{\Delta\tau_{\mathrm{in}}^2}\cdot\frac{\lambda^2}{2\pi c}\cdot D_\lambda L_{\mathrm{exp}}\right)^2}\,, \tag{3.2}$$

where $\Delta\tau_{\mathrm{in}}$ is the input pulse duration, $\lambda = 1550\,\mathrm{nm}$ the considered wavelength, $L_{\mathrm{exp}} = c \cdot \Delta\tau_{\mathrm{exp}}\,[\mathrm{km}]$ the longest passed fibre length and c the speed of light in the fibre. For standard single mode fibres (type SMF28), the dispersion coefficient is specified with $D_\lambda \leq 18.0 \frac{\mathrm{ps}}{\mathrm{nm}\cdot\mathrm{km}}$ [130] for a wavelength of $\lambda = 1550\,\mathrm{nm}$, as we consider here. To guarantee that we can resolve the different time bins, we artificially halved the number of available time bins from equation (3.1) as equation (3.2) applies to the FWHM of the output pulses.

The results for the maximally available number of time bins is plotted in figure 3.2. To consider the behaviour of the available time bins on both the repetition rate and input pulse duration, we consider figure 3.2(a). We depict only repetition rates below 1 MHz as they give us sufficient time between consecutive experiments. Furthermore, we do not consider any input pulse lengths above 10 ps, as the effect of the dispersion becomes more and more negligible for long pulses. Then the maximum number of time bins is bounded by the input pulse duration $\Delta\tau_{\mathrm{in}}$

$$N_{\mathrm{max}} = \frac{\Delta\tau_{\mathrm{exp}}}{\Delta\tau_{\mathrm{in}}}\,. \tag{3.3}$$

Interestingly, for the considered range of parameters, the maximal number of available time bins is bounded by approximately $2.5 \cdot 10^5$ time bins, even for low repetition rates (i.e. long time between experiments) and long input pulses (low dispersion effect). This result is quite devastating, considering that we need around 10^4 bins to perfectly discriminate between the $|9\rangle$ and $|10\rangle$ Fock states without losses [128]. As such, already the dispersion has a profound impact on the discrimination of large photon number states.

In figure 3.2(b), we slice the plot from (a) at different input pulse durations to gain more insight to the dispersion effect. We depict the durations of 250 fs in pink, 1 ps in orange, 5 ps in green and 9 ps in black. It becomes clear that decreasing the repetition rate to gain more bins does not help. The reason is that the longer time between the experiments also brings longer distances of fibre that the photons have to pass. As such, the dispersion stretching of the input pulses completely eats up the advantage of lower repetition rates. Consecutively increasing the input pulse duration lessens the effect of fibre dispersion such that we can observe a noticeable increase in the available bin numbers. Then, the advantage of longer time between experiments is not fully compensated by the dispersion and yields higher available bin numbers [127].

3.1.2 Limitation via Loss

After we considered the geometrical limit of the time-multiplexing setup by dispersion, we investigate the effects of loss and convolution (i.e. the distribution of n photons in N time bins after passing the TMD) on the measured photon number statistics (click statistics). The figure of merit that we use is the overlap of Fock states after passing the TMD [127], see figure 3.3(b) for an example with the two Fock states $|10\rangle$ and $|12\rangle$. The advantage of this approach is that the Fock states form an orthonormal basis of the photon numbers and therefore any overlap in the photon number statistics after passing the TMD will be due to the effects of loss or convolution. We review the model and the effects of these two mechanisms in the following.

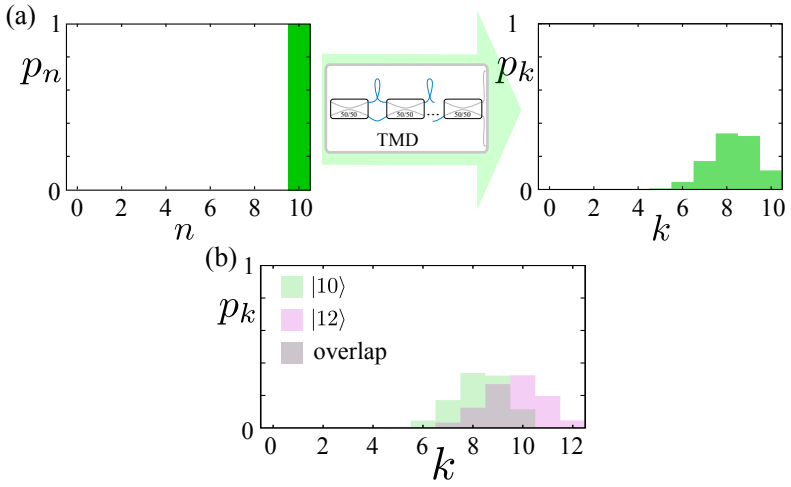

Figure 3.3 – Deterioration of Fock state photon number statistics after passing the TMD (a) and overlap of click statistics as a figure of merit (b).

Model and Parameters

The distribution of photons in a TMD is governed by two processes: the convolution process describes the probabilistic division of N photons in k time bins and losses deteriorate the photon number statistics. The effect of the convolution can be understood in the following: ideally, we wish to distribute our photons such that only one photon is in any bin of the TMD. However, if we have $N > k$ photons we will not be able to hold to this condition. As such, a low number of bins will also destroy information about the high photon numbers and deteriorate the photon number statistics. In this work, we assume only probabilistic splitting of our photons at the perfectly even 50/50 beam splitters, as proposed by Sperling et al. [128]. While we can try to replicate such a perfect system in any experiment, it will not perfectly recount the action of a realistic TMD with imbalanced splitting ratios. Nevertheless, as we are only interested in the fundamental limits of the measurement technique, it will provide a sufficiently good approximation. In this framework the convolution matrix that gives the probability to measure k clicks, when l photons impinge on the TMD is defined by

$$C_{l,k} = \begin{cases} \frac{1}{N^l}\binom{N}{k}\sum_{j=0}^{k}(-1)^j\binom{k}{j}(k-j)^l, & \text{if } l \geq k \\ 0, & \text{else} \end{cases} . \tag{3.4}$$

In our case, we consider $N = 2^b$ time bins, with b as the number of used beam splitters. The second mechanism that deteriorates the photon number statistics is loss. This effect has been extensively investigated and the governing matrix that describes the probability to retain l photons

after n photons have undergone a loss of $1-\eta$ is [28]

$$L_{n,l} = \binom{n}{l} \eta^l (1-\eta)^{n-l} \,. \tag{3.5}$$

In our case, the losses comprise the finite transmission of the beam splitters, absorption in the fibres and also a combined setup transmission and detection efficiency η_{ex}.

Finally, we have to combine both effects and apply both matrices to the input photon number statistics to retain the final, measured click statistics [28]

$$p_k^{(\mathrm{out})} = C_{l,k}\, L_{n,l}\, \rho_n^{(\mathrm{in})} \,. \tag{3.6}$$

To simplify the treatment of the TMD operation, we consider losses and the convolution as two separate processes. While this is not fully correct[3], it is a justifiable approximation and makes the simulations significantly easier. As such, the photons will undergo a collected loss, where we use the worst case scenario, containing all possible beam splitter losses and the longest fibre length in the TMD. We sketch the effect of an imperfect TMD with convolution effects and losses on the click statistics in figure 3.3(a).

For the simulation [127], we use realistic parameters for state-of-the-art fibre components. We assume that each beam splitter has a loss value of $0.05\,\mathrm{dB}$ [131] and a fibre absorption of $0.2\,\frac{\mathrm{dB}}{\mathrm{km}}$ [130]. We neglect losses that are introduced during the splicing process[4], as they are very low compared to the loss values of the beam splitters and the fibre absorption. As detection units, we assume superconducting nano-wire detectors, where a dead time of 10 ns is a realistic value that defines our time-bin separation and therefore our needed fibre lengths [132]. If not specified otherwise, we assume perfect setup transmission and detection efficiencies, otherwise we specify a collective detection efficiency η_{ex}.

Photon Number Discrimination

As we already stated above, we use the overlap of click statistics from different Fock states as our figure of merit. The results are shown in figure 3.4. To illustrate the separate effects of loss and convolution, we have first plotted the overlap of the click statistics of the Fock state combination $\langle 15|\, 20\rangle$ for different TMD sizes in figure 3.4(a). In black, we only consider the effect of the convolution on the measured statistics. As expected, it decreases towards large TMDs with many bins. Contrary to the influence of convolution, the losses increase with large bin numbers, since the photons have to pass through longer fibres and more beam splitters, as shown with the blue curve. As such, we have to make a trade-off between the deterioration via the convolution at low bin numbers or the deterioration via loss at large bin numbers. We can find this optimal trade-off point by considering both effects on the click statistics, as shown in red. For this particular combination, the optimum is at 256 time bins with a minimal overlap of around $25\,\%$ [127].

[3] Different losses in the fibres can be transformed into an overall loss in front of the TMD. This however changes the beam splitter ratios of the model slightly [28].

[4] Basically, one melts two fibre ends together.

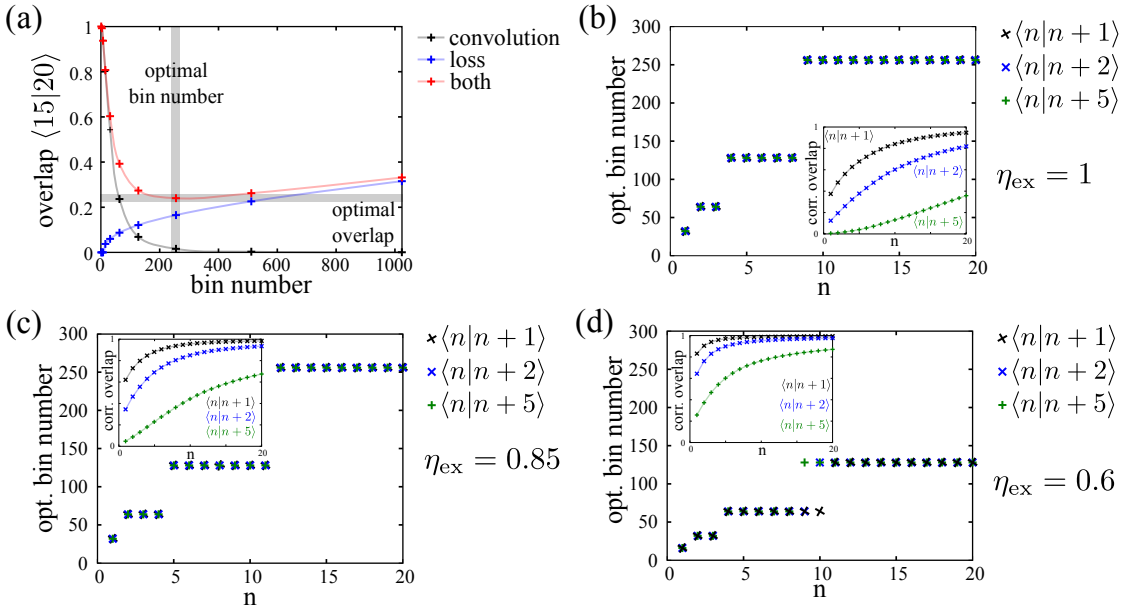

Figure 3.4 – Overlap of the click statistics for different Fock states after the TMD [127]. To give an insight into the loss and convolution processes, we plot the overlap of the $\langle 15|\,20\rangle$ click statistics after passing TMDs of different sizes. While the effect of the convolution decreases for large TMDs, the losses increase in this regime and we find an optimal bin number for this Fock state combination. From (b) to (d), we scan different Fock states from $|1\rangle$ to $|20\rangle$ for different detection efficiencies η_{ex} and find the optimal bin number and the corresponding minimal overlap. The combination of neighbouring Fock states is given in black, leaving one Fock state in between is shown in blue and the combination of $\langle n|\,n+5\rangle$ is given in green. The lines are only shown to provide a guide to the eye and hold no physical meaning.

In figure 3.4(b), we scan the Fock state basis from $|1\rangle$ to $|20\rangle$ and look at the overlap to its nearest neighbour in black, skipping one in between in blue and the fifth-nearest neighbour in green. For each combination, we have extracted the optimal bin number and the corresponding overlap in the measured click statistics. In the case of perfect detection efficiencies η_{ex}, we already see that even for large Fock states of $|20\rangle$, the optimal bin number does not exceed $256 = 2^8$ bins. Furthermore, we observe that the minimal overlap that we can reach with this method increases monotonically and reaches one asymptotically, i.e. the states become indistinguishable at the output. Especially in the case of discriminating nearest neighbour Fock states this is a rather pronounced effect. Even for low Fock states, the minimal overlap does not fall below $50\,\%$ which makes a distinction difficult.

This behaviour even worsens when considering finite detection efficiencies. In figure 3.4(c), we investigate a high, but realistic detection efficiency of $\eta_{\mathrm{ex}} = 0.85$. Even though the optimal bin number for $|n\rangle = |20\rangle$ is still 256 bins, the overlap between the click statistics increases quite drastically compared to unit detection efficiency. Nevertheless for even lower detection

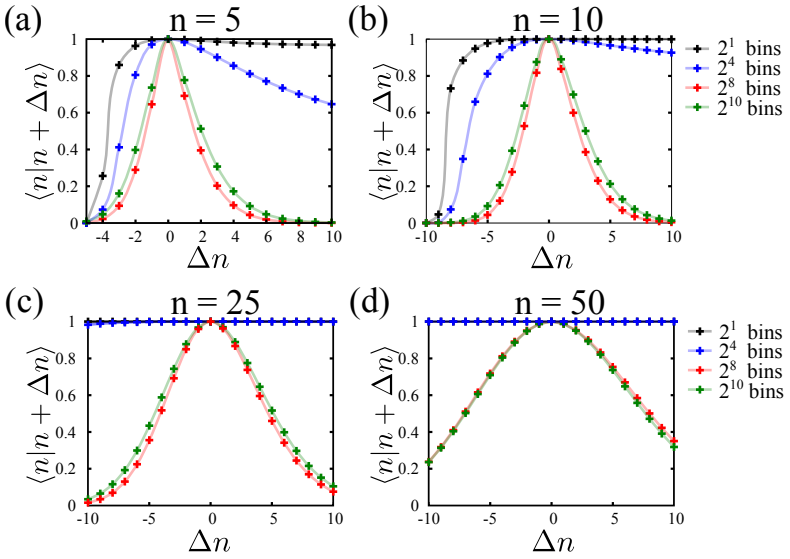

Figure 3.5 – Overlap of Fock states after passing a TMD [127]. We consider a fixed Fock state n from $n = 5$ in (a) up to $n = 50$ in (d) and calculate the overlap to the adjacent ± 10 Fock states. This curve shows us how well we are able to distinguish between the different click statistics and gives us a crude error bar or precision for the reconstruction for the Fock state from the click statistics. In black, we consider a 2 bin TMD, in blue 16 bins, in red 256 bins (our optimum from the last section) and in green 1024 bins. The small improvement towards larger TMDs in the overlap curves does not justify the effort to implement high-quality TMDs of this size. The lines only provide a guide to the eye and hold no physical meaning.

efficiency of $\eta_{\mathrm{ex}} = 0.6$ in figure 3.4(d), the additional loss deteriorates the photon number statistics much more. Here, even the optimal bin number decreases compared to the previous cases, while the minimal overlap already approaches unity for low bin numbers. Summarising our discussion, we can conclude that for our figure of merit and Fock states up to $n = 20$ it holds no advantage to use TMDs that are larger than 256 bins [127].

Photon Number Reconstruction

In the previous section, we regarded the overlap between click statistics for the discrimination of neighbouring Fock states. However, this is not the only aim for which one might want to use photon number resolved detection techniques. Another very important field is the reconstruction of the impinging state from the click statistics. To this aim, a lot of theoretical work has been done to improve and optimise the reconstruction techniques [133–135]. In the scope of this work, we do not discuss the different reconstruction algorithms and only approach this topic from a purely experimental point of view.

The aim of this section is to assign something similar to error bars on the impinging state from the click statistics or in other words, a precision with which the input state may be reconstructed.

To achieve this, we again consider Fock states as our input for the TMD and calculate the overlap of the click statistics for adjacent states. The results are shown in figure 3.5.

Consider figure 3.5(a). The different colours denote different TMD sizes, black for a 2 bin TMD, blue for 16 bins, red for 256 bins (our optimum from the last section) and green for 1024 bins. We want to know the precision with which we can reconstruct $|5\rangle$ from the measured click statistics. This precision is directly related to the overlap of the click statistics with neighbouring Fock states, as we cannot discriminate them perfectly. As such, we plot the overlap of the click statistics between $|n\rangle$ and $|n + \Delta n\rangle$, where Δn denotes how far the two Fock states are separated from each other (i.e. $\Delta n = 1$ means that they are neighbours). Consider the red curve for 256 bins. It peaks at $\Delta n = 0$, as the same input state enters the TMD. For further separated Fock states, the overlap diminishes and the width of the curve gives us a measure for the precision with which we can reconstruct the initial Fock state [127]. The curves are slightly asymmetric for the higher and lower photon numbers, as the binomial coefficients that govern the overlap are different. This effect decreases towards higher photon numbers (see figure 3.5(d)) as the relative difference between the Fock states decreases.

Towards high number Fock states, the overlap curve between the neighbouring Fock states becomes broader and broader (figures 3.5(b)-(d)). The broadening is expected, as the effect of the convolution matrix is more and more pronounced for large photon numbers. Therefore, while for Fock states up to $n = 25$ a 256 bin TMD shows the narrowest curve, this changes at around $n = 50$. However, the improvement for large TMDs is not very pronounced such that it does not really justify the effort to fabricate a high-quality 1024 bin TMD over a 256 bin TMD. Furthermore, we have only considered perfect detection efficiency $\eta_{\mathrm{ex}} = 1$. In the previous section, we have seen that finite detection efficiencies deteriorate the click statistics quite drastically, such that we do not expect that TMD sizes larger than 256 bins hold significant advantages in an experimental implementation [127].

Summary

In summary, we investigated the limitations of the time-multiplexed detection technique for photon counting, which we presented in [127]. We saw that the fibre dispersion bounds the maximum number of bins to $2.5 \cdot 10^5$ for repetition rates below $R_{\mathrm{rep}} < 1\,\mathrm{MHz}$ and input pulse durations of $\Delta\tau_{\mathrm{in}} = 10\,\mathrm{ps}$. Furthermore, we considered the effects of convolution and loss for a realistic simulation of the TMD and extracted the optimal number of time bins for the discrimination of different Fock states up to $n = 20$. Finally, we investigated the precision with which we can reconstruct Fock states from the measured click statistics. For these figures of merit, we find that it holds no advantage to implement TMDs larger than 256 bins.

3.2 Detector Calibration with Click Moments

In the previous section, we probed the limits of time-multiplexed detection technique. Now, we bring this concept to the laboratory to experimentally calibrate a TMD with 8 bins. This calibration of the measurement device is important for the reliable measurement of our generated

quantum states with high photon numbers, as we do in section 3.3. However, the calibration of detection systems is not only necessary to reliably measure high photon number contributions. Since general quantum networks with high photon numbers are a promising candidate for secure quantum communication channels and quantum computing applications [1, 136], reliable verification procedures in the high-photon number regime are an indisputable necessity. In general, a lot of work concerning this topic has been done with various approaches. However, the tomography of detectors is a very difficult endeavour, because it necessitates a very precise generation of specific probe states for the experimental characterisation.

There are different approaches to calibrate or characterise detectors with quantum states. The most general one is a full detector tomography [137–140]. In this scenario, one uses precisely defined probe states that are measured with the detector of interest. For this technique, we do not assume any *a priori* knowledge about the detector and try to reconstruct the positive operator-valued measures (POVMs) $\hat{\pi}_n$ from the probability distributions measured with the probe states. This universal method has been applied successfully for general detectors but also for time-multiplexed devices [126, 140–146]. Nevertheless, it features several down sides. Conceptually, the technique has the intrinsic problem that we try to infer POVMs acting on an infinite Hilbert space (i.e. the photon number basis) from a *finite* set of measurement outcomes, which is an ill-defined problem. This introduces a large systematic error already into the POVM reconstruction, additionally to the numerical errors in the data analysis which have to be propagated. Furthermore, as we do not assume any *a priori* knowledge about the detectors, we have no knowledge about the shape of the POVMs and have to scan a huge parameter space to achieve a converging result for the tomography.

Another, way to calibrate detectors is the use of well-defined two-mode squeezed states [66, 147–150]. Due to the photon number correlation between the two arms of the state, this method is able to extract the detector efficiency from the detectors of interest. However, as this method critically relies on the exact form of the correlations between the two arms, the probing quantum states have to be prepared with high precision. Furthermore, the true photon statistics that underlie this method cannot be measured (as we discussed in the previous section) due to imperfect photon number resolution of the probed detector. While there exist methods to reconstruct the impinging quantum states from the measured click statistics, they suffer from systematic errors which scales as $1/N$ [128], where N is the number of detector bins (i.e. time-bins for a TMD).

The method that we developed [151] in collaboration with Martin Bohmann from Werner Vogel's group in Rostock addresses and largely circumvents these problems. We assume some *a priori* knowledge about the detector (that it is a photon number resolved detector with N bins) and can therefore reduce the huge number of free parameters from detector tomography. In our case, we only need the parameters for efficiency and dark count rate, for each of the two detection modes A and B, see figure 3.6. Furthermore, our method does not rely on correlations between twin beams and therefore works with readily available coherent states.

This section is structured as follows, first, we present the method that directly extracts the detector response function from the measured click statistics and therefore circumvents problems like the finite to infinite Hilbert space mapping and reduces the number of free parameters to only 2 for each mode. Second, we describe our experimental setup that we use to take the calibration data. Then, we apply our method to the experimental data and extract the detector

response function for superconducting nanowire detectors from *QuantumOpus*. Finally, we discuss experimental imperfections from the calibration of the attenuation factor of the coherent states, as well as polarisation mixing effects in the fibres of our 8 bin TMD.

3.2.1 Moment-based Detector Calibration

The aim of this section is to find a technique that directly extracts the detector response function $\hat{\Gamma}$ [compare equation (3.11)] [152, 153] from the measured click statistics. Such a function describes the response of the physical detector to the impinging light field and is therefore a function of the photon number operators $\hat{n}$. Considering our physical superconducting nano-wire detectors, our detector response function reflects the central defining quantities of the detection unit, i.e. the quantum efficiencies η and the dark count rate ν. In our model, these two quantities are the only free parameters that we have to estimate from our data.

While we have already introduced a description for the measured click statistics with equation (3.6), we would like to introduce an, in this context more expedient, definition to calculate the click statistics corresponding to the operators of the higher click moments.

We begin with a full formal definition of the system that we consider here. We regard a two mode detection system (a TMD system as in figure 3.1) that comprises N bins ($N = 8$ for our experiment) for each of the $j = A, B$ modes. We model the on-off detectors that detect the photons after the TMD with the two operators [128]

$$\hat{\pi}_0 = |0\rangle\langle 0| =: \hat{m} : \quad \text{and} \quad \hat{\pi}_1 = \hat{1} - \pi_0 \,, \tag{3.7}$$

where the expectation value of $\langle\hat{\pi}_0\rangle$ describes the probability to measure "no-click" and $\langle\hat{\pi}_1\rangle$ the probability to measure a "click" event. Then (assuming equal splitting among all bins), the joint click counting probability c_{k_A,k_B}, i.e. the probability to measure k_A clicks in mode A and k_B clicks in mode B (with $0 \leq k_j \leq N_j$), can be constructed by an operator-valued binomial distribution [128, 154]

$$c_{k_A,k_B} = \left\langle : \binom{N_A}{k_A} \hat{m}_A^{N_A-k_A} (\hat{1}_A - \hat{m}_A)^{k_A} \times \binom{N_B}{k_B} \hat{m}_B^{N_B-k_B} (\hat{1}_B - \hat{m}_B)^{k_B} : \right\rangle \,, \tag{3.8}$$

where $\langle : \ldots : \rangle$ denotes the expectation value of a normally-ordered operator expression [2]. The joint click statistics c_{k_A,k_B} is a probability distribution and has to fulfil the conventional requirements. All probabilities sum up to unity, i.e. $\sum_{k_A,k_B}^{N} c_{k_A,k_B} = 1$ and the marginal distributions of the joint probability are given by tracing over one of the two modes, meaning for mode A $c_{k_A} = \sum_{k_B}^{N_B} c_{k_A,k_B}$ and $c_{k_B} = \sum_{k_A}^{N_A} c_{k_A,k_B}$ for mode B, respectively.

The operators $\hat{m}_j$ that appear in the binomial distribution are the "no-click" operators of equation (3.7) for modes A and B, respectively. For an ideal on-off detector, they are directly related to the photon number operator via

$$\hat{m} = e^{-\hat{n}} \,, \tag{3.9}$$

however, in a realistic case, we have to consider different detector properties, such as finite

detection efficiencies and dark count[5] rates, that influence the response of the detector (and hence the "click" and "no-click" operators) [151]

$$\hat{m}_j = e^{-\Gamma_j(\hat{n})}\,, \tag{3.10}$$

where we encoded the detector response in the function $\Gamma_j(\hat{n})$ [154]. This is the function that we finally want to evaluate with our experimental data. For a polarisation sensitive detector (as the one we use), it can be written in the form $\hat{\Gamma}_j = \Gamma_j(\frac{\hat{n}_j^{\mathrm{H}}}{N_j}, \frac{\hat{n}_j^{\mathrm{V}}}{N_j})$ for each polarisation component. Here, we consider a linear detector response function and include a finite dark count rate ν_j for a typical response function in the following form [151]

$$\hat{\Gamma}_j = \Gamma_j\left(\frac{\hat{n}_j^{\mathrm{H}}}{N_j}, \frac{\hat{n}_j^{\mathrm{V}}}{N_j}\right) = \frac{\eta_j^{\mathrm{H}}\hat{n}_j^{\mathrm{H}}}{N_j} + \frac{\eta_j^{\mathrm{V}}\hat{n}_j^{\mathrm{V}}}{N_j} + \nu_j\,, \tag{3.11}$$

where $\eta_j^{\mathrm{H/V}}$ are the detection efficiencies of the detector for horizontal and vertical polarisation, respectively.

The only thing left to do to reach our aim is to express the detector response function in terms of the measured click statistics. As such, we write down the normally ordered moments of the no-click operators $\hat{m}_j$

$$\left\langle :\hat{m}_A^{l_A}\hat{m}_B^{l_B}: \right\rangle = \left\langle :e^{-l_A\hat{\Gamma}_A}e^{-l_B\hat{\Gamma}_B}: \right\rangle\,, \tag{3.12}$$

with $l_A = 0, ...N_A$ (and for B equivalent) are the moments of the click statistics. They are obtained from the measured click statistics via the sampling formula [154]

$$\left\langle :\hat{m}_A^{l_A}\hat{m}_B^{l_B}: \right\rangle = \sum_{k_A=0}^{N_A-l_A}\sum_{k_B=0}^{N_B-l_B}\frac{\binom{N_A-k_A}{l_A}\binom{N_B-k_B}{l_B}}{\binom{N_A}{l_A}\binom{N_B}{l_B}}c_{k_A,k_B}\,, \tag{3.13}$$

which is the inverse function of equation (3.8).

Consider equation (3.12) for the situation that we want to use for our calibration technique. We wish to calibrate our click detectors with well-defined coherent states. Evaluating the normally-ordered expectation value (as an example for mode A and horizontally polarised light without dark counts) for coherent states yields [151]

$$\begin{aligned}\langle :\hat{m}_j: \rangle &= \sum_k \frac{1}{k!}\langle :\hat{\Gamma}_A^k: \rangle \\ &= \sum_k \frac{1}{k!}\,\langle\gamma_j| : \left(\frac{\eta_j^{\mathrm{H}}\hat{n}_j^{\mathrm{H}}}{N_j}\right) : |\gamma_A\rangle \quad = e^{-\Gamma_j(|\gamma_j|^2/N_j)}\,.\end{aligned} \tag{3.14}$$

As such, we generalise this to the higher order moments and for two modes with

$$\left\langle :\hat{m}_A^{l_A}\hat{m}_B^{l_B}: \right\rangle = e^{-l_A\Gamma_A(|\gamma_A|^2/N_A)}e^{-l_B\Gamma_B(|\gamma_B|^2/N_B)}\,, \tag{3.15}$$

[5] Everything that clicks in the detector when there is no impinging light is a "dark count".

where $|\gamma_j|^2$ is the intensity of the coherent state that hits detector j. This is one of the main steps of this approach, as equation (3.15) connects the measured click statistics with the coherent probe states. Choosing one of the $l_j = 0$, this relation reduces to the single mode form, that we have already seen for the first order moment in equation (3.14)

$$\left\langle : \hat{m}_j^{l_j} : \right\rangle = e^{-l_j \Gamma_j(|\gamma|^2/N_j)}\,, \tag{3.16}$$

where $|\gamma|^2$ is the intensity of the coherent field in the considered mode. This offers the neat advantage that we can directly express the detector response function in terms of the measured click statistics [151]

$$\begin{aligned} \Gamma_j\left(\frac{|\gamma^{\mathrm{H}}|^2}{N_j}, \frac{|\gamma^{\mathrm{V}}|^2}{N_j}\right) &= -\frac{1}{l_j}\ln\left(\left\langle : \hat{m}_j^{l_j} : \right\rangle\right) \\ &= -\frac{1}{l_j}\ln\left(\sum_{k_j=0}^{N_j-l_j} \frac{\binom{N_j-k_j}{l_j}}{\binom{N_j}{l_j}} c_{k_j}\left(|\gamma^{\mathrm{H}}|^2, |\gamma^{\mathrm{V}}|^2\right)\right) \end{aligned} \tag{3.17}$$

for a single detector mode j. In this equation, we separated the coherent intensity into its horizontal $|\gamma^{\mathrm{H}}|^2$ and vertical $|\gamma^{\mathrm{V}}|^2$ components as our detector will be polarisation sensitive. As we can control the polarisation state of the incoming light, we obtain the intensities for the respective polarisations[6]. Applying equation (3.17) to experimental data with coherent states, i.e. a set of $\{|\gamma_n|^2\}$, we infer the functional behaviour of the detector response function with an appropriate regression of the acquired data $\{|\gamma_n|^2, \Gamma_j(|\gamma_n|^2/N_j)\}$. With the identification of the detector response function, the detector is fully characterised. In particular, its POVMs are given by [151]

$$\hat{\pi}_{k_A,k_B} =: \binom{N_A}{k_A} e^{-(N_A-k_A)\hat{\Gamma}_A}(\hat{1}_A - e^{-\hat{\Gamma}_A})^{k_A} \times \binom{N_B}{k_B} e^{-(N_B-k_B)\hat{\Gamma}_B}(\hat{1}_B - e^{-\hat{\Gamma}_B})^{k_B} : \,. \tag{3.18}$$

In principle, we can use N_j different ways to characterise each mode of the detection system (the different moments $\langle : \hat{m}^{l_j} : \rangle$ with $l_j = 1, ..., N_j$), which corresponds to a different evaluation of the measured click statistics c_{k_A,k_B}. However, we only consider the first moment of the click statistics ($l_j = 1$) as the statistical significance of the higher order moments is lower and we get more reliable information about the response function with this contribution [151].

The main advantage of our scheme is the resource efficiency, both from a theoretical and experimental point of view. Experimentally, we only need to perform phase-insensitive measurements with power-controlled coherent states. Theoretically, we reduce the complexity of a full detector tomography with the only assumption that we characterise a click-counting device to evaluating equation (3.17). With the detector response function obtained from this equation, we directly gain information about the defining quantities of the system, i.e. both detection efficiency and dark count rate [151]. This knowledge about detector efficiency and dark count rate is another advantage compared to general detector tomography. Here, this specific information

[6] Ideally. In section 3.2.4, we discuss why this is not always the case and what goes wrong if it isn't.

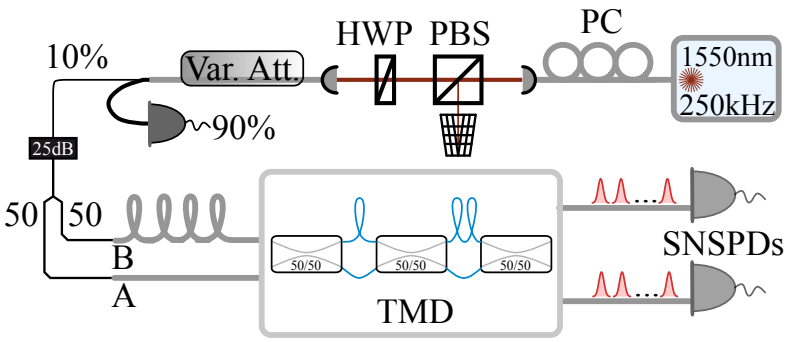

Figure 3.6 – Setup for the detector calibration [151]. We use picosecond pulses from a fibre-coupled 1550 nm laser diode and clean the polarisation at a polarising beam splitter (PBS). Afterwards, we change the input polarisation with a half-wave plate (HWP) and couple the pulses to an electronic variable attenuator (Var. Att.). We monitor the pulses with a power meter at a 90 % and couple the remaining 10 % to another 25 dB attenuation, before splitting the pulses at a 50/50 beam splitter. Finally, we feed the pulses into an 8 bin TMD and measure the resulting output distribution with superconducting nanowire detectors (SNSPDs) by *QuantumOpus*.

is not easily accessible in the general model, as the parameters of the reconstructed POVMs do not necessarily identify with the physical properties of the detector. Only for more specific detector models, such information can be extracted [126].

3.2.2 Setup

To obtain experimental data for our detector calibration, we implemented the setup in figure 3.6. We perform our experiment with pulses from a picosecond diode laser (PicoQuant) that produces a pulse duration of about 35 ps at a wavelength of 1550 nm with a repetition rate of 250 kHz. Afterwards, we clean the polarisation of the incoming pulses with a bulk polarising beam splitter (PBS), rotate the polarisation of our light with a half-wave plate (HWP). We then couple the light into a single mode fibre (SMF 28) attenuator, which reduces the laser power by a given value. For each attenuation level, we record data for an integration time of $T_{\text{int}} = 50\,\text{s}$ and lower the laser power by an additional 0.2 dB after each measurement. We monitor the action of the attenuator at a 90 % tap-off with a power meter (Thorlabs). The remaining 10 % undergoes further 25 dB attenuation and is split at a single mode fibre 50/50 beam splitter to feed both input fibres of the 8 bin time-multiplexed network[7] with polarisation maintaining fibres. Finally, we record the click statistics with superconducting nano-wire detectors (SNSPDs) from QuantumOpus.

[7] 125ns nominated time-bin separation due to detector relaxation time after detection event, fibres: Fujikura SM15-PS-U25D, loss 0.25 $\frac{\text{dB}}{\text{km}}$, splitters: Evanescent Optics 954P, loss $\approx$ 0.1 dB, overall TMD transmission $\approx$ 90 % for both modes

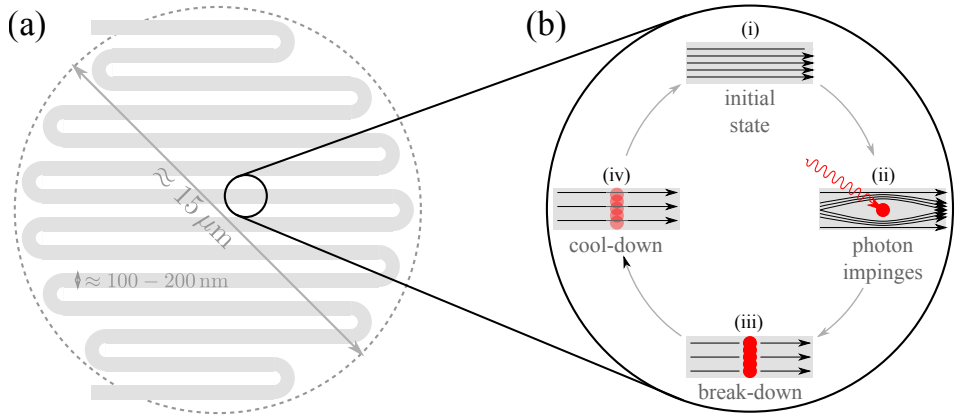

Figure 3.7 – Superconducting nano-wire detectors. Figure (a) shows an example geometry for the folding of the nano-wire (adapted from [155]) and (b) the working principle of the single photon detection (adapted from [146]).

Each of the used SNSPDs comprises a long ($\approx 100\,\mu$m) and thin ($\approx$ 100 nm width and $\approx$ 5 nm height) wire made from a superconducting material, e.g. Tungsten Silicide, which is folded in a parallel orientation, see figure 3.7(a) [155]. It is operated slightly below the critical temperature (the point where the material transitions from superconducting to normal conducting state), however, we apply a bias voltage (≈ 0.64 V, corresponding to $\approx 65\,\%$ detection efficiency) which leads to a current density in the wire that is just below the critical current density (the current, where the material becomes normal conducting) [146].

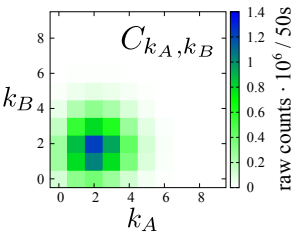

Figure 3.8 – Typical result for measured click statistics C_{k_B,k_B} (HWP = 0°, no attenuation).

The photon detection process is sketched schematically in figure 3.7(b). In the undisturbed system (i) the current may flow through the wire unhindered. The impinging photon in (ii) creates a local hotspot, where the material becomes normal conducting. The current is then pressed to the outer sides of the wire, as the material is still superconducting outside the hotspot. Yet, the accordingly increased current density at the edges of the wire exceeds the critical current density, which leads to the full breakdown of the superconductivity in (iii). This leads to a voltage spike, which can be amplified and finally passed on to be registered as a detection event at a time tagging mode, as in our case. After the breakdown, the wire needs some cool-down time to regain the equilibrium (vi).

Contrary to the APDs which we used in the previous chapter (compare section 2.4), the SNSPDs are *free-running*, meaning that they do not require a trigger signal to open a detection window, but are able to detect photons continuously over time. As such, we sent a copy of the diode laser trigger to the time tagging module (AIT, TTM-8000, resolution: 82ps) and recorded the relative arrival times of the SNSPD detection signal to the trigger. Finally, we first

evaluated the time traces of the TMD signal [as an example for such a time trace, see figure 3.11(b)] and introduced time gates of 10ns width in the post-processing step to cut out each of the different time bins separately. Counting the number of detection events between two trigger events for each detection mode (the first $N/2 = 4$ bins belong to mode A, while the other $N/2 = 4$ bins belong to mode B) and accumulating the results for all trigger events yields the final measured, but unnormalised click statistics C_{k_A,k_B}, see figure 3.8 for a typical result.

Due to the internal structure of the SNSPDs, as shown in figure 3.7(a), their detection efficiency shows a significant dependency on the input polarisation of the incident light [145, 146]. Although we have implemented our TMD with polarisation maintaining fibres, our attenuator and the other fibre components are based on single mode fibres. As those are not polarisation maintaining, we do not enter the TMD with a well-defined polarisation. As polarisation maintaining fibres are only maintaining the polarisation for horizontal and vertical polarisation, we still see polarisation mixing for the different time bins at the detector due to the different fibre lengths in the TMD. For a full discussion of the experimental imperfections and the effects on the analysis, see section 3.2.4.

3.2.3 Data Analysis and Application of the Method

In this section, we perform the analysis of the experimental data for the above described 8 bin TMD. First, we extract the detector response function for the inserted horizontal and vertical polarisation into the fibre network. Secondly, we investigate the behaviour of a TMD for intermediate polarisations.

Evaluation of the Detector Response Function

To extract the detector response function, we first analyse the measured data to evaluate the click statistics. We measure the event distribution C_{k_A,k_B}, see figure 3.8, which we have to normalise by $C = \sum_{k_A=0}^{N_A} \sum_{k_B=0}^{N_B} C_{k_A,k_B}$ to obtain the joint click statistics c_{k_A,k_B}. With equation (3.13), we extract the corresponding moments $\overline{\langle{:}\hat{m}_A^{l_A}\hat{m}_B^{l_B}{:}\rangle}$ from the experimental data. In our notation, the overline denotes the mean value of the sampled distribution. We calculate the statistical errors by error propagation and obtain [151]

$$\sigma\left(\overline{\langle{:}\hat{m}_A^{l_A}\hat{m}_B^{l_B}{:}\rangle}\right) = \frac{1}{\sqrt{C-1}}\sqrt{\sum_{k_A=0}^{N-l_A}\sum_{k_B=0}^{N-l_B} c_{k_A,k_B}\left(\frac{\binom{N-k_A}{l_A}\binom{N-k_B}{l_B}}{\binom{N}{l_A}\binom{N}{l_B}} - \overline{\langle{:}\hat{m}_A^{l_A}\hat{m}_B^{l_B}{:}\rangle}\right)^2}. \quad (3.19)$$

Then, we estimate the moments with $\langle{:}\hat{m}_A^{l_A}\hat{m}_B^{l_B}{:}\rangle = \overline{\langle{:}\hat{m}_A^{l_A}\hat{m}_B^{l_B}{:}\rangle} \pm \sigma\left(\overline{\langle{:}\hat{m}_A^{l_A}\hat{m}_B^{l_B}{:}\rangle}\right)$. With the estimated moments, we directly evaluate $\Gamma_j\left(\frac{|\gamma^{\mathrm{H}}|^2}{N_j}, \frac{|\gamma^{\mathrm{V}}|^2}{N_j}\right)$. Note, that we extract the moments directly from the measured data and do not apply any post-processing. As such, we do not generate computational overhead, such as loss inversion or other data reconstruction techniques [151].

Now that we obtained the complete data set with the measured moments, we have to eval-

uate the corresponding coherent state intensity γ for each data point. We monitor the power that impinges on the TMD via the $90\,\%$ tap-off with a power meter (see figure 3.6). We introduce a power operator $\hat{P}$ for the measured power and express the corresponding photon number operator via [151]

$$\hat{n}_j = \chi \hat{P}\,, \tag{3.20}$$

with $j = A, B$ and $\chi = (1.77 \pm 0.17) \cdot 10^8\,\mathrm{W}^{-1}$ is the measured attenuation factor between the $90\,\%$ tap-off and the power that enters the TMD. The error for χ is obtained via error propagation for the uncertainties of the power measurements, which are specified with a relative error of $\pm 5\,\%$[8]. The coherent state intensities are given by $|\gamma_k|^2 = \langle \hat{n}_j \rangle$.

With the full data set of coherent intensities and the extracted moments, we now analyse the detector response function for the different modes and polarisations. For both horizontal and vertical polarisation, we consider the click-counting statistics for 45 different power levels. We plot the results in figure 3.9. The blue data points denote the measured data sets, where we propagated the errors from the click statistics (in y-direction), however the uncertainties are so small that they are not observable in the plot. The larger uncertainty is from the calibration of the coherent intensities (error bars in x-direction) which stem from the uncertainties of the power meter and the uncertainty in the calibration of the attenuation. As we see from the depicted data sets, the uncertainties in the coherent intensities outweigh the statistical errors of the measured data.

To obtain the functional behaviour of the detector response function, we have to find an appropriate regression for the measured data sets. For any general response function, we can express it in terms of a Taylor expansion [151]

$$\Gamma_j(\hat{P}_j/N_j) = \sum_{t=0}^{\infty} \tilde{\Gamma}_j^{(t)} (\hat{P}_j/N_j)^t\,. \tag{3.21}$$

Here, we use the power operator $\hat{P}_j$ so that we can perform the data analysis directly with the measured click statistics, independent of the power calibration of the coherent state inputs. Any quantity related to the power operator is marked with a tilde. With this notation, the weights for the linear and quadratic terms of the Taylor expansion are $\tilde{\Gamma}_j^{(1)}$ and $\tilde{\Gamma}_j^{(2)}$, respectively.

In order to ascertain the functional behaviour of the detector response function, we first consider the impact of the non-linear terms of the Taylor expansion. Therefore, we perform a full regression with a polynomial up to the third order and compare the higher order coefficients to the linear one. This yields a contribution for the quadratic term of $\tilde{\Gamma}_j^{(2)}/\tilde{\Gamma}_j^{(1)} \approx 10^{-3}$ and for the cubic term $\tilde{\Gamma}_j^{(3)}/\tilde{\Gamma}_j^{(1)} \approx 10^{-4}$. From this regression, we see that a linear function is sufficient to describe the functional behaviour of the detector response function [151]

$$\Gamma_j(\hat{P}_j/N_j) = \tilde{\eta}_j \hat{P}_j/N_j + \tilde{\nu}_j\,, \tag{3.22}$$

with $\tilde{\Gamma}_j^{(0)} = \tilde{\nu}_j$ as the dark count rate. Comparing the dark count rates $\tilde{\nu}_j$ with the linear coefficient $\tilde{\Gamma}_j^{(1)}$, we find that the dark count rate is approximately zero, such that we can neglect

[8] From the specifications of the used Thorlabs power meter.

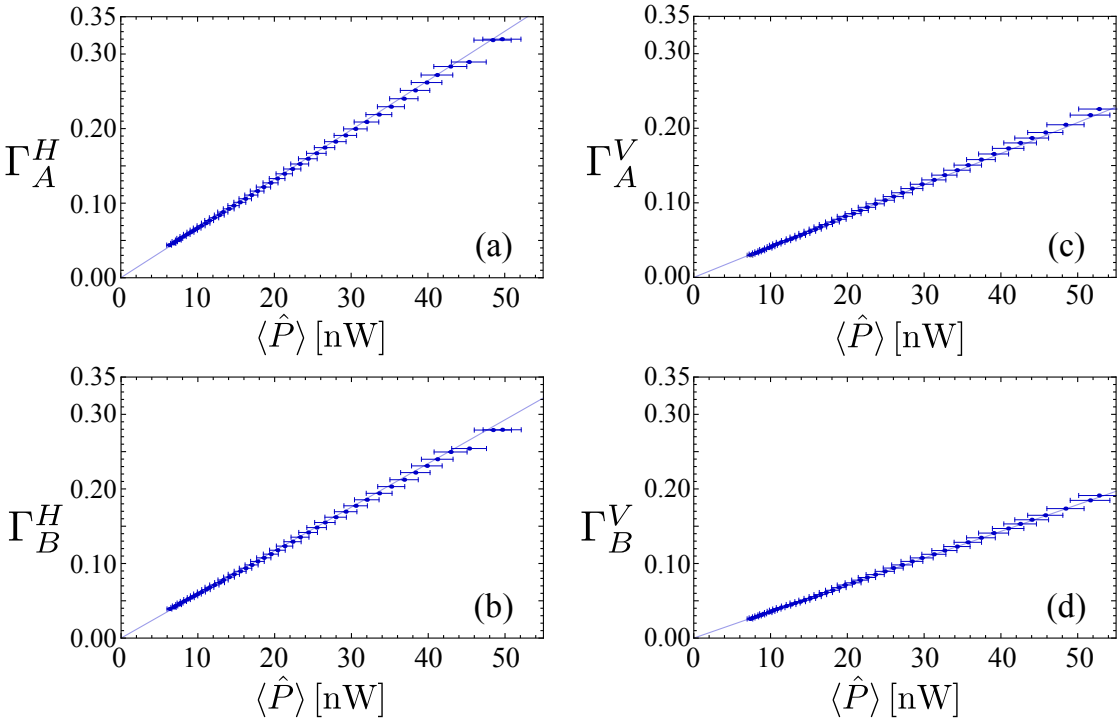

Figure 3.9 – Detector response functions for the two modes with horizontal and vertical polarisation [151]. (a) shows mode A with horizontal and (c) with vertical polarisation. (b) and (d) show mode B with horizontal and vertical polarisation, respectively. All detector modes show a clear linear dependence on the input intensity and the detection efficiency for vertical polarisation is well below the one for horizontal polarisation, as expected by the internal structure of the detectors.

this contribution and perform a regression of the form $f(x) = ax$. This fits to the known behaviour of SNSPDs that are virtually dark count free [156]. As a regression algorithm, we use a weighted total least-squares method [157], which also considers the measurement and statistical uncertainties. We plot the regression curves as light blue lines in figure 3.9 and have additionally summarised the results from the linear regressions for both modes A and B, as well as the two polarisations H and V in table 3.1.

As we already stated above, the accurate determination of the detector response function characterises the considered detector completely (for photo-electric models). Therefore, with the parameters from our linear regression in table 3.1, we can evaluate the accuracy of our characterisation method. Excluding the errors from the attenuation measurement, we first consider the quantity that directly depends on the power operator, $\tilde{\eta}$. In our method, it is the slope of the regression curve of the data points and it can be determined with a relative uncertainty of up to $0.04\,\%$. This is a very good relative error compared to conventional approaches. Methods that use twin beam characterisations have achieved relative uncertainties of $0.18\,\%$ [147], $0.04\,\%$

Γ	$\tilde{\eta}$ (1/nW)	$\sigma_{\tilde{\eta}}$ (1/nW)	η [%]	σ_η [%]	Figure
Γ_A^{H}	$52.86 \cdot 10^{-3}$	$0.04 \cdot 10^{-3}$	29.8	2.8	3.9(a)
Γ_B^{H}	$46.83 \cdot 10^{-3}$	$0.02 \cdot 10^{-3}$	26.4	2.5	3.9(b)
Γ_A^{V}	$33.23 \cdot 10^{-3}$	$0.04 \cdot 10^{-3}$	18.7	1.8	3.9(c)
Γ_B^{V}	$28.63 \cdot 10^{-3}$	$0.01 \cdot 10^{-3}$	16.1	1.6	3.9(d)

Table 3.1 – Parameters and error estimates (σ) of the linear detector response in equation (3.22) [151].

[148], 0.39 % [149] and 5 % [150] up to now. In general detector tomography, a relative error of about 8 % [126] has been achieved. Compared to these benchmarks in the literature, our method performs as good or even better than what has been shown previously [151].

Up to now, we have only considered the quantities that directly depend on the measured power $\langle \hat{P} \rangle$. To gain information about the "real" detection efficiencies, we need to include the scaling factor for the single photon level. Note, that this quantity gives the net efficiency of the whole detector system, accounting for losses inside and after the TMD, as well as the detection efficiencies of the SNSP detector itself. The detection efficiency is given by η in table 3.1. With this information, we discuss the accuracy of the overall measurement process, which we can estimate to an uncertainty of 9.4 % for the quantum efficiency. The absolute error for the detection efficiency is determined and limited by the accuracy of the attenuation parameter $\chi = (1.77 \pm 0.17) \cdot 10^8\,\mathrm{W}^{-1}$. As we already stated above, this measurement was limited by the accuracy of the used power meter at small powers, which causes a large error for the absolute determination of the quantum efficiency. However, the optimisation of this measurement is a purely experimental problem and does not affect our general characterisation method [151].

Investigation of the Polarisation Dependence

Previously, we investigated the response of our TMD system for the two principal polarisations H and V. As the nanowire detectors possess a strong polarisation dependence for the detection efficiency, we now analyse this effect with our time-multiplexed detector. We perform a characterisation measurement for 17 different polarisations and extract the detector response function from the measured data. Since the detector response function is purely linear and we can neglect dark counts, we only need to compare the extracted quantum efficiencies.

The results are shown in figure 3.10 for the two detector modes A in figure 3.10(a) and B in figure 3.10(b). The blue dots denote the extracted quantum efficiencies with our method and the light blue lines indicate a cosine fit with

$$\eta(\phi) = \frac{\eta_{\max} - \eta_{\min}}{2} \cos[4(\phi + \phi_0)] + \frac{\eta_{\max} + \eta_{\min}}{2}\,. \tag{3.23}$$

Here, we have chosen ϕ as the angle of the initial HWP (see figure 3.6) and $\eta_{\min}$, $\eta_{\max}$ as the minimal and maximal quantum efficiency, respectively.

Consider mode A in figure 3.10(a) first. We find a minimal and maximal quantum efficiency of $\eta_{A,\min} = 19.3\,\%$ and $\eta_{A,\max} = 30.2\,\%$. The offset from the nominal zero-value is $\phi_{0,A} = 1.5°$.

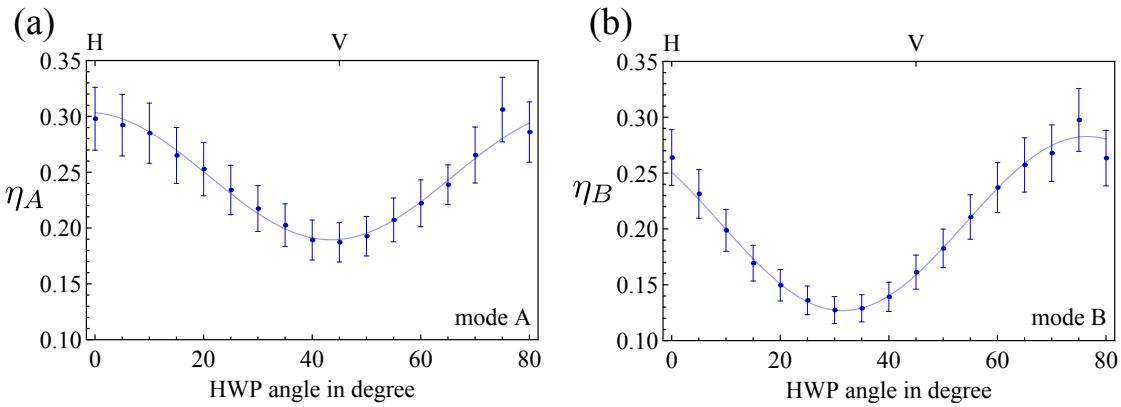

Figure 3.10 – Polarisation dependence of the measured quantum efficiencies for detector modes A in (a) and B in (b) [151]. The dots denote the measured data points and the light blue lines denote the sinusoidal fit. The exceptional values for horizontal and vertical polarisation are indicated.

This shows that the principal axes for the detected horizontal and vertical polarisation coincide well with the used angle of the half wave plate. In summary, this behaviour is expected due to the geometry of the nanowire detectors [158].

For mode B in figure 3.10(b), the behaviour is different. We still see a clear sinusoidal behaviour depending on the initial HWP angle, but it is drastically shifted. For this curve, we find minimal and maximal quantum efficiencies of $\eta_{B,\min} = 12.8\,\%$ and $\eta_{B,\max} = 28.2\,\%$ with a nominal zero-value shift of $\phi_{0,B} = 13.5°$. As such it is clear that the detected horizontal and vertical polarisation for the A and B modes do not coincide. Additionally, the ratio between the A and B modes for the minimal quantum efficiency is $\eta_{B,\min}/\eta_{A,\min} \approx 0.66$, while this ratio for the maximal quantum efficiency is $\eta_{B,\max}/\eta_{A,\max} \approx 0.93$. This discrepancy raises the question why the two detector modes yield such different behaviour for the minimal quantum efficiency, while the maximal quantum efficiency is comparable. Furthermore, from the layout of our detection scheme, we would not expect such a huge difference, as the same physical detectors are used.

To understand these discrepancies, we consider the layout of the TMD. While we have used polarisation maintaining fibres for the TMD itself, the fibre network in front of the detection system is *not* polarisation maintaining. This means, in general, that the impinging light will not be fully aligned to the primary axes of the fibre core of the polarisation maintaining fibre and we obtain polarisation rotations due to the birefringence of the fibre itself. As the B mode travels an additional length of fibre compared to the A mode, this explains the overall shift in the polarisation dependence in figure 3.10(b). Nevertheless, it does not explain the significant difference in the minimal quantum efficiencies. Therefore, we discuss the impact of experimental imperfections, in particular of inaccurately aligned polarisation states on TMD measurements.

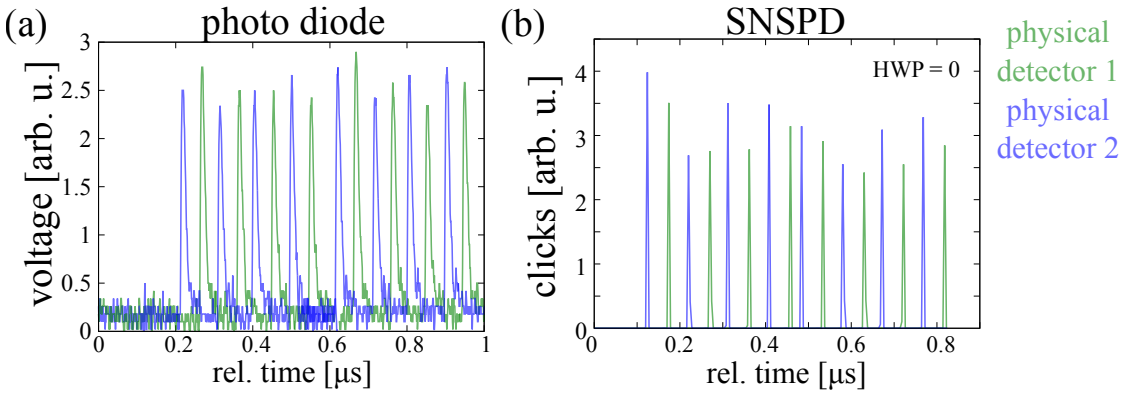

Figure 3.11 – Comparison of the different time bin efficiencies with a photo-diode and with the SNSPDs [151]. In (a), we have measured the intensity of the time-bins with a polarisation insensitive photo-diode. Figure (b) shows the same measurement with the nano-wire detectors. The strong difference in the detected intensities of figure (b) cannot be explained by imperfect splitting ratios, as the photo-diode measurement shows similar peak heights for all time bins. This hints at a polarisation dependent imperfection due to the sensitivity of the nano-wire detectors.

3.2.4 Discussion of Experimental Imperfections and Impact on the Model

In the previous sections, we introduced and applied our method to infer the detector response function directly from the measured data. We showed that our method is both reliable, resource efficient from the theoretical and experimental side and provides an accurate estimation of the characterising parameters such as detection efficiency. However, our model depends on several assumptions that might not always be justified in an experiment. Here, we discuss the impact of these experimental imperfections on our model.

The most critical assumption in our model is that the photons get split according to a binomial distribution, compare equation (3.8), in the TMD. Experimentally, this means that the probability of finding a photon in any time bin is equal and that we have perfectly even splitting in the beam splitters. However, this is also the assumption that is most difficult to realise in an experiment. In our experiments, we additionally found a strong polarisation dependence for the detection efficiency which might affect separate time bins differently [151].

To investigate a possible effect of polarisation dependence on different time bins, consider figure 3.11. In figure 3.11(a), we have recorded the time bin dependent intensity after the TMD with a polarisation insensitive photo diode and an oscilloscope. The peak height is not fully equal for all bins, however this small variation is within the specified fabrication imperfections of the used fibre splitters. Compare figure 3.11(b), where we recorded the time bin resolved photon counts from the SNSPDs, exemplarily for a half wave plate angle of $\phi = 0$. Here, we observe a significant difference in the separate bin count rates. We attribute this to a polarisation mixing in the polarisation maintaining fibres of the TMD, as we do not observe this effect in the measurement with the polarisation insensitive photo-diode.

The observed polarisation mixing is due to the single mode fibre components in front of the TMD. We enter the single mode fibre network with e.g. horizontally polarised light. Then, due to the low birefringence in unavoidable fibre bendings of the single mode fibres, the polarisation state is slightly rotated, depending on the positioning of the single mode fibres. Since polarisation maintaining fibres only maintain purely horizontally or vertically polarised light, a mixed polarisation state at the input of the fibre gets projected onto this basis. Due to the intrinsic birefringence of polarisation maintaining fibres, the phases between horizontal and vertical axis change, depending on the passed fibre length. Coming back to our TMD implementation, this means that, depending on which fibre length the light has passed, we end up with different polarisation states. In the corresponding time bins, we will therefore find different polarisation states impinging on the nano-wire detectors and measure the bins with different detection efficiency.

In our model, we do not include such an effect [151]. Therefore, the imbalance and polarisation mixing mean that we do not estimate the detection efficiency for each time bin separately, but only an averaged efficiency over all bins. This effect impacts especially mode B in our case, consider figure 3.10(b) and the corresponding discussion.

Theoretically, this polarisation effect means the following for our model. Let us consider a coherent state $|\alpha\rangle$ that enters our TMD. It gets split on N bins as before, but with unequal splitting ratios, i.e. $|t_1\alpha, ...t_N\alpha\rangle$ and $\sum_i |t_i|^2 \leq 1$ to account for the losses. Compare the ideal case of perfectly equal splitting and no loss with $|t_i|^2 = 1/N$. In this case, we can only evaluate the average of the time bin statistics and therefore get a superposition of the response functions for the separate bins [151]

$$\ln\langle :e^{\Gamma_1(\hat{n}_1)} \dots e^{\Gamma_N(\hat{n}_N)}: \rangle = \sum_{i=1}^{N} \Gamma_i(|\alpha|^2/|t_i|^2)\,. \tag{3.24}$$

If we perform a Taylor expansion on this quantity, as before, we obtain

$$\overline{\Gamma}(|\alpha|^2) = \sum_{j=0}^{\infty} \sum_i c_i^{(j)} (|\alpha|^2)^j = \sum_{j=0}^{\infty} \overline{c^{(j)}} (|\alpha|^2)^j\,, \tag{3.25}$$

where we again identify especially the linear coefficient of the expansion with the averaged quantum efficiency $\overline{\eta} = \overline{c^{(1)}}$ and the overlines denote the average over all time bins . Following this expression, we find that we can characterise the TMD with an averaging over the time bins and cannot resolve the individual detector response for each time bin. In this sense we also have to regard the discussions in section 3.2.3, where we only estimate the average detector response for all time bins [151]. Again, this imbalanced splitting is not a fundamental problem of our calibration method, as in principle it can be adapted to arbitrary splitting ratios[9].

From the experimental point of view, there are several possibilities to ensure that we obtain an equally split distribution for our TMD. Either, we use polarisation independent detectors, such as avalanche photo-diodes or we ensure that purely horizontally or vertically polarised light enters the multiplexing part of the TMD. To achieve this we have two possibilities. First, we could use a fully polarisation maintaining fibre network, including the fibre based electronic

[9] It involves heavy math to obtain the correct moments.

attenuators or couplers. The second possibility is to insert a polarisation control in front of the TMD network to re-align the polarisation state after the single mode fibres. This solution is very practical, however, one has to carefully align the polarisation state, as the unequal splitting from the imperfect beam splitters is indistinguishable from the effect of the polarisation mixing.

Summary

In summary, we introduced and applied a slim and efficient calibration technique for time-multiplexed detectors [151]. We used the measured click statistics to obtain the click moments that directly depend on the detector response function. With this function, we are able to fully characterise the detector and can, in principle, reconstruct the POVMs of the system. We experimentally measured the click statistics for coherent states and calibrated a time-multiplexed detector system together with superconducting nano-wire detectors. We found a strong polarisation dependence for the detection efficiency and investigated a possible polarisation mixing effect in the TMD with respect to the calibration of our detector. We quantified the resulting experimental imperfections and discussed their effect on our method.

3.3 Testing Quantum Free-space Channels by Lab Experiments

In the previous sections, we investigated the limits of the time-multiplexed photon counting method and developed a new, efficient detector calibration method for a time-multiplexed detector. Now, we apply time-multiplexed detection and simulate an atmospheric quantum communication free-space link. To set the correct framework for our experiment, we comment briefly on the aims and intentions of quantum communication in general.

The dream of quantum communication is to span a earth-wide quantum-secure communication network. There are two necessary parts to achieve this dream. First, we have to develop quantum-secure communication *protocols*. A lot of work has already been invested into the development of these protocols since the 1980s and many of them have been successfully demonstrated in the laboratory (for the early and most known protocols, see [3, 4, 159–162]). This is the first part of the dream achieved. The second part is still work-in-progress. We need to span an earth-wide communication network, which is quantum-enabled. This is a bit more complicated. Usually, we need a *nonclassical resource* to transmit the desired information in a quantum channel. Unfortunately, however these nonclassical states are rather fragile and not very resilient against losses, noise and other undesirable processes that may deteriorate a communication channel.

In classical communication, this is not really an issue. There, we can use coherent, *classical* light to transmit the information through existing glass fibre networks. Of course, also coherent light experiences losses in a fibre. Yet in classical optics, we can use amplifiers to compensate for the losses that a coherent state experiences. As it is, this is not possible with a quantum resource, it is forbidden by the *no-cloning theorem* [163, 164]. This theorem forbids to deterministically and perfectly clone a quantum state. Perfect amplification falls under this category,

as splitting the quantum state at a 50/50 beam splitter and amplifying both channels afterwards would constitute a cloning procedure [1].

In practice, this poses a highly non-trivial problem. Due to the no-cloning theorem, we cannot compensate for fibre losses. The compensation of noise effects is also difficult, as the light field is too weak for a parallel monitoring of the noise. Furthermore, the nonclassical states are fragile and once the nonclassicality is destroyed, it is virtually impossible to recover it. As such, quantum communication has to put in a lot of effort to optimise or at least characterise the properties of quantum channels *themselves* in order to enable secure communication.

Let us consider different quantum communication channels. Since we use light as a signal, we can use the standard classical communication architecture. This means on the one hand fibre links, which are buried underground and already optimised with respect to losses. Due to the encapsulated transfer under the earth, this communication link is quite stable with respect to noise. On the other hand, we use satellite communication systems to transfer TV, radio or communication signals. As these signals are transmitted through the atmosphere, they suffer from any atmospheric instability, the most obvious one being the weather. Already small changes in the temperature or the pressure induce small changes in the refractive index of our transfer medium. Due to the long distance between the orbit of the satellite and a ground station, these small changes induce turbulent losses.

It becomes clear that atmospheric links require both a careful theoretical, as well as experimental analysis. As free-space atmospheric quantum communication channels have been successfully implemented over the years [165–171] and now with a real-life quantum communication satellite in the orbit [172–176], the behaviour of quantum light in such turbulent atmospheric conditions has to be well investigated [177]. Based on optical measurements of the atmosphere, several models for turbulent losses in quantum communication links have been developed in the past [178–180]. They have been applied to various classes of nonclassical states and their robustness under fluctuating losses has been investigated [181–189]. Another approach is to re-create the atmospheric conditions in the laboratory with turbulence cells [190, 191] or with a moving lens [192]. Also modulated phase-screens have been utilised [193, 194], however they do not re-create the observed intensity fluctuations of a realistic scenario. As such, this approach is limited to specialised applications [39, 195].

Here, we apply the click-counting method that we successfully utilised for detector characterisation also for the characterisation of nonclassicality under turbulent losses, as experienced in the atmosphere. As such, we develop a simulation procedure to simplify the laboratory experiments and eliminate the need for bulky equipment, such as turbulence cells.

Many quantum communication protocols use pulsed light to transmit the information over the channel. Due to this fact, the turbulent nature of the atmosphere affects each transmitted pulse separately. This fact enables us to simulate the turbulence via an *incoherent mixing of constant loss values*. Imagine the following. We take one pulse, which experiences a loss of $25\,\%$. the next one a slightly different one of $35\,\%$, the one after again $25\,\%$. Since the pulses are independently affected, we can sort them by their losses and count their relative frequencies. Hence, experimentally, it does not make a difference, if the pulses were recorded in a *turbulent* manner or if the different loss levels were recorded separately and mixed afterwards.

This is exactly what we are going to do here. We develop our simulation procedure based on

the description of the turbulent atmosphere via probability distributions of transmittance [177]. Furthermore, as we are interested in the robustness of the nonclassicality of our state, we briefly review the nonclassicality criteria for click-counting methods [154]. Afterwards, we describe the experimental setup and analyse three different cases of probability distributions with our measured data. First, we consider general temperature and pressure fluctuations the main contributions to strong turbulence, as modelled by a log-normal distribution [168]. Second, we investigate the effect of beam wandering the main contribution to weak turbulence, given by the Weibull distribution [178] and finally, we show the general applicability of our method by applying our measured data to the general family of the beta-binomial probability distributions [196].

3.3.1 Simulation of Atmospheric Channels with Click Counting Experiments

To sketch our simulation approach for the effects of atmospheric free-space channels in the laboratory, we have to incorporate the atmospheric models in the transmitted quantum state and describe the experienced deterioration in an appropriate formalism. Optical transmittance through the atmosphere is difficult, as we have already elaborated above. The atmosphere is a medium which is constantly changing. Depending on the illumination of the sun, it gets heated selectively only from one side, the oceans warm up differently than the land etc. This leads to the well-known phenomenon that we colloquially describe as weather. As we know from everyday experience[10], optical transmission through the atmosphere is difficult on a cloudy day, as the water in the cloud absorbs the transmission signal. However, also on sunny days the atmosphere is not a still medium. The air is still flowing around and this leads to small pressure and temperature fluctuations. This leads to minimal, random changes in the refractive index of our transmission channel. As such, our optical beam is affected and gets deteriorated by effects, such as beam broadening, beam wandering, scattering and beam deformation.

The ground station or the satellite measure the light beam with a finite aperture detector. Then, the degradation of the beam in form of wandering or distortion translates as different detection efficiency or different losses on the detector. As such, we can in general describe the effect of the atmosphere with a loss probability distribution $\mathcal{P}(\eta)$ [177]. In this function $1-\eta$ is the loss of the channel and $\mathcal{P}(\eta)$ describes with which probability a certain loss is to appear. In the literature, this type of function is called probability distribution of transmittance (PDT) and describes the free space channel completely.

The effect of the PDT on the transmitted quantum state is best described in terms of the Glauber-Sudarshan P-function [62, 63]

$$P_{\mathrm{out}}(\alpha) = \int_0^1 \mathrm{d}\eta \, \frac{1}{\eta} \, \mathcal{P}(\eta) \, P_{\mathrm{in}}\left(\frac{\alpha}{\sqrt{\eta}}\right) . \tag{3.26}$$

The P-function is one possibility to transfer the classical concept of a phase-space function into the quantum domain and describes the state fully, see chapter 1. The output state after passing a free space communication channel, is then given by a convolution of the P-function of the

[10] Evil tongues would argue that we should know it best in Paderborn...

input state with the PDT and we obtain the output P-function. However, we work directly with the measured click statistics to simulate the atmospheric effects and therefore need a different approach.

We wish to simulate the effects of an arbitrary atmospheric free-space link on our quantum state in the laboratory. To do this, we take a finite, discrete number of different loss levels that we can afterwards merge according to the PDT in question. However, the PDT is, in general, a continuous function in the interval $[0, 1]$. We therefore need an appropriate discretisation routine for the PDTs to apply them in our experiment. Here, we use the approach of probability mass functions. In our case, the discrete PDT version is given by [197]

$$\tilde{\mathcal{P}}(\eta_k) = \frac{\mathcal{P}(\eta_k)}{\sum_{j=0}^{n} \mathcal{P}(\eta_j)} \tag{3.27}$$

This discretised distribution gives the probability to find a transmissivity η_k in a signal transmission of the quantum channel. It is given by the value of the continuous PDT $\mathcal{P}(\eta_k)$, normalised to the sum of the discretised probability over all discretisation points ($n = 100$ in our case).

With this discrete probability distribution, we are now able to merge the different measured constant loss settings to simulate the atmosphere. In the experiment, we take a data set $x(\eta_k)$, where with η_k as the transmission efficiency of the k-th measurement. Then, we merge the data according to the discretised PDT via [198]

$$x^{\text{atm.}} = \sum_{k=k_{\min}}^{k_{\max}} \tilde{\mathcal{P}}(k)\, x(\eta_k)\,. \tag{3.28}$$

Naturally, the measured data sets are not turbulent. The different loss levels are measured in an ordered fashion and independent from each other. However, even in the turbulent atmosphere, consecutive transmissions are independent from each other, since the transmission of a single pulse is the interesting figure of merit. As such, we can sort the transmission events according to the experienced losses without changing the problem. Therefore, it does not make a difference, if we first measure the turbulent data and sort them afterwards (as we would do with the data taken from the atmosphere) or measure them in an ordered fashion and mix them afterwards (as we do here). Thus, our simulation method represents a realistic model of the atmospheric free-space channel.

Now, we have a simulation routine for the effect of atmospheric channels on quantum states on the laboratory scale. The only thing that is missing is the verification of the nonclassicality in the transmitted signal. To this aim, we use click-counting detectors to take our measurement data by means of time-multiplexed detection. As we have already discussed in sections 3.1 and 3.2, the normalised click counting probabilities c_i are given by a binomial distribution [128, 154]

$$c_i = \left\langle : \binom{N}{i} \hat{m}^{N-i} (\hat{1} - \hat{m})^i : \right\rangle . \tag{3.29}$$

Note, that this is the one-dimensional version of equation (3.8). As for equation (3.8), N is the number of detectors (or time bins) and the normally ordered expectation value of $\hat{m}$ give

the no-click probability. As in section 3.2, we obtain the expectation values of $\hat{m}$ from the click statistics c_i via (3.13). In our case, the different measured sets of $\{c_i\}_k$ represent our $x(\eta_k)$ for the simulation of the atmospheric channel. For our investigation we only use the one-dimensional representation of the click statistics, as the utilised source produces two copies of the same state.

In order to identify the nonclassicality in the transmitted signal, we use the eigenvalues of the matrix of moments, which is defined by [154]

$$M^{(2)} = \begin{pmatrix} 1 & \langle : \hat{m} : \rangle \\ \langle : \hat{m} : \rangle & \langle : \hat{m}^2 : \rangle \end{pmatrix} . \tag{3.30}$$

This is the smallest possible matrix, as it contains only the lowest moments of $\hat{m}$. The superscript (K) denotes the highest moment of $\hat{m}$, which is contained in the matrix. For a click detector with N bins, $M^{(N)}$ is the highest matrix of moments with dimension 5×5 for $N = 8$, as we consider here. The general construction rule for the matrix of moments is given by [154]

$$M^{(K)} = \left(\langle : \hat{m}^{s+t} : \rangle \right)_{(s,t)} , \tag{3.31}$$

where $s, t = 0, ..., \frac{K}{2} \leq \frac{N}{2}$ for even K and even N. It can be shown that this matrix of moments is positive-semidefinite for all classical states [154], which means that all eigenvalues $e_i^{(K)}$ fulfil

$$e_i^{(K)} \geq 0 . \tag{3.32}$$

By implication, this means that if we find any eigenvalue $e_i^{(K)} < 0$, this is a sufficient condition to verify the nonclassicality of the measured state [154]. Additionally to the simplicity and elegance of this approach, we retain the advantage that we directly work with the measured click statistics and do not have to use post-processing algorithms. This makes this method to analyse the nonclassicality very efficient in terms of computation time and stability.

3.3.2 Setup

To simulate the influence of atmospheric free space links on nonclassical states, we utilise the setup shown in figure 3.12. We use the dual-path source that we discussed in chapter 2 [70]. Due to the integrated design, it is intrinsically stable and can be well-integrated into existing networks in the satellite that guarantee a stable source function in space. Additionally, we have the advantage that we gain two communication channels in one, as the dual-path source generates two copies of the same nonclassical state [70], i.e. the two single-mode squeezed states discussed in section 2.5. Nevertheless, we consider only one in the analysis, as the other arm contains an exact copy of the state.

We pump the source with picosecond pulses (from *Coherent* MIRA900-D, $R_{\mathrm{Rep}} = 100\,\mathrm{kHz}$) at the two-photon N00N state generation wavelength of $\lambda_p \approx 758\,\mathrm{nm}$. We choose the pump power such that we measure $\langle n_{\mathrm{detected}} \rangle \approx 2.7\,\frac{\mathrm{photons}}{\mathrm{pulse}}$ without additional attenuation [198]. This few photon regime is particularly interesting in free-space experiments [165–170, 172–174]. After the source, we clean the generated state from remaining pump light and unwanted

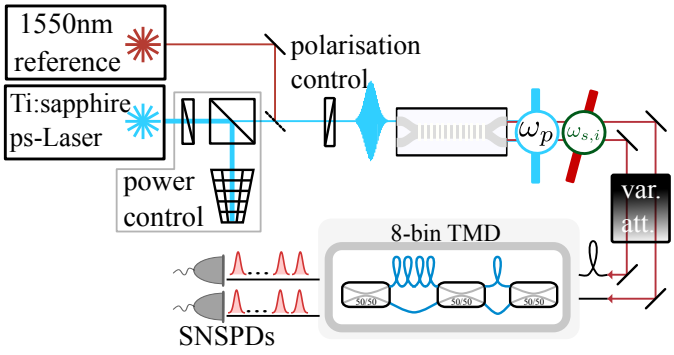

Figure 3.12 – Experimental setup to obtain the simulation data for the atmosphere [198]. We use our dual-path source from chapter 2 to generate our nonclassical state [70]. After the source we clean the light from the remaining pump and unwanted background in the telecom regime. To realise the different attenuation levels $x(\eta_k)$, we use a motorised half-wave plate with a polarising beam splitter and measure $n = 100$ different attenuations with equal spacing. Finally, the remaining state impinges on the combination of 8-bin TMD and superconducting nano-wire detectors that we calibrated in section 3.2.

background in the telecom regime. To implement the different measurement settings for $x(\eta_k)$, we use a combination of a motorised half-wave plate and polarising beam splitter (var. att.) to realise $n = 100$ different, constant attenuation levels with equal spacing on both arms of the state. For no artificial attenuation, we obtain an overall detection efficiency of $\eta_{\text{detection}} \approx 22\,\%$ [198]. Finally, the light impinges on the time-multiplexed detection system [25–28] that we investigated in section 3.2.

To exclude artefacts in our setup that might introduce false nonclassicalities (i.e. saturation of the TMD or false counts in the SNSPDs), we prepare a classical reference beam with a picosecond pulsed laser source at $\lambda_{\text{ref}} = 1550\,\text{nm}$ (PicoQuant, 35 ps pulse duration, 100 kHz repetition rate). Analogously to the quantum state, we also implement and measure the click counting statistics for $n = 100$ attenuation levels for a detected mean photon number of $\langle n^{\text{ref}}_{\text{detected}} \rangle < 1$ [198]. In figure 3.13, we depict typical results for the click counting statistics for the PDC state (a) and the classical reference (b). Note, that the classical reference is plotted in log-scale, since we used a low mean photon number. As both arms are symmetric, we only consider the marginal distribution of one arm to perform our nonclassicality analysis.

3.3.3 Analysis of Transmitted Nonclassicality

After performing the different attenuation measurements $x(\eta_k)$, we now merge them appropriately to simulate the effects of atmospheric turbulences on the nonclassicality of the transmitted quantum state. First, we perform a sanity check on the raw data to exclude any artificial nonclassicality effects with the classical reference beam. Furthermore, we analyse two matrices of moments $M^{(2)}$ and $M^{(8)}$, see equation (3.31). to check which approach shows the nonclassi-

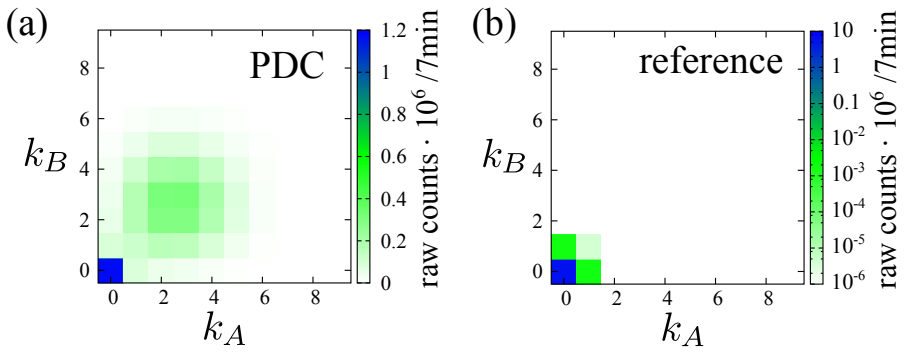

Figure 3.13 – Typical results for the click statistics for PDC (a) and classical reference (b). As the two arms of the distribution (A and B) are fully symmetric, we only consider one for the analysis.

cality of the quantum state in a more pronounced way. After these preliminary investigations of our data, we begin to merge the raw data according to different models of the atmosphere and analyse the retained nonclassicality. We begin with an investigation of general temperature and pressure fluctuations in the atmosphere contributing to strong turbulence which is described by a log-normal distribution [179]. Furthermore, we consider the effect of beam wandering, the main contribution to weak turbulence, as given by the Weibull distribution [178, 180]. Finally, to demonstrate that our simulation method is applicable to any probability distribution, we merge our raw data according to a whole family of probability distributions, the beta-binomial distributions and check for remaining nonclassicality.

Sanity Check: Constant Losses

We begin our data analysis with the evaluation of the raw data with fixed attenuation levels. To exclude any artificial nonclassicality introduced by the setup, we extract the minimal eigenvalue of the matrix $M^{(8)}$ for the classical reference beam. The results are given in figure 3.14. For all implemented attenuation levels, the minimal eigenvalue $e^{(8)} \approx 0$. This means that we do not introduce any false nonclassicality and our setup works as expected [154]. The error bars for low transmission values increase, as we measure more vacuum compared to high transmission values, which decreases the statistical significance of the detected signal [198].

Now, we consider the nonclassicality of our quantum signal. In figure 3.15, we consider two figures of merit for the nonclassicality. With the use of an $N = 8$ TMD, we can construct the matrices of moments from the simplest case in equation (3.30) up to the order of $M^{(8)}$. Figure 3.15(a) contains the minimal eigenvalue of the second order matrix $M^{(2)}$, while figure 3.15(b) contains the minimal eigenvalue of $M^{(8)}$. Both figures of merit show negative eigenvalues and therefore nonclassicality for all constant transmission levels η. Yet, if we consider the statistical significance of the result, i.e. the value is negative under consideration of the error bars, we only achieve significant nonclassicality for $\eta_{\min}^{(2)} \approx 0.34$ in the case of the second order matrix of moments $M^{(2)}$. For the eighth order matrix of moments $M^{(8)}$, more data is considered in the

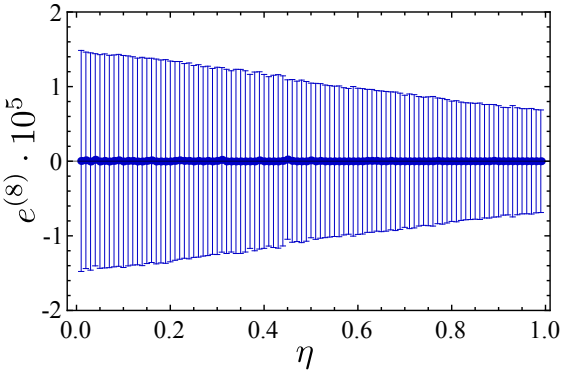

Figure 3.14 – Nonclassicality of the classical reference for the different attenuation levels [198]. We depict the minimal eigenvalue $e^{(8)}$ of $M^{(8)}$. The constant value of $e^{(8)} \approx 0$ for all attenuation levels shows that we do not introduce any false nonclassicality in our setup and that it works as expected. For low transmission, the error bars increase, as we retain less non-vacuum events to get good statistics.

evaluation, which decreases the threshold of significance is at $\eta_{\min}^{(8)} \approx 0.18$. Due to this fact, we will continue to use the minimal eigenvalue of $M^{(8)}$ to verify the remaining nonclassicality of our transmitted signal as this value is more robust against constant losses [198].

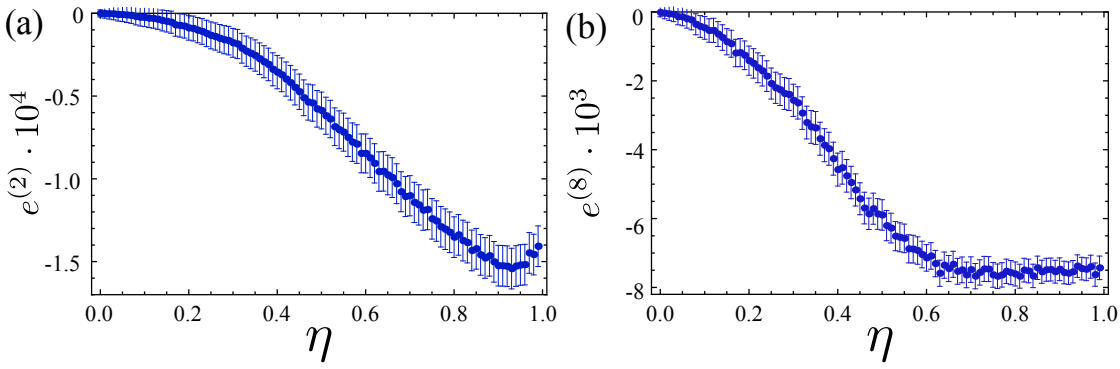

Figure 3.15 – Nonclassicality analysis for constant transmission values η [198]. We consider two figures of merit to verify the nonclassical behaviour of our detected state, the minimal eigenvalue of $M^{(2)}$ in (a) and the minimal eigenvalue of $M^{(8)}$ in (b). Both figures of merit remain negative for all transmission levels η, but the statistical significance of $e^{(8)}$ in (b) is better than the one of $e^{(2)}$. Therefore, we will use $e^{(8)}$ for the rest of our analysis.

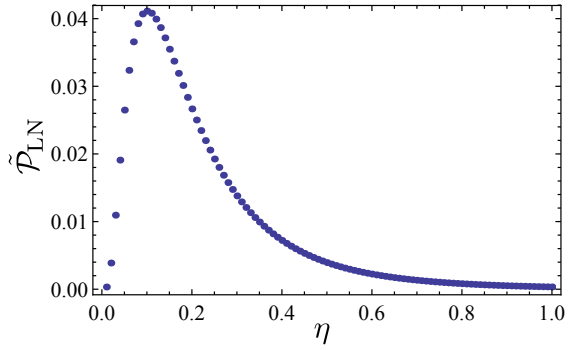

Figure 3.16 – Discretised probability mass function of the log-normal distribution [198]. We choose $n = 100$ discretisation points to match the experiment. For this number of discretisation points, we find good agreement to the continuous version. See table 3.2 for numbers.

Strong Turbulence: Log-normal Distribution

We begin our analysis of atmospheric effects on the transmitted nonclassicality with a simulation of the temperature and pressure fluctuations in the atmosphere. This type of fluctuating losses can be approximated by a log-normal distribution and describes a quantum channel under strong turbulence [168, 179]. It is defined via

$$\mathcal{P}_{\mathrm{LN}}(\eta) = \frac{1}{\eta\sigma\sqrt{2\pi}} \exp\left(-\frac{(\ln\eta - \mu)^2}{2\sigma^2}\right) \tag{3.33}$$

and characterised by the location parameter $\mu \in \mathbb{R}$ and the scale parameter $\sigma > 0$. In this thesis, we follow the theoretical analysis of Vasylyev et al. [179] and use the parameter set $\mu = -1.75$ and $\sigma^2 = 0.55$ for the atmospheric fluctuations.

As $\mathcal{P}_{\mathrm{LN}}$ is a continuous function in η, we have to apply the discretisation routine described in equation (3.27). We plotted the resulting probability mass function in figure 3.16.

To evaluate the quality of the discretisation routine, we compare the mean η, variance σ^2 and skewness v of the continuous and discretised PDT and summarised the relative errors in table 3.2. The low relative errors show a good quality of the discretisation routine and justify the use of a discretised PDT to simulate the atmospheric turbulences. As we described in the introduction to this section, we now merge the measured click statistics according to the distribution in figure 3.16.

$\Delta\overline{\eta}$	$\Delta\sigma^2$	Δv
$0.6 \cdot 10^{-3}$	$2.1 \cdot 10^{-3}$	$4.7 \cdot 10^{-3}$

Table 3.2 – Relative errors of the discretisation for the mean $\Delta\overline{\eta}$, the variance $\Delta\sigma^2$ and the skewness Δv compared to the continuous log-normal distribution [198].

The main question that we have to answer now, is whether the nonclassicality of the light is preserved after passing the modelled free-space channel. As such, we evaluate the minimal eigenvalue of the eighth order matrix of moments and find [198]

$$e_{\mathrm{LN}}^{(8)} = (2.34 \pm 0.05) \cdot 10^{-2} \,. \tag{3.34}$$

This value is significantly larger than zero and the transmitted light does not exhibit any nonclassicality. This is a surprising result, considering our analysis with the constant losses, where we found nonclassicality for all attenuation levels. One could assume that a mixing of nonclassical statistics would retain the nonclassicality, which is however clearly not the case. Particularly, it becomes clear that turbulent loss channels have to be evaluated with care and that they cannot be approximated by a single loss channel with the mean transmission of the turbulent one. Indeed the fluctuating loss channel yields a statistical mixture of the input state in equation (3.26). Such a statistical mixture might lose all the nonclassical features of the original input state [198].

While the destruction of the nonclassicality in the channel is a quite disappointing result, there are some ways to modify the measurement on the channel and therefore recover the nonclassicality as resource for secure quantum communication. One possibility that we consider here is a post-selection method [171, 178], where we only consider events, if the transmittance is above a certain threshold value η_{PS}.

The resulting minimal eigenvalues for different post-selection thresholds are depicted in figure 3.17. Towards higher post-selection thresholds η_{PS}, the minimal eigenvalue drops, as we approximate a constant loss scenario and consider less mixing. For a value of $\eta_{\mathrm{PS}} \gtrsim 0.59$ [198], we regain nonclassical behaviour with more than three standard deviations. This is not only a promising result for the recovery of secure communication, but also shows the versatility of our simulation approach. We are not only able to simulate the atmospheric losses, but are also able to directly test a post-selection protocol with the same data sets.

Weak Turbulence: Weibull Distribution

As a second example, we consider the effect of beam wandering, which is the dominant contribution to weakly turbulent channels [178]. Due to the atmospheric flows, the beam position is not fixed on a finite aperture, which causes fluctuating losses depending on the beam position. The effect of beam wandering in a single spatial mode is given by a log-negative Weibull distribution [178, 180, 187], which is defined as

$$\mathcal{P}_{\mathrm{WB}}(\eta) = \frac{S^2}{\sigma_R^2 \zeta T} \left[\ln\left(\frac{\eta_0}{\eta}\right)\right]^{\frac{2}{\zeta}-1} \exp\left\{-\frac{S^2}{2\sigma_R^2}\left[\ln\left(\frac{\eta_0}{\eta}\right)\right]^{\frac{2}{\zeta}}\right\} ,$$

with

$$\begin{aligned} \eta_0 &= 1 - \exp\left(-2\frac{a^2}{w^2}\right) , \\ w &= w_0 \sqrt{1 + \left(\frac{z\lambda}{\pi w_0^2}\right)} \end{aligned} \tag{3.35}$$

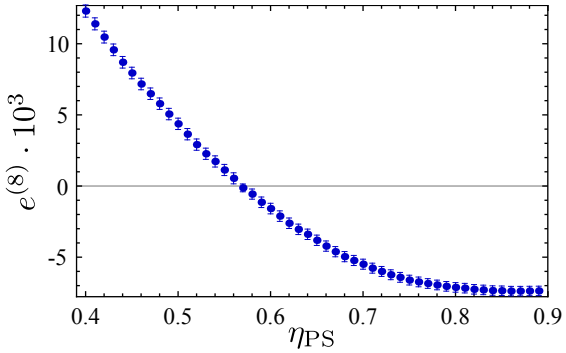

Figure 3.17 – Minimal eigenvalues of the eighth order matrix of moments for different threshold transmissivities η_{PS} [198]. We only consider events with transmission higher than η_{PS} and observe for $\eta_{\mathrm{PS}} \gtrsim 0.59$ a recovery of the nonclassicality.

$$\zeta = 8\frac{a^2}{w^2}\frac{\exp\left(-4\frac{a^2}{w^2}\right) I_1\left(4\frac{a^2}{w^2}\right)}{1-\exp\left(-4\frac{a^2}{w^2}\right) I_0\left(4\frac{a^2}{w^2}\right)}\left[\ln\left(\frac{2\eta_0}{1-\exp\left(-4\frac{a^2}{w^2}\right) I_0\left(4\frac{a^2}{w^2}\right)}\right)\right]^{-1}$$

and

$$S = a\left[\ln\left(\frac{2\eta_0^2}{1-\exp\left(-4\frac{a^2}{w^2}\right) I_0\left(4\frac{a^2}{w^2}\right)}\right)\right]^{-\frac{1}{\zeta}}.$$

Here, I_0 is the modified Bessel function of the 0-th order, S and ζ are the scale and shape parameters of the function. The parameters z and σ_R describe the fluctuation of the beam. Specifically, σ_R^2 is the variance around a point on the aperture, which has the distance z to the centre of the detector. Furthermore, w_0 the radius of the beam at the source and w consequently the radius of the beam at the aperture, which has radius a.

However, the detailed shape of this equation is not crucial to the understanding of the concept, but used to model the experimental parameters of a specific free-space link. The critical parameter is the Rytov parameter σ_R^2. The Rytov parameter classifies the strength of the turbulence. If $\sigma_R^2 = 0$ the channel is not turbulent, $0 < \sigma_R^2 < 1$ describes a weakly turbulent channel and for $\sigma_R^2 \approx 1...10$, we simulate moderate turbulence strength. For our analysis, we use the same parameters as in [179] which describe a 1.6 km long free-space channel, see table 3.3. As before, we discretise the PDT with the algorithm of equation (3.27) and achieve the relative errors of table 3.4.

Again, we merge our constant loss data according to the Weibull distribution and analyse the transmitted nonclassicality for varying strength of the turbulence. The result is depicted in figure 3.18. We calculate the minimal eigenvalue of the eighth order matrix of moments and retain negativity up to a turbulence strength of $\sigma_r^2 \lesssim 1$ [198]. This means that we retain nonclassicality only for weakly turbulent channels, before it vanishes already at moderate turbulence strengths. This result is consistent with the evaluation in the last section, where we could not establish

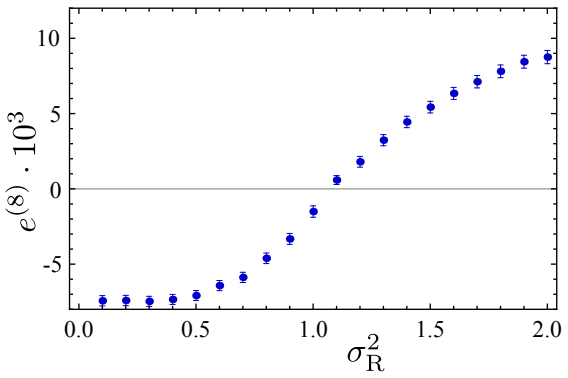

Figure 3.18 – Evaluation of the nonclassicality with the Weibull distribution for different turbulence strengths σ_R^2 [198]. For $\sigma_R^2 \lesssim 1$, we retain nonclassicality. This means that for the effect of beam wandering, we observe nonclassicality only for weakly turbulent channels, before it vanishes.

nonclassicality for our states after a strongly turbulent channel. With this analysis, we tested our simulation approach for atmospheric turbulence conditions of a full-scale atmospheric transmission setup in the laboratory. From our simulation results, we could observe that even for weak turbulences, the nonclassicality vanishes.

General Applicability: Beta-binomial Distributions

In the final section of this chapter, we examine the general applicability of our simulation method to generic probability distributions. To this aim, we employ a family of probability distributions, the beta-binomial distributions. This family of distributions depends on two parameters α and β and is given by

$$\tilde{\mathcal{P}}_{\mathrm{BB}}(\eta|n,\alpha,\beta) = \binom{n}{\eta} \frac{B(\eta+\alpha, n-\eta+\beta)}{B(\alpha,\beta)} \,. \tag{3.36}$$

a [mm]	w_0 [mm]	z [km]	λ [nm]	S
75	20	1.6	809	1.17582

Table 3.3 – Parameters for the Weibull distribution from [179], which we utilise for our analysis [198].

$\Delta\overline{\eta}$	$\Delta\sigma^2$	Δv
0.75 %	1.48 %	2.2 %

Table 3.4 – Relative errors of the discretisation for the mean $\Delta\overline{\eta}$, the variance $\Delta\sigma^2$ and the skewness Δv compared to the continuous Weibull distribution [198].

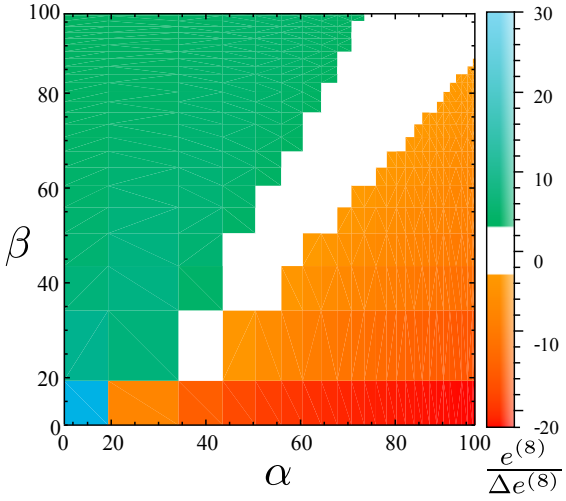

Figure 3.19 – Nonclassicality analysis for a family of beta-binomial distributions [198]. We plot the signed significance of the minimal eigenvalue $e^{(8)}$ as a figure of merit and identify two large regions. In green (orange), we denote a classical (nonclassical) behaviour of the detected light. White regions denote the case, where the signed significance is below three standard deviations.

Here, n ($= 100$ in our case) denotes the number of discretisation points and η is the transmission in $\%$. The function B is the beta-distribution, defined as

$$B(\alpha, \beta) = \frac{\Gamma(\alpha)\Gamma(\beta)}{\Gamma(\alpha) + \Gamma(\beta)}\,, \tag{3.37}$$

with $\Gamma(\alpha)$ as the well-known Γ-function. The best way to understand the beta-binomial distribution is with the corresponding urn model, the Pólya urn [196, 199]. Consider an urn that contains α blue balls and β black balls and we draw balls randomly. Each time we draw a ball, two balls of the same colour which was just drawn are put back into the bowl. If this is repeated n times, the resulting probability distribution for blue and black is the beta-binomial distribution with the parameters n, α and β. In our case, η is then the value of the random variable.

As the beta-binomial distribution is inherently discrete, we do not have to apply the discretisation routine in this case. To cover a whole family of the beta-binomial distributions, we vary the two parameters α and β independently to merge the constant loss data accordingly.

Analogously to the previous sections, we extract the minimal eigenvalue of the eighth order matrix of moments. However, for better visibility, we plot the signed significance ($\frac{e^{(8)}}{\Delta e^{(8)}}$) dependent on α and β in figure 3.19. We find two large regions in the parameter space, separated by a white region. The orange region denotes parameters, where we find nonclassicality after transmission through a channel with these properties. Accordingly, the green regions denote parameter combinations, where the nonclassicality is *not* retained after the transmission. In between, we find a large region, where the signed significance does not exceed three standard

deviations from zero and distinguishing classical and nonclassical behaviour with respect to the error bars is not possible [198].

With this result, we have shown that our simulation approach is very versatile and may be used to simulate all types of fluctuating loss channels. The application of the beta-binomial distribution to our data and the subsequent analysis of nonclassicality shows that our approach is also valid for a broad range of probability distributions and not restricted to known atmospheric functions.

Summary

In summary, we introduced a method to simulate the effect of fluctuating loss channels on quantum states [198]. This is an important capability, as it allows us to simulate the effect of atmospheric free space links for quantum communication in the laboratory. We used the dual-path source, described in chapter 2 and measured constant attenuation levels with our TMD, which we later mixed for the simulation of the atmospheric channel. We analysed two PDTs, the log-normal distribution to simulate the effects of temperature and pressure fluctuations and the Weibull distribution, which describes beam wandering. Finally, we applied our method to a wide family of probability distributions and showed that we are able to simulate a wide range of turbulent channels and are not restricted only to known models of atmospheric channels.

Down through the ribbon highway I will go
Searching for a brighter spotlight, a brighter sun
I am out on the open road
I'm more than a kick, and I'm more than a spark
I'm more than a flash in the dark

Katzenjammer - Flash in the dark

4

High-dimensional non-linear systems

Contents

In the previous chapters, we investigated the properties of a non-linear two-coupled waveguide structure, both in the two-photon regime in chapter 2 and for higher photon numbers in section 3.3. Now, we are prepared to tackle the upscaling of the system to many spatial modes, i.e. many non-linear coupled waveguides: a uniform waveguide array. Such a system, see figure 4.1(a), comprises a large, but finite number of waveguides that are weakly coupled. Similar to the two-waveguide system described in chapter 2, we consider an implementation that comprises many parallel, weakly coupled waveguides that are periodically poled to enable photon pair generation via PDC.

The linear part of the structure, i.e. the weakly coupled waveguide array, is a widely studied platform in the context of transport properties in continuous time quantum walks [16–24]. In the wider context of quantum walks [200], a lot of theoretical and experimental progress has been achieved on a variety of platforms. Quantum search algorithms have been developed [201–204] and it has been shown that quantum walks present a building block for universal quantum computing [6, 205, 206]. Due to the static implementation of quantum walks in integrated photonic platforms, an alternative has been developed: discrete quantum walks [207] in bulk optical implementations [15, 208, 209]. This approach offers more flexibility and control over the quantum walk parameters and has been shown to be (in special configurations [30–33]) intrinsically scalable. We give a more detailed introduction to quantum walks in section 4.2.1 and recommend [33] and [210] as a comprehensive introduction into the topic.

Additionally to the linearly coupled waveguide array structure, we now implement a periodic poling on top of the waveguides [99, 100]. Analogously to the dual-path source, this enables

the PDC process [67, 68, 98]. As such, the photon pair generation is integrated into the linear structure, which opens up new dynamics in the context of transport phenomena or quantum walks.

The detailed study of these modified transport properties by integration of the photon pair generation into the linear structure will be one of the main aims in this chapter. We begin this chapter with a review of the PDC process in a non-linear waveguide array system in section 4.1 based on work done prior to this thesis [57, 211, 212]. After this mathematical description of the process, we move on to interpret the process in terms of *driven* quantum walks in section 4.2, as developed in cooperation with C. Hamilton from the group of I. Jex in Prague. Additionally to the study of the modified transport properties, we introduce a novel type of search algorithm that exploits the unique dynamics of the driven quantum walk. Using the formalism introduced in section 4.2, we map, for the first time, a genuinely non-linear implementation to the (usually) linear computational problem of BosonSampling in section 4.3. Finally, again together with C. Hamilton from Prague, we take the non-linear waveguide array as a motivation to develop the general concept of a truly *Gaussian* BosonSampling problem in section 4.4.

4.1 Non-linear Waveguide Arrays

This section is a short summary of the results presented in [57, 212] and independent work from the group of Y. Kivshar [211, 213]. Historically, we began our work with the non-linear waveguide array system [57]. Since this was before the starting point of this thesis, this section should be considered state-of-the-art.

As in the dual-path source from chapter 2, the overall process is governed by two intertwined mechanisms; the linear coupling between waveguides and the non-linear PDC process. In the following, we first describe the coupling mechanism in infinite waveguide arrays via the Bloch wave expansion [214]. Next, we consider a very simple adaptation to model periodic boundary conditions. Finally, the effect of the coupling is included in the PDC process, analogously to the calculations for the dual-path source.

4.1.1 Linear Coupling in Infinite Waveguide Arrays

To describe the coupling process on the propagation of the electric fields in a waveguide array, we employ coupled-mode theory [104, 106], similar to the dual-path source. The electric field amplitudes are given by the following equation system[1] [214]

$$\begin{aligned} i\frac{\partial}{\partial z}E_n(x,y)e_n(z) = &-\beta^{(0)}(\omega)E_n(x,y)e_n(z) \\ &- C(E_{n-1}(x,y)e_{n-1}(z) + E_{n+1}(x,y)e_{n+1}(z))\,. \end{aligned} \tag{4.1}$$

In this differential equation system, $E_n(x,y)$ is again the spatial mode profile of a single, undisturbed waveguide n, while $e_n(z,\omega)$ is the corresponding excitation amplitude that we are

[1] Compared to equation (2.3) the signs of the propagation terms are different. This change in convention yields equivalent results, but has the advantage that the eigenvalues of the propagation matrix become real-valued.

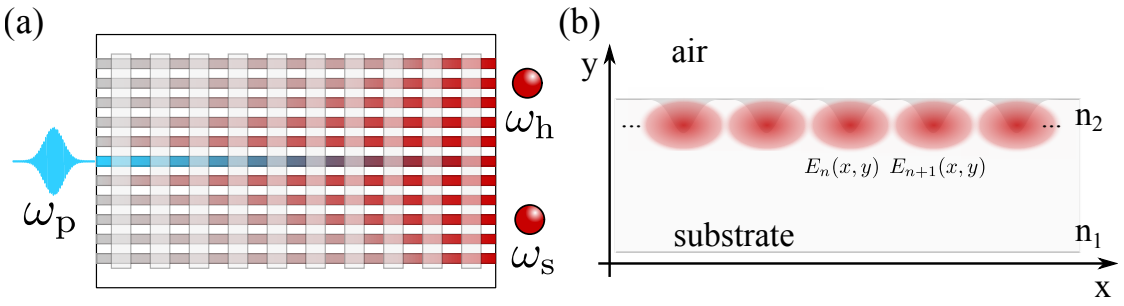

Figure 4.1 – Schematic system sketch (a) and assumed field distribution (b). In the non-linear waveguide array (a), a strong, non-coupling pump field generates photon pairs in the telecom regime. Here, the generated photons with frequencies ω_s and ω_i couple between waveguides, which leads to unique dynamics. In (b), we depict a field distribution for the spatial modes of the waveguide array. As they are identical, we are only interested in the corresponding excitation amplitudes, as for the dual-path source in chapter 2.

interested in. As before with the dual-path source, we assume all spatial modes $E_n(x,y)$ to be identical and cancel them from equation (4.1). The quantity $\beta^{(0)}(\omega)$ is the propagation constant for the undisturbed waveguide and C the coupling parameter. In general, the coupling parameter may also depend on ω, but we will neglect this dependence here since we only consider small frequency ranges. Solving the equation for the excitation amplitudes $e_n(z)$ with a Bloch ansatz[2] [214], we obtain

$$e_n(z) = e_n(0)\exp\left[i\left(k^{\perp}n + \kappa_z(k^{\perp})z\right)\right], \tag{4.2}$$

which yields the band-structure for the uniformly coupled waveguide array

$$\beta(\omega, k^{\perp}) = \beta^{(0)}(\omega) + 2C\cos(k^{\perp}). \tag{4.3}$$

The interpretation of equation (4.3) is the same as for the eigensolutions of the dual-path source, compare equations (2.5) and (2.6). The band-structure solution describes the impact of the eigenmode, labelled with the transverse momentum $k^{\perp}$, on the propagation constant in z-direction $\beta(\omega, k^{\perp})$. Using this description, we can write the fields for the down-conversion process in the waveguide basis [57, 211, 212]

$$\begin{aligned}
\mathcal{E}^{(+)}_{p,n}(z,t) &= \int_{-\infty}^{\infty} \mathrm{d}\omega_p \int_{-\pi}^{\pi} \mathrm{d}k_p^{\perp}\alpha(\omega_p)\left[\frac{1}{2\pi}\sum_{n'} A(n')e^{-ik_p^{\perp}n'}\right] e^{i(\beta^{(0)}(\omega_p)z-\omega_p t)}e^{ik_p^{\perp}n} \\
\hat{E}^{(-)}_{\mu,n}(z,t) &= B\int_{-\infty}^{\infty} \mathrm{d}\omega_\mu \int_{-\pi}^{\pi} \mathrm{d}k_\mu^{\perp} e^{-i(\beta(\omega_\mu,k_\mu^{\perp})z-\omega_\mu t)}e^{-ik_\mu^{\perp}n}\hat{a}^{\dagger}(\omega_\mu, k_\mu^{\perp}),
\end{aligned} \tag{4.4}$$

[2] $\kappa_z(k^{\perp})$ is an auxiliary variable that contains the part of the z-propagation constant that is influenced by the coupling.

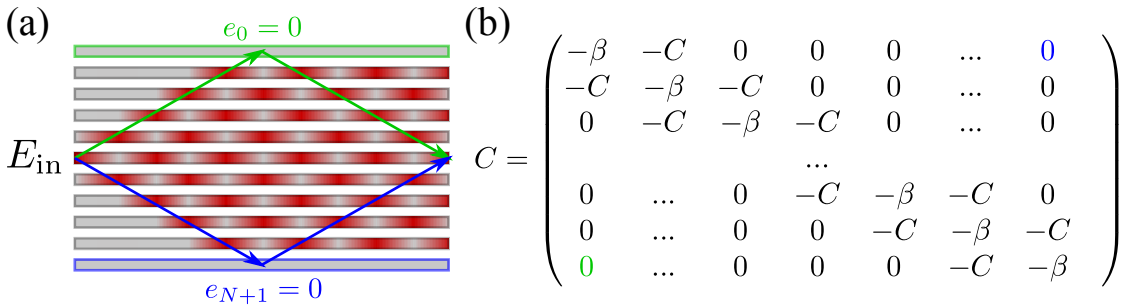

Figure 4.2 – Schematic representation of fixed boundary conditions. In (a), we interpret the fixed boundary conditions by introducing an amplitude constraint $E_0 = E_{N+1} = 0$ for the two additional outermost waveguides of the array. (b) represents a coupling matrix that encodes the fixed boundary conditions in the $C_{0,N+1} = C_{N+1,0} = 0$ elements.

where $\mu = s, h$ denote signal and herald, respectively. We consider the spatial distribution of the pump field in the waveguide array via $A(n')$, which is connected to the eigenmode basis via a Fourier transformation. In the quantum fields, we considered again a type-I PDC process that allows us to use the same electric field representation for the signal and herald fields. To achieve a description of the electric fields in the waveguide basis, we included an inverse Fourier transform $\int_{-\pi}^{\pi} \dots e^{-ik^{\perp}n} \mathrm{d}k^{\perp}$. For more details concerning the solution of this system, see [214–218].

4.1.2 Linear Coupling with Boundary Conditions

While the coupling in a waveguide array is described sufficiently well by the band-structure, it cannot account for modified propagation when the light reaches the boundaries of the sample [22]. There exists a lot of literature on the treatment of boundary conditions for the three main scenarios [219]

a) open boundaries: the light has not touched the boundaries of the array

b) intermediate case: the light has touched the boundaries and is reflected back

c) steady-state case: an equilibrium has been reached between the propagating and back-reflected light.

The first case is sufficiently described with the infinite waveguide array description. The cases b) and c) require the introduction of boundary conditions. In this thesis, we assume *fixed boundary conditions* [220], which means that the light in the outermost waveguides is reflected back into the array, compare figure 4.2(a).

To achieve this, we add two unphysical outermost waveguides to the array, waveguide 0 and waveguide $N+1$ and set the boundary conditions $e_0 = e_{N+1} = 0$. Mathematically, this situation

is encoded in the coupling matrix A that represents the equation system (4.1)

$$i\frac{\partial}{\partial z}\vec{e}(z) = C\vec{e}(z)\,, \tag{4.5}$$

where $\vec{e}(z)$ is the vector that contains the excitation amplitudes of all $N+2$ waveguides. Then, A is an $(N+2)\times(N+2)$ matrix with its representation given in figure 4.2(b). Compared to the infinite case, where the matrix is infinite-dimensional, the dimensions are fixed. The fixed boundary conditions are encoded by the entries $A_{0,N+1} = A_{N+1,0} = 0$[3].

We can solve this differential equation system analogously by diagonalisation and find a closed form expression for both the eigenvalues and eigenfunctions [220]

$$\begin{aligned}\beta(\omega,k) &= \beta^{(0)}(\omega) + 2C\cos\left(\frac{k\pi}{N+2}\right)\\ e_k &= \sqrt{\frac{2}{N}}\sum_{j=1}^{N}\sin\left(\frac{jk\pi}{N+2}\right)e_j\,.\end{aligned} \tag{4.6}$$

Compared to the solution of the infinite case in equation (4.3), we retain the cosine shape of the bandstructure and only find a discretisation of the transverse momenta $k_k^\perp = \frac{k\pi}{N+2}$. As such, fixed boundaries allow for a sufficient description of the light propagation under boundary conditions, while retaining the simple solution of the infinite array.

4.1.3 The Down-conversion State

As with the two-coupled waveguide source in section 2.2, we perform the calculation of the down-conversion state with the eigenmodes of the linearly coupled system. For simplicity, we restrict the discussion of the down-conversion state to a type-I process in an array with open boundary conditions, i.e. the system is sufficiently large such that the light does not touch the outermost waveguides. In this case, we consider the Hamiltonian of equation (2.9) and insert the fields we derived in the previous sections [57]. We obtain

$$\begin{aligned}\hat{H}_{\text{Array}} = \mathcal{B}\sum_n \int_{-L}^{0}\mathrm{d}z\int_{-\infty}^{\infty}\mathrm{d}\omega_p\int_{-\infty}^{\infty}\mathrm{d}\omega_s\int_{-\infty}^{\infty}\mathrm{d}\omega_i\int_{-\pi}^{\pi}\mathrm{d}k_p^\perp\int_{-\pi}^{\pi}\mathrm{d}k_s^\perp\int_{-\pi}^{\pi}\mathrm{d}k_h^\perp\,\alpha(\omega_p)\tilde{A}(k_p^\perp)e^{i(\beta^{(0)}(\omega_p)z-\omega_p t)}e^{ik_p^\perp n}\\ \times e^{-i(\beta(\omega_s,k_s^\perp)z-\omega_s t)}e^{-ik_s^\perp n}e^{-i(\beta(\omega_h,k_h^\perp)z-\omega_h t)}e^{-ik_h^\perp n}\hat{a}^\dagger(\omega_s,k_s^\perp)\hat{a}^\dagger(\omega_h,k_h^\perp) + \text{h.c.}\,,\end{aligned} \tag{4.7}$$

where $\tilde{A}(k_p^\perp)$ denotes the Fourier transform of the pump distribution $A(n)$ at the input in the waveguide basis.

Solving this Hamiltonian in the two-photon picture analogously to section 2.2, we arrive at the output state of the waveguide array [57, 211, 221]. Similarly to the two-coupled waveguide

[3] One could also use *periodic* boundary conditions. Here, the light exiting the right hand side of the array (waveguide N) is inserted at the left hand side of the array (waveguide 1) and vice versa. The corresponding $N\times N$ coupling matrix would be modified with $A_{1N} = A_{N1} = -C$. However, periodic boundary conditions support a different type of eigenfunctions, i.e. $k^\perp = \pm\frac{2\pi k}{N}$ [220].

source, we can express the PDC state in two different bases, i.e. the momentum or eigenmode basis

$$|\Psi\rangle = \frac{1}{\sqrt{\mathcal{N}}} \int_{-\infty}^{\infty} \mathrm{d}\omega_s \int_{-\infty}^{\infty} \mathrm{d}\omega_h \int_{-\pi}^{\pi} \mathrm{d}k_s^{\perp} \int_{-\pi}^{\pi} \mathrm{d}k_h^{\perp}\, \alpha(\omega_s+\omega_h)\tilde{A}(k_s^{\perp}+k_h^{\perp})\Phi(\omega_s,\omega_h,k_s^{\perp},k_h^{\perp}) \times a^{\dagger}(\omega_s,k_s^{\perp})a^{\dagger}(\omega_h,k_h^{\perp})\,|0\rangle \tag{4.8}$$

and the waveguide basis, which is given by a Fourier transform on the $k^{\perp}$ variables. For a detailed interpretation and analysis of the PDC state in a non-linear waveguide array system, see [57, 212].

With this brief review of non-linear coupled waveguide arrays, we move on to the theoretical concepts in quantum information science that were inspired by this system.

4.2 Driven Quantum Walks

One of the aims of the following section, originating from a close collaboration with Craig S. Hamilton in Prague, is to interpret the non-linear system of the coupled waveguide array in terms of quantum information language [65]. Specifically, we relate non-linear coupled waveguide arrays to the theoretical framework of quantum walks and develop the new concept of *driven quantum walks*. The main difference of a driven quantum walk to a known, passive quantum walk is that we generate photons *during* the evolution of the walk, instead of using a fixed state at the beginning. This enables us to formulate a tailored search problem for our driven quantum system that outperforms a classical search algorithm.

This section is structured as follows: We first review the concept and the properties of a *passive* quantum walk, before we begin our discussion about driven quantum systems and identify two possible driving forces, lasing and squeezing. For both cases, we show that we can decompose the output state of a driven quantum walk system into a passive quantum walk evolution and a complex input state. Furthermore, we consider the impact of the different driving terms on the system separately and investigate their effect on the system dynamics. Finally, we formulate a search problem that demonstrates a speedup of a driven quantum walk system compared to classical walker.

4.2.1 Passive Continuous-time Quantum Walk

Up to this point in this thesis, we only used the state description of non-linear processes in coupled systems, see equation (2.13) in chapter 2 and equation (4.8) in section 4.1. As we now want to transfer this description to the context of quantum information, especially to the context of quantum walks, we first have to define what a quantum walk is and what it actually does.

Consider the classical analogue, the random walk [222]. An example system for this situation is e.g. the Galton board, where a ball is inserted at the top of the board and is deflected left *or* right at the pins that make up the board, see figure 4.3(a). If we repeat this board game with many classical particles, we find that the output probability distribution of the corresponding random

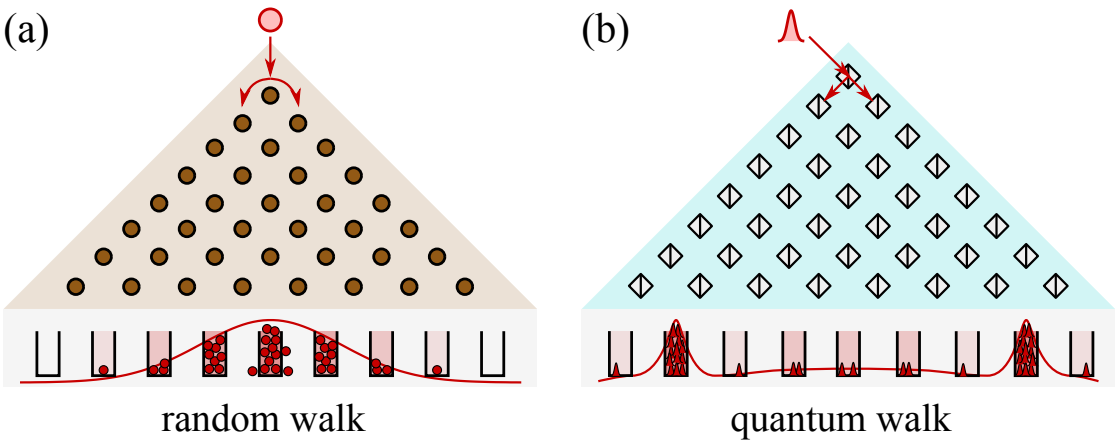

Figure 4.3 – Discrete *random* and *quantum* walk. The ball on the Galton board in (a) has the possibility to go left *or* right at all pins on the board. The resulting distribution in the buckets resembles a binomial distribution. In (b), we have sketched a quantum walk, where the walker (represented by a laser pulse) has the possibility to go left *and* right at the beam splitters on the board [15]. The resulting distribution in the buckets is distinctly different than for the random walk and has two characteristic lobes that travel to the edges.

walk is a gaussian distribution. While this example is very much *discrete* in the sense that we deflect the balls only at certain positions, we are also able to define a *continuous* type, where we consider a continuous spread of the particles. A prime example for this type of continuous random walks [223] is diffusion [224] or heat transfer [225] that obey the diffusion equation

$$\frac{\partial}{\partial t} f(\vec{r},t) = D\nabla^2 f(\vec{r},t)\,, \tag{4.9}$$

where D is the diffusion constant, a parameter that describes the *coupling* of heat, concentration, etc., as represented by the density function $f(\vec{r},t)$, to adjacent space units.

For the transition from classical to quantum [200], one replaces the classical ball with e.g. a laser pulse and the pins of the Galton board with beam splitters [15]. Instead of deflecting a classical particle left *or* right, a quantum particle as represented by the laser pulse, is deflected left *and* right to form a superposition. This directly gives a setup for a discrete quantum walk. Due to interference effects of the quantum particle with itself (or other indistinguishable particles), the probability distribution at the output of the quantum walker differs drastically from the classical gaussian one, compare figure 4.3(b). One particular difference is the change of the variance, i.e. the wider spread [210]. Compared to a classical walker that has the the variance of the gaussian distribution, i.e. $\sigma^2 = s$, where s is the number of steps, or layers on the Galton board, a quantum walker has a variance of $\sigma^2 = s^2$. This allows search algorithms to proceed faster than a classical one, we utilise a quantum speedup [201–204]. In practice, building a quantum walk setup analogously to the Galton board is rather involved [15], as the alignment of the

different interfering paths is exponentially difficult. An elegant solution has been demonstrated by time-multiplexing of the Galton board setup [30–33] which has coined the term *discrete-time quantum walk*.

As for the classical case, we also find a continuous type of quantum walk. Here, contrary to the discrete quantum walks, we observe a continuous coupling to adjacent space units for a quantum particle. This type of quantum walks has been successfully implemented in waveguide arrays, see the array in figure 4.2(a) [16–24]. As such, we already encountered the equation of motion for the passive continuous-time quantum walk in equation (4.1). However, this description is limited in the sense that it does not use the quantum information formalism. As such, we have to formulate the Hamiltonian of the linear system[4], which is given by e.g. [65]

$$\hat{H}_{\text{passive}} = \sum_{i,j} C_{j,k} \hat{a}_j^\dagger \hat{a}_k + \text{h.c.}\,. \tag{4.10}$$

This Hamiltonian basically encodes the following situation: A photon from mode k gets destroyed and is coupled to the mode j (where it is created) with the probability of $|C_{j,k}|^2$. The matrix C encodes the different coupling strengths between the different modes of the continuous time quantum walk system[5]. The dynamics of the continuous time quantum walk is governed by the Schrödinger equation, where the initial state is localised in a single spatial mode $|\Psi(t=0)\rangle = \hat{a}_{j_0}^\dagger |0\rangle$.

As we did with the coupled differential equation system, we use the eigenmode description of the Hamiltonian which effectively diagonalises the system. We write

$$\hat{H}_{\text{passive}} = \sum_k \Omega_k \hat{A}_k^\dagger \hat{A}_k\,. \tag{4.11}$$

In this description Ω_k denote the eigenvalues of the system and $\hat{A}_k$ represent the corresponding eigenmodes. The transformation between the waveguide modes and the eigenmode basis is given by the transformation matrix T via

$$\hat{A}_k = \sum_j T_{j,k} \hat{a}_j\,. \tag{4.12}$$

Due to the diagonalisation of the system, the dynamics of the eigenmodes mirror the dynamics of free particle propagation. The traditional implementation of a quantum walk only uses the Hamiltonian of equation (4.10). It encodes a passive transformation which means that the number of particles inserted into the network remains constant during the propagation. Only the phase evolution between the different eigenmodes of the system leads to the well-known quantum walk properties. Contrary to this *passive continuous time quantum walk*, we strive to incorporate a non-particle number preserving transformation that increases the number of particles during the walk. We wish to investigate a *driven quantum walk* system.

[4] The free propagation is included in the C_{jj}. In the following, we use time and length of the chip synonymously, as they are directly connected via $L = ct$.

[5] An example of a coupling matrix with nearest neighbour coupling and periodic boundary conditions is given in figure 4.2(b).

4.2.2 Lasing Term

The key point to driven quantum systems is the choice of the driving Hamiltonian. In this thesis, we selected two different driving forces, lasing and squeezing. We begin with a discussion on lasing quantum walks, as the calculations are simpler and the method is easier to grasp. The squeezing quantum walk, as represented by the non-linear waveguide array, will be discussed in the following section.

As the driving force for the lasing quantum walk [65], we use the Hamiltonian

$$\hat{H}_{\text{lasing}} = \sum_k \Gamma_{L,k}(t)\hat{a}_k^\dagger + \Gamma_{L,k}^*(t)\hat{a}_k \,, \tag{4.13}$$

which generates photons *continuously* during the walk, such that we receive a coherent state at the output, compare chapter 1. Figure 4.4(a) shows such a system. The vector $\vec{\Gamma}_L(t)$, which describes the spatial pump pattern for the lasing process at the input of the waveguide array, is depicted in blue and creates photons according to the Hamiltonian of the process in red. Here, we consider two degrees of freedom for the pump, i.e. the spatially resolved driving amplitude $|\Gamma_k|$ and the time dependence $e^{i\omega_p t}$. In an experiment, the lasing term can be realised in a discrete quantum walk case, it can be achieved by inserting additional pulses after each step[6].

Figure 4.4 shows the main goal of this subsection. We aim to find a decomposition of the driven quantum system into a complex initial state $|\alpha_{L,\text{in}}\rangle$ and a passive quantum walk unitary $\hat{U}_{\text{PQW}}$. If we assume that the driving is happening continuously during the propagation and that the pump is an undepleted classical field (i.e. a large amplitude coherent state), we can write the full Hamiltonian of the system as

$$\hat{H} = \hat{H}_{\text{passive}} + \hat{H}_{\text{lasing}} = \sum_k \left[\Omega_k \hat{A}_k^\dagger \hat{A}_k + S_k(t)\hat{A}_k^\dagger + \text{h.c.}\right] . \tag{4.14}$$

Here, we transform the spatial pump shape Γ_L via $\vec{S}(t) = T^{-1}\vec{\Gamma}_L(t)$ to the eigenbasis. Moving to the rotating frame, we transfer the Hamiltonian to the interaction picture by applying the unitary transformation $\hat{U}_{\text{int}} = \Pi_k \exp(i\Omega_k \hat{A}_k^\dagger \hat{A}_k)$ [227] and remove the free propagation term from equation (4.14)

$$\hat{H}_{\text{int, lasing}} = \sum_k S_k(t)\hat{A}_k^\dagger e^{i\Omega_k t} + \text{h.c.}\,. \tag{4.15}$$

The output state is then given by a time-integration of the Hamiltonian[7]

$$|\Psi\rangle_{\text{int}} = \exp\left(-i\int_0^t \mathrm{d}t'\, \hat{H}_{\text{int, lasing}}(t')\right)|0\rangle \ . \tag{4.16}$$

[6] Which was later studied in [226].

[7] Time evolution in the interaction picture is given by $U_T = \exp(-\frac{i}{\hbar}\int_{t_0}^T \hat{H}(t')dt')$ [1]. As this is a theory proposal, we work in units of $\hbar$.

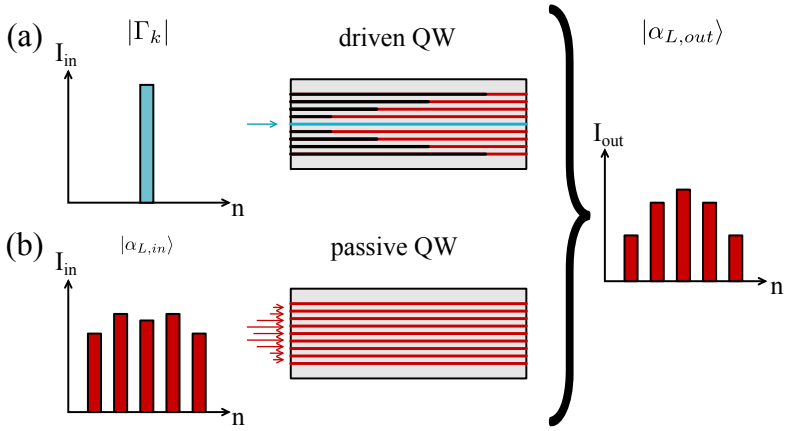

Figure 4.4 – In a driven quantum walk system, a simple pump input distribution can be used to generate $|\alpha_{L,\mathrm{out}}\rangle$ due to the continuous creation of photons during the walk, as shown in (a). The same output state may also be created by a passive quantum walk in (b), however the necessary input state is much more involved [65].

This yields

$$\exp\left(-i\int_0^t \mathrm{d}t'\,\hat{H}_{\mathrm{int,\,lasing}}(t')\right) = \exp\left(-\frac{i}{2}\sum_k z_k\hat{A}_k^\dagger + \mathrm{h.c.}\right) = \exp\left(\frac{\vec{z}\vec{\hat{A}}^\dagger}{2} - \frac{\vec{z}^*\vec{\hat{A}}}{2}\right), \tag{4.17}$$

where $\vec{z} = \int \mathrm{d}t'\vec{S}(t')$ is the time-integrated pump profile. We can simplify this expression to [228]

$$\exp\left(\frac{\vec{z}\vec{\hat{A}}^\dagger}{2} - \frac{\vec{z}^*\vec{\hat{A}}}{2}\right) = \exp\left(\vec{z}'\vec{\hat{A}}^\dagger\right)\exp\left(f(\vec{z})\vec{\hat{A}}^\dagger\vec{\hat{A}}\right)\exp\left(\vec{z}'^*\vec{\hat{A}}\right), \tag{4.18}$$

and the reason for this becomes clear when we apply the transformation on the vacuum state. Then, the last two exponential functions vanish, as they contain annihilation operators acting on vacuum. Finally, we leave the rotating frame by adding $\hat{U}_{\mathrm{int}}^\dagger$

$$\begin{aligned}|\alpha_{\mathrm{L,\,out}}\rangle &= \underbrace{\exp\left(-it\sum_{k,k'}C_{k,k'}\hat{a}_k^\dagger\hat{a}_{k'}\right)}_{\hat{U}_{\mathrm{PQW}}}\underbrace{\exp\left(-i\sum_k z'_k\hat{a}_k^\dagger\right)}_{|\alpha_{\mathrm{L,\,in}}\rangle}|0\rangle \\ &= \hat{U}_{\mathrm{PQW}}\,|\alpha_{\mathrm{L,\,in}}\rangle\end{aligned} \tag{4.19}$$

and see that we can decompose the output state into a complicated input state $|\alpha_{\mathrm{L,\,in}}\rangle$ and a passive quantum walk transformation $\hat{U}_{\mathrm{PQW}}$, which we wanted to show [65].

This interpretation depends on the overall output state of our driven quantum walk system and

therefore the overall length of the walk. As such, the input state and passive evolution are not independent from each other. For different overall lengths of the walk, the combination of input state and passive evolution will change accordingly. Due to the decomposition, we are quite restricted in the realisation of the input states. However, we may lift this restriction to a certain extent by inserting a non-vacuum state at the beginning of our evolution. In this case, we have to consider extra terms (e.g. the $f(\vec{z})$ term) but the overall decomposition in input state and passive evolution still holds.

The evolution and therefore our "input" state to our system are determined by the shape and time-dependence of the driving pump contained in the vector $\vec{S}$. As such, a driving term can only create photons into eigenmodes, with which it has a finite overlap. First, we select the eigenmode excitation at the beginning by the spatial shape of the pump given by the absolute value of the elements $|S_k|^2$. Only eigenmodes that have a finite overlap with our spatial pattern can be driven by the pump. Additionally, we retain the frequency (i.e. the time-dependence) of the pump field ω_p as a degree of freedom. This leads to a phase-matching condition that only allows photon creation in eigenmodes whose eigenvalues are sufficiently close to the pump frequency

$$\hat{H}_{\text{int}} = \sum_k S_k \exp[i(\Omega_k - \omega_p)t]\hat{A}_k^\dagger + \text{h.c.}\,. \tag{4.20}$$

This effect manifests in the dynamics through different growth in the eigenmodes, as shown in figure 4.5(b). Here, the first eigenmode $k = 1$ is phase-matched with $\omega_p = \Omega_1$. During the time evolution, the phase-matched eigenmode grows roughly on a linear scale, while the growth for non-phase-matched eigenmodes gets weaker, the higher the frequency mismatch $\omega_p - \Omega_k$ gets. For highly non-phase-matched eigenmodes (roughly starting at eigenmode $k = 10$), no continuous growth is observable and the photon numbers show an oscillating behaviour over time[8].

To consider the dynamics of a lasing quantum walk in more depth, we simulate a typical passive quantum walk unitary with nearest neighbour coupling

$$\hat{H}_{\text{passive}} = \omega \sum_{k=1}^{N} \hat{a}_k^\dagger \hat{a}_k + C \sum_{k=1}^{N-1} \hat{a}_k^\dagger \hat{a}_{k+1} + \text{h.c.} \tag{4.21}$$

and add the driving term for a single waveguide excitation $k = 0$ and a continuous wave pump field $\Gamma_0 e^{-i\omega_p t}$

$$\hat{H}_{\text{lasing}} = \Gamma_0 e^{-i\omega_p t}\hat{a}_0^\dagger + \text{h.c.}\,. \tag{4.22}$$

We summarise the results in figure 4.5. Figure 4.5(a) shows the photon number distribution during the evolution in the waveguide basis. The photons remain localised around the pumped waveguide $k = 0$, which differs drastically from the photon spread that characterises a passive quantum walk system. There, the photons travel away from a single, localised input in two lobes with a speed of $\pm\sqrt{2}C$. Calling on our decomposition of input state and passive evolution

[8] This is the same effect that happens during a non-phase-matched PDC process, see e.g. [229]. Even for almost phase-matched modes, the growth is not linear, but oscillating. However, the oscillation period is so large that it is not observable in figure 4.5(b).

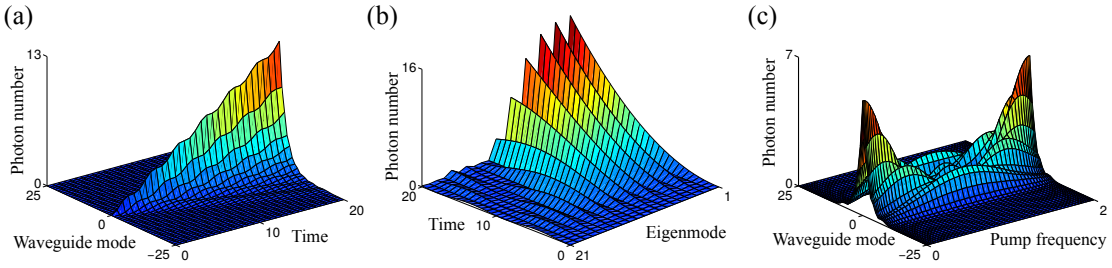

Figure 4.5 – Dynamics of the lasing quantum walk [65]. (a) shows the photon number growth over time in the waveguide basis for a single waveguide pump in the middle[9]. (b) gives the corresponding evolution in the eigenmode basis. Only the phase-matched eigenmode $k = 1$ shows a photon number growth that is linear in time, while the others oscillate with varying period. In (c), we investigate the dependence of the spatial spread at the end of the driven quantum walk depending on the pump frequency. While we retain a peaked structure around the pumped waveguide at the edges $\omega_p = 0; 2$, the photons spread outwards for intermediate frequencies (i.e. $\omega_p = 1$).

unitary, this means that we need a highly delocalised input state in a passive quantum walk to mimic the output distribution of a driven quantum walk system.

As we already mentioned above, we find a nice illustration of the phase-matching behaviour of the driven quantum walk system in figure 4.5(b). The phase-matched eigenmode $\omega_p = \Omega_1$ grows linearly over time, while the others oscillate. The total number of photons in both figures 4.5(a) and (b) is equal and grows quadratically over the length of the evolution in the lasing case. Furthermore, we calculate how the spatial spread of the photons in the waveguide basis behaves as a function of the pump wavelength in figure 4.5(c). We achieve a highly localised structure around the input location for pump frequencies at the edges $\omega_p = 0; 2$, while the photons experience a spatial spread for intermediate frequencies, which is a highly unusual behaviour as the spread of a passive continuous-time quantum walk depends on the coupling strength C, which monotonically depends on the inserted wavelength [57].

Nevertheless, we can quantify it with the typical measure for quantum walk propagation, the variance of the position

$$\sigma^2(t) = \sum_x x^2 \overline{n}_x(t)\,. \tag{4.23}$$

In a driven quantum walk system, such as the one we are considering, two different mechanisms contribute to the spatial spread of walkers, the coupling of the walker itself as well as the photon number growth due to the driving. The examples in figures 4.5(a) and (b) exhibit a cubic growth in the variance. However, renormalising this spread with the growth in the photon number $\sigma^2 \propto t^2$, we end up only with a linear spatial-only variance. Compared to a passive walker (which has a $\sigma^2 = t^2$ variance) this slower spread can be explained by the injection of additional

[9] Simulation parameters: $N = 51$, $-25 \leq k \leq 25$, $C = 0.5$, $\Gamma_0 = 1$, $\omega_p = \Omega_1$ and $t_{\max} = 20$ in dimensionless units.

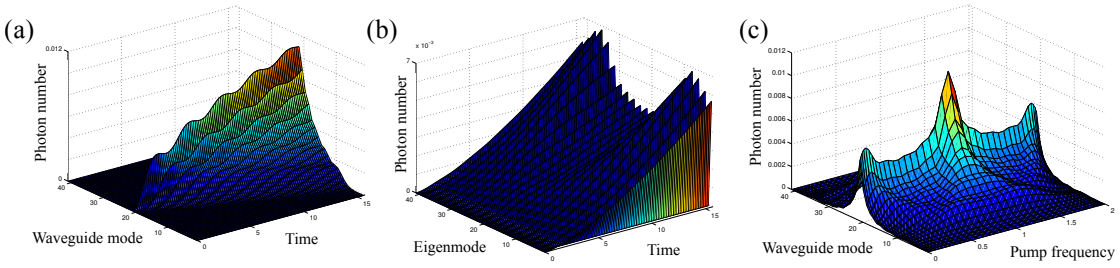

Figure 4.6 – Dynamics of the squeezing quantum walk [65]. (a) shows the evolution in the waveguide basis. As for the lasing quantum walk, the spatial distribution is peaked around the pumped waveguide[10]. In the eigenmode basis (b), we observe a double peaked phase-matching for the outer eigenmodes, which is due to the modified phase-matching condition. (c) plots the spatial distribution of photons depending on the pumped frequency. Opposite to the lasing quantum walk, the spatial distribution remains peaked for all pump frequencies.

photons along the walk in the central channel. Photons that are created at the beginning of the walk would spread with a t^2-variance, but due to the rescaling with the photon number these contributions are suppressed [65].

4.2.3 Squeezing Term

In this section, we summarise the results for a driving Hamiltonian that produces squeezed vacuum states at the output, see chapter 1,

$$\hat{H}_{\text{squeezing}} = \sum_k \Gamma_{S,k}(t)\hat{a}_k^{\dagger 2} + \Gamma_{S,k}^*(t)\hat{a}_k^2\,, \tag{4.24}$$

where $\Gamma_{S,k}$ is again the distribution of the driving pump field and $\hat{a}_k$ is an annihilation operator working on waveguide k. Such a system may be implemented with the non-linear waveguide array from section 4.1 and was the inspiration for this work. Analogously to the previous section, we define the full system Hamiltonian in the eigenmode basis via [65]

$$\hat{H} = \hat{H}_{\text{passive}} + \hat{H}_{\text{squeezing}} = \sum_k \Omega_k \hat{A}_k^\dagger \hat{A}_k + \sum_{k,k'} S_{k,k'}(t)\hat{A}_k^\dagger \hat{A}_{k'}^\dagger + \text{h.c.}\,. \tag{4.25}$$

Note, that the pump distribution in the eigenmode basis is not a vector anymore, but a matrix depending on k, k', as we have to include the basis transformation $\boldsymbol{S}(t) = T^{-1}\vec{\Gamma}_S(t)T$ of two creation operators at the same time. Following the calculation with the lasing term in section

[10] Simulation parameters: $N = 51$, $-25 \leq k \leq 25$, $C = 0.5$, $\Gamma_0 = 0.1$, $\omega_p = \Omega_{25}$ and $t_{\max} = 20$ in dimensionless units.

4.2.2, we arrive at the output state

$$\begin{aligned}|\Psi_{\mathrm{S,\,out}}\rangle &= \hat{U}\exp\left(\frac{\vec{\hat{A}}^{\dagger T}\boldsymbol{z}\vec{\hat{A}}^{\dagger}}{2}-\frac{\vec{\hat{A}}^{T}\boldsymbol{z}^{*}\vec{\hat{A}}}{2}\right)|0\rangle \\ &= \prod_{k}\exp(i\Omega_k\hat{A}_k^{\dagger}\hat{A}_k)\exp\left(\frac{\vec{\hat{A}}^{\dagger T}\boldsymbol{z}'\vec{\hat{A}}^{\dagger}}{2}\right)\exp(f(\boldsymbol{z})\vec{\hat{A}}^{\dagger}\vec{\hat{A}})\exp\left(\frac{\vec{\hat{A}}^{T}\boldsymbol{z}'^{*}\vec{\hat{A}}}{2}\right)|0\rangle\ .\end{aligned} \tag{4.26}$$

As the last two terms of this state operate on vacuum, they can be neglected. Finally, we transform back to the waveguide basis and find

$$\begin{aligned}|\Psi_{\mathrm{S,\,out}}\rangle &= \exp\left(-it\sum_{k,k'}C_{k,k'}\hat{a}_k^{\dagger}\hat{a}_{k'}\right)\exp\left(-i\sum_{k,k'}z''_{k,k'}\hat{a}_k^{\dagger}\hat{a}_{k'}^{\dagger}\right)|0\rangle \\ &= \hat{U}_{\mathrm{PQW}}\,|\zeta_{\mathrm{S,\,in}}\rangle\ ,\end{aligned} \tag{4.27}$$

which reproduces the decomposition to a delocalised (squeezed) input state $|\zeta_{\mathrm{S,\,in}}\rangle$ and passive state evolution $\hat{U}_{\mathrm{PQW}}$ of section 4.2.2.

Having confirmed that the decomposition of passive walk and intricate input state is also valid for driving with a squeezing term, we now focus on the dynamics present in the squeezing quantum walk. The results for this system are summarised in figure 4.6, where we implemented the driving term for a single waveguide excitation $k = 0$ and a continuous wave pump field $\Gamma_0 e^{-i\omega_p t}$

$$\hat{H}_{\mathrm{squeezing}} = \Gamma_0 e^{-i\omega_p t}\hat{a}_0^{\dagger 2} + \mathrm{h.c.}\,. \tag{4.28}$$

Figure 4.6(a) shows the photon number in the waveguide basis during the length of the walk. As in the lasing case, the state remains localised around the input channel. However, the behaviour in the eigenmode basis in figure 4.6(b) differs drastically compared to the lasing Hamiltonian. This is due to the fact that we have a modified phase-matching condition due to the $\hat{a}^{\dagger 2}$ photon creation that reads

$$\hat{H}_{\mathrm{squeezing,\,int}} = \sum_{k,k'}S_{k,k'}\exp(-i[(\Omega_k+\Omega_{k'})-\omega_p]t)\hat{A}_k^{\dagger}\hat{A}_{k'}^{\dagger} + \mathrm{h.c.}\,. \tag{4.29}$$

This means that we will, in general, phase-match two or even more eigenmodes symmetrically around the driving frequency of the pump. In the figure, this is evident by the symmetric gain of the eigenmodes around the $k = 25$-th eigenmode in the centre. The fact that we can use different combinations of eigenmodes to achieve phase-matching leads to the broadening of the gain in the eigenmode basis. Figure 4.6(c) shows another distinct difference to the lasing quantum walk. While the spatial distribution of the lasing quantum walk spreads at several pump frequencies, the spatial distribution in the squeezing case always remains localised around the pump channel.

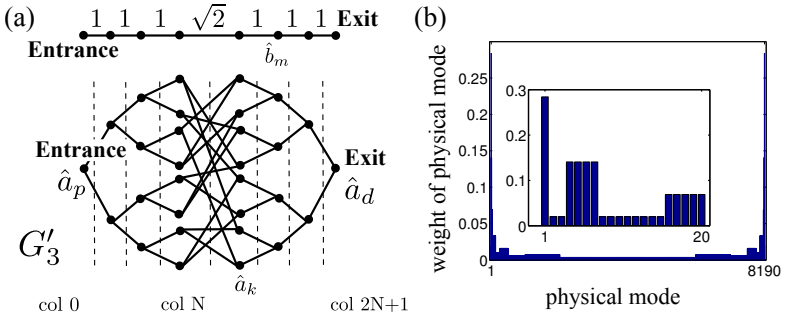

Figure 4.7 – Layout and eigenmodes of the glued trees graph [65]. (a) shows an example tree of depth $N = 3$ and its representation on the linear chain [230]. All vertices in a column of the glued trees graph are grouped together to a single vertex on the linear chain, where the coupling coefficients are $C_{m,m+1} = 1$ and $C_{N,N+1} = \sqrt{2}$. In (b), we have depicted an eigenmode of the glued trees graph of depth of $N = 11$ (inlay for the first 20 vertices). The large weights on the entry and target mode ($k = 1;\ 8190$) make this eigenmode specifically interesting for the construction of our search algorithm.

4.2.4 Search Algorithm

In the previous sections, we investigated the behaviour of different driving terms in a continuous time quantum walk system. Now, we want to exploit the unique dynamics of these systems and apply it to implement a search algorithm. To this end, we go back to the lasing term, because it is mathematically simpler to describe and investigate the spread of the walkers along the search graph.

The reason why quantum walks are so interesting for search problems lies in the increased spread of quantum walkers compared to classical particles (compare section 4.2.2). An example, perhaps even the most famous one, for a quantum search algorithm is the Grover Search [201, 202]. In this case, a particular state is inserted into a discrete quantum walk and it can find a marked vertex, a position on a lattice or a node of the quantum walk graph (i.e. the goal of the search), in $t \propto \sqrt{N}$ time, where N is the overall number of vertices. This particular property has sparked several other proposals for search algorithms that are closely related [231–234].

Let us consider a well-investigated graph structure for the construction of our search problem, the *glued trees graph* [230] in figure 4.7(a). It is characterised by its depth of N layers which contain a total number of $2^{N+2} - 2$ vertices. To gain a description of the glued trees graph as a linear chain that would represent our continuous time quantum walk system, all vertices $\hat{a}_k$ of a layer, or a *column*, are grouped to a single vertex $\hat{b}_m$ of the linear chain, as indicated in figure 4.7(a). The coupling coefficients between the nodes on the linear chain are given by $C_{m,m+1} = 1$, except for the central coupling, which is $C_{N,N+1} = \sqrt{2}$. It has been shown that a classical walker traverses this particular type of graph in an exponential time from entrance to target mode, while a quantum walker only needs polynomial time [230]. It is our aim to construct a search algorithm with driven quantum walks that also traverses the graph in polynomial time.

To construct our search algorithm, we consider the following problem. We start our search at

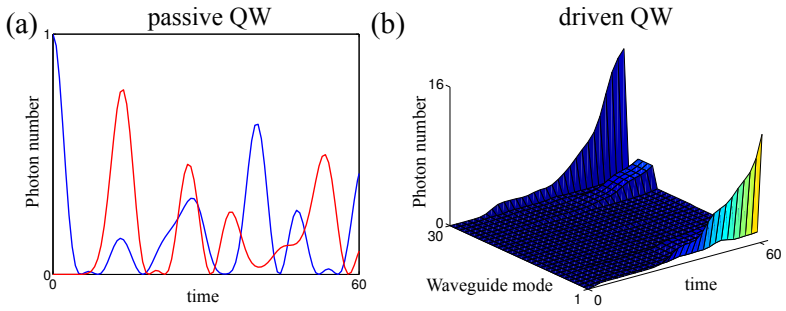

Figure 4.8 – Comparison between target probabilities in passive and driven continuous time quantum walk [65]. In the passive quantum walk in (a), the probabilities of finding the quantum walker in either the entry (blue) or target (red) vertex of the graph oscillates strongly due to the phase evolution between different eigenmodes of the graph. In contrast, the probabilities to find the walker in the entry or target mode monotonously increases in the driven quantum walk (b). As we phase-match an eigenmode that has significant overlap only with the entry and target modes, the walkers are only created in these two vertices and the phase evolution between the eigenmodes does not play a role. This provides a significant advantage compared to passive quantum walk systems.

an entrance, or pump mode $\hat{a}_p$ on the glued trees graph[11] and want to find our marked vertex, the target or exit vertex, by having more walkers there than on any other parts of the graph, except for the pumped waveguide. In the driven quantum walks setting, the first step is to choose a suitable eigenmode of the graph that shows significant overlap with both the entrance and target mode, i.e. $\hat{A}_D \approx \mu_{D,e}\hat{a}_e + \mu_{D,d}\hat{a}_d$. Here, μ_D is the weight of the waveguide mode in the composition of the eigenmode and we require $\mu_{D,e} \approx \mu_{D,d} \approx \frac{1}{\sqrt{2}}$. Secondly, we match our pump frequency $\omega_p = \Omega_N$ to the eigenfrequency of the selected eigenmode. This will cause a continuous photon growth in this particular eigenmode and therefore favour photon growth on both the entrance and target sites. This behaviour is in stark contrast to a passive quantum walk search.

We compare the passive and driven search in figure 4.8. In figure 4.8(a), we consider a passive quantum walk search, where blue gives the occupation probability on the entrance and red on the target mode. At the start of the search the walker is localised in the entrance mode and due to the phase rotations between the eigenmodes of the walk, we find a peaked probability of presence on the target mode after some time. However, as the evolution is not complete, the phases go out of turn and the probability to find the walker on the target mode diminishes again. This oscillating behaviour means that the walker may only be found on the target mode at specific points in time. Opposed to the passive search, the driven quantum walk search favours walkers to be created in the entrance and target modes, as shown in figure 4.8(b). In turn, we observe a continuous growth of probability of presence on both sites. This is a massive advantage to the passive search, as we only have to wait for some minimum time before we can choose to

[11] Represented by a linear chain, as shown in figure 4.7(a).

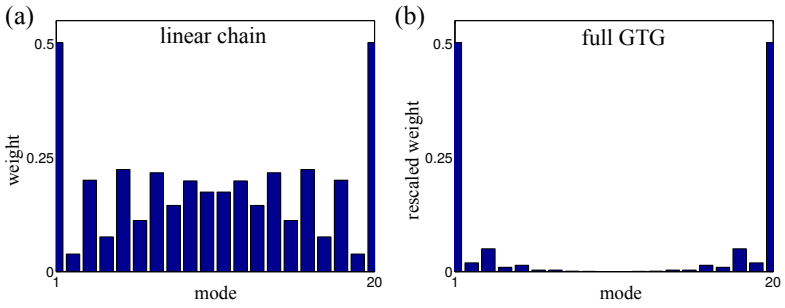

Figure 4.9 – Eigenmode of the glued trees graph and its linear chain representation [65]. In (a), we plot the weights of the eigenmode on the vertices in the linear chain representation of the glued trees graph. In (b), we rescale the weights to the total number of glued trees graph vertices in a single column. As the number of vertices in a column decreases to the sides, the eigenmode weights on the entry and target vertices increase exponentially.

measure our system and do not have to rely on specific timings for the walker to be present in the target mode.

To show that our scheme enables a quantum walker to traverse the graph in only polynomial time, we have to consider two main factors for an increasing system size, the weight of the chosen eigenmode on the entrance and target modes, as well as the spacing of the eigenfrequencies between adjacent eigenmodes of the system. We begin with the weights that the entrance and target modes contribute to the chosen eigenmode for the search.

As we consider a defect in the centre of the linear chain ($C_{N,N+1} = \sqrt{2}$), the eigenvalues of this system are not given by equation (4.6), but have to satisfy [235]

$$U_N(\lambda_j) = U_{N-1}(\lambda_j)\,, \tag{4.30}$$

where U_N is the Chebyshev polynomial of the second kind of degree N. However, the eigenvectors are given by [235] and are the same for the linear chain with and without the defect. The difference in the shape of the eigenfunctions stems from the fact that they have to be evaluated at the eigenvalues, which differ for the two systems. As the size of the system increases ($N \to \infty$), the eigenvalues of the two systems become more and more similar and therefore also the eigenmodes converge to one another. The weight of the j-th vertex to the k-th eigenmode of the linear chain is given by [235]

$$v_{j,k} = \sqrt{\frac{1}{N}} \sin\left(\frac{jk\pi}{2N+1}\right) \tag{4.31}$$

and we find that the mode with most weight at the edges of the chain is, for large N and $k = N$,

$$v_{j,N} = \sqrt{\frac{1}{N}} \sin\left(\frac{jN\pi}{2N+1}\right) \approx \sqrt{\frac{1}{N}} \sin\left(\frac{j\pi}{2}\right)\,. \tag{4.32}$$

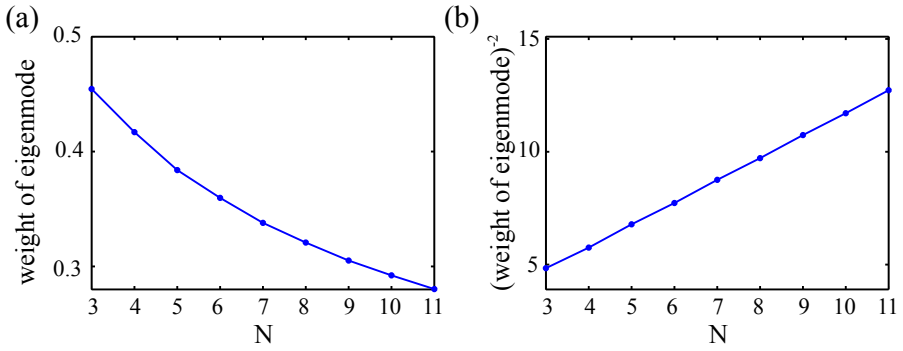

Figure 4.10 – Numerically calculated weights of entrance and exit modes contributing to eigenmode $\hat{A}_D$ on the glued trees graph [65]. (a) shows the direct dependence on the depth of the full glued trees graph, whereas (b) shows a linear behaviour with respect to a $\frac{1}{\sqrt{N}}$-scaled y-axis. This confirms that the weight contributing to the eigenmode decreases only polynomially up to a depth of $N = 11$.

We plotted this mode already in figure 4.7(b) for vertices of the full glued trees graph. Furthermore, we depict the mode also directly for the vertices of the linear chain in figure 4.9. Figure 4.9(a) shows the unscaled weights, as given by equation (4.32). In figure 4.9(b) we rescale the weights to the full number of vertices in a column of the glued trees graph. The weight on the outer modes increases exponentially compared to the middle, as the number of vertices in the middle of the glued trees graph increases exponentially with the depth of the graph.

We considered the eigenmode structure of the linear chain in such detail to answer whether the weight of the entrance and target mode that contributes to the chosen eigenmode of the search algorithm declines only polynomially with increasing system size. To answer this question, we numerically calculate the weights of entrance and target mode for different depths of the glued trees graph up to $N = 11$ in figure 4.10(a) and find a slow decrease in the weights. To quantify this behaviour, we re-scale the y-axis of this plot with $\frac{1}{\sqrt{N}}$ in figure 4.10(b). The linear behaviour evident in this figure gives numerical evidence that the weights of entrance and target mode to the chosen search mode decline by $\frac{1}{\sqrt{N}}$ up to $N = 11$. Therefore, we do not have to compensate an exponential escape of walkers to other positions on the graph due to the structure of the eigenmode.

The second factor that we have to investigate is the spacing of the eigenfrequencies with increasing system size. For large system sizes, the eigenfrequencies are roughly given by

$$\Omega_k \approx \cos\left(\frac{k\pi}{2N+1}\right) . \tag{4.33}$$

Therefore, the minimal phase-mismatch Δ between the chosen eigenmode with $\omega_p = \Omega_N$ and the adjacent ones $\Omega_{N\pm1}$ decreases only polynomially. As the photon growth in the adjacent eigenmodes $K = N \pm 1$ oscillates with a period of $\frac{1}{\Delta}$, the polynomial decrease in Δ only causes a polynomial increase in the minimum time that we have to wait before measuring.

To summarise, we investigated the shape of the optimal eigenmode for the search algorithm and showed that the weights of the entrance and target mode contributing to it decrease as $\frac{1}{\sqrt{N}}$ with the system size. This shows that we do not have to compensate an exponential escape of walkers to unneeded positions on the graph, but only need to use a polynomial increase in resources such as pump power. Secondly, we showed that the minimum time needed to drown out the population on positions other than the entrance or target mode also increases only polynomially with the system size. This is due to the polynomial decrease in the phase-mismatch between the optimal and adjacent eigenmodes. From these two effects, we conclude that the walker in the driven quantum walk system can traverse the glued trees graph in polynomial time and with polynomial resources, which is a clear advantage over the classical walker that needs exponential time to traverse the graph.

Summary

In conclusion, we introduced a new type of continuous-time quantum walk systems, driven quantum walks. We investigated two driving mechanisms for the photon creation, a lasing and a squeezing term. We showed fundamentally different dynamics compared to a passive quantum walk and quantified that for the lasing case with the variance of the walkers of $\sigma^2 \propto t^3$, where an increase of t^2 comes from the photon creation.
Furthermore, we constructed a search problem with the well-investigated glued trees graph and showed that a walker of a driven quantum walk system can traverse this graph in polynomially increasing time and with polynomially increasing resources. This gives us an exponential speed-up compared to a classical walker, which traverses the graph only in exponential time.

4.3 BosonSampling in Non-linear Waveguide Arrays

Using the formalism and the concepts that we derived in the previous section, we are now able to apply the non-linear waveguide array system from section 4.1 to the computationally hard problem of BosonSampling [7, 236]. This non-universal model of quantum computation is, at the moment, the most promising candidate to show quantum-over-classical advantages. The conventional approach to BosonSampling involves either deterministic or post-selected probabilistic single-photon sources coupled to a passive, linear chip that encodes a sufficiently complex unitary transformation [237–242]. In this section, we show that BosonSampling is also possible in a genuinely non-linear system.

To do this, we use the previously introduced concepts to map a non-linear waveguide array to a protocol called *Scattershot* BosonSampling [243]. First, we discuss the general problem of BosonSampling and motivate its impact on the quantum optics and computational science community. Second, we review the protocol of Scattershot BosonSampling, which we utilise for the non-linear waveguide array. After this introductory part, we go into detail about the considered non-linear waveguide array system and map it to a linear system by deriving the passive transfer unitary that is sampled during a BosonSampling experiment. This passive transfer

unitary provides a novel matrix connection between the spatial modes of the signal and herald photons and may provide new insights for the state interpretation, also in other fields. Following this derivation, we investigate whether the transfer matrix is complex enough to allow for valid BosonSampling runs. We find however, that the symmetry of the derived transfer matrix prohibits us to give a final answer, since the complexity to calculate Permanents of symmetric matrices has not been investigated before. Finally, we give an outlook on the prospects for an experimental implementation of our scheme [236].

4.3.1 What is BosonSampling?

With a question like this, one usually first looks it up on Wikipedia [244], which says the following: *Boson sampling constitutes a restricted model of non-universal quantum computation introduced by S. Aaronson and A. Arkhipov.*.While this is a well-designed answer and very much correct, it does not provide an insight to what BosonSampling does and why it is so interesting.

The motivation to introduce a non-universal quantum computational problem such as BosonSampling is straightforward from a computational point of view. Consider the *Extended Church-Turing Thesis* (ECT), which says that "all computational problems that are efficiently solvable by realistic physical devices, are efficiently solvable by a probabilistic Turing machine" [7]. However since 1994, when Peter Shor [245] presented his famous algorithm which says that *predicting the results of a given quantum-mechanical experiment, to finite accuracy cannot be done by a classical computer in probabilistic polynomial time, unless factoring integers can as well* to the computational science community, it has been clear that the ECT does not fit very well to the accepted laws of quantum mechanics. Therefore, as Scott Aaronson presented during his talk "The Limits of Quantum Computers (or: What We Can't Do With Computers We Don't Have)"[12] there are three possibilities

1.: The ECT is false.
2.: Textbook quantum mechanics is false. (4.34)
3.: There exists an efficient classical factoring algorithm.

Unfortunately, the existence of Shor's algorithm means that one of them *must* be the case. As physicists, we believe that quantum mechanics is correct[13]. At the moment, the most acceptable solution to this dilemma seems to be that proving the ECT false would have the least bad consequences. Yet, the implementation of Shor's algorithm to verify the function of this protocol would require a universal quantum computer. Unfortunately, those are quite difficult to come by, even though a lot of progress has been made towards this goal [246–251]. Nevertheless, we would like to find a protocol on the photonic platform that does not have to be universal but still shows a quantum advantage compared to the classical computation.

In 2004 Stefan Scheel [252] derived that the probability to measure a specific photon pattern $\overline{n}$ at the end of a transformation matrix T depends on the photonic input state (which comprises vacuum and specified inputs of indistinguishable single photons) and the transformation matrix.

[12] First given at: University of Waterloo, 19.2.2007
[13] Hopefully.

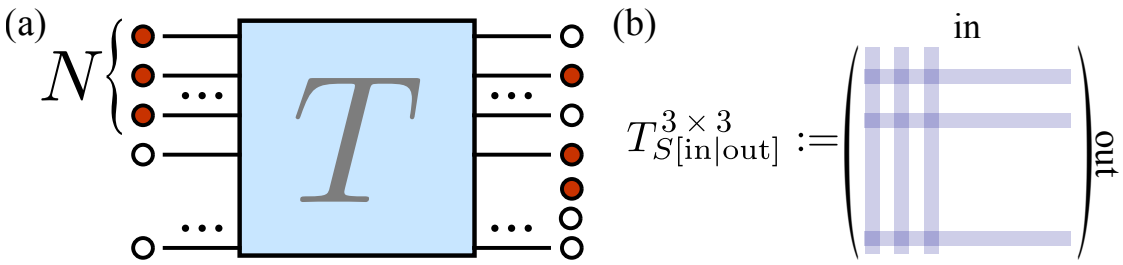

Figure 4.11 – Schematic of the Aaronson & Arkhipov BosonSampling scheme [7] and selection rules for the sampled matrix [253]. In (a), N photons are inserted into a transformation matrix T and the photon patterns at the output are detected. As the photon pattern probabilities are proportional to the Permanent of the sampled submatrix T_S [252], the BosonSampling problem is in the #P computational complexity class. The submatrix T_S is sketched in (b), the columns are selected by the input pattern and the rows by the modes, where a photon was detected. At the intersection, the entries of T are selected. As such, the sketched matrix for $N = 3$ is a 3×3-dimensional T_S.

An example of the setup is given in figure 4.11(a). Scheel showed that for such a setup the output probabilities are given by the Permanent of a submatrix T_S

$$P(\overline{n}) = |\mathrm{Perm}(T_{[\mathrm{in}|\mathrm{out}]})|^2 := |\mathrm{Perm}(T_S)|^2 = \left| \sum_{\sigma \in P_N} \prod_{i=1}^{N} T_{S_{i,\sigma(i)}} \right|^2 , \tag{4.35}$$

where [inlout] is the combination of the single photon input and occupied output modes of $\overline{n}$ and P_N are all symmetric permutations from 1 to N. While this notation for the Permanent may look complicated, its calculation becomes intuitive if we note that the Permanent is calculated in the same way as the determinant, however all signs in the summation are positive. The selection process for the submatrix T_S is sketched for three photons in 4.11(b). From the overall transfer matrix T we first select the columns where we input a photon, i.e. the first three in our example. The rows are selected by the output pattern $\overline{n}$, where we detect a photon. At the intersection points of the rows and columns, we retain the entries and use the obtained 3×3-dimensional matrix to calculate the Permanent.

So far, we only drew on the results as published by S. Scheel in 2004 and did not even touch the achievements of Scott Aaronson and Alex Arkhipov in 2011 [7]. Their achievement was to use this probability formula in the context of computational complexity and develop a quantum sampling problem that can disprove either of the noted claims in (4.34). In order to appreciate the full scope of their results we summarise a few main points of their derivation[14]. We entrust anybody interested in their full proof to the metaphorical hands of the 96 pages of their conference paper [7]. Everybody else may follow the summary below.

[14] We need a few of their main conjectures and theorems for the proof in section 4.4

Consider the scheme in figure 4.11(a). It is identical to the setup used for the interpretation of the Permanent relation by Scheel. We input N photons into adjacent modes of a linear transformation and measure the output probabilities. The calculation of all output pattern probabilities falls into the #P complexity class[15], as the generating function, the Permanent, is #P-complete [255]. As such, they define the classically hard to solve problem of BosonSampling. Then, for this particular setup, Aaronson and Arkhipov show 2 main theorems

- "The *exact* BosonSampling problem is not efficiently solvable by a classical computer, unless $\mathsf{P}^{\#\mathsf{P}} = \mathsf{BPP}^{\mathsf{NP}}$."[16] To prove this theorem, they need to show that the approximation of the Permanent up to a multiplicative constant is in #P and that *if* we had a classical algorithm for the BosonSampling problem, then we *could* approximate the Permanent up to a multiplicative constant and the polynomial hierarchy collapses[17].

- As we wish to implement this BosonSampling computer, we have to allow for errors and therefore *approximate* BosonSampling. In detail, this means that the BosonSampling computer does not sample directly from an ideal distribution, $\mathcal{D}_A$, but from an approximate one $\mathcal{D}'_A$, with an additive error tolerance $|\mathcal{D}_A - \mathcal{D}'_A| < \epsilon$. Therefore, Aaronson and Arkhipov show that also an approximate BosonSampling problem is hard to solve. This is a bit more complicated both to understand and to prove. In principle, they suppose that a classical adversary machine might know which BosonSampling probability we would like to sample and promptly corrupt this probability by inserting a classical approximation of the corresponding click probability. While the value for the probability that the corrupted BosonSampling machine spits out is a valid approximation, it will not provide a solution to the #P-complete problem we want to investigate.

We will not use the proofs necessary for theorem 1 in this thesis. Therefore, it suffices to just know that exact BosonSampling is hard. Nevertheless, we want to comment on the proof for theorem 2 and the technical requirements for the sampled matrices.

The main requirement of Aaronson and Arkhipov that they need to prove theorem 2 is that a BosonSampling computer is able to use a "robust" BosonSampling encoding, such that if a small fraction ϵ of all events are "badly wrong", it retains the complementary $1 - \epsilon$ as valid results. If we suppose that an approximate BosonSampling computer indeed works this way, we use this property to trick a possible classical adversary. The way to show that approximate BosonSampling up to an additive error (Problem $|\mathrm{GPE}|^2_{\pm}$ in [7]) is hard uses the fact that we smuggle the interesting probability into the scheme as a random output of the BosonSampling computer. Heuristically, the adversary will not know which instance we are interested in and cannot corrupt this result with a large probability. However, if the adversary (which is classical) can approximate *most* of the results of our approximate BosonSampling computer[18] and therefore corrupt our result, also the Permanent can be approximated in polynomial time. This would be bad, as it implies a collapse of the polynomial hierarchy.

[15] For an introduction in computational complexity theory, see [254].
[16] AA 2011: Theorem 1
[17] Which the computational scientists strongly believe will not happen.
[18] Because of the robust encoding only ϵ results are allowed to be wrong.

So, the answer we have to find is: How do we hide our interesting result in the output of a BosonSampling computer and how do we make such a device robust? The technical component that we need to make this argument valid is a special choice of the transformation matrix T. If we choose a unitary transformation matrix of dimension $M \times M$ according to the Haar measure, then there exists a proof that the entries of any $N \times N$ submatrix ($M > N^2$) are in variation distance to a matrix of *independent and identically distributed* (i.i.d.) Gaussian matrices[19] [7]. The sampling from such a device is random, meaning that even if we put in a defined input photon pattern into the first N inputs of the transformation matrix, we cannot predict where the photons will come out at the end. This fulfils the robustness criterion for our BosonSampling computer. Furthermore, as we demand that the transformation matrix is much larger than our photon number, we can also hide the interesting probability in the multitude of other randomly sampled output patterns. As such, we conclude that given the choice of the Haar random unitary transformation matrix, an approximate BosonSampling problem up to additive error is difficult to solve, or more specifically in $\mathsf{FBPP}^{\mathsf{NP}^{\mathcal{O}}}$.

However, Aaronson and Arkhipov remain short on the final proof that the approximate BosonSampling problem up to additive error is actually in the #P complexity class. Nevertheless, they base this claim on two conjectures, the Permanent-of-Gaussians conjecture, which says that estimating the Permanent of i.i.d. Gaussian matrices really is #P-hard ($\mathrm{GPE}_{\times}$ in [7]). The other conjecture, the Permanent anti-concentration conjecture connects the absolute square of the Permanent that we sample, directly to the complexity of the Permanent itself and matches them to the same complexity class, i.e. #P. With these two conjectures, Aaronson and Arkhipov conclude BosonSampling is indeed not solvable by a classical computer, unless $\mathsf{P}^{\#\mathsf{P}} = \mathsf{BPP}^{\mathsf{NP}}$, which implies a collapse of the polynomial hierarchy.

The BosonSampling problem is very interesting not only from a quantum computing point of view, but as it is also almost experimentally feasible, many groups implemented such a system as proof of principle experiments [237–242]. Unfortunately, the main issue to achieve a scalable experimental implementation is the reliable generation of *pure and indistinguishable single photons*. Using probabilistic single photon sources, e.g. heralded sources of parametric down-conversion, scales *exponentially* bad to high photon numbers, as the state creation is probabilistic. While a lot of progress has been achieved on the field of deterministic single photon sources from semiconductor quantum dots, the generation of indistinguishable photon sources with perfect collection efficiency is still up to technological optimisation [256–261] and proof-of-principle BosonSampling experiments have recently been published [262–264].

In this regard, Lund et al. [243] have proposed a conceptual improvement on the BosonSampling scheme for the implementation with probabilistic down-conversion sources. The schematic is given in figure 4.12(a).

Contrary to the original BosonSampling scheme, we now allow that all inputs of the Haar random transfer matrix T are connected to probabilistic single photon sources. In this instance they are realised by two-mode squeezers where one half of the created photon pairs is connected to heralding detectors and the other half is coupled to the transformation matrix. A heralding event of N photons, as well as a detection event of the other N photons constitutes a valid BosonSampling instance.

[19] This means that all matrix entries are randomly chosen according to the complex normal distribution.

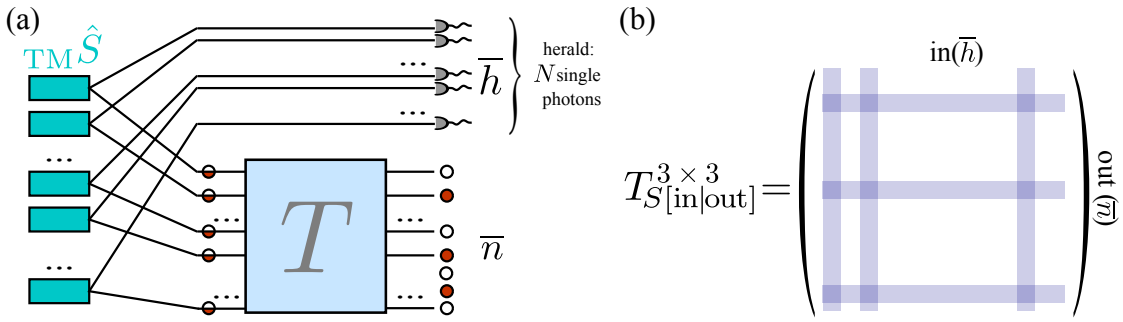

Figure 4.12 – Schematic of the Scattershot BosonSampling scheme, as proposed by Lund et al. [243]. Contrary to the original BosonSampling protocol, the input ports are coupled to two-mode squeezers and the input photons to the transformation matrix are heralded separately.

As they consider a randomised photon state input, they can improve the scaling of the generation probability for N photons by a binomial factor $\binom{M}{N}$, where M is the number of modes and $N = \sqrt{M}$ is the number of photons needed for the BosonSampling experiment. This gives them a $\frac{1}{\sqrt{N}}$-scaling to generate large photon numbers N, compared to the exponentially small probability to generate N photons in a specific pattern. As they are only combining a multitude of BosonSampling instances of the Aaronson and Arkhipov scheme, the complexity arguments for this scheme propagate through to this proposal, called *Scattershot* BosonSampling. However, the same multiplexing argument makes their scheme a zero sum game in terms of statistical significance, compared to the Aaronson and Arkhipov scheme. Since we are sampling from $\binom{M}{N}$ instances of the original scheme with exactly $\binom{M}{N}$ more photons, we do not gain any improvement per individual sampling problem. Nevertheless, the Scattershot scheme is the most general scheme up to date and was experimentally implemented as a proof-of-principle by the group of Fabio Sciarrino in Rome [265].

On a related note, the group of T. Ralph also tackled the question of BosonSampling from a general Gaussian input state [266] (i.e. squeezed states or thermal light). However, while they have shown that sampling from thermal light is not in the same complexity class as BosonSampling with single photon states, it is still not easy to simulate. However, they have not found a conclusive argument for squeezed states or Gaussian states in general. This is the question we will answer in section 4.4.

As a concluding remark, we would like to point out that this abstract construction of the BosonSampling computer may also be used in real life problems. In 2015, the group of A. Aspuru-Guzik found a way to use BosonSampling to simulate the shape of molecular vibronic spectra [267].

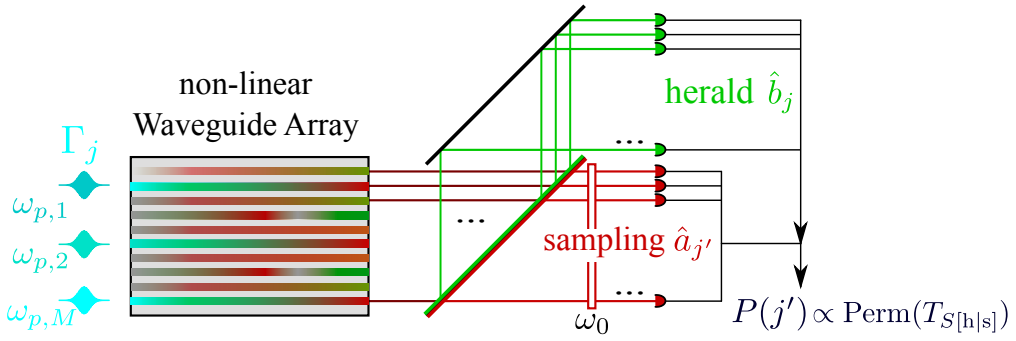

Figure 4.13 – Schematic of the proposed waveguide array BosonSampling experiment [236]. We use a highly non-degenerate down-conversion process and pump each waveguide with a different pump frequency. After the state generation, we split of one half of the generate photons as heralds. As their wavelength is in the near infrared regime $C_h = 0$, the photons exit the waveguide in which they were created. The other half that is generated in the telecom regime passes a single-frequency filter $\omega_{\mathrm{filter}} = \omega_0$ to make them indistinguishable. Finally, we also detect the sampling patterns depending on the heralding pattern.

4.3.2 System Design and Derivation of the BosonSampling Matrix

To utilise the non-linear waveguide array for BosonSampling experiments [236], we designed the system depicted in figure 4.13. Our potential BosonSampling device comprises N weakly coupled waveguides for the telecom regime, while we exclude coupling in the near infrared or visible wavelength range [57, 211]. Additionally, we enable the process of parametric down-conversion in a highly non-degenerate regime. This means that we use pump photons in the green ($\lambda_p \approx 530\,\mathrm{nm}$) that decay into photons in the near infrared ($\lambda_h \approx 800\,\mathrm{nm}$, our herald) and the telecom regime ($\lambda_s \approx 1550\,\mathrm{nm}$, our sampling photons). As already discussed, parametric down-conversion has to obey energy $\omega_p = \omega_h + \omega_s$ and momentum conservation $k_p = k_h + \kappa_s$. The coupling of the signal photons in the telecom regime between the waveguides modifies the propagation vectors [214] and therefore the momentum conservation and phase-matching function.

To achieve a mapping of such a non-linear waveguide array system to the protocol of Scattershot BosonSampling, we split the sampling and herald photons on a dichroic mirror. We detect the herald photons directly and obtain a pattern $\hat{b}_j$. The sampling photons pass a single frequency filter with $\omega_{\mathrm{filter}} = \omega_0$ to ensure their indistinguishability in the frequency domain. Finally, we also detect the patterns of the sampling photons $\hat{a}_{j'}$, which can couple back and forth and evaluate them according to the corresponding heralding pattern. After we derive the mathematical structure of our system, we will discuss, why we need to pump each waveguide of the array with a different pump frequency [236].

BosonSampling experiments strongly depend on the implementation of the unitary transformation matrix T [7]. This T is usually implemented by a passive, linear coupling matrix, i.e. an array of beam splitters. In our case however, we allow for photon creation inside our non-linear

waveguide array and the overall transformation that we implement is decidedly *non-passive*. In the following, we show how to extract a passive transformation matrix T between the heralding pattern (depending on index j) and the sampling pattern (depending on index j'). This result is already interesting, as it establishes a novel description of correlations between the signal and herald photons that is not restricted to the scope of non-linear waveguide arrays.

To derive the transformation matrix for BosonSampling in non-linear waveguide arrays, we use the notation introduced in section 4.2 [65]. We begin with the full Hamiltonian of the coupled, non-linear system [236]

$$\begin{aligned}\hat{H}(z,t) = \sum_{j=1}^{N} \beta_h(\omega_h)\hat{b}_j^\dagger \hat{b}_j \; + \; \sum_{j=1}^{N} \beta_s(\omega_s)\hat{a}_j^\dagger \hat{a}_j \; + \; C_s \sum_{N.N.} \hat{a}_j^\dagger \hat{a}_{j+1} \\ + \sum_{j=1}^{N} \Gamma_j(t)\hat{a}_j^\dagger e^{-i\omega_s t}\, \hat{b}_j^\dagger e^{-i\omega_h t} \; + \; \text{h.c.}\,,\end{aligned} \tag{4.36}$$

where $\beta_\nu(\omega_\nu)$ is the propagation constant of a light field in an uncoupled waveguide at frequency ω_ν, C_s is the coupling parameter for the sampling photons and $\Gamma_j(t)$ denotes the undepleted pump field in waveguide j. The first two terms encode the free propagation of the herald and sampling photons in the waveguide array, while the third term adds a finite coupling probability to adjacent waveguides only for the sampling photons, i.e. $C_p = C_h = 0$. Finally, the forth term encodes the non-linear parametric down-conversion process, where a pump photon decays into a herald $\hat{b}_j$ and a sampling photon $\hat{a}_j$.

We solve this Hamiltonian by transforming it to the eigenmode picture for the sampling photons and obtain [236]

$$\hat{H}(z,t) = \sum_{k=1}^{N} \kappa_{s,k}\hat{A}_k^\dagger \hat{A}_k + \sum_{j=1}^{N} \beta_h(\omega_h)\hat{b}_j^\dagger \hat{b}_j + \sum_{j=1}^{N} \Gamma_j(t)\hat{b}_j^\dagger e^{-i\omega_h t}\, e^{-i\omega_s t} \sum_{k=1}^{N} \overline{\mu_{jk}^*}\hat{A}_k^\dagger + \text{h.c.}\,, \tag{4.37}$$

where $\kappa_{s,k} = \beta_s(\omega_s) + 2C_s \cos\left(\frac{k\pi}{N+2}\right)$ is the eigenvalue for the k-th eigenmode of the finite waveguide array with fixed boundary conditions, see section 4.1.2. The transformation from waveguide to eigenmode basis is encoded by $\hat{A}_k = \sum_{j=1}^{N} \mu_{jk}\hat{a}_j$ for the k-th eigenmode [220]. We move to the interaction picture, which removes the free propagation terms and enter the classical pump field $\Gamma_j(t) = \Gamma_j \exp\left[i\,\omega_{p,j}t\right]$. This yields [236]

$$\begin{aligned}\hat{H}_{\text{int}}(z,t) = \sum_{j=1}^{N}\sum_{k=1}^{N} \Gamma_j \exp\left[i\left(\omega_{p,j} - (\omega_s + \omega_h)\right)t\right] \\ \times \exp\left[i\left(\beta_p - (\kappa_{s,k} + \beta_h)\right)z\right] \overline{\mu_{jk}^*}\hat{A}_k^\dagger \hat{b}_j^\dagger \; + \text{h.c.}\,.\end{aligned} \tag{4.38}$$

Note, that we allow for waveguide dependent pump frequencies $\omega_{p,j}$. To obtain the final output state from a down-conversion source, we have to integrate over time and the crystal length. This

yields the known generation unitary for a parametric down-conversion device [109]

$$\exp\left(-\frac{i}{\hbar}\int \hat{H}_{\mathrm{PDC}}\mathrm{d}t\right) = \exp\left(-\frac{i}{\hbar}\sum_{j=1}^{N}\sum_{k=1}^{N} \Gamma_j\overline{\mu^*_{jk}}\delta(\omega_{p,j}-(\omega_s+\omega_h))\right.$$
$$\left.\times\,\mathrm{sinc}\left[(\beta_p-(\kappa_{s,k}+\beta_h))\frac{L}{2}\right]\exp\left[-i(\beta_p-(\kappa_{s,k}+\beta_h))\frac{L}{2}\right]\hat{A}^\dagger_k\hat{b}^\dagger_j+\mathrm{h.c.}\right), \tag{4.39}$$

where the δ-distribution encodes the energy conservation in the process, while the sinc-function contains the momentum conservation. For simplicity, we ignore time-ordering effects and neglect the h.c.-part in the following discussion to simplify the notation.

To find the transformation matrix for a BosonSampling experiment, we have to connect the patterns of the herald photons with the sampling patterns. Therefore, we apply the back-transformation from the eigenmodes $\hat{A}_k$ to the waveguide basis, which we denote $\hat{a}_{j'}$[20]. This finally yields the unitary for the down-conversion state in the two-photon picture

$$\begin{aligned}|\Psi\rangle_{2\,\mathrm{photon}} &= \sum_{j,k}\sum_{j'=1}^{N}\Gamma_j\mu^*_{kj'}\overline{\mu^*_{jk}}\delta(\omega_{p,j}-(\omega_s+\omega_h))\\ &\qquad\times\mathrm{sinc}\left[(\beta_p-(\kappa_{s,k}+\beta_h))\frac{L}{2}\right]\exp\left[-i(\beta_p-(\kappa_{s,k}+\beta_h))\frac{L}{2}\right]\hat{a}^\dagger_{j'}\hat{b}^\dagger_j|0\rangle\\ &=:\sum_{j=1}^{N}\sum_{j'=1}^{N}T_{jj'}\hat{a}^\dagger_{j'}\hat{b}^\dagger_j|0\rangle\end{aligned} \tag{4.40}$$

where the matrix T is the desired BosonSampling transformation matrix that connects the heralding photons $\hat{b}_j$ to the sampling photons $\hat{a}_{j'}$ [236]. The transformation matrix $T_{j,j'}$ contains the linear properties of the array with the band-structure for the sampling photons $\kappa_{s,k}$ and the basis transformation to the eigenmode transformations $\mu^*_{kj'}$ and $\overline{\mu^*_{jk}}$. Additionally, the non-linear properties of the array are encoded through the energy conservation $\delta(\omega_{p,j}-(\omega_s+\omega_h))$ and the phase-matching function $\mathrm{sinc}\left[(\beta_p-(\kappa_{s,k}+\beta_h))\frac{L}{2}\right]\exp\left[-i(\beta_p-(\kappa_{s,k}+\beta_h))\frac{L}{2}\right]$.

For BosonSampling, the description of the output state in the two-photon picture is not sufficient. In general, we want to consider many photons for this application. Using higher-order contributions, we can write the output state, as [236]

$$|\Psi\rangle_{\mathrm{out}} = \exp\left[-\frac{i}{\hbar}\int\hat{H}_{\mathrm{PDC}}\mathrm{d}t\right]|0\rangle = \sum_{n=0}^{\infty}\frac{1}{n!}\left(-\frac{i}{\hbar}\sum_{j=1}^{N}\sum_{j'=1}^{N}T_{jj'}\hat{a}^\dagger_{j'}\hat{b}^\dagger_j\right)^n|0\rangle\ . \tag{4.41}$$

To understand the effect of the heralding scheme in the system, consider the example of measuring a single herald photon $\hat{b}_j$ in mode 1 ($\hat{b}_1$) and another photon in mode 2 ($\hat{b}_2$). This configura-

[20] As coupling might have happened between the generation waveguide and the detection waveguide, we use a new label j' for this basis transformation.

tion selects the columns 1 and 2 from T for the sampling pattern

$$\langle 1_1, 1_2 | \Psi \rangle_{\text{out}} = \frac{1}{2} \left(\sum_{k=1}^{N} T_{1,k} \hat{a}_k^\dagger \right) \left(\sum_{l=1}^{N} T_{2,l} \hat{a}_l^\dagger \right) |0\rangle \tag{4.42}$$

and the probability to measure two $\hat{a}$ photons in the two modes k and l, is given by

$$P(1_k, 1_l) \propto |\text{Perm}(T_{S[12|kl]}))|^2 , \tag{4.43}$$

where $T_{S[12|kl]}$ is the sampled 2×2 submatrix. In terms of Scattershot BosonSampling, we interpret $T_{S[12|kl]}$ as $T_{S[\text{in}|\text{out}]}$, see figure 4.12(b).

Finally, we comment on the conditions to obtain a valid heralding procedure. The most important thing that we need to guarantee is that we reproducibly sample a unique row and column for each heralding and sampling pattern [236]. Considering equation (4.39), this necessitates a unique mapping from the heralded waveguides to the eigenmode, where a photon pair was created. To understand this condition, consider the following counter example. We pump two waveguides (i, j) of the array with the same pump frequency $\omega_{p,j} = \omega_p$. Then, the two pumped waveguides generate photon pairs in the same eigenmode of the array. However, as the two corresponding heralding photons will contribute to the same sampling pattern $\hat{a}$, it is not clear which sampling photon belongs to which generation event. As such, we cannot make a definite statement which columns of the matrix T have been sampled in this experiment. To eliminate this problem, we need to pump separate eigenmodes in different waveguides by adapting the pump frequency in the k-th waveguide to pump also the k-th eigenmode of the waveguide array. With this configuration, an ambiguous heralding event is not possible [236].

4.3.3 Complexity of the Transformation Matrix

To gain an idea about the computational complexity of our problem, we investigate the different contributions to the transformation matrix T first. As we have shown above, it comprises the basis transformation from waveguide to eigenmode basis, the phase-matching and energy conservation conditions together with the pump shape and the back transformation to the waveguide basis.

In this thesis, we consider a finite size waveguide array for which the basis transformation is given by [65]

$$\hat{A}_k = \sum_{j=1}^{N} \mu_{jk} \hat{a}_j = \sqrt{\frac{2}{N}} \sum_{j=1}^{N} \sin\left(\frac{jk\pi}{N+2} \right) \hat{a}_j , \tag{4.44}$$

as we have discussed in section 4.1. This real-valued transformation rule means that the transformation into the eigenmode basis μ_{jk} and the back transformation $\overline{\mu_{kj'}}$ are equivalent and the matrix T becomes symmetric [236].

The non-linear part of the matrix promises more complexity. We can select our pump frequencies for the different waveguides, such that
$\text{sinc}\left[(\beta_p - (\kappa_{s,k} + \beta_h))\frac{L}{2}\right] \exp\left[-i(\beta_p - (\kappa_{s,k} + \beta_h))\frac{L}{2}\right] \approx 1$ and therefore negligible. Then,

our final matrix can be decomposed in

$$T = \overline{\mu} \Gamma \mu \tag{4.45}$$

where Γ is a diagonal matrix that contains the intensity of the pump distribution and the corresponding phase for each waveguide input $\Gamma = \Gamma_0 \oplus_{j=1}^{N} e^{-i\phi_j}$. The matrices μ and $\overline{\mu}$ encode the basis transformations. If we now select a pump phase distribution according to the Haar measure (i.e. the phases are randomly chosen), the matrix T is also a Haar random unitary. This is due to the symmetry of the Haar group, which is invariant under unitary transformations [268, 269].

As such, the sampled matrix T fulfils the requirement for the approximate sampling condition, i.e. that it belongs to the Haar random group. Furthermore, it is even reconfigurable as we can change the pump phase distribution along the input waveguides [236]. However, if the unitary transformation does not fulfil the criteria to make exact sampling hard, there is no point in considering an approximate sampling problem. Indeed, the symmetry of the matrix already presents a problem for the complexity of exact sampling, as the complexity to sample Permanents from symmetric matrices is not finally answered. As such, the implemented matrix T might be too simple due to its symmetry.

4.3.4 Prospects for Experimental Implementation

The greatest challenge from an experimental point of view is to guarantee a valid heralding procedure. It demands that we pump separate eigenmodes in separate pump waveguides. However, this also places a restriction on the minimal spectral separation of the corresponding phase-matching conditions in frequency space. Consider the situation sketched in figure 4.14(a). There, we illustrate the phase-matching conditions for different eigenmodes in the frequency space spanned by the herald ω_h and sampling ω_s frequencies. The separation of the phase-matching conditions in this frequency space is indicated by $\Delta\omega_{\mathrm{EM}}$ and depends solely on the coupling strength of the sampling photons C_s. Additionally, due to the finite waveguide length, the phase-matching conditions have a finite width in frequency space, as defined by $\Delta\omega_{\mathrm{PM}}$. They are represented by the small Gaussian curves on top of the phase-matching conditions. To guarantee that we only pump one eigenmode per waveguide, we have to ensure that these phase-matching conditions do not overlap in frequency space [236]. Otherwise the same pump frequency could generate photon pairs in more than one eigenmode and we cannot be sure, which columns of T are sampled in an experiment.

We plot this situation for a realistic system in figure 4.14(b). We assume that the sampling photons passed the single-frequency filter and set $\omega_s = \omega_0$. Then we depict the spectral separation of the eigenmodes depending on the herald wavelength (for better intuition of the dimensions) in the upper panel. We inverted the the axes of the usual bandstructure plot, such that the typical cosine bandstructure for the array is tilted by 90°. We mark the spectral separation of the eigenmodes for the undisturbed waveguide (which coincides with the $k = N/2$ eigenmode, depicted in black). In the lower panel, we plot the corresponding phase-matching functions depending on the herald wavelength and associated the colour coding to the different eigenmodes of the system. From this figure, we already find a finite overlap between adjacent phase-matching conditions. Especially for the outer phase-matching functions this overlap increases drastically,

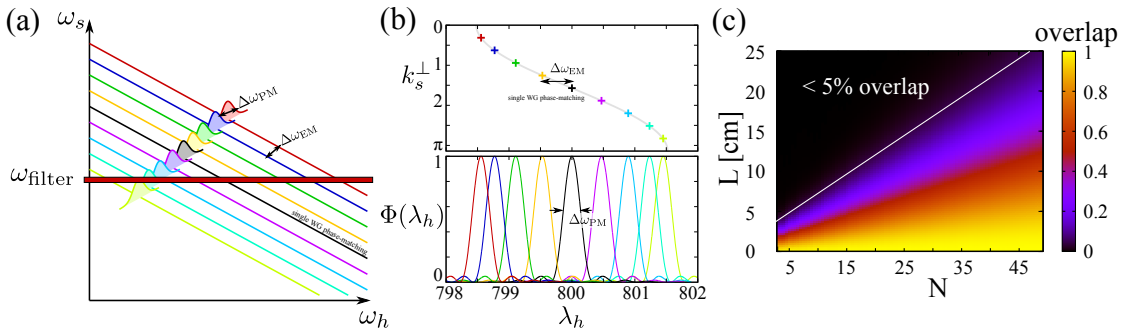

Figure 4.14 – Distance of phase-matching curves in the waveguide array down-conversion [236]. In (a), we depict the condition for a valid heralding procedure, i.e. the phase-matching curves must not overlap. To investigate this situation for a realistic waveguide array [21], in (b) we plot the spectral separation of different eigenmodes (upper panel) and the corresponding widths of the phase-matching (lower panel). To quantify the resulting overlap between adjacent phase-matching conditions, we vary the number of waveguides in the array and its length in (c). For large arrays and short waveguides the overlap approaches unity and reduces for long arrays and few waveguides. The white line denotes the parameter combinations, where the overlap equals $5\,\%$.

as the eigenmode separation decreases due to the cosine shape.

In figure 4.14(c), we plot the overlap of the phase-matching functions between the central $k = N/2$ and the adjacent $k = N/2 + 1$ eigenmodes, which is the best case available. The two main parameters for determining the overlap are the length of the waveguides (they determine $\Delta\omega_{\text{PM}}$) and the number of waveguides N (determines $\Delta\omega_{\text{EM}}$ for a fixed coupling constant). For this calculation, we do not consider the full description of the phase-matching function, but use the gaussian approximation [271]

$$\text{sinc}(x) \approx \exp(-0.193x^2)\,. \tag{4.46}$$

The separation between the eigenmodes becomes smaller for many waveguides, as we have to fit more eigenmodes onto the cosine bandstructure and the overlap between the phase-matching functions increases for large arrays [236]. Contrarily, the width of the phase-matching functions decreases with longer waveguides ($\Delta\omega_{\text{PM}} \propto 1/L$), the overlap decreases for long arrays. In white, we highlighted the $5\,\%$ isoline, which we can use as a maximally tolerable overlap between the two central phase-matching conditions. As we are limited with the available waveguide size for an experimental implementation in $LiNbO_3$ to approximately $L_{\text{max}} \approx 10\,\text{cm}$, we are limited to approximately 15-20 waveguides in an experimental implementation of our scheme. Although this means that our system does not provide the necessary scalablility to high photon numbers for an experiment, it can provide a simple platform to study BosonSampling using non-linear processes. Furthermore, one might consider other material systems for the im-

[21] Simulation parameters: $C_s = 350\,\text{m}^{-1}$ [70], $N = 9$, $L = 0.04\,\text{cm}$, refractive indices: [270]

plementation of non-linear waveguide arrays that are not subject to such stringent wafer size requirements, such as silica. However, they do not possess the necessary $\chi^{(2)}$-non-linearity, that is needed for the parametric down-conversion process. Then, less efficient $\chi^{(3)}$-processes, such as four-wave mixing have to be considered and the results of this section have to be generalised [272].

Summary

In summary, we mapped the non-linear system of waveguide arrays to the context of BosonSampling experiments. We derived the transformation matrix that connects the spatial properties of the herald to the signal photons, which is a completely new approach in quantum information. As such, our result may not only be applicable in the context of non-linear waveguide arrays, but also provide new insights into the quantum states of other systems. Furthermore, we analysed the available complexity that we encode in the transformation matrix. Finally, we investigated the prospects for the experimental implementation of such a scheme and found that we are limited by the available length of waveguides for an implementation in $LiNbO_3$. While this system is not intrinsically scalable due to the interplay of waveguide number and necessary waveguide length, other material platforms such as silica might provide a solution with $\chi^{(3)}$-processes, such as four-wave mixing which is beyond the scope of this thesis. Nevertheless, our non-linear waveguide array sparked research to investigate BosonSampling schemes in the regime of non-linear systems, such as *Driven* BosonSampling [273] that is not part of this thesis, as well as the protocol of *Gaussian* BosonSampling, which we consider in the final section of this thesis.

4.4 Gaussian BosonSampling

In the previous section, we mapped a Scattershot BosonSampling problem to the system of non-linear waveguide arrays. While this is interesting both from a theoretical and experimental point of view, it does not answer the fundamental theoretical question to the computational complexity from a general Gaussian state since the experiment is performed with heralded single photons. Here, we now strive to construct the most general problem of BosonSampling and answer this question [274, 275]. We first derive a general matrix relation that relates general Gaussian input states to the probability of measuring a specific single photon output pattern $\overline{n}$ after a linear transformation. From this result, we construct a BosonSampling problem that takes Gaussian input states and show that it retains the complexity of the original scheme by Aaronson and Arkhipov. Finally, we compare our scheme to the most efficient known single photon BosonSampling scheme (Scattershot BosonSampling [243]) and show that our scheme saves *quadratically* on the number of needed input states. As such, our scheme places the experimental investigation of quantum supremacy into reach of current technology [274, 275].

4.4.1 Photo-count Probabilities from a Gaussian State

Before we can construct a BosonSampling scheme akin to Aaronson and Arkhipov [7], we have to find a closed-formula description for the probability to measure a specific photon pattern $\overline{n}$ from a Gaussian state, akin to the results of the Scheel paper [252]. In this section, we show that this probability is related to the Hafnian [276, 277], a matrix function that is more general than the Permanent.

To do so, we begin with the phase space representation, see chapter 1, (similar to the approaches used in [266, 278]) for the probability to measure $\overline{n}$

$$\mathrm{P}(\overline{n}) = \pi^M \int \prod_{j=1}^{M} \mathrm{d}\alpha_j \mathrm{d}\alpha_j^* Q_{\hat{\rho}}(\boldsymbol{\alpha}) P_{\overline{n}}(\boldsymbol{\alpha}) \tag{4.47}$$

with $Q_{\hat{\rho}}$ is the Q-function representation of the Gaussian state and $P_{\overline{n}}$ is the P-representation of the photon number measurement operator $\hat{\overline{n}} = \otimes_{j=1}^{M} \hat{n}_j$ to measure n photons in the j-th mode.

We characterise a Gaussian input state solely by its $2M \times 2M$ covariance matrix σ and a displacement vector d [279]

$$\sigma_{ij} = \frac{1}{2}\langle\{\hat{\zeta}_i, \hat{\zeta}_j\}\rangle - d_i d_j \quad d_j = \langle \hat{a}_j \rangle, \tag{4.48}$$

where $\hat{\zeta}$ run over all $\hat{a}_j, \hat{a}_j^\dagger$ and we assume $d = 0$. From the covariance matrix we can construct the Q-function of the state, which is given by the convolution of the corresponding Wigner function with another Gaussian function [227]

$$Q_{\hat{\rho}}(\alpha) = \frac{1}{|\pi\sigma_Q|} \exp\left[-\frac{1}{2}\alpha_\nu^t \sigma_Q^{-1} \alpha_\nu\right], \tag{4.49}$$

where we substituted $\sigma_Q = \sigma + \mathbb{I}_{2M}/2$ and use the vector representation for $\alpha_\nu = [\alpha_1, \alpha_2 ... \alpha_M, \alpha_1^*, \alpha_2^* ... \alpha_M^*]$. Note, that only the modes that include a detector at the output contribute to σ_Q. If we do not measure a mode at all, the corresponding rows and columns are removed.

With the P-function of the n-photon Fock state

$$P_n(\alpha) = \frac{e^{|\alpha|^2}}{n!} \left(\frac{\partial^2}{\partial\alpha\partial\alpha^*}\right)^n \delta(\alpha)\delta(\alpha^*) \tag{4.50}$$

we evaluate equation (4.47)

$$\mathrm{P}(\overline{n}) = \frac{1}{\overline{n}!\sqrt{|\sigma_Q|}} \prod_{j=1}^{M} \left(\frac{\partial^2}{\partial\alpha\partial\alpha^*}\right)^{n_j} \exp\left[\frac{1}{2}\alpha_\nu^t \mathbf{A} \alpha_\nu\right]\Bigg|_{\alpha=0}, \tag{4.51}$$

with

$$\mathbf{A} = \begin{pmatrix} 0 & \mathbb{I}_M \\ \mathbb{I}_M & 0 \end{pmatrix} \left[\mathbb{I}_{2M} - \sigma_Q^{-1}\right]. \tag{4.52}$$

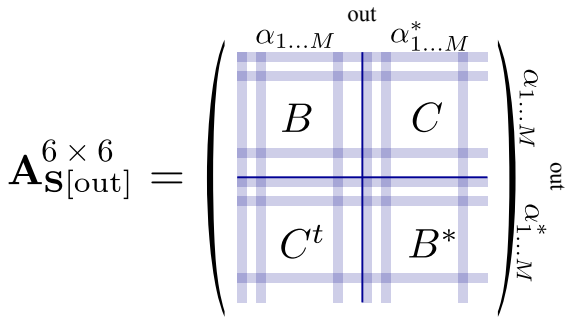

Figure 4.15 – Construction of the sampled submatrix $\mathbf{A_S}$ from the overall matrix $\mathbf{A}$ for a three photon pattern [274, 275]. Contrary to the single photon BosonSampling schemes, our matrix entries are only selected by the measured output photon pattern. Due to the symmetry of the problem in phase-space, we have a pattern in the selection of the entries.

To further evaluate equation (4.50), we use Faà di Bruno's formula [280] to calculate the derivatives. We restrict ourselves to measuring either $n_j = \{0, 1\}$ photons in mode j as for the original BosonSampling proposal. For N photons in total that means we have $2N$ remaining derivatives. Expanding the derivatives yields [281]

$$\frac{\partial^{2N} e^{\frac{1}{2}\alpha_\nu^t \mathbf{A}\alpha_\nu}}{\prod_i^N \partial\alpha_i \partial\alpha_i^*} = e^{\frac{1}{2}\alpha_\nu^t \mathbf{A}\alpha_\nu} \sum_\pi \prod_{\chi\in\pi} \frac{\partial^{|\chi|}\alpha_\nu^t \mathbf{A}\alpha_\nu}{\prod_{i\in\chi}\partial\alpha_i^{(*)}}\,, \tag{4.53}$$

where the sum runs over all partitions π over the possible combinations of $\{\alpha_i^{(*)} = \alpha_i, \alpha_i^*\}$ and the product over all the subgroups of π. An example term for two photons in modes 1 and 2 is $\{\alpha_1\}, \{\alpha_1^*, \alpha_2, \alpha_2^*\}$ and has the following term in the summation

$$\frac{1}{4}\frac{\partial\alpha_\nu^t \mathbf{A}\alpha_\nu}{\partial\alpha_1}\frac{\partial^3\alpha_\nu^t \mathbf{A}\alpha_\nu}{\partial\alpha_1^*\partial\alpha_2\partial\alpha_2^*}\,. \tag{4.54}$$

Calculating the derivatives of α_ν, we find that the exponent has a quadratic dependency $\alpha_\nu^t\mathbf{A}\alpha_\nu$ and all derivatives of third order or higher vanish. Furthermore, the first order derivatives also vanish as we evaluate equation (4.50) at $\alpha = 0$. As such, the final expansion of the $2N$ derivatives can be sorted into N sets of size 2, the perfect matching permutations (PMP). As an example on how to construct the $(2N-1)!!$ PMP[22] for $2N$ indices, we consider the numbers $1, 2, 3, 4$ and gain 3 possible PMPs

$$\{12\}\{34\}, \{13\}\{24\}, \{14\}\{23\}\,. \tag{4.55}$$

[22] $(.)!!$ denotes the double factorial.

Using this construct, we write down the final result for equation (4.50) [274, 275]

$$\mathrm{P}(\overline{n}) = \frac{1}{\overline{n}!\sqrt{|\sigma_Q|}} \sum_{\mu \in PMP} \prod_{j=1}^{N} \mathbf{A}_{\mathbf{S}_{\mu(2j-1),\mu(2j)}} , \tag{4.56}$$

where we stored the indices of the $2N$ derivatives in the vector μ. As it happens, Caianiello [276, 277] defined this sum over the PMP as the Hafnian of a submatrix $\mathbf{A_S}$, which is defined by the rows and columns that are selected by the detection events of $\overline{n}$

$$\mathrm{P}(\overline{n}) = \frac{1}{\overline{n}!\sqrt{|\sigma_Q|}} \mathrm{Haf}(\mathbf{A_S}) . \tag{4.57}$$

This closed-formula expression relates the photon counting probability for a specific detection pattern to a well-defined matrix function, the Hafnian [276, 277]. With this approach, we can include the covariance matrix of any Gaussian state, including squeezed ($B \neq 0$) and thermal ($C \neq 0$) states, compare figure 4.15, as well as all combinations.

One main advantage of our approach is that we can absorb loss and noise dynamics directly into the matrix $\mathbf{A}$ as they are Gaussian operations. As such, they do not deteriorate our statistics, but only influence the shape of the matrix $\mathbf{A_S}$. Especially for the case of loss, we note that squeezed contributions are transferred to thermal contributions and we move from a matrix with only squeezing contributions ($B \neq 0$) to a matrix with squeezing and thermal contributions, ($B \neq 0$) and ($C \neq 0$), in the presence of loss. However, we have to leave open the question on how much loss we may tolerate, as sampling from thermal states only ($B = 0$ and $C \neq 0$) is not in #P but $\mathsf{BPP}^{\mathsf{NP}}$ [266], which is not as hard.

As in the paper by Scheel [252], our photon counting probability depends on a submatrix $\mathbf{A_S}$. To clarify the definition of the submatrix for our case, we sketch the construction of $\mathbf{A_S}$ in figure 4.15. The full matrix of dimension $2M \times 2M$ can be divided into four blocks of dimension $M \times M$ according to the combination of phase space variables α and α^*. Due to the symmetry of the phase space construction, we find correlations between the single blocks. The matrix is symmetric, as α_i, α_j^* has the same entry as α_j^*, α_i, i.e. the lower anti-diagonal block C^t has to be the transposed matrix of the upper anti-diagonal block C. Similarly the diagonal blocks are related, the lower diagonal block is the conjugated upper diagonal block. Then, an N photon detection event selects a $2N \times 2N$ submatrix $\mathbf{A_S}$ where a click in mode j selects the columns j and $j + M$ and the corresponding rows j and $j + M$.

Extending this probability to the case where we measure more than one photon in one mode, we still retain equation (4.57), however we have to modify the sampled submatrix [275]. Consider a single spatial mode as an example. Then, the matrix $\mathbf{A}$ is of dimension 2×2

$$\mathbf{A} = \begin{pmatrix} A_{11} & A_{12} \\ A_{21} & A_{22} \end{pmatrix} . \tag{4.58}$$

If we detect two photons in the same mode, we have to evaluate

$$\mathrm{P}(n_1 = 2) = \frac{1}{\sqrt{|\sigma_Q|}} \frac{1}{2!} \frac{\partial^2}{\partial \alpha_1^2} \frac{\partial^2}{\partial \alpha_1^{*2}} \, e^{\frac{1}{2}\alpha_\nu^t \mathbf{A} \alpha_\nu} \Big|_{\alpha=0} \, . \tag{4.59}$$

We can circumvent this problem by "inventing" a second mode and repeating the rows and columns of $\mathbf{A}$, i.e.

$$\mathrm{P}(n_1 = 1, n_2 = 1) = \frac{1}{2!\sqrt{|\sigma_Q|}} \frac{\partial}{\partial \alpha_1} \frac{\partial}{\partial \alpha_1^*} \frac{\partial}{\partial \alpha_2} \frac{\partial}{\partial \alpha_2^*} \, e^{\frac{1}{2}\alpha_\nu^t \mathbf{A}' \alpha_\nu} \Big|_{\alpha=0} \, , \tag{4.60}$$

with $\mathbf{A}'$ as a new matrix that is given by

$$\mathbf{A}' = \begin{pmatrix} A'_{11} & A'_{12} & A'_{13} & A'_{14} \\ A'_{21} & A'_{22} & A'_{23} & A'_{24} \\ A'_{31} & A'_{32} & A'_{33} & A'_{34} \\ A'_{41} & A'_{42} & A'_{43} & A'_{44} \end{pmatrix} = \begin{pmatrix} A_{11} & A_{12} & A_{11} & A_{12} \\ A_{21} & A_{22} & A_{21} & A_{22} \\ A_{11} & A_{12} & A_{11} & A_{12} \\ A_{21} & A_{22} & A_{21} & A_{22} \end{pmatrix} \, . \tag{4.61}$$

Naturally, $\mathbf{A}'$ cannot be related to a proper quantum covariance matrix. It is just a mathematical tool to express the higher order photon detection events in the Hafnian form [275].

With this expression, we now construct a BosonSampling problem analogously to the Aaronson and Arkhipov scheme, however with Gaussian states. In this thesis, we will consider squeezed states only, which means that the anti-diagonal blocks of $\mathbf{A}$ vanish, i.e. $C = 0$.

4.4.2 Construction of Gaussian BosonSampling

The main idea behind the construction of the original BosonSampling protocol was to find a system which is classically hard to solve. In the original scheme, this argument relied on the fact that the calculation of the Permanent belongs to the #P complexity class. As our scheme relies on the Hafnian, we have to comment on the complexity of this function.

The Hafnian is a more general function than the Permanent. Comparing the definitions of the Permanent [equation (4.35)] and the Hafnian [equation (4.56)], it becomes clear that whereas the the Permanent only counts the perfect matchings on a bipartite graph [282] (encoded in the summation over P_N with the indices $i, \sigma(i)$), the Hafnian counts all perfect matchings on a general graph (encoded in the indices $\mu(2j-1), \mu(2j)$). As such, it is trivial to see from a computational point of view to see that the Hafnian is at least as complex as the Permanent[23]. Furthermore, we can re-write the Permanent as the Hafnian of a special matrix [282]

$$\mathrm{Perm}(G) = \mathrm{Haf}\left[\begin{pmatrix} 0 & G \\ G^t & 0 \end{pmatrix} \right] \, . \tag{4.62}$$

As such, if we *had* an efficient algorithm to calculate the Hafnian, we could just dial up the matrix $\begin{pmatrix} 0 & G \\ G^t & 0 \end{pmatrix}$ and have an efficient algorithm for the Permanent. This argument also holds true

[23] Thanks to Andreas Björklund for pointing this out.

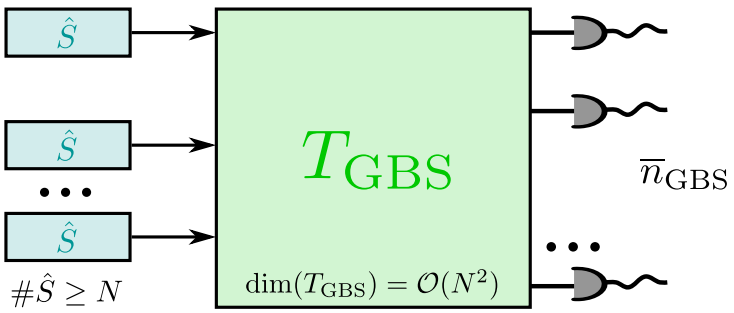

Figure 4.16 – Schematic of a Gaussian BosonSampling computer [274]. A Gaussian BosonSampling computer takes at least N single mode squeezed states at the input of an M-dimensional Haar random unitary transformation T_{GBS}. At the output, the state is measured in the photon number basis, where the size of the interferometer ($M = \dim(T_{\mathrm{GBS}}) = \mathcal{O}(N^2)$) guarantees that only single photons are measured.

for the approximation proofs of the Permanent, at least for this specific matrix shape. Furthermore, we can decompose the Hafnian of a general matrix into a sum over Hafnians, a Permanent and other terms

$$\begin{aligned} \mathrm{Haf}(R) &= \mathrm{Haf}\begin{pmatrix} A & B \\ B^t & C \end{pmatrix} \\ &= \mathrm{Haf}(A)\mathrm{Haf}(C) + \mathrm{Perm}(B) + \text{other terms}\,, \end{aligned} \tag{4.63}$$

where we can still decompose the Hafnians of A and C into smaller submatrices and the other terms are given by Hafnians over submatrices of R. As such, there exists strong evidence that a multiplicative approximation of the Hafnian of a general matrix is in #P. This evidence fulfils the criteria to show that exact sampling from a Gaussian state[24] is in the same complexity class as the scheme from Aaronson and Arkhipov.

With this argument, we proceed to construct a BosonSampling scheme based on Gaussian states, as depicted in figure 4.16. We connect an array of single mode squeezers to the inputs of an M-dimensional interferometer T_{GBS}, which is represented by a Haar random unitary to keep the technical conditions for the approximate sampling proof intact. At the output, we measure all M modes with single photon detectors and record all clicks [274, 275].

Then, we can describe the effect of the squeezing on our system by the matrix

$$S = \begin{pmatrix} \bigoplus_{j=1}^{M} \mathrm{cosh}r_j & \bigoplus_{j=1}^{M} \mathrm{sinh}r_j \\ \bigoplus_{j=1}^{M} \mathrm{sinh}r_j & \bigoplus_{j=1}^{M} \mathrm{cosh}r_j \end{pmatrix}\,, \tag{4.64}$$

where r_j is the squeezing parameter in the j-th mode and $\bigoplus_{j=1}^{M} A_j = \mathrm{diag}(A_1, A_2, ...A_M)$ is a

[24] This is a different concept than in Scattershot BosonSampling, where we sample from heralded single photons generated via Gaussian states.

direct sum of block matrices. We write down the covariance matrix of the output state as

$$\sigma = \frac{1}{2}\begin{pmatrix} T_{\mathrm{GBS}} & 0 \\ 0 & T^*_{\mathrm{GBS}} \end{pmatrix} SS^\dagger \begin{pmatrix} T^\dagger_{\mathrm{GBS}} & 0 \\ 0 & T^t_{\mathrm{GBS}} \end{pmatrix} \tag{4.65}$$

and arrive at $A = B \oplus B^*$, with

$$B = T_{\mathrm{GBS}} \left(\bigoplus_{j=1}^{M} \tanh r_j \right) T^t_{\mathrm{GBS}} \,. \tag{4.66}$$

Here, we used that there are no thermal contributions to our state and therefore the anti-diagonal blocks are $C = 0$. With this expression, we simplify equation (4.57) to

$$\mathrm{P}(\overline{n}) = \frac{1}{\sqrt{|\sigma_Q|}} |\mathrm{Haf}(B_S)|^2 \,, \tag{4.67}$$

where we restrict ourselves to the measurement of $\{0, 1\}$ photons per mode. The construction of the submatrix B_S follows the construction of $\mathbf{A_S}$ of equation (4.57). However, this formula is not enough to fulfil all the criteria of a valid BosonSampling experiment. Below, we comment on different aspects of our scheme.

Approximate Gaussian BosonSampling

To show that approximate Gaussian BosonSampling up to an additive error is computationally hard, we have to show that a classical adversary may not corrupt a large fraction of the results from a Gaussian BosonSampling computer. In the Aaranson-Arkhipov proof, they use randomised sampling to hide the interesting probability in the randomised output of the BosonSampling computer. The technical claim that they have to fulfil is that the sampled entries are within variation distance of independent and identically distributed (i.i.d.) Gaussian matrices. To guarantee this condition, they use a transformation matrix according to the Haar measure and sample only with $N \approx \mathcal{O}(\sqrt{M})$ photons. Then, the entries are distributed according to the complex normal distribution and in variation distance to an i.i.d. Gaussian matrix.

In our scheme, we do not sample T directly, but submatrices of B. If we assume equal squeezing parameters for all modes $r_j = r$, we can simplify $B = \tanh r \, TT^t$, where TT^t is from the circular orthogonal ensemble of random matrices [283, 284]. For this class of matrices it is known that a sufficiently small subset [$N = \mathcal{O}(\sqrt{M})$] is in variation distance to a product of i.i.d. Gaussian matrices [285].

Consider now a classical adversary that wants to corrupt our BosonSampling experiment. We believe that our BosonSampling computer is a "robust" one, i.e. a fraction of ϵ of the results might be corrupted by the adversary[25]. However, as the measured output pattern is random in the sense that we cannot anticipate which pattern we measure next, we and a possible adversary do not know which probability (and therefore which submatrix) we will be interested in. Then,

[25] As the Hafnian is a more general function than the Permanent, it seems justified that it also allows for robust encoding.

if the adversary could approximate a large fraction of the probabilities to corrupt our result this would contradict the assumed robust encoding. As such a classical adversary must be able to approximate the problem, which implies a collapse of the polynomial hierarchy. Since the approximation proof of Aaronson and Arkhipov only refers to the random sampling and the hiding procedure of the sampled matrices, it is largely independent from the use of the Permanent and is applicable to the situation at hand and we conclude that approximate Gaussian Boson Sampling is also in $\mathsf{FBPP}^{\mathsf{NP}^{\mathcal{O}}}$. The only problem that we may encounter is the symmetric sampling of B (compare figure 4.15). However, since the Hafnian only considers the entries above the main diagonal of B [277] and the randomness of B, we believe that the used sampling technique is random enough.

As Aaronson and Arkhipov, we have to leave the final proof that approximate Gaussian BosonSampling is in #P open. We can only conjecture that the complexity arguments of the *Permanent-of-Gaussians Conjecture* and the *Permanent-Anti-Concentration Conjecture* hold true for the Hafnians [274]. We believe that these two conjectures are justified as the Hafnian is a more general function than the Permanent.

Dilute BosonSampling

For our scheme, we require that we only measure $\{0, 1\}$ photons at the output in order to avoid the repetition of rows and columns in the B_S-matrix [275]. This has the simple reason that the increased number of photons does not increase the complexity of this problem. As such, we show that the probability to measure more than one photon at the output is sufficiently low. Consider N single mode squeezers at the input that produce N photons on average. Then, if we consider an $M = \mathcal{O}(N^2)$ sized interferometer, we retain on average $\frac{1}{N}$ photons per mode at the output. If we consider a single mode subsystem (and trace out over all others, we retain a thermal state with mean photon number $\langle n \rangle \approx 1/N$. From the photon number statistics of a thermal state, we calculate the ratio between the probabilities of two clicks versus one click and find that

$$\frac{\mathrm{P}(n_j = 2)}{\mathrm{P}(n_j = 1)} \approx 0.1\,, \tag{4.68}$$

which is sufficient to fulfil the condition.

Valid BosonSampling Events

For experiments with Fock states, as the original BosonSampling scheme from Aaronson and Arkhipov or the Scattershot BosonSampling scheme, a fixed number of photons N enters and exits the linear interferometer. Therefore, these experiments sample the pattern probabilities p_j from the family of photon patterns with N photons $\{P_N\}$

$$\{p_1, p_2, ...p_{C_N}\}_N = \{P_N\}\,, \tag{4.69}$$

where $C_N = \binom{M}{N}$ is the number of possible photon patterns of N single photons in M modes. As the photons will leave the interferometer in any of these configurations, the probabilities have to add up to unity, i.e. $\sum_j p_j = 1$. For our scheme, this condition does not hold true anymore

[274]. A single mode squeezed state may *on average* create N photons, but with a finite variance according to its photon number statistics. Therefore, we sample from photon pattern families with different photon numbers, i.e.

$$\{\{p_0 = |\sigma_Q|\}_0, \{p_1, p_2, ..., p_{C_1}\}_1, ..., \{p_1, p_2, ..., p_{C_N}\}_N, ...\} = \{\{P_0\}, \{P_1\}, ..., \{P_N\}, ...\} \tag{4.70}$$

with $\sum_N \{P_N\} = 1$. In principle this summation over photon number patterns runs from $N \in [0, \infty)$. However, in certain circumstances we might have to discard events as the complexity of the BosonSampling experiment is in question. Especially, if $N \geq \sqrt{M}$, the complexity of the problem is an open question, as the entries of the sampled submatrix may not be i.i.d. anymore.

Optimising Input Events

In order to optimise the input states and the complexity for an experimental implementation of our BosonSampling scheme, we have to consider the photon pair event (PPE) probabilities for photons from multiple (in our case K) single mode squeezed states.

Since the number of single mode squeezers at the input is directly absorbed in B, the overall complexity of the BosonSampling scheme depends on the number of pumped input modes [274, 275]. If we pump K of our M input modes, B is a matrix of rank K (due to the diagonal squeezing matrix). Since the matrix rank determines the complexity of the Permanent [286, 287], we can assume a similar result for the Hafnian. Then, we have to pump at least $K = N$ input modes with single mode squeezed states to saturate the possible complexity of our N photon experiment in $M = N^2$ modes. Therefore, we require that at least $K \geq N$ modes are pumped at the input of the transformation matrix.

With this information, we can now adapt the operation regime of the squeezers at the input to generate N PPEs. The probability to obtain such an event is determined by the negative binomial distribution [288]

$$\begin{aligned} P_K(N) &= \binom{K/2 + N - 1}{N} \mathrm{sech}^K(r) \tanh^{2N}(r) \\ &= \frac{\Gamma(K/2 + N)}{\Gamma(K/2) N!} \mathrm{sech}^K(r) \tanh^{2N}(r) \end{aligned} \tag{4.71}$$

for N PPEs from K single mode squeezers. This curve is plotted in figure 4.17 for $K = 14$ single mode squeezed states with squeezing parameters $r_j = r = 0.8814$. The average number of photons per squeezer is $\langle n \rangle \approx 1$. Therefore, for the complete distribution, we find a mean photon number of $\langle n \rangle = K \sinh^2(r) \approx 14$ and the modal number is $(K-1)\sinh^2(r) \approx 13$.

To estimate the optimal number of photons for our BosonSampling experiment, we have to trade between too few photons (not difficult to simulate) and too many photons (complexity of the problem not known). In the case we consider here, we assume an interferometer with $M = 14^2 = 196$ modes and can therefore retain all events up to $N = 7$ PPEs from our squeezing distribution (highlighted in green). A good estimate for a classically hard to solve problem would be an implementation with around 10 photons, so the interesting target range would only start at around $N = 5$ PPEs. The uninteresting regions are shaded in grey.

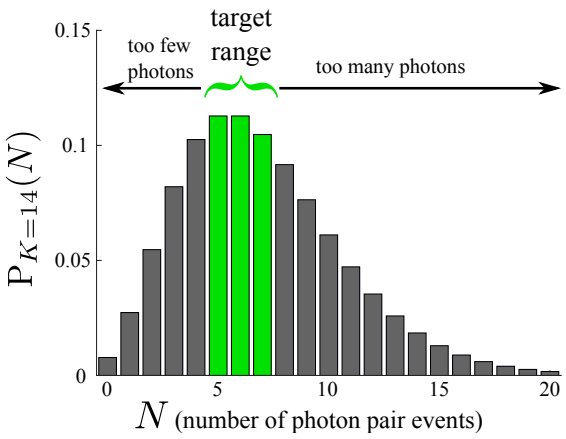

Figure 4.17 – Probability distribution to generate N photon pair events from $K = 14$ single mode squeezers with squeezing parameter $r = 0.8814$ [275]. In the $14^2 = 196$ modes of our system, we can retain 10-14 photons for a "useful" BosonSampling experiment. As the mean photon number per single mode squeezer is $\langle n \rangle \approx 1$ the pump power is much higher than for the single photon experiments.

In general, we can perform our Gaussian BosonSampling scheme in two regimes [274, 275]. Either, we decide to retain only a fixed photon number (i.e. $2N$) and choose the squeezing parameter such that the modal number of the distribution obeys $N = (K-1)\sinh^2(r)$. In the other regime, we consider a band of possible photon numbers (e.g. the highlighted band in figure 4.17), that saturates the complexity of the problem. In this case, the squeezing parameter is slightly different, such that each single mode squeezer generates $\langle n \rangle \approx 1$ on average.

4.4.3 Relation to Scattershot BosonSampling

The most general BosonSampling scheme up to now was Scattershot BosonSampling. In this section, we show that our Gaussian BosonSampling scheme is a more general problem than Scattershot BosonSampling, which is only a very restricted subset. To do so, we first express the Scattershot scheme in terms of our proposal. Consider the sketch in figure 4.18. If we regard only the outer structure, we recognise the single mode squeezed inputs, a large green unitary T_{GBS} and a detection unit as in Gaussian BosonSampling. However, in order to reproduce the Scattershot scheme, we have to choose a special T_{GBS} and introduce a specific structure to our general matrix. First, we have to specify the first layer of our transformation unitary. While we use single-mode squeezed states in Gaussian BosonSampling, we need two-mode squeezed states for the Scattershot scheme. As such, we begin with $2M$ single-mode squeezed states at the beginning and pass them pairwise through an array of phase-shifters and beam splitters encoded with the unitaries

$$U_{\mathrm{PS}} = \begin{pmatrix} 1 & 0 \\ 0 & i \end{pmatrix} \quad U_{\mathrm{BS}} = \frac{1}{\sqrt{2}} \begin{pmatrix} 1 & 1 \\ -1 & 1 \end{pmatrix} . \tag{4.72}$$

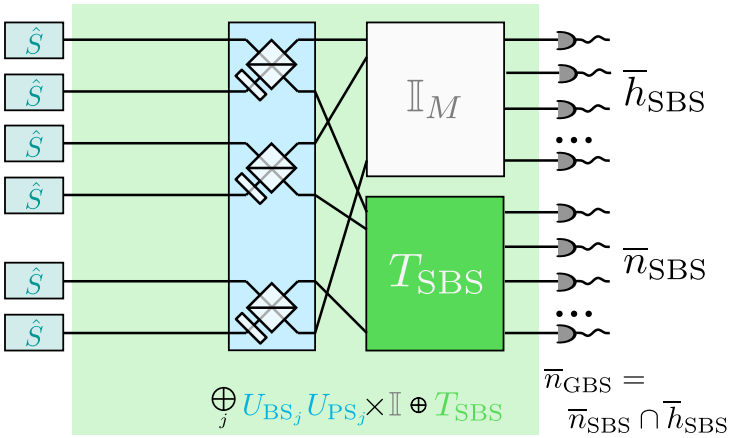

Figure 4.18 – Interpretation of Scattershot BosonSampling in terms of Gaussian BosonSampling [275]. In Gaussian BosonSampling, single-mode squeezers generate the photons and enter a general transformation matrix T_{GBS}. To map this to Scattershot BosonSampling, we have to implement a specific matrix structure for T_{GBS}. We transform the single-mode squeezers to the two-mode squeezers of Scattershot BosonSampling by inserting an array of phase-shifters U_{PS} and beam splitters U_{BS}. Then, we implement a special transformation matrix that contains only the identity in the upper half and a Haar random matrix in the lower half. Then, the overall transformation matrix is given by $T_{\mathrm{GBS}} = \oplus_j U_{\mathrm{BS}_j} U_{\mathrm{PS}_j} \times \mathbb{I}_M \oplus T_{\mathrm{SBS}_2 M}$. While we can retain all patterns in Gaussian BosonSampling, we have to select specific heralding patterns $\overline{h}$ for a valid Scattershot BosonSampling experiment.

After this transformation, our photons enter a very specific type of interferometer. The upper half of the photons in figure 4.18 enter an identity transformation of dimension M ($\mathbb{I}_M$) and pass on directly to the detection unit. The other half enters a Haar random unitary transformation T_{SBS}, also of dimension M, before they enter the detection setup.

In total, we can therefore encapsulate the ingredients of a Scattershot BosonSampling experiment into a specific shape of Gaussian BosonSampling interferometer [275]

$$T_{\mathrm{GBS}} = \mathbb{I}_M \oplus T_{\mathrm{SBS}} \times \oplus_j U_{\mathrm{BS}_j} U_{\mathrm{PS}_j} \,. \tag{4.73}$$

Due to the identity transformation in the upper half of the scheme, we have to reduce the squeezing parameter to perform Scattershot BosonSampling. While in our case, *all* photons are on average distributed over *all* modes equally (as guaranteed by the Haar random transformation), the identity prohibits a mixing of the heralding photons. As such, in order to prevent higher order photon detection events in the heralding arm, the squeezing parameter has to be significantly lower (usually around an order of magnitude). Finally, we detect a combined photon pattern $\overline{h} \cap \overline{n}$ of the heralding $\overline{h}$ and the sampling $\overline{n}$ photons. Then, the probability for a valid

Scattershot BosonSampling experiment is given by [275]

$$\mathrm{P}_{\mathrm{SBS}}(\overline{n}) = \mathrm{P}(\overline{n}|\overline{h}) = \frac{\mathrm{P}_{\mathrm{GBS}}(\overline{n} \cap \overline{h})}{\mathrm{P}(\overline{h})}\,, \tag{4.74}$$

where we have related the probability to generate a Scattershot event to the probability of a Gaussian BosonSampling event via Bayes' theorem. We find the probability to generate a valid heralding event in the denominator, as we have to consider that a valid Scattershot experiment only happens when we find a valid heralding event of N single photons in the heralding detectors.

While we have shown the relation between Scattershot BosonSampling and our scheme already by relating the pattern probabilities to each other, we can also use a more formal proof using the matrix relations of the systems. We begin with the Scattershot experiment, where we pump every mode of a Haar random interferometer with one arm of M two mode squeezed states with the same squeezing parameter $r_j = r$. Then, the probability to measure a specific combination of heralding $\overline{h}$ and sampling $\overline{n}$ pattern is [275]

$$\mathrm{P}_{\mathrm{SBS}}(\overline{n}|\overline{h}) = \frac{|\mathrm{Perm}(T_S)|^2}{\overline{n}!\,\overline{h}!} = \frac{\mathrm{Perm}(T_S)\mathrm{Perm}(T_S^*)}{\overline{n}!\,\overline{h}!}\,, \tag{4.75}$$

where T_S is again the submatrix that is sampled by the photons.

In order to map this probability to the Gaussian BosonSampling scheme, we now have to consider the Scattershot scheme in terms of covariance matrices. The output state of a Scattershot interferometer has a covariance matrix of the form

$$\sigma = \frac{1}{2}(\mathbb{I} \otimes T_{\mathrm{SBS}} \otimes \mathbb{I} \otimes T_{\mathrm{SBS}}^*) S_{\mathrm{TM}} S_{\mathrm{TM}}^\dagger (\mathbb{I} \otimes T_{\mathrm{SBS}} \otimes \mathbb{I} \otimes T_{\mathrm{SBS}}^*)^\dagger\,, \tag{4.76}$$

where

$$S_{\mathrm{TM}} = \left(\begin{array}{cc|cc} \multicolumn{2}{c|}{\multirow{2}{*}{$\cosh(r)\,\mathbb{I}_{2M}$}} & 0_M & \sinh(r)\,\mathbb{I}_M \\ & & \sinh(r)\,\mathbb{I}_M & 0_M \\ \hline 0_M & \sinh(r)\,\mathbb{I}_M & \multicolumn{2}{c}{\multirow{2}{*}{$\cosh(r)\,\mathbb{I}_{2M}$}} \\ \sinh(r)\,\mathbb{I}_M & 0_M & & \end{array}\right) \tag{4.77}$$

encodes the operation of the two mode squeezers[26]. The ordering of the modes in this case is $[\hat{a}_1, ...\hat{a}_M, \hat{b}_1, ..., \hat{b}_M, \hat{a}_1^\dagger, ...\hat{a}_M^\dagger, \hat{b}_1^\dagger, ..., \hat{b}_M^\dagger]$, where $\hat{a}$ denote the M herald modes and $\hat{b}$ denote the other M sampling modes.

Coming from the other side, we know the that the probability for Gaussian BosonSampling in this scenario is [275]

$$\mathrm{P}_{\mathrm{GBS}}(\overline{n} \cap \overline{h}) = \frac{\mathrm{Haf}(A_S)}{\overline{n}!\,\overline{h}!\sqrt{|\sigma_Q|}}\,, \tag{4.78}$$

with $\sqrt{|\sigma_Q|} = \mathrm{sech}^M(r)$ for M two mode squeezed states. The matrix A_S in this case is rather

[26]The vertical and horizontal bar are just for better readability of the four blocks.

simple and has the following shape

$$A_S = -\tanh(r) \begin{pmatrix} 0 & T_S^\dagger & 0 & 0 \\ T_S^* & 0 & 0 & 0 \\ 0 & 0 & 0 & T_S^t \\ 0 & 0 & T_S & 0 \end{pmatrix} = B_S \oplus B_S^* \,. \tag{4.79}$$

As our submatrix B_S has the shape $\begin{pmatrix} 0 & B_S \\ B_S^* & 0 \end{pmatrix}$, we can use equation (4.62) to express the Hafnian in terms of the Permanent

$$\begin{aligned} \mathrm{Haf}(A_S) &= \mathrm{Haf}(B_S)\mathrm{Haf}(B_S^*) \\ &= (\tanh(r))^{2N}\mathrm{Perm}(T_S)\mathrm{Perm}(T_S^*) \\ &= (\tanh(r))^{2N}|\mathrm{Perm}(T_S)|^2 \,. \end{aligned} \tag{4.80}$$

Putting all of this together, we arrive at

$$\mathrm{P}_{\mathrm{GBS}} = \mathrm{P}(\overline{n} \cap \overline{h}) = \frac{\mathrm{Haf}(A_S)}{\overline{n}!\,\overline{h}!\sqrt{|\sigma_Q|}} = \frac{\tanh^{2N}(r)|\mathrm{Perm}(T_S)|^2 \mathrm{sech}^{2M}(r)}{\overline{n}!\,\overline{h}!} \tag{4.81}$$

and

$$\mathrm{P}(\overline{h}) = \mathrm{sech}^{2M}(r)\tanh^{2N}(r) \tag{4.82}$$

and see that therefore

$$\frac{\mathrm{P}_{\mathrm{GBS}}(\overline{n} \cap \overline{h})}{\mathrm{P}(\overline{h})} = \frac{|\mathrm{Perm}(T_S)|^2}{\overline{n}!\,\overline{h}!} = \mathrm{P}_{\mathrm{SBS}} \,, \tag{4.83}$$

as expected [275].

As we have now shown the relation between Scattershot and Gaussian BosonSampling, let us stress that Gaussian BosonSampling is not restricted to the specific transformation that we used for our comparison. In principle, we allow for any random transformation T_{GBS} and therefore Scattershot BosonSampling is a subset of our Gaussian BosonSampling.

4.4.4 Success Probabilities with Gaussian States

The previous discussions about the shape of different BosonSampling schemes are valuable from a theoretical point of view and also answer the fundamental question about the computational complexity of sampling from Gaussian states. However, what are the experimental improvements of our scheme compared to the state of the art? We claimed at the beginning that our Gaussian BosonSampling scheme saves quadratically on the number of required input states, compared to the Scattershot scheme. In this section, we discuss this experimental advance of our scheme.

Consider equation (4.71) for the generation probability of N photon pair events from $2K$

squeezers[27] with equal squeezing parameter r

$$P_{2K,\mathrm{GBS}}(N) = \binom{K+N-1}{N}\mathrm{sech}^{2K}(r)\tanh^{2N}(r)\,. \tag{4.84}$$

Contrary to our Gaussian BosonSampling scheme, Scattershot BosonSampling [243] may only retain the first photon pair event from a single two mode squeezer (higher orders are forbidden as they would sample the same row). Therefore, the probability to generate N photon pair events from K two mode squeezed states and equal squeezing parameter r follows the binomial distribution

$$P_{K,\mathrm{SBS}}(N) = \binom{K}{N}\mathrm{sech}^{2K}(r)\tanh^{2N}(r)\,, \tag{4.85}$$

which will always have lower generation probabilities than the Gaussian BosonSampling scheme [274]. Experimentally, we can explain this behaviour with the possible photon combinations. Consider two photon pair events, with the probability to generate one pair event being p. Then, the probability to create two photon pairs from two separate squeezers is[28] p^2. However, the probability to generate two photon pairs from the *same* two mode squeezer is also p^2, but we have to throw these events away in Scattershot! As such, our Gaussian BosonSampling scheme will always scale better towards higher photon numbers as we do not throw out the double and triple photon pair events from the same squeezer.

Quantitatively, we can calculate this advantage by dividing the Scattershot generation probability by the Gaussian generation probability for equal squeezing parameters $r_{\mathrm{SBS}} = r_{\mathrm{GBS}}$

$$\begin{aligned}\frac{\mathrm{P}_{\mathrm{SBS}}(N)}{\mathrm{P}_{\mathrm{GBS}}(N)} &= \binom{K}{N}\left[\binom{K+N-1}{N}\right]^{-1} \\ &= \frac{K!(K-1)!}{(K-N)!(K+N-1)!} \\ &\approx \lim_{N\to\infty,K>N}\left(\frac{K-N}{K-1}\right)^{N}\,.\end{aligned} \tag{4.86}$$

This probability gives an e-fold improvement to Scattershot BosonSampling in the success probability with the required $K = N^2$ squeezers. However, our scheme does not require to pump all N^2 modes, but only $K = N$. As such, we can save on $N(N-1)$ squeezers and use quadratically fewer resources than Scattershot. Furthermore, our scheme scales exponentially better in terms of success probability as N probabilistic sources [274].

To summarise the generation advantages for Gaussian BosonSampling compared to Scattershot BosonSampling, the first thing that comes to mind is that we do not use half of the generated photons as a herald. This gives us a factor of 2 in favour of our scheme. Furthermore, we can retain the higher photon pair events from a single squeezer which gives us an e-fold increase in the generation probability. Finally, we only need $K = N$ squeezers to saturate the complexity

[27] We consider $2K$ single mode squeezers as we want to compare it to K two mode squeezers. From figure 4.18, we know that we need $2K$ single mode squeezers to generate K two mode squeezers.

[28] We are not counting all possible combinations. These are encoded in the binomial factors and we are only interested in a heuristic argument.

of the problem, which saves quadratically on the number of required squeezers [274, 275].

Summary

In conclusion, we related the photon counting probabilities of a Gaussian state to a matrix function, the Hafnian. With this result, we argued that the Hafnian is in the #P complexity class and constructed a BosonSampling experiment akin to the proposal from Aaronson and Arkhipov. As losses and other noise can be described as a Gaussian operation, we can absorb them directly into the sampled matrix. However, we leave open the question how much loss we can tolerate before the scheme loses the original complexity. Furthermore, we showed that Scattershot BosonSampling is a special subclass of Gaussian BosonSampling experiments and presented a quadratic save in resources in favour of Gaussian BosonSampling. With this result, we place the experimental proof of quantum supremacy, which was the original idea behind all BosonSampling experiments, into the reach of current technology.

These are the last words I have to say
That's why this took so long to write
There will be other words some other day
But that's the story of my life

Billy Joel - Famous Last Words

5

Conclusion

In this thesis, we discussed several new techniques and their application in the field of high-dimensional quantum optics. Due to the vast possibilities in the field, we introduced many different aspects that improve the achievability of high-dimensional systems for quantum information science. We used different encodings and different degrees of freedom to probe the possibilities in the field.

Starting in chapter 2, we specifically tailored the photonic quantum state from a down-conversion process by exploiting the underlying linear waveguide structure of the device. Due to the coupled waveguide structure, we found that the resulting eigenvalue splitting in the propagation constant influences the spectral phase-matching structure of the parametric down-conversion process drastically. Thus, we could use the pump frequency to tune the spatial properties of the generated state. Due to an intrinsic Hong-Ou-Mandel interference effect of the generated photons in the basis transformation from generation to measurement basis, we produced post-selection free two-photon N00N states. Experimentally, we implemented this source and characterised both the linear and non-linear properties of the chip. In the quantum experiments, we could achieve a state fidelity of $\mathcal{F} = (84.2 \pm 2.6)\,\%$ for the two-photon N00N state and a N00N fringing visibility of $\mathcal{V} = (93.3 \pm 3.7)\,\%$ which was comparable to the classical reference. With this result, we showed that we implemented a compact dual-path source that produces tailored photonic quantum states with a clever use of the linear waveguide properties.

Chapter 3 provided an application of our implemented dual-path source in the higher order photon number regime by means of the time-multiplexed photon counting method. However, in order to guarantee that this detection scheme works properly, we first investigated the limitations of this measurement technique. We analysed the resulting click-statistics in a time-multiplexed detector, under consideration of finite bin number and accounted for losses. In total, we found that the optimal bin number for this type of measurement scheme is 256 bins for a discrimination and reconstruction of Fock states up to $n = 20$.

Afterwards, we used the click-statistics of a time-multiplexed detector to perform a novel, slim and efficient detector tomography scheme and inferred the detector response function Γ from the measured click statistics with coherent states. We found that the experimental limitations of the scheme are both the absolute calibration of the coherent state power to a reliable reference, as well as the polarisation sensitivity of the detectors. Due to the used single-mode

fibre components, we could not guarantee a well-oriented polarisation state entering the time-multiplexed detector and found that the polarisation scrambling in the fibre delays introduces a strong asymmetry in the detected time bin signal. Our model is therefore affected by an averaging effect of different detection efficiencies, which lowers the total measured efficiency of the detector system. However, these limitations are not fundamental to the method and may be eliminated firstly with a well-calibrated reference measurement for the powers (e.g. NIST calibrated power meter) and the use of either polarisation maintaining components throughout the experimental setup or a separate polarisation control directly in front of the multiplexing detector.

The final task in chapter 3 was to apply our implemented dual-path source together with time-multiplexed detection to probe the surviving non-classicality under the effect of turbulent channels. We developed a laboratory-scale simulation method of atmospheric links, i.e. from satellites to ground stations. Our method uses separate measurements with different attenuation levels to model the turbulent behaviour with appropriate post-processing of the measurements according to the probability distribution of transmittance. We applied our method to probe the effects of strong turbulences with a log-normal distribution and found that for a direct application the non-classicality does not survive, but may be recovered with a fitting post-selection protocol. Furthermore, we probed the effect of weak turbulence with the Weibull distribution and found that non-classicality only survives for weak turbulences, which agrees with the previous result from the log-normal distribution. At the end of this chapter, we demonstrated the general applicability of our simulation method by applying it to a general family beta-binomial distributions.

Finally in chapter 4, we extended the concepts of chapter 2 to modify the state generation properties in non-linear coupled waveguide arrays. We gave a quick introduction into this type of systems and reviewed their properties. Based on this idea, we developed several new theoretical core concepts, such as the driven quantum walks. Here, we reviewed the concept of passive quantum walks and introduced the idea of a driving term into this basic building block of quantum computation. With this idea, we found that we can probe genuinely different quantum dynamics not available with passive quantum systems. We discussed two driving possibilities in the system, lasing and squeezing and proved that the output state of the driven quantum walk may be decomposed into a highly intricate input state and a passive quantum walk evolution. This effect may be used to either generate complex spatially distributed quantum states by applying a passive evolution afterwards or to exploit the unique dynamics in quantum computation applications. We have directly used it to construct a search algorithm on the glued trees graph and shown that it performs better than a classical system.

In the last two sections of this thesis, we were concerned with the improved performance of quantum systems over classical ones. In particular, we investigated the quantum computational test bed of BosonSampling, which is a promising candidate to finally show the supremacy of quantum concepts over their classical counterparts. We first reviewed the idea behind BosonSampling and discussed the state of the art. Then, we aimed to map the non-linear waveguide array system into this framework with the use of the formalism that we introduced in section 4.2. This gave us a compact and reconfigurable device to perform BosonSampling experiments. However, we also found that this approach is not scalable to high photon numbers and many

modes, as an overlap in the down-conversion phase-matching functions prohibits the unique heralding procedure that is needed to guarantee the proper function of the protocol.

As a final concept, we developed the protocol of Gaussian BosonSampling. Here, we answered the last remaining question on the computational complexity of sampling from Gaussian states in the Fock basis. Under several conditions on the input states, we could prove that indeed sampling from Gaussian states is hard. Our protocol fulfils the complexity requirements, if we input at least N single-mode squeezed states into an N^2-dimensional Haar random interferometer and measure the output distributions of N photons at the output. We related this output probabilities at the output to the matrix function of the Hafnian. Finally, we investigated the experimental feasibility of this approach by comparing the generation probability for N photons to known protocols and found that for N squeezers we scale exponentially better than probabilistic single photon sources, while for N^2 squeezers we achieve a constant improvement of e, compared to the most general protocol up to now, Scattershot BosonSampling.

In total, we provided a survey over several research topics in the field of high-dimensional quantum optics. We introduced new techniques for the state generation by means of the dual-path waveguide source. We probed high-dimensional state manipulation in combination with state generation with the concepts of the driven quantum walk and the waveguide array BosonSampling proposal. We also showed highly complex passive quantum protocols with our protocol of Gaussian BosonSampling. However, we did not only cover state generation and manipulation, but we contributed to the field of state detection. We investigated the limits of time-multiplexed photon counting and performed a detector calibration with this technique. Furthermore, we probed the detected non-classicality after it was deteriorated by a atmospheric quantum communication link. As such, we contributed to the three fundamental aspects of quantum information science in this thesis: quantum state generation, quantum state manipulation and quantum state detection.

6

References

[1] M. A. Nielsen and I. L. Chuang. *Quantum Computation and Quantum Information*. Cambridge University Press, 2000.

[2] R. Loudon. *The Quantum Theory of Light*. Oxford University Press, 2000.

[3] C. Bennett and G. Brassard. "Quantum cryptography: Public key distribution and coin tossing". In: *Proceedings of IEEE International Conference on Computers, Systems and Signal Processing*. Vol. 175. New York, 1984, p. 8.

[4] A. K. Ekert. "Quantum cryptography based on Bell's theorem". In: *Physical Review Letters* 67.6 (1991), pp. 661–663.

[5] E. Knill, R. Laflamme, and G. J. Milburn. "A scheme for efficient quantum computation with linear optics". In: *Nature* 409.6816 (2001), pp. 46–52.

[6] A. M. Childs. "Universal Computation by Quantum Walk". In: *Physical Review Letters* 102.18 (2009), p. 180501.

[7] S. Aaronson and A. Arkhipov. "The computational complexity of linear optics". In: ACM Press, 2011, p. 333.

[8] A. N. Boto, P. Kok, D. S. Abrams, et al. "Quantum Interferometric Optical Lithography: Exploiting Entanglement to Beat the Diffraction Limit". In: *Physical Review Letters* 85.13 (2000), pp. 2733–2736.

[9] J. P. Dowling. "Quantum optical metrology – the lowdown on high-N00N states". In: *Contemporary Physics* 49.2 (2008), pp. 125–143.

[10] R. W. Boyd and J. P. Dowling. "Quantum lithography: status of the field". In: *Quantum Information Processing* 11.4 (2012), pp. 891–901.

[11] S. Lloyd. "Universal Quantum Simulators". In: *Science* 273.5278 (1996), pp. 1073–1078.

[12] T. Schaetz, C. R. Monroe, and T. Esslinger. "Focus on quantum simulation". In: *New Journal of Physics* 15.8 (2013), p. 085009.

[13] T. H. Johnson, S. R. Clark, and D. Jaksch. "What is a quantum simulator?" In: *EPJ Quantum Technology* 1.1 (2014), p. 10.

[14] I. M. Georgescu, S. Ashhab, and F. Nori. "Quantum simulation". In: *Reviews of Modern Physics* 86.1 (2014), pp. 153–185.

[15] D. Bouwmeester, I. Marzoli, G. P. Karman, W. Schleich, and J. P. Woerdman. “Optical Galton board”. In: *Physical Review A* 61.1 (1999), p. 013410.

[16] J. Du, H. Li, X. Xu, et al. “Experimental implementation of the quantum random-walk algorithm”. In: *Physical Review A* 67.4 (2003), p. 042316.

[17] Y. Lahini, A. Avidan, F. Pozzi, et al. “Anderson Localization and Nonlinearity in One-Dimensional Disordered Photonic Lattices”. In: *Physical Review Letters* 100.1 (2008), p. 013906.

[18] A. Rai, G. S. Agarwal, and J. H. H. Perk. “Transport and Quantum Walk of Nonclassical Light in Coupled Waveguides”. In: *arXiv:0807.3063* (2008).

[19] A. Rai, S. Das, and G. S. Agarwal. “Non-Gaussian and Gaussian Entanglement in Coupled Leaky Waveguides”. In: *arXiv:0907.2432* (2009).

[20] A. Peruzzo, M. Lobino, J. C. F. Matthews, et al. “Quantum Walks of Correlated Photons”. In: *Science* 329.5998 (2010), pp. 1500–1503.

[21] J. O. Owens, M. A. Broome, D. N. Biggerstaff, et al. “Two-photon quantum walks in an elliptical direct-write waveguide array”. In: *New Journal of Physics* 13.7 (2011), p. 075003.

[22] J. D. A. Meinecke, K. Poulios, A. Politi, et al. “Coherent Time Evolution and Boundary Conditions of Two-Photon Quantum Walks”. In: *arXiv:1209.1599* (2012).

[23] L. Sansoni, F. Sciarrino, G. Vallone, et al. “Two-Particle Bosonic-Fermionic Quantum Walk via Integrated Photonics”. In: *Physical Review Letters* 108.1 (2012), p. 010502.

[24] K. Poulios, R. Keil, D. Fry, et al. *Quantum walks of correlated photon pairs in two-dimensional waveguide arrays*. arXiv e-print 1308.2554. 2013.

[25] D. Achilles, C. Silberhorn, C. Śliwa, K. Banaszek, and I. A. Walmsley. “Fiber-assisted detection with photon number resolution”. In: *Optics Letters* 28.23 (2003), p. 2387.

[26] J. Řeháček, Z. Hradil, O. Haderka, J. Peřina, and M. Hamar. “Multiple-photon resolving fiber-loop detector”. In: *Physical Review A* 67.6 (2003), p. 061801.

[27] M. J. Fitch, B. C. Jacobs, T. B. Pittman, and J. D. Franson. “Photon-number resolution using time-multiplexed single-photon detectors”. In: *Physical Review A* 68.4 (2003), p. 043814.

[28] D. Achilles, C. Silberhorn, C. Sliwa, et al. “Photon-number-resolving detection using time-multiplexing”. In: *Journal of Modern Optics* 51.9-10 (2004), pp. 1499–1515.

[29] E. Waks, E. Diamanti, B. C. Sanders, S. D. Bartlett, and Y. Yamamoto. “Direct Observation of Nonclassical Photon Statistics in Parametric Down-Conversion”. In: *Physical Review Letters* 92.11 (2004), p. 113602.

[30] A. Schreiber, K. N. Cassemiro, V. Potoček, et al. “Photons Walking the Line: A Quantum Walk with Adjustable Coin Operations”. In: *Physical Review Letters* 104.5 (2010), p. 050502.

[31] A. Schreiber, K. N. Cassemiro, V. Potoček, et al. “Decoherence and Disorder in Quantum Walks: From Ballistic Spread to Localization”. In: *Physical Review Letters* 106.18 (2011), p. 180403.

[32] A. Schreiber, A. Gábris, P. P. Rohde, et al. “A 2D Quantum Walk Simulation of Two-Particle Dynamics”. In: *Science* 336.6077 (2012), pp. 55–58.

[33] A. Schreiber. “Quantum Walks in Time”. PhD thesis. Erlangen: Erlangen-Nuremberg, 2013.

[34] W. Mauerer, M. Avenhaus, W. Helwig, and C. Silberhorn. “How colors influence numbers: Photon statistics of parametric down-conversion”. In: *Physical Review A* 80.5 (2009), p. 053815.

[35] B. Brecht, A. Eckstein, R. Ricken, et al. “Demonstration of coherent time-frequency Schmidt mode selection using dispersion-engineered frequency conversion”. In: *Physical Review A* 90.3 (2014), p. 030302.

[36] B. Brecht, D. V. Reddy, C. Silberhorn, and M. G. Raymer. “Photon Temporal Modes: A Complete Framework for Quantum Information Science”. In: *Physical Review X* 5.4 (2015), p. 041017.

[37] V. Ansari, M. Allgaier, L. Sansoni, et al. “Temporal-mode tomography of single photons”. In: *arXiv:1607.03001 [quant-ph]* (2016).

[38] R. Morandotti, U. Peschel, J. S. Aitchison, H. S. Eisenberg, and Y. Silberberg. “Dynamics of Discrete Solitons in Optical Waveguide Arrays”. In: *Physical Review Letters* 83.14 (1999), pp. 2726–2729.

[39] H. H. Arnaut and G. A. Barbosa. “Orbital and Intrinsic Angular Momentum of Single Photons and Entangled Pairs of Photons Generated by Parametric Down-Conversion”. In: *Physical Review Letters* 85.2 (2000), pp. 286–289.

[40] C. K. Law and J. H. Eberly. “Analysis and Interpretation of High Transverse Entanglement in Optical Parametric Down Conversion”. In: *Physical Review Letters* 92.12 (2004), p. 127903.

[41] J. Leach, B. Jack, J. Romero, et al. “Quantum correlations in optical angle-orbital angular momentum variables”. In: *Science* 662 (2010), p. 329.

[42] S. Braun, J. P. Ronzheimer, M. Schreiber, et al. “Negative Absolute Temperature for Motional Degrees of Freedom”. In: *Science* 339.6115 (2013), pp. 52–55.

[43] G. J. de Valcárcel, G. Patera, N. Treps, and C. Fabre. “Multimode squeezing of frequency combs”. In: *Physical Review A* 74.6 (2006), p. 061801.

[44] O. Pinel, P. Jian, R. M. de Araújo, et al. “Generation and Characterization of Multimode Quantum Frequency Combs”. In: *Physical Review Letters* 108.8 (2012), p. 083601.

[45] R. Medeiros de Araújo, J. Roslund, Y. Cai, et al. “Full characterization of a highly multimode entangled state embedded in an optical frequency comb using pulse shaping”. In: *Physical Review A* 89.5 (2014), p. 053828.

[46] J. Roslund, R. M. de Araújo, S. Jiang, C. Fabre, and N. Treps. "Wavelength-multiplexed quantum networks with ultrafast frequency combs". In: *Nature Photonics* 8.2 (2014), pp. 109–112.

[47] M. Kiffner, W. Li, and D. Jaksch. "Magnetic Monopoles and Synthetic Spin-Orbit Coupling in Rydberg Macrodimers". In: *Physical Review Letters* 110.17 (2013), p. 170402.

[48] M. Mitrano, G. Cotugno, S. R. Clark, et al. "Pressure-Dependent Relaxation in the Photoexcited Mott Insulator: Influence of Hopping and Correlations on Quasiparticle Recombination Rates". In: *Physical Review Letters* 112.11 (2014), p. 117801.

[49] P. Schindler, M. Müller, D. Nigg, et al. "Quantum simulation of dynamical maps with trapped ions". In: *Nature Physics* 9.6 (2013), pp. 361–367.

[50] B. P. Lanyon, M. Zwerger, P. Jurcevic, et al. "Experimental Violation of Multipartite Bell Inequalities with Trapped Ions". In: *Physical Review Letters* 112.10 (2014), p. 100403.

[51] T. Monz, D. Nigg, E. A. Martinez, et al. "Realization of a scalable Shor algorithm". In: *Science* 351.6277 (2016), pp. 1068–1070.

[52] M. Brandl, M. van Mourik, L. Postler, et al. "Cryogenic setup for trapped ion quantum computing". In: *Review of Scientific Instruments* 87.11 (2016), p. 113103.

[53] A. Einstein. "Über einen die Erzeugung und Verwandlung des Lichtes betreffenden heuristischen Gesichtspunkt". In: *Annalen der Physik* 322.6 (1905), pp. 132–148.

[54] M. Planck. "Ueber das Gesetz der Energieverteilung im Normalspectrum". In: *Annalen der Physik* 309.3 (1901), pp. 553–563.

[55] W. Heisenberg. "Über den anschaulichen Inhalt der quantentheoretischen Kinematik und Mechanik". In: *Zeitschrift für Physik* 43.3-4 (1927), pp. 172–198.

[56] A. Eckstein, B. Brecht, and C. Silberhorn. "A quantum pulse gate based on spectrally engineered sum frequency generation". In: *Optics Express* 19.15 (2011), pp. 13770–13778.

[57] R. Kruse, F. Katzschmann, A. Christ, et al. "Spatio-spectral characteristics of parametric down-conversion in waveguide arrays". In: *New Journal of Physics* 15.8 (2013), p. 083046.

[58] A. Christ, K. Laiho, A. Eckstein, et al. "Spatial modes in waveguided parametric down-conversion". In: *Phys. Rev. A* 80 (2009), p. 033829.

[59] C. K. Hong, Z. Y. Ou, and L. Mandel. "Measurement of subpicosecond time intervals between two photons by interference". In: *Physical Review Letters* 59.18 (1987), pp. 2044–2046.

[60] B. T. Gard, J. P. Olson, R. M. Cross, et al. "Inefficiency of classically simulating linear optical quantum computing with Fock-state inputs". In: *Physical Review A* 89.2 (2014), p. 022328.

[61] W. P. Schleich. *Quantum Optics in Phase Space*. 1st ed. Berlin ; New York: Wiley-VCH Verlag GmbH & Co. KGaA, 2001.

[62] R. J. Glauber. “Coherent and Incoherent States of the Radiation Field”. In: *Physical Review* 131.6 (1963), pp. 2766–2788.

[63] E. C. G. Sudarshan. “Equivalence of Semiclassical and Quantum Mechanical Descriptions of Statistical Light Beams”. In: *Physical Review Letters* 10.7 (1963), pp. 277–279.

[64] K. Husimi. “Some Formal Properties of the Density Matrix”. In: *Proceedings of the Physico-Mathematical Society of Japan. 3rd Series* 22.4 (1940), pp. 264–314.

[65] C. S. Hamilton, R. Kruse, L. Sansoni, C. Silberhorn, and I. Jex. “Driven Quantum Walks”. In: *Physical Review Letters* 113.8 (2014), p. 083602.

[66] D. N. Klyshko. “Use of two-photon light for absolute calibration of photoelectric detectors”. In: *Soviet Journal of Quantum Electronics* 10.9 (1980), p. 1112.

[67] W. H. Louisell, A. Yariv, and A. E. Siegman. “Quantum Fluctuations and Noise in Parametric Processes. I.” In: *Physical Review* 124.6 (1961), pp. 1646–1654.

[68] D. C. Burnham and D. L. Weinberg. “Observation of Simultaneity in Parametric Production of Optical Photon Pairs”. In: *Physical Review Letters* 25.2 (1970), pp. 84–87.

[69] R. W. Boyd. *Nonlinear optics*. San Diego, CA (United States); Academic Press Inc., 1992.

[70] R. Kruse, L. Sansoni, S. Brauner, et al. “Dual-path source engineering in integrated quantum optics”. In: *Physical Review A* 92.5 (2015), p. 053841.

[71] B. C. Sanders. “Quantum dynamics of the nonlinear rotator and the effects of continual spin measurement”. In: *Physical Review A* 40.5 (1989), pp. 2417–2427.

[72] G. A. Durkin and J. P. Dowling. “Local and Global Distinguishability in Quantum Interferometry”. In: *Physical Review Letters* 99.7 (2007), p. 070801.

[73] C. C. Gerry and R. A. Campos. “Generation of maximally entangled photonic states with a quantum-optical Fredkin gate”. In: *Physical Review A* 64.6 (2001), p. 063814.

[74] P. Kok, H. Lee, and J. P. Dowling. “Creation of large-photon-number path entanglement conditioned on photodetection”. In: *Physical Review A* 65.5 (2002), p. 052104.

[75] G. G. Lapaire, P. Kok, J. P. Dowling, and J. E. Sipe. “Conditional linear-optical measurement schemes generate effective photon nonlinearities”. In: *Physical Review A* 68.4 (2003), p. 042314.

[76] K. T. Kapale and J. P. Dowling. “Bootstrapping Approach for Generating Maximally Path-Entangled Photon States”. In: *Physical Review Letters* 99.5 (2007), p. 053602.

[77] N. M. VanMeter, P. Lougovski, D. B. Uskov, et al. “General linear-optical quantum state generation scheme: Applications to maximally path-entangled states”. In: *Physical Review A* 76.6 (2007), p. 063808.

[78] M. W. Mitchell, J. S. Lundeen, and A. M. Steinberg. “Super-resolving phase measurements with a multiphoton entangled state”. In: *Nature* 429.6988 (2004), pp. 161–164.

[79] P. Walther, J.-W. Pan, M. Aspelmeyer, et al. “De Broglie wavelength of a non-local four-photon state”. In: *Nature* 429.6988 (2004), pp. 158–161.

[80] K. J. Resch, K. L. Pregnell, R. Prevedel, et al. “Time-Reversal and Super-Resolving Phase Measurements”. In: *Physical Review Letters* 98.22 (2007), p. 223601.

[81] T. Nagata, R. Okamoto, J. L. O’Brien, K. Sasaki, and S. Takeuchi. “Beating the Standard Quantum Limit with Four-Entangled Photons”. In: *Science* 316.5825 (2007), pp. 726–729.

[82] I. Afek, O. Ambar, and Y. Silberberg. “High-NOON States by Mixing Quantum and Classical Light”. In: *Science* 328.5980 (2010), pp. 879–881.

[83] Y.-A. Chen, X.-H. Bao, Z.-S. Yuan, et al. “Heralded Generation of an Atomic NOON State”. In: *Physical Review Letters* 104.4 (2010), p. 043601.

[84] D. Rodriguez-Mendez and H. Moya-Cessa. “NOON states in entangled cavities”. In: *Optics Communications* 284.13 (2011), pp. 3345–3347.

[85] H. Cable, F. Laloë, and W. J. Mullin. “Formation of NOON states from Fock-state Bose-Einstein condensates”. In: *Physical Review A* 83.5 (2011), p. 053626.

[86] Y.-X. Gong, P. Xu, Y. F. Bai, et al. “Multiphoton path-entanglement generation by concurrent parametric down-conversion in a single $\chi^{(2)}$ nonlinear photonic crystal”. In: *Physical Review A* 86.2 (2012), p. 023835.

[87] S.-Y. Lee, T. Paterek, H. S. Park, and H. Nha. “Linear optical scheme for producing polarization-entangled NOON states”. In: *Optics Communications* 285.3 (2012), pp. 307–310.

[88] Y. Israel, I. Afek, S. Rosen, O. Ambar, and Y. Silberberg. “Experimental tomography of NOON states with large photon numbers”. In: *Physical Review A* 85.2 (2012), p. 022115.

[89] D. Rodríguez-Méndez and H. Moya-Cessa. “High NOON states in trapped ions”. In: *Physica Scripta* 2012.T147 (2012), p. 014028.

[90] W. Feng, K. Jiang, M. L.-J. Lollie, M. S. Zubairy, and J. P. Dowling. “Super-resolving single-photon number-path-entangled state and its generation”. In: *Physical Review A* 89.4 (2014), p. 043824.

[91] S. Sivakumar. “Superposed Coherent States improve fidelity of NOON states generated in post-selection”. In: *Canadian Journal of Physics* (2014).

[92] J. S. Fakonas, A. Mitskovets, and H. A. Atwater. “Path entanglement of surface plasmons”. In: *New Journal of Physics* 17.2 (2015), p. 023002.

[93] K. Jiang, C. J. Brignac, Y. Weng, et al. “Strategies for choosing path-entangled number states for optimal robust quantum-optical metrology in the presence of loss”. In: *Physical Review A* 86.1 (2012), p. 013826.

[94] J. C. Matthews, X.-Q. Zhou, H. Cable, et al. “Towards practical quantum metrology with photon counting”. In: *npj Quantum Information* 2 (2016), npjqi201623.

[95] A. E. Ulanov, I. A. Fedorov, D. Sychev, P. Grangier, and A. I. Lvovsky. “Loss-tolerant state engineering for quantum-enhanced metrology via the reverse Hong–Ou–Mandel effect”. In: *Nature Communications* 7 (2016).

[96] J. W. Silverstone, D. Bonneau, K. Ohira, et al. “On-chip quantum interference between silicon photon-pair sources”. In: *Nature Photonics* 8.2 (2014), pp. 104–108.

[97] H. Jin, F. M. Liu, P. Xu, et al. “On-Chip Generation and Manipulation of Entangled Photons Based on Reconfigurable Lithium-Niobate Waveguide Circuits”. In: *Physical Review Letters* 113.10 (2014), p. 103601.

[98] S. Tanzilli, H. De Riedmatten, H. Tittel, et al. “Highly efficient photon-pair source using periodically poled lithium niobate waveguide”. In: *Electronics Letters* 37.1 (2001), pp. 26–28.

[99] M. Fejer, G. Magel, D. H. Jundt, and R. Byer. “Quasi-phase-matched second harmonic generation: tuning and tolerances”. In: *IEEE Journal of Quantum Electronics* 28.11 (1992), pp. 2631–2654.

[100] M. Yamada, N. Nada, M. Saitoh, and K. Watanabe. “First-order quasi-phase matched $LiNbO_3$ waveguide periodically poled by applying an external field for efficient blue second-harmonic generation”. In: *Applied Physics Letters* 62.5 (1993), pp. 435–436.

[101] T. Tamir, ed. *Integrated Optics*. 2nd ed. Springer-Verlag, 1979.

[102] R. C. Alferness, R. V. Schmidt, and E. H. Turner. “Characteristics of Ti-diffused lithium niobate optical directional couplers”. In: *Applied Optics* 18.23 (1979), pp. 4012–4016.

[103] J. Ctyroky, M. Hofman, J. Janta, and J. Schrofel. “3-D analysis of LiNbO3: Ti channel waveguides and directional couplers”. In: *IEEE Journal of Quantum Electronics* 20.4 (1984), pp. 400–409.

[104] T. Tamir, D. H. Auston, W. Engl, T. Sugano, and H. K. V. Lotsch, eds. *Guided-Wave Optoelectronics*. Vol. 26. Springer Series in Electronics and Photonics. Berlin, Heidelberg: Springer Berlin Heidelberg, 1988.

[105] W. K. Burns, A. F. Milton, A. B. Lee, and E. J. West. “Optical modal evolution 3-dB coupler”. In: *Applied Optics* 15.4 (1976), pp. 1053–1065.

[106] A. Yariv. *Quantum Electronics 3e*. 3. Auflage. John Wiley & Sons, 1989.

[107] A. Christ. “Theory of waveguided type-II parametric down-conversion: from fundamentals to applications”. PhD thesis. University of Paderborn, 2012.

[108] G. Harder. “Optimized Down-Conversion Source and State-Characterization Tools for Quantum Optics”. PhD thesis. University of Paderborn, 2016.

[109] A. Migdall, S. Polyakov, J. Fan, and J. Bienfang. *Single-Photon Generation and Detection*. 1st ed. 2013.

[110] A. Christ, B. Brecht, W. Mauerer, and C. Silberhorn. “Theory of quantum frequency conversion and type-II parametric down-conversion in the high-gain regime”. In: *New Journal of Physics* 15.5 (2013), p. 053038.

[111] A. Gábris. “The Hamiltonian for PDC in waveguide arrays”. 2012.

[112] F. Setzpfandt, A. S. Solntsev, J. Titchener, et al. “Tunable generation of entangled photons in a nonlinear directional coupler”. In: *Laser & Photonics Reviews* 10.1 (2016), pp. 131–136.

[113] R. Regener and W. Sohler. "Loss in low-finesse Ti:$LiNbO_3$". In: *Applied Physics B* 36.3 (1984), pp. 143–147.

[114] E. Schmidt. "Zur Theorie der linearen und nichtlinearen Integralgleichungen". In: *Mathematische Annalen* 63.4 (1907), pp. 433–476.

[115] S. L. Braunstein. "Squeezing as an irreducible resource". In: *Physical Review A* 71.5 (2005), p. 055801.

[116] G. Harder, V. Ansari, B. Brecht, et al. "An optimized photon pair source for quantum circuits". In: *Optics Express* 21.12 (2013), p. 13975.

[117] B. Cabrera, R. M. Clarke, P. Colling, et al. "Detection of single infrared, optical, and ultraviolet photons using superconducting transition edge sensors". In: *Applied Physics Letters* 73.6 (1998), pp. 735–737.

[118] A. J. Miller, S. W. Nam, J. M. Martinis, and A. V. Sergienko. "Demonstration of a low-noise near-infrared photon counter with multiphoton discrimination". In: *Applied Physics Letters* 83.4 (2003), pp. 791–793.

[119] D. Rosenberg, A. E. Lita, A. J. Miller, and S. W. Nam. "Noise-free high-efficiency photon-number-resolving detectors". In: *Physical Review A* 71.6 (2005), p. 061803.

[120] A. E. Lita, D. Rosenberg, S. Nam, et al. "Tuning of tungsten thin film superconducting transition temperature for fabrication of photon number resolving detectors". In: *IEEE Transactions on Applied Superconductivity* 15.2 (2005), pp. 3528–3531.

[121] T. E. Ingerson, R. J. Kearney, and R. L. Coulter. "Photon counting with photodiodes". In: *Applied Optics* 22.13 (1983), pp. 2013–2018.

[122] A. E. Lita, A. J. Miller, and S. W. Nam. "Counting near-infrared single-photons with 95% efficiency". In: *Optics Express* 16.5 (2008), p. 3032.

[123] D. Fukuda, G. Fujii, T. Numata, et al. "Titanium-based transition-edge photon number resolving detector with 98% detection efficiency with index-matched small-gap fiber coupling". In: *Optics Express* 19.2 (2011), pp. 870–875.

[124] T. Gerrits, B. Calkins, N. Tomlin, et al. "Extending single-photon optimized superconducting transition edge sensors beyond the single-photon counting regime". In: *Optics Express* 20.21 (2012), pp. 23798–23810.

[125] F. Marsili, V. B. Verma, J. A. Stern, et al. "Detecting single infrared photons with 93% system efficiency". In: *Nature Photonics* 7.3 (2013), pp. 210–214.

[126] P. C. Humphreys, B. J. Metcalf, T. Gerrits, et al. "Tomography of photon-number resolving continuous-output detectors". In: *New Journal of Physics* 17.10 (2015), p. 103044.

[127] R. Kruse, J. Tiedau, T. J. Bartley, S. Barkhofen, and C. Silberhorn. "Limits of the time-multiplexed photon-counting method". In: *Physical Review A* 95.2 (2017), p. 023815.

[128] J. Sperling, W. Vogel, and G. S. Agarwal. "True photocounting statistics of multiple on-off detectors". In: *Physical Review A* 85.2 (2012), p. 023820.

[129] J.-C. Diels and W. Rudolph. *Ultrashort Laser Pulse Phenomena, Second Edition*. Ed. by P. F. Liao and P. Kelley. 2 edition. Amsterdam ; Boston: Academic Press, 2006.

[130] Corning Optical Fibre. *Optical Specifications of SMF28e fibres*. 2007.

[131] Evanescent Optics Inc. *Low loss in fibre-integrated beam splitters*. private communication. 2016.

[132] A. J. Annunziata, O. Quaranta, D. F. Santavicca, et al. "Reset dynamics and latching in niobium superconducting nanowire single-photon detectors". In: *Journal of Applied Physics* 108.8 (2010), p. 084507.

[133] G. Zambra, A. Andreoni, M. Bondani, et al. "Experimental Reconstruction of Photon Statistics without Photon Counting". In: *Physical Review Letters* 95.6 (2005), p. 063602.

[134] A. V. Dodonov, S. S. Mizrahi, and V. V. Dodonov. "Engineering quantum jump superoperators for single-photon detectors". In: *Physical Review A* 74.3 (2006), p. 033823.

[135] A. Allevi, M. Bondani, and A. Andreoni. "Photon-number correlations by photon-number resolving detectors". In: *Optics Letters* 35.10 (2010), p. 1707.

[136] N. Gisin and R. Thew. "Quantum communication". In: *Nature Photonics* 1.3 (2007), pp. 165–171.

[137] A. Luis and L. L. Sánchez-Soto. "Complete Characterization of Arbitrary Quantum Measurement Processes". In: *Physical Review Letters* 83.18 (1999), pp. 3573–3576.

[138] J. Fiurášek. "Maximum-likelihood estimation of quantum measurement". In: *Physical Review A* 64.2 (2001), p. 024102.

[139] G. M. D'Ariano, L. Maccone, and P. L. Presti. "Quantum Calibration of Measurement Instrumentation". In: *Physical Review Letters* 93.25 (2004), p. 250407.

[140] J. S. Lundeen, A. Feito, H. Coldenstrodt-Ronge, et al. "Tomography of quantum detectors". In: *Nature Physics* 5.1 (2009), pp. 27–30.

[141] A. Feito, J. S. Lundeen, H. Coldenstrodt-Ronge, et al. "Measuring measurement: theory and practice". In: *New Journal of Physics* 11.9 (2009), p. 093038.

[142] H. B. Coldenstrodt-Ronge, J. S. Lundeen, K. L. Pregnell, et al. "A proposed testbed for detector tomography". In: *Journal of Modern Optics* 56.2-3 (2009), pp. 432–441.

[143] V. D'Auria, N. Lee, T. Amri, C. Fabre, and J. Laurat. "Quantum Decoherence of Single-Photon Counters". In: *Physical Review Letters* 107.5 (2011), p. 050504.

[144] M. K. Akhlaghi, A. H. Majedi, and J. S. Lundeen. "Nonlinearity in single photon detection: modeling and quantum tomography". In: *Optics Express* 19.22 (2011), pp. 21305–21312.

[145] J. J. Renema, G. Frucci, Z. Zhou, et al. "Modified detector tomography technique applied to a superconducting multiphoton nanodetector". In: *Optics Express* 20.3 (2012), pp. 2806–2813.

[146] C. M. Natarajan, M. G. Tanner, and R. H. Hadfield. "Superconducting nanowire single-photon detectors: physics and applications". In: *Superconductor Science and Technology* 25.6 (2012), p. 063001.

[147] S. V. Polyakov and A. L. Migdall. "High accuracy verification of a correlated-photon-based method for determining photon-counting detection efficiency". In: *Optics Express* 15.4 (2007), pp. 1390–1407.

[148] A. P. Worsley, H. B. Coldenstrodt-Ronge, J. S. Lundeen, et al. "Absolute efficiency estimation of photon-number-resolving detectors using twin beams". In: *Optics Express* 17.6 (2009), pp. 4397–4412.

[149] J. Peřina, O. Haderka, V. Michálek, and M. Hamar. "Absolute detector calibration using twin beams". In: *Optics Letters* 37.13 (2012), pp. 2475–2477.

[150] J. P. Jr, O. Haderka, A. Allevi, and M. Bondani. "Absolute calibration of photon-number-resolving detectors with an analog output using twin beams". In: *Applied Physics Letters* 104.4 (2014), p. 041113.

[151] M. Bohmann, R. Kruse, J. Sperling, C. Silberhorn, and W. Vogel. "Direct calibration of click-counting detectors". In: *Physical Review A* 95.3 (2017), p. 033806.

[152] P. L. Kelley and W. H. Kleiner. "Theory of Electromagnetic Field Measurement and Photoelectron Counting". In: *Physical Review* 136.2A (1964), A316–A334.

[153] W. Vogel and D.-G. Welsch. *Quantum Optics: An Introduction*. 3rd ed. Weinheim: Wiley-VCH Verlag GmbH & Co. KGaA, 2006.

[154] J. Sperling, W. Vogel, and G. S. Agarwal. "Correlation measurements with on-off detectors". In: *Physical Review A* 88.4 (2013), p. 043821.

[155] E. A. Dauler, M. E. Grein, A. J. Kerman, et al. "Review of superconducting nanowire single-photon detector system design options and demonstrated performance". In: *Optical Engineering* 53.8 (2014), pp. 081907–081907.

[156] H. Shibata, K. Shimizu, H. Takesue, and Y. Tokura. "Superconducting Nanowire Single-Photon Detector with Ultralow Dark Count Rate Using Cold Optical Filters". In: *Applied Physics Express* 6.7 (2013), p. 072801.

[157] M. Krystek and M. Anton. "A weighted total least-squares algorithm for fitting a straight line". In: *Measurement Science and Technology* 18.11 (2007), p. 3438.

[158] S. N. Dorenbos, E. M. Reiger, N. Akopian, et al. "Superconducting single photon detectors with minimized polarization dependence". In: *Applied Physics Letters* 93.16 (2008), p. 161102.

[159] C. H. Bennett, F. Bessette, G. Brassard, L. Salvail, and J. Smolin. "Experimental quantum cryptography". In: *Journal of Cryptology* 5.1 (1992), pp. 3–28.

[160] C. H. Bennett. "Quantum cryptography using any two nonorthogonal states". In: *Physical Review Letters* 68.21 (1992), pp. 3121–3124.

[161] R. J. Hughes, D. M. Alde, P. Dyer, et al. "Quantum cryptography". In: *Contemporary Physics* 36.3 (1995), pp. 149–163.

[162] A. Muller, H. Zbinden, and N. Gisin. "Quantum cryptography over 23 km in installed under-lake telecom fibre". In: *Europhysics Letters* 33.5 (1996), pp. 335–340.

[163] W. K. Wootters and W. H. Zurek. "A single quantum cannot be cloned". In: *Nature* 299.5886 (1982), pp. 802–803.

[164] D. Dieks. "Communication by EPR devices". In: *Physics Letters A* 92.6 (1982), pp. 271–272.

[165] R. Ursin, F. Tiefenbacher, T. Schmitt-Manderbach, et al. "Entanglement-based quantum communication over 144 km". In: *Nature Physics* 3.7 (2007), pp. 481–486.

[166] T. Scheidl, R. Ursin, A. Fedrizzi, et al. "Feasibility of 300 km quantum key distribution with entangled states". In: *New Journal of Physics* 11.8 (2009), p. 085002.

[167] A. Fedrizzi, R. Ursin, T. Herbst, et al. "High-fidelity transmission of entanglement over a high-loss free-space channel". In: *Nature Physics* 5.6 (2009), pp. 389–392.

[168] I. Capraro, A. Tomaello, A. Dall'Arche, et al. "Impact of Turbulence in Long Range Quantum and Classical Communications". In: *Physical Review Letters* 109.20 (2012), p. 200502.

[169] J. Yin, J.-G. Ren, H. Lu, et al. "Quantum teleportation and entanglement distribution over 100-kilometre free-space channels". In: *Nature* 488.7410 (2012), pp. 185–188.

[170] X.-S. Ma, T. Herbst, T. Scheidl, et al. "Quantum teleportation over 143 kilometres using active feed-forward". In: *Nature* 489.7415 (2012), pp. 269–273.

[171] C. Peuntinger, B. Heim, C. R. Müller, et al. "Distribution of Squeezed States through an Atmospheric Channel". In: *Physical Review Letters* 113.6 (2014), p. 060502.

[172] G. Vallone, D. Bacco, D. Dequal, et al. "Experimental Satellite Quantum Communications". In: *Physical Review Letters* 115.4 (2015), p. 040502.

[173] D. Dequal, G. Vallone, D. Bacco, et al. "Experimental single-photon exchange along a space link of 7000 km". In: *Physical Review A* 93.1 (2016), p. 010301.

[174] G. Vallone, D. Dequal, M. Tomasin, et al. "Interference at the Single Photon Level Along Satellite-Ground Channels". In: *Physical Review Letters* 116.25 (2016), p. 253601.

[175] A. Carrasco-Casado, H. Kunimori, H. Takenaka, et al. "LEO-to-ground polarization measurements aiming for space QKD using Small Optical TrAnsponder (SOTA)". In: *Optics Express* 24.11 (2016), pp. 12254–12266.

[176] K. Günthner, I. Khan, D. Elser, et al. "Quantum-limited measurements of optical signals from a geostationary satellite". In: *arXiv:1608.03511 [physics, physics:quant-ph]* (2016).

[177] A. A. Semenov and W. Vogel. "Quantum light in the turbulent atmosphere". In: *Physical Review A* 80.2 (2009), p. 021802.

[178] D. Y. Vasylyev, A. A. Semenov, and W. Vogel. "Toward Global Quantum Communication: Beam Wandering Preserves Nonclassicality". In: *Physical Review Letters* 108.22 (2012), p. 220501.

[179] D. Vasylyev, A. A. Semenov, and W. Vogel. "Atmospheric Quantum Channels with Weak and Strong Turbulence". In: *Physical Review Letters* 117.9 (2016), p. 090501.

[180] V. C. Usenko, B. Heim, C. Peuntinger, et al. “Entanglement of Gaussian states and the applicability to quantum key distribution over fading channels”. In: *New Journal of Physics* 14.9 (2012), p. 093048.

[181] N. Hosseinidehaj and R. Malaney. “Gaussian entanglement distribution via satellite”. In: *Physical Review A* 91.2 (2015), p. 022304.

[182] N. Hosseinidehaj and R. Malaney. “Entanglement generation via non-Gaussian transfer over atmospheric fading channels”. In: *Physical Review A* 92.6 (2015), p. 062336.

[183] J. Peřina, V. Peřinová, M. C. Teich, and P. Diament. “Two Descriptions for the Photocounting Detection of Radiation Passed through a Random Medium: A Comparison for the Turbulent Atmosphere”. In: *Physical Review A* 7.5 (1973), pp. 1732–1737.

[184] P. W. Milonni, J. H. Carter, C. G. Peterson, and R. J. Hughes. “Effects of propagation through atmospheric turbulence on photon statistics”. In: *Journal of Optics B: Quantum and Semiclassical Optics* 6.8 (2004), S742.

[185] A. A. Semenov and W. Vogel. “Entanglement transfer through the turbulent atmosphere”. In: *Physical Review A* 81.2 (2010), p. 023835.

[186] M. O. Gumberidze, A. A. Semenov, D. Vasylyev, and W. Vogel. “Bell nonlocality in the turbulent atmosphere”. In: *Physical Review A* 94.5 (2016), p. 053801.

[187] M. Bohmann, J. Sperling, and W. Vogel. “Entanglement and phase properties of noisy NOON states”. In: *Physical Review A* 91.4 (2015), p. 042332.

[188] M. Bohmann, A. A. Semenov, J. Sperling, and W. Vogel. “Gaussian entanglement in the turbulent atmosphere”. In: *Physical Review A* 94.1 (2016), p. 010302.

[189] M. Bohmann, J. Sperling, A. A. Semenov, and W. Vogel. “Higher-order nonclassical effects in fluctuating-loss channels”. In: *arXiv:1610.09053 [quant-ph]* (2016).

[190] B.-J. Pors, C. H. Monken, E. R. Eliel, and J. P. Woerdman. “Transport of orbital-angular-momentum entanglement through a turbulent atmosphere”. In: *Optics Express* 19.7 (2011), pp. 6671–6683.

[191] M. V. da Cunha Pereira, L. A. P. Filpi, and C. H. Monken. “Cancellation of atmospheric turbulence effects in entangled two-photon beams”. In: *Physical Review A* 88.5 (2013), p. 053836.

[192] J.-P. Bourgoin, B. L. Higgins, N. Gigov, et al. “Free-space quantum key distribution to a moving receiver”. In: *Optics Express* 23.26 (2015), pp. 33437–33447.

[193] B. Rodenburg, M. Mirhosseini, M. Malik, et al. “Simulating thick atmospheric turbulence in the lab with application to orbital angular momentum communication”. In: *New Journal of Physics* 16.3 (2014), p. 033020.

[194] Y. Zhang, S. Prabhakar, A. H. Ibrahim, et al. “Experimentally observed decay of high-dimensional entanglement through turbulence”. In: *Physical Review A* 94.3 (2016), p. 032310.

[195] A. Mair, A. Vaziri, G. Weihs, and A. Zeilinger. “Entanglement of the orbital angular momentum states of photons”. In: *Nature* 412.6844 (2001), pp. 313–316.

[196] H. Mahmoud. *Polya Urn Models*. Taylor & Francis, 2008.

[197] S. Chakraborty. "Generating discrete analogues of continuous probability distributions-A survey of methods and constructions". In: *Journal of Statistical Distributions and Applications* 2.1 (2015), p. 6.

[198] M. Bohmann, R. Kruse, J. Sperling, C. Silberhorn, and W. Vogel. "Probing free-space quantum channels with laboratory-based experiments". In: *Physical Review A* 95.6 (2017), p. 063801.

[199] F. M. Hoppe. "Pólya-like urns and the Ewens' sampling formula". In: *Journal of Mathematical Biology* 20.1 (1984), pp. 91–94.

[200] Y. Aharonov, L. Davidovich, and N. Zagury. "Quantum random walks". In: *Physical Review A* 48.2 (1993), pp. 1687–1690.

[201] L. K. Grover. "Quantum Mechanics Helps in Searching for a Needle in a Haystack". In: *Physical Review Letters* 79.2 (1997), pp. 325–328.

[202] N. Shenvi, J. Kempe, and K. B. Whaley. "Quantum random-walk search algorithm". In: *Physical Review A* 67.5 (2003), p. 052307.

[203] A. Ambainis, J. Kempe, and A. Rivosh. "Coins make quantum walks faster". In: *Proceedings of the 16th ACM-SIAM symposium on Discrete algorithms*. Piladelphia, USA, 2005, pp. 1099–1108.

[204] V. Potoček, A. Gábris, T. Kiss, and I. Jex. "Optimized quantum random-walk search algorithms on the hypercube". In: *Physical Review A* 79.1 (2009), p. 012325.

[205] N. B. Lovett, S. Cooper, M. Everitt, M. Trevers, and V. Kendon. "Universal quantum computation using the discrete-time quantum walk". In: *Physical Review A* 81.4 (2010), p. 042330.

[206] A. M. Childs, D. Gosset, and Z. Webb. "Universal computation by multi-particle quantum walk". In: *arXiv:1205.3782* (2012).

[207] C. A. Ryan, M. Laforest, J. C. Boileau, and R. Laflamme. "Experimental implementation of a discrete-time quantum random walk on an NMR quantum-information processor". In: *Physical Review A* 72.6 (2005), p. 062317.

[208] B. Do, M. L. Stohler, S. Balasubramanian, et al. "Experimental realization of a quantum quincunx by use of linear optical elements". In: *JOSA B* 22.2 (2005), pp. 499–504.

[209] M. A. Broome, A. Fedrizzi, B. P. Lanyon, et al. "Discrete Single-Photon Quantum Walks with Tunable Decoherence". In: *Physical Review Letters* 104.15 (2010), p. 153602.

[210] J. Kempe. "Quantum random walks: An introductory overview". In: *Contemporary Physics* 44.4 (2003), pp. 307–327.

[211] A. S. Solntsev, A. A. Sukhorukov, D. N. Neshev, and Y. S. Kivshar. "Spontaneous Parametric Down-Conversion and Quantum Walks in Arrays of Quadratic Nonlinear Waveguides". In: *Physical Review Letters* 108.2 (2012), p. 023601.

[212] R. Kruse. "State Characterisation and Preparation in Periodically Poled Lithium Niobate Waveguide Arrays". Paderborn, 2013.

[213] A. S. Solntsev, F. Setzpfandt, A. S. Clark, et al. “Generation of Nonclassical Biphoton States through Cascaded Quantum Walks on a Nonlinear Chip”. In: *Physical Review X* 4.3 (2014), p. 031007.

[214] F. Lederer, G. I. Stegeman, D. N. Christodoulides, et al. “Discrete solitons in optics”. In: *Physics Reports* 463.1–3 (2008), pp. 1–126.

[215] T. Pertsch, T. Zentgraf, U. Peschel, A. Bräuer, and F. Lederer. “Anomalous Refraction and Diffraction in Discrete Optical Systems”. In: *Physical Review Letters* 88.9 (2002), p. 093901.

[216] D. N. Christodoulides, F. Lederer, and Y. Silberberg. “Discretizing light behaviour in linear and nonlinear waveguide lattices”. In: *Nature* 424.6950 (2003), pp. 817–823.

[217] D. Mandelik, H. S. Eisenberg, Y. Silberberg, R. Morandotti, and J. S. Aitchison. “Band-Gap Structure of Waveguide Arrays and Excitation of Floquet-Bloch Solitons”. In: *Physical Review Letters* 90.5 (2003), p. 053902.

[218] R. Iwanow, R. Schiek, G. Stegeman, et al. “Arrays of weakly coupled, periodically poled lithium niobate waveguides: beam propagation and discrete spatial quadratic solitons”. In: *Opto-Electron. Rev.* 13 (2005), p. 113.

[219] A. Szameit, T. Pertsch, F. Dreisow, et al. “Light evolution in arbitrary two-dimensional waveguide arrays”. In: *Physical Review A* 75.5 (2007), p. 053814.

[220] C. Kittel. *Introduction to Solid State Physics*. 8th ed. Wiley, 2004.

[221] F. Setzpfandt, A. S. Solntsev, D. N. Neshev, et al. “Temporal dynamics of spatially localized waves in quadratic nonlinear waveguide arrays”. In: *Physical Review A* 89.3 (2014), p. 033863.

[222] K. Pearson. “The problem of the random walk”. In: *Nature* 72 (1905), p. 294.

[223] A. Einstein. “Die von der molekularkinetischen Theorie der Wärme geforderte Bewegung von in ruhenden Flüssigkeiten von suspendierten Teilchen”. In: *Annalen der Physik* 18.8 (1905), p. 599.

[224] A. Fick. “Ueber Diffusion”. In: *Pogg. Ann. Phys. Chem.* 170 (1855), p. 59.

[225] J. B. J. Fourier. “Theorie analytique de la chaleur”. In: *Didot* (1822), p. 499.

[226] C. S. Hamilton, S. Barkhofen, L. Sansoni, I. Jex, and C. Silberhorn. “Driven discrete time quantum walks”. In: *New Journal of Physics* 18.7 (2016), p. 073008.

[227] S. M. Barnett and P. M. Radmore. *Methods in Theoretical Quantum Optics*. Oxford University Press, USA, 1997.

[228] X. Ma and W. Rhodes. “Multimode squeeze operators and squeezed states”. In: *Physical Review A* 41.9 (1990), pp. 4625–4631.

[229] R. V. Roussev. *Optical-frequency Mixers in Periodically Poled Lithium Niobate: Materials, Modeling and Characterization*. Stanford University, 2006.

[230] A. M. Childs, R. Cleve, E. Deotto, et al. “Exponential algorithmic speedup by quantum walk”. In: *arXiv:quant-ph/0209131* (2003), p. 59.

[231] E. Farhi and S. Gutmann. “Quantum computation and decision trees”. In: *Physical Review A* 58.2 (1998), pp. 915–928.

[232] A. M. Childs and J. Goldstone. “Spatial search by quantum walk”. In: *Physical Review A* 70.2 (2004), p. 022314.

[233] E. Feldman, M. Hillery, H.-W. Lee, et al. “Finding structural anomalies in graphs by means of quantum walks”. In: *Physical Review A* 82.4 (2010), p. 040301.

[234] S. Cottrell and M. Hillery. “Finding Structural Anomalies in Star Graphs Using Quantum Walks”. In: *Physical Review Letters* 112.3 (2014), p. 030501.

[235] Y. Ide, N. Konno, E. Segawa, and X.-P. Xu. “Localization of Discrete Time Quantum Walks on the Glued Trees”. In: *Entropy* 16.3 (2014), pp. 1501–1514.

[236] R. Kruse, C. S. Hamilton, S. Barkhofen, et al. “Non-linear waveguide arrays and Boson Sampling applications”. In: (in preparation).

[237] M. A. Broome, A. Fedrizzi, J. Rahimi-Keshari S.and Dove, et al. “Photonic Boson Sampling in a Tunable Circuit”. In: *Science* (2012).

[238] M. Tillmann, B. Dakić, R. Heilmann, et al. “Experimental boson sampling”. In: *Nature Photonics* 7.7 (2013), pp. 540–544.

[239] J. B. Spring, B. J. Metcalf, P. C. Humphreys, et al. “Boson Sampling on a Photonic Chip”. In: *Science* (2012).

[240] A. Crespi, R. Osellame, R. Ramponi, et al. “Integrated multimode interferometers with arbitrary designs for photonic boson sampling”. In: *Nature Photonics* 7.7 (2013), pp. 545–549.

[241] N. Spagnolo, C. Vitelli, M. Bentivegna, et al. “Experimental validation of photonic boson sampling”. In: *Nature Photonics* 8.8 (2014), pp. 615–620.

[242] J. Carolan, J. D. A. Meinecke, P. J. Shadbolt, et al. “On the experimental verification of quantum complexity in linear optics”. In: *Nature Photonics* 8.8 (2014), pp. 621–626.

[243] A. P. Lund, A. Laing, S. Rahimi-Keshari, et al. “Boson Sampling from a Gaussian State”. In: *Physical Review Letters* 113.10 (2014), p. 100502.

[244] QUCHIP Project Partners. “Boson sampling”. In: *Wikipedia* (2016).

[245] P. Shor. “Polynomial-Time Algorithms for Prime Factorization and Discrete Logarithms on a Quantum Computer”. In: *SIAM Journal on Computing* 26.5 (1997), pp. 1484–1509.

[246] J. H. Plantenberg, P. C. de Groot, C. J. P. M. Harmans, and J. E. Mooij. “Demonstration of controlled-NOT quantum gates on a pair of superconducting quantum bits”. In: *Nature* 447.7146 (2007), pp. 836–839.

[247] L. DiCarlo, J. M. Chow, J. M. Gambetta, et al. “Demonstration of two-qubit algorithms with a superconducting quantum processor”. In: *Nature* 460.7252 (2009), pp. 240–244.

[248] T. D. Ladd, F. Jelezko, R. Laflamme, et al. “Quantum computers”. In: *Nature* 464.7285 (2010), pp. 45–53.

[249] A. Fedorov, L. Steffen, M. Baur, M. P. da Silva, and A. Wallraff. "Implementation of a Toffoli gate with superconducting circuits". In: *Nature* 481.7380 (2012), pp. 170–172.

[250] M. D. Reed, L. DiCarlo, S. E. Nigg, et al. "Realization of three-qubit quantum error correction with superconducting circuits". In: *Nature* 482.7385 (2012), pp. 382–385.

[251] R. Barends, J. Kelly, A. Megrant, et al. "Superconducting quantum circuits at the surface code threshold for fault tolerance". In: *Nature* 508.7497 (2014), pp. 500–503.

[252] S. Scheel. "Permanents in linear optical networks". In: *Acta Physica Slovaca* 58 (2004), p. 675.

[253] J. B. Spring. "Single Photon Generation and Quantum Computing with Integrated Photonics". PhD thesis. Oxford: Oriel College, Oxford, 2014.

[254] M. Sipser. *Introduction to the Theory of Computation*. Cengage Learning, 2012.

[255] L. G. Valiant. "The complexity of computing the permanent". In: *Theoretical Computer Science* 8.2 (1979), pp. 189–201.

[256] P. Michler, A. Kiraz, C. Becher, et al. "A Quantum Dot Single-Photon Turnstile Device". In: *Science* 290.5500 (2000), pp. 2282–2285.

[257] C. Santori, D. Fattal, J. Vučković, G. S. Solomon, and Y. Yamamoto. "Indistinguishable photons from a single-photon device". In: *Nature* 419.6907 (2002), pp. 594–597.

[258] S. Buckley, K. Rivoire, and J. Vučković. "Engineered quantum dot single-photon sources". In: *Reports on Progress in Physics* 75.12 (2012), p. 126503.

[259] Y.-M. He, Y. He, Y.-J. Wei, et al. "On-demand semiconductor single-photon source with near-unity indistinguishability". In: *Nature Nanotechnology* 8.3 (2013), pp. 213–217.

[260] X. Ding, Y. He, Z.-C. Duan, et al. "On-Demand Single Photons with High Extraction Efficiency and Near-Unity Indistinguishability from a Resonantly Driven Quantum Dot in a Micropillar". In: *Physical Review Letters* 116.2 (2016), p. 020401.

[261] N. Somaschi, V. Giesz, L. D. Santis, et al. "Near-optimal single-photon sources in the solid state". In: *Nature Photonics* 10.5 (2016), pp. 340–345.

[262] H. Wang, Y. He, Y.-H. Li, et al. "High-efficiency multiphoton boson sampling". In: *Nature Photonics* 11.6 (2017), pp. 361–365.

[263] Y. He, X. Ding, Z.-E. Su, et al. "Time-Bin-Encoded Boson Sampling with a Single-Photon Device". In: *Physical Review Letters* 118.19 (2017), p. 190501.

[264] J. C. Loredo, M. A. Broome, P. Hilaire, et al. "Boson Sampling with Single-Photon Fock States from a Bright Solid-State Source". In: *Physical Review Letters* 118.13 (2017), p. 130503.

[265] M. Bentivegna, N. Spagnolo, C. Vitelli, et al. "Experimental scattershot boson sampling". In: *Science Advances* 1.3 (2015), e1400255.

[266] S. Rahimi-Keshari, A. P. Lund, and T. C. Ralph. "What Can Quantum Optics Say about Computational Complexity Theory?" In: *Physical Review Letters* 114.6 (2015), p. 060501.

[267] J. Huh, G. G. Guerreschi, B. Peropadre, J. R. McClean, and A. Aspuru-Guzik. "Boson sampling for molecular vibronic spectra". In: *Nature Photonics* 9.9 (2015), pp. 615–620.

[268] A. Haar. "Die Maßbegriffe in der Theorie der kontinuierlichen Gruppen". In: *Annalen der Mathematik* 34 (1933), pp. 147–169.

[269] G. B. Folland. *A Course in Abstract Harmonic Analysis, Second Edition*. 2nd ed. Textbooks in Mathematics. CRC Press, 2015.

[270] D. H. Jundt. "Temperature-dependent Sellmeier equation for the index of refraction, n_e, in congruent lithium niobate". In: *Optics Letters* 22 (1997), pp. 1553–1555.

[271] A. B. U'Ren, C. Silberhorn, R. Erdmann, et al. "Generation of Pure-State Single-Photon Wavepackets by Conditional Preparation Based on Spontaneous Parametric Downconversion". In: *Las. Phys. 15 146 (2005)* (2005).

[272] A. S. Solntsev, A. A. Sukhorukov, D. N. Neshev, and Y. S. Kivshar. "Photon-pair generation in arrays of cubic nonlinear waveguides". In: *Optics Express* 20.24 (2012), pp. 27441–27446.

[273] S. Barkhofen, T. J. Bartley, L. Sansoni, et al. "Driven Boson Sampling". In: *Physical Review Letters* 118.2 (2017), p. 020502.

[274] C. S. Hamilton, R. Kruse, L. Sansoni, et al. "Gaussian Boson Sampling". In: *arXiv:1612.01199 [quant-ph]* (2016).

[275] R. Kruse, C. S. Hamilton, S. Barkhofen, et al. "A detailed study of Gaussian Boson Sampling". In: (in preparation).

[276] E. R. Caianiello. "On quantum field theory — I: explicit solution of Dyson's equation in electrodynamics without use of feynman graphs". In: *Il Nuovo Cimento (1943-1954)* 10.12 (1953), pp. 1634–1652.

[277] E. R. Caianiello. *Combinatorics and Renormalization in Quantum Field Theory*. Benjamin-Cummings Publishing Company, 1973.

[278] V. V. Dodonov, O. V. Man'ko, and V. I. Man'ko. "Photon distribution for one-mode mixed light with a generic Gaussian Wigner function". In: *Physical Review A* 49.4 (1994), pp. 2993–3001.

[279] A. Ferraro, S. Olivares, and M. G. A. Paris. "Gaussian states in continuous variable quantum information". In: *arXiv:quant-ph/0503237* (2005).

[280] L. Comtet. *Advanced Combinatorics: The Art of Finite and Infinite Expansions*. Springer Science & Business Media, 1974.

[281] M. Hardy. "Combinatorics of partial derivatives". In: *The Electronic Journal of Combinatorics* 13.1 (2006).

[282] H. Minc and M. Marcus. *Permanents*. Cambridge University Press, 1984.

[283] F. J. Dyson. "Statistical Theory of the Energy Levels of Complex Systems. I". In: *Journal of Mathematical Physics* 3.1 (1962), pp. 140–156.

[284] M. L. Mehta. *Random Matrices*. Academic Press, 2004.

[285] T. Jiang. “The entries of circular orthogonal ensembles”. In: *Journal of Mathematical Physics* 50.6 (2009), p. 063302.

[286] A. I. Barvinok. “Two Algorithmic Results for the Traveling Salesman Problem”. In: *Mathematics of Operations Research* 21.1 (1996), pp. 65–84.

[287] R. Kan. “From moments of sum to moments of product”. In: *Journal of Multivariate Analysis* 99.3 (2008), pp. 542–554.

[288] J. M. Hilbe. *Negative Binomial Regression*. Cambridge University Press, 2011.

[289] T. Suhara and M. Fujimura. *Waveguide Nonlinear-Optic Devices*. Springer, 2003.

And I want to thank you
For giving me the best day of my life
And, oh, just to be with you
Is having the best day of my life

Dido - Thank you

Acknowledgements

Well, it's done. You have finally made it through 144 pages of thesis and references. So, first of all: Thank you dear Reader for reading. I hope that you had at least a little bit of fun and learned something.

Furthermore, I would like to thank Prof. Dr. Christine Silberhorn for giving me the opportunity to write my thesis in her group. I would also like to thank her, as well as my second referee Prof. Dr. Torsten Meier for the evaluation of my thesis and writing of the reports.

I would further like to acknowledge the german and european tax-payer, i.e. you (most likely) for my financial support via the grants SFB/TRR 142 from the Deutsche Forschungsgesellschaft and from the European Union's Horizon 2020 projects QCUMbER (No. 665148) and QUCHIP (No. 641039).

Apart from the financial support, I thank my collaborators from the theory side, especially the groups from Werner Vogel in Rostock, where I had the pleasure to work with Martin Bohmann on the time-multiplexing projects and the group from Igor Jex in Prague, where I worked with Craig Hamilton on the non-linear waveguide array and BosonSampling projects. Thanks to you both, Martin and Craig for the fruitful cooperation and stimulating discussions.

But I did not only have collaborators from outside. I also would like to thank all of my co-authors from Paderborn, in alphabetical order: Sonja Barkhofen, Tim Bartley, Sebastian Brauner, Georg Harder, Raimund Ricken, Linda Sansoni and Johannes Tiedau. Thanks for reading my literary attempts, correcting my grammar and reminding me, when I had forgotten to define a mathematical symbol in the text.

Furthermore, I would like to thank the rest of the group for the good time that I had here. I learned a lot from discussions with you and it was really a pleasure to be your co-worker. Again in alphabetical order, I would like to thank Vahid Ansari, Melanie Engelkemeier, Kerstin Falke, Harald Herrmann, Mahnaz Kejdehi, Sebastian Lengeling, Kai-Hong Lou, Marcello Massaro, Florian Meier, Evan Meyer-Scott, Nicola Montaut, Thomas Nitsche, Rita Prevor, Viktor Quiring, Helge Rütz, Matteo Santandrea, Michael Stefszky and the alumnis Malte Avenhaus, Benjamin Brecht (who let me use his LaTeX layout), Fabian Elster, Stephan Krapick, Kaisa Laiho, Andreas Schreiber and Hubertus Suche. If I have forgotten anyone, please forgive me. There are (and have been) too many people in this group during my time.

How would I ever be able to thank my office mates? Thanks to Laura Padberg and Christof Eigner for the fun work days. Especially, I would like to thank Laura for waiting with the punchlines until I had swallowed my sip of water. Oh dear, your surprisingly dark humour made me want to spit my water over the desk more often than not. Also dear Christof, thank you for the $8\frac{1}{2}$ years since the "Mathematik Vorkurs", where we have now spent every work day

together. It was an honour and a pleasure to work with you. And, as I promised: Christof Eigner rendered foodnancial support in form of a miniKnoppers. There, you have it. Happy now?

In the context of proof-reading this thesis, I would like to thank especially Inka Haak for valuable feedback on the introduction of this thesis. It was fascinating to get a different perspective on the framework of quantum optics. Furthermore, I appreciate the feedback that I got from Markus Allgaier, Patrick Bartkowiak, Andreas Christ, Johannes Tiedau, Georg Harder, Benjamin Brecht, Martin Bohmann and Tim Bartley.

I would especially like to thank my break partners Philipp Mönkebüscher for lunch and Markus Allgaier for coffee. Breaking is only half the fun[1], when you do it alone. Thanks for the mutual support and all the discussion topics that ranged from everything to nothing.

Finally, I want to thank my family for the unending support of my work. For the sound advice that you gave me during this time and for the sweets that I could always find in the usual place. Last, but not least, I would like to thank my dear Andi for the support, which was more important to me than my first cup of coffee in the morning.

[1] Pun intended. Even, if it was a bad one.

A List of Scientific Contributions

A.1 Publications and Author Contributions

Ordered after first appearance in table of contents:

(1) Dual-path source engineering in integrated quantum optics [70]

Regina Kruse, Linda Sansoni, Sebastian Brauner, Raimund Ricken, Craig S. Hamilton, Igor Jex and Christine Silberhorn
Phys. Rev. A 92, 053841 (2015)

R.R. prepared the samples and S.B. performed the classical characterisation. R.K. and L.S. conceived the idea. R.K. conducted the experiment. R.K. and L.S. executed the data analysis and prepared the manuscript. I.J. and C.S. supervised the work. All authors contributed to the final manuscript.

(2) Limits of the time-multiplexed photon-counting method [127]

Regina Kruse, Johannes Tiedau, Tim J. Bartley, Sonja Barkhofen and Christine Silberhorn
Phys. Rev. A 95,023815 (2017)

R.K. developed the idea, performed the calculations and wrote the paper. J.T. helped to conceive the correct figures of merit. T.J.B. and S.B. helped to supervise the project. All authors contributed to the final version of the manuscript.

(3) Direct calibration of click-counting detectors [151]

Martin Bohmann, Regina Kruse, Jan Sperling, Christine Silberhorn and Werner Vogel
Phys. Rev. A 95, 033806 (2017)

M.B. developed the theory for the calibration method. R.K. designed and performed the experiment and analysed the raw data and experimental imperfections. M.B. analysed the click statistics for the calibration. Both wrote the first version of the paper. J.S. helped with paper refinements. C.S. and W.V. supervised the work.

(4) Probing free-space quantum channels with laboratory-based experiments [198]

Martin Bohmann, Regina Kruse, Jan Sperling, Christine Silberhorn and Werner Vogel
Phys. Rev. A 95, 063801 (2017)

R.K. designed and performed the experiment and analysed the raw data. M.B. used his expertise in atmospheric communication to test the non-classicality of the generated quantum state for different atmospheric models. Both wrote the first version of the manuscript. J.S. helped with the refinement of the manuscript. C.S. and W.V. supervised the work.

(5) Driven Quantum Walks [65]

Craig S. Hamilton, Regina Kruse, Linda Sansoni, Christine Silberhorn and Igor Jex
Phys. Rev. Lett. 113, 083602 (2014)

C.S.H. conceived the idea and performed the calculations. R.K. and L.S. helped C.S.H. with the clarification of the concept and paper writing. C.S. and I.J. supervised the work. All authors contributed to the final version of the manuscript.

(6) Non-linear waveguide arrays for Boson Sampling applications [236]

Regina Kruse, Craig S. Hamilton, Linda Sansoni, Sonja Barkhofen, Igor Jex, and Christine Silberhorn
in preparation

R.K. and C.S.H. analysed the system and calculated the transfer matrix for Boson Sampling. R.K. wrote the paper. L.S., S.B. helped to supervise the project. I.J. and C.S. supervised the work.

(7) Gaussian Boson Sampling [274]

Craig S. Hamilton, Regina Kruse, Linda Sansoni, Sonja Barkhofen, Christine Silberhorn and Igor Jex
arXiv:1612.01199 (2016), submitted to Phys. Rev. Lett.

C.S.H. developed the idea and performed the calculations, R.K. helped with the clarification of the concept and provided the proof for approximate sampling. R.K. and C.S.H. wrote the manuscript. S.B. and L.S. helped to supervise the project. I.J. and C.S. supervised the work. All authors contributed to the final manuscript.

(8) A detailed study of Gaussian Boson Sampling [275]

Regina Kruse, Craig S. Hamilton, Linda Sansoni, Sonja Barkhofen, Igor Jex and Christine Silberhorn
to be submitted to Phys. Rev. A

C.S.H. developed the idea and performed the calculations, R.K. helped with the clarification of the concept and provided the proof for approximate sampling. R.K. wrote the manuscript. S.B. and L.S. helped to supervise the project. I.J. and C.S. supervised the work. All authors contributed to the final manuscript.

A.1.1 Additional Publications

(9) Spatio-spectral characteristics of parametric down-conversion in waveguide arrays

Regina Kruse, Fabian Katzschmann, Andreas Christ, Andreas Schreiber, Sarah Wilhelm, Kaisa Laiho, Aurél Gábris, Craig S. Hamilton, Igor Jex, Christine Silberhorn
New J. Phys. 15, 083046 (2013)

(10) Driven Boson Sampling

Sonja Barkhofen, Tim J. Bartley, Linda Sansoni, Regina Kruse, Craig S. Hamilton, Igor Jex, Christine Silberhorn
Phys. Rev. Lett. 118, 020502 (2017)

(11) Staking Out the Physical Sectors of Hilbert Spaces

Dmitri Mogilevtsev, Yong Siah Teo, Jaroslav Rehacek, Zdenek Hradil, Johannes Tiedau, Regina Kruse, Georg Harder, Christine Silberhorn and Luis L. Sanchez-Soto
arXiv:1609.02797 (2016), submitted to New Jour. Phys.

(12) Heralded orthogonalisation of coherent states and their conversion to discrete-variable superpositions

Regina Kruse, Christine Silberhorn and Tim J. Bartley
arXiv:1702.00200 (2017), submitted to Phys. Rev. A

A.2 Conference Contributions

2014:

(1) Talk: Characterisation of Spatial Correlations of PDC in Waveguide Arrays

Regina Kruse, Fabian Katzschmann, Benjamin Brecht, Linda Sansoni, and Christine Silberhorn
DPG Spring Meeting, Berlin

(2) Poster: Generation of genuine 2-photon N00N states in non-linear coupled waveguides

Regina Kruse, Linda Sansoni, Sebastian Brauner, Raimund Ricken, Craig S. Hamilton, Igor Jex, Christine Silberhorn
QCMC, Hefei, China

(3) Poster: Driven Quantum Walks

Craig S. Hamilton, Regina Kruse, Linda Sansoni, Christine Silberhorn, Igor Jex
QCMC, Hefei, China

2015:

(1) Talk: N00N states from a single non-linear device

Regina Kruse, Linda Sansoni, Sebastian Brauner, Raimund Ricken, Craig S. Hamilton, Igor Jex, Christine Silberhorn
DPG Spring Meeting, Heidelberg

(2) Talk: A single non-linear directional coupler to generate N00N states

Regina Kruse, Linda Sansoni, Sebastian Brauner, Raimund Ricken, Craig S. Hamilton, Igor Jex, Christine Silberhorn
CLEO Europe, Munich

(3) Poster: Dual-path photon pair sources by coupled non-linear waveguides

Regina Kruse, Linda Sansoni, Sebastian Brauner, Raimund Ricken, Craig S. Hamilton, Igor Jex, Christine Silberhorn
CoQuS Summer School, Vienna

2016:

(1) Poster: Gaussian Boson Sampling

Craig S. Hamilton, Regina Kruse, Linda Sansoni, Sonja Barkhofen, Christine Silberhorn, Igor Jex
Workshop on Quantum Simulation and Quantum Walks, Prague

2017:

(1) Poster: Limits on the time-multiplexed photon counting method

Regina Kruse, Johannes Tiedau, Tim J. Bartley, Sonja Barkhofen, and Christine Silberhorn
DPG Spring Meeting, Mainz

(2) Talk: Gaussian Boson Sampling

Craig S. Hamilton, Regina Kruse, Linda Sansoni, Sonja Barkhofen, Christine Silberhorn and Igor Jex
CLEO US, San José

B Derivation of the Dual-path PDC State

In this appendix, we present a detailed version of the derivation for the final down-conversion output state from the non-linear coupler in section 2.2. In section 2.1, we introduced the coupling behaviour of classical light in a coupled waveguide structure and derived the eigensolutions of the coupled system.

In order to calculate the down-conversion state, we also have to consider the pump field representation in the eigenbasis of the coupled system. We assume, that the pump field has an extremely small mode overlap between the two waveguides because its wavelength is in the near infrared regime and far off the wavelength of the generated quantum fields. As the coupling behaviour crucially depends on the mode overlap, the pump light does not couple significantly and we therefore assume $C_p \approx 0$.

With this, we can write the pump field as

$$\mathcal{E}_p^{(+)} = \mathcal{B}_p \int d\omega_p \alpha(\omega_p)(\gamma S + \delta A) e^{i[\beta(\omega_p)z - \omega_p t]}\,, \tag{B.1}$$

where $\alpha(\omega_p)$ is the spectral shape of the pump, γ and δ are the coefficients containing the spatial excitation of the system

$$\begin{aligned} \gamma &= \frac{1}{\sqrt{2}}\left(p_1 + e^{i\Delta_p} p_2\right) \\ \delta &= \frac{1}{\sqrt{2}}\left(p_1 - e^{i\Delta_p} p_2\right) \end{aligned} \tag{B.2}$$

and $\mathcal{B}_p$ collects all constants. The two amplitudes p_1 and p_2 denote the pump excitation in waveguides 1 and 2 respectively and the input field is given by

$$E_{\text{in}} = p_1 E_1(x,y) + e^{i\Delta_p} p_2 E_2(x,y)\,, \tag{B.3}$$

where $E_i(x,y)$ denotes the spatial mode of the pump in waveguide i.

B.1 Quantum Fields and PDC State

With the description of the pump field in the eigenbasis of the coupled waveguides, we have all ingredients that we need to calculate the output state of the non-linear coupler. We write our quantum fields as

$$\hat{E}^{(-)} = \mathcal{B}_q \int d\omega (S^* e^{-i[\beta_S(\omega)z - \omega t]} \hat{a}_S^\dagger(\omega) + A^* e^{-i[\beta_A(\omega)z - \omega t]} \hat{a}_A^\dagger(\omega))\,, \tag{B.4}$$

where $\beta_S(\omega)$ [$\beta_A(\omega)$] is the propagation constant of the symmetric (antisymmetric) mode, $\hat{a}_S^\dagger$ [$\hat{a}_A^\dagger$] creates a photon in the symmetric (antisymmetric) mode and $\mathcal{B}_q$ collects all constants.

Using the expressions for pump and quantum fields in the eigenbasis of the coupler, we can

insert them into the Hamiltonian of equation (2.9) in section 2.2 and gain

$$\begin{aligned}\hat{H}_{\mathrm{int}} &= \chi^{(2)} \int\limits_V \mathrm{d}^3 r \, (\mathcal{E}_p^{(+)} \hat{E}^{(-)} \hat{E}^{(-)} + \mathrm{h.c.}) \\ &= B \int \mathrm{d}x \int \mathrm{d}z \int \mathrm{d}\omega_p \int \mathrm{d}\omega_s \int \mathrm{d}\omega_i \, \Big[\alpha(\omega_p)(\gamma S + \delta A) e^{i[\beta(\omega_p) z - \omega_p t]} \\ &\quad \times (S^* e^{-i[\beta_S(\omega_s) z - \omega_s t]} \hat{a}_S^\dagger(\omega_s) + A^* e^{-i[\beta_A(\omega_s) z - \omega_s t]} \hat{a}_A^\dagger(\omega_s)) \\ &\quad \times (S^* e^{-i[\beta_S(\omega_i) z - \omega_i t]} \hat{a}_S^\dagger(\omega_i) + A^* e^{-i[\beta_A(\omega_i) z - \omega_i t]} \hat{a}_A^\dagger(\omega_i)) + \mathrm{h.c.} \Big] \,,\end{aligned} \tag{B.5}$$

where $\chi^{(2)}$ is the non-linear coefficient of our selected process[1] and B collects all constants.

As we are considering a type-I process, the signal and idler photons are fundamentally indistinguishable, therefore, we loose the indices in the electric quantum fields and the creation operators. Multiplying the electric fields and introducing the following abbreviations

$$\begin{aligned} \Delta\beta_{S,S} &= \beta(\omega_p) - \beta_S(\omega_s) - \beta_S(\omega_i) \\ \Delta\beta_{S,A} &= \beta(\omega_p) - \beta_S(\omega_s) - \beta_A(\omega_i) \\ \Delta\beta_{A,S} &= \beta(\omega_p) - \beta_A(\omega_s) - \beta_S(\omega_i) \\ \Delta\beta_{A,A} &= \beta(\omega_p) - \beta_A(\omega_s) - \beta_A(\omega_i) \,, \end{aligned} \tag{B.6}$$

we can rewrite the Hamiltonian as

$$\begin{aligned}\hat{H}_{\mathrm{int}} = B \int \mathrm{d}z \int \mathrm{d}\omega_p \int \mathrm{d}\omega_s \int \mathrm{d}\omega_i \, \alpha(\omega_p) \\ \Bigg[\gamma \underbrace{\int \mathrm{d}x \, S S^* S^*}_{2\sqrt{2}} e^{i(\Delta\beta_{S,S} z - [\omega_p - (\omega_s + \omega_i)]t)} \hat{a}_S^\dagger(\omega_s) \hat{a}_S^\dagger(\omega_i) \\ + \delta \underbrace{\int \mathrm{d}x \, A S^* S^*}_{0} e^{i(\Delta\beta_{S,S} z - [\omega_p - (\omega_s + \omega_i)]t)} \hat{a}_S^\dagger(\omega_s) \hat{a}_S^\dagger(\omega_i) \\ + \gamma \underbrace{\int \mathrm{d}x \, S S^* A^*}_{0} e^{i(\Delta\beta_{S,A} z - [\omega_p - (\omega_s + \omega_i)]t)} \hat{a}_S^\dagger(\omega_s) \hat{a}_A(\omega_i) \\ + \delta \underbrace{\int \mathrm{d}x \, A S^* A^*}_{2\sqrt{2}} e^{i(\Delta\beta_{S,A} z - [\omega_p - (\omega_s + \omega_i)]t)} \hat{a}_S^\dagger(\omega_s) \hat{a}_A^\dagger(\omega_i) \\ + \gamma \underbrace{\int \mathrm{d}x \, S A^* S^*}_{0} e^{i(\Delta\beta_{A,S} z - [\omega_p - (\omega_s + \omega_i)]t)} \hat{a}_A^\dagger(\omega_s) \hat{a}_S(\omega_i)\end{aligned} \tag{B.7}$$

[1] The considered *type-I* process uses the d_{33} coefficient in $LiNbO_3$ [289].

$$
\begin{aligned}
&+ \delta \underbrace{\int \mathrm{d}x\, AA^*S^*}_{2\sqrt{2}}\, e^{i(\Delta\beta_{A,S}z-[\omega_p-(\omega_s+\omega_i)]t)}\hat{a}_A^\dagger(\omega_s)\hat{a}_S^\dagger(\omega_i) \\
&+ \gamma \underbrace{\int \mathrm{d}x\, SA^*A^*}_{2\sqrt{2}}\, e^{i(\Delta\beta_{A,A}z-[\omega_p-(\omega_s+\omega_i)]t)}\hat{a}_A^\dagger(\omega_s)\hat{a}_A(\omega_i) \\
&+ \delta \underbrace{\int \mathrm{d}x\, AA^*A^*}_{2\sqrt{2}}\, e^{i(\Delta\beta_{A,A}z-[\omega_p-(\omega_s+\omega_i)]t)}\hat{a}_A^\dagger(\omega_s)\hat{a}_A^\dagger(\omega_i)\Bigg] .
\end{aligned}
$$

With this Hamiltonian, we can calculate the generated output state of the non-linear coupler system. We construct a generation unitary from the Hamiltonian by the usual Schrödinger rules with [2]

$$
\hat{U}_{\mathrm{PDC}} = \exp\left(-\frac{i}{\hbar}\hat{H}_{\mathrm{int}}\right) . \tag{B.8}
$$

Using a Taylor expansion up to first order and neglecting the vacuum term, we gain the wanted output state in the two-photon picture

$$
\begin{aligned}
|\Psi\rangle^{\mathrm{eig}} = \frac{1}{\mathcal{N}} \int \mathrm{d}\omega_s \int \mathrm{d}\omega_i\, \alpha(\omega_s+\omega_i) \\
\times \Bigg[\gamma\,\mathrm{sinc}\left(\Delta\beta_{S,S}\frac{L}{2}\right) e^{-i\Delta\beta_{S,S}\frac{L}{2}}\hat{a}_S(\omega_s)\hat{a}_S(\omega_i) \\
+ \delta\,\mathrm{sinc}\left(\Delta\beta_{S,A}\frac{L}{2}\right) e^{-i\Delta\beta_{S,A}\frac{L}{2}}\hat{a}_S(\omega_s)\hat{a}_A(\omega_i) \\
+ \delta\,\mathrm{sinc}\left(\Delta\beta_{A,S}\frac{L}{2}\right) e^{-i\Delta\beta_{A,S}\frac{L}{2}}\hat{a}_A(\omega_s)\hat{a}_S(\omega_i) \\
+ \gamma\,\mathrm{sinc}\left(\Delta\beta_{A,A}\frac{L}{2}\right) e^{-i\Delta\beta_{A,A}\frac{L}{2}}\hat{a}_A(\omega_s)\hat{a}_A(\omega_i)\Bigg] |0\rangle
\end{aligned} \tag{B.9}
$$

in the eigenbasis of the coupled system, where $\mathcal{N}$ is the normalisation constant of our state.

However in the laboratory, we do not measure in the eigenbasis of the coupled waveguide system, but in the waveguide basis directly. As such, we have to apply the corresponding back-transformation

$$
\begin{aligned}
E_1 &= \frac{1}{\sqrt{2}}(S+A) \\
E_2 &= \frac{1}{\sqrt{2}}(S-A)
\end{aligned} \tag{B.10}
$$

to the output state in the eigenbasis. As this is the transformation associated with a 50:50 beam splitter, we will observe Hong-Ou-Mandel interference effects [59] for indistinguishable photons and some terms will cancel out in the basis transformation, generating the desired two-photon

N00N state. With the applied back-transformation, the output state in the waveguide basis reads

$$
\begin{aligned}
|\Psi\rangle^{\mathrm{WG}} &= \frac{1}{2\sqrt{\mathcal{N}}}\int \mathrm{d}\omega_s \mathrm{d}\omega_i\, \alpha(\omega_s+\omega_i) \\
&\times \Bigg[\Bigg(\gamma\left\{\operatorname{sinc}\left(\Delta\beta_{S,S}\frac{L}{2}\right)e^{-i\Delta\beta_{S,S}\frac{L}{2}} + \operatorname{sinc}\left(\Delta\beta_{A,A}\frac{L}{2}\right)e^{-i\Delta\beta_{A,A}\frac{L}{2}}\right\} \\
&\quad +\delta\left\{\operatorname{sinc}\left(\Delta\beta_{S,A}\frac{L}{2}\right)e^{-i\Delta\beta_{S,A}\frac{L}{2}} + \operatorname{sinc}\left(\Delta\beta_{A,S}\frac{L}{2}\right)e^{-i\Delta\beta_{A,S}\frac{L}{2}}\right\}\Bigg)\hat{a}_1^\dagger(\omega_s)\hat{a}_1^\dagger(\omega_i) \\
&+\Bigg(\gamma\left\{\operatorname{sinc}\left(\Delta\beta_{S,S}\frac{L}{2}\right)e^{-i\Delta\beta_{S,S}\frac{L}{2}} - \operatorname{sinc}\left(\Delta\beta_{A,A}\frac{L}{2}\right)e^{-i\Delta\beta_{A,A}\frac{L}{2}}\right\} \\
&\quad -\delta\underbrace{\left\{\operatorname{sinc}\left(\Delta\beta_{S,A}\frac{L}{2}\right)e^{-i\Delta\beta_{S,A}\frac{L}{2}} - \operatorname{sinc}\left(\Delta\beta_{A,S}\frac{L}{2}\right)e^{-i\Delta\beta_{A,S}\frac{L}{2}}\right\}}_{=0}\Bigg)\hat{a}_1^\dagger(\omega_s)\hat{a}_2^\dagger(\omega_i) \\
&+\Bigg(\gamma\left\{\operatorname{sinc}\left(\Delta\beta_{S,S}\frac{L}{2}\right)e^{-i\Delta\beta_{S,S}\frac{L}{2}} - \operatorname{sinc}\left(\Delta\beta_{A,A}\frac{L}{2}\right)e^{-i\Delta\beta_{A,A}\frac{L}{2}}\right\} \\
&\quad +\delta\underbrace{\left\{\operatorname{sinc}\left(\Delta\beta_{S,A}\frac{L}{2}\right)e^{-i\Delta\beta_{S,A}\frac{L}{2}} - \operatorname{sinc}\left(\Delta\beta_{A,S}\frac{L}{2}\right)e^{-i\Delta\beta_{A,S}\frac{L}{2}}\right\}}_{=0}\Bigg)\hat{a}_2^\dagger(\omega_s)\hat{a}_1^\dagger(\omega_i) \\
&+\Bigg(\gamma\left\{\operatorname{sinc}\left(\Delta\beta_{S,S}\frac{L}{2}\right)e^{-i\Delta\beta_{S,S}\frac{L}{2}} + \operatorname{sinc}\left(\Delta\beta_{A,A}\frac{L}{2}\right)e^{-i\Delta\beta_{A,A}\frac{L}{2}}\right\} \\
&\quad -\delta\left\{\operatorname{sinc}\left(\Delta\beta_{S,A}\frac{L}{2}\right)e^{-i\Delta\beta_{S,A}\frac{L}{2}} + \operatorname{sinc}\left(\Delta\beta_{A,S}\frac{L}{2}\right)e^{-i\Delta\beta_{A,S}\frac{L}{2}}\right\}\Bigg)\hat{a}_2^\dagger(\omega_s)\hat{a}_2^\dagger(\omega_i)\Bigg]|0\rangle\,.
\end{aligned}
\tag{B.11}
$$

The contributions from the antisymmetric eigenmode in the cross-coincidences (i.e. coincidences between the two waveguides 1 and 2: $\hat{a}_1^\dagger(\omega_s)\hat{a}_2^\dagger(\omega_i)$ and $\hat{a}_2^\dagger(\omega_s)\hat{a}_1^\dagger(\omega_i)$) disappear because of the symmetry in the phase-mismatch between S, A and A, S. This is the influence of the Hong-Ou-Mandel effect in the basis transformation, as the two phase-matching conditions are indistinguishable.

C Setup Characterisation of the Dual-Path source

In this appendix, we discuss the characterisation of the dual-path source setup in section 2.4. To this aim, we first performed a detection efficiency measurement by means of Klyshko efficiency [66], see figure C.1. This characterisation measurement relies on the fact that PDC always generates photons in pairs. By splitting up the two arms of the PDC and assuming finite transmission and detection efficiencies η_1 and η_2, we can measure these quantities by relating the singles S_i and coincidence counts CC in both arms via

$$\eta_1 = \frac{CC}{S_2} \qquad \eta_2 = \frac{CC}{S_1} \,. \tag{C.1}$$

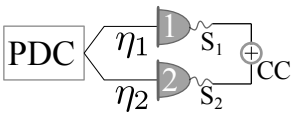

Figure C.1 – Schematic for efficiency calibration after Klyshko [66].

In figures C.2(a_{1-3}), we depict the measured efficiencies η_1 and η_2 in dependence of the incoupled pump power, where the error bars are given by error propagation from the square-root-error of the raw count rates. Since we do not employ photon number resolving detectors for this measurement, we cannot distinguish the single pair contribution from the higher-order photon numbers, which artificially increase the ratio between coincidences and singles. To compensate for this artificial increase of the detection efficiencies, we use the y-intercept of the graph for the estimation of the physical, raw detection efficiency of the overall setup. The results of

coincidence measurement	η_1 [%]	η_2 [%]
pumped WG	3.03 ± 0.06	2.8 ± 0.04
unpumped WG	3.71 ± 0.04	3.74 ± 0.07
cross coinc.	0.35 ± 0.01	0.33 ± 0.01

Table C.1 – Resulting efficiencies for the Klyshko characterisation.

this measurement are summarised in table C.1 for the different coincidence measurements in the pumped wavguide, the unpumped wavguide and between waveguides. The measured efficiencies are quite low, however, as we used comparatively inefficient GaAs APDs with a detection efficiency of $\eta_{\mathrm{APD}} = 20\,\%$ and a 50/50 beam splitter to probabilistically split the generated photons, the values are in the expected range and tolerable for the measurement at hand.

Comparing the values for the pumped and the unpumped waveguide of the source, we find comparable detection efficiences of around $3 - 4\,\%$. In contrast, the efficiency measurement for the cross coincidences shows a value that is an order of magnitude lower, although exactly the same components and detectors were used in this measurement run. The reason for this disagreement lies in the generated state of the dual-path source. Due to the state structure of two

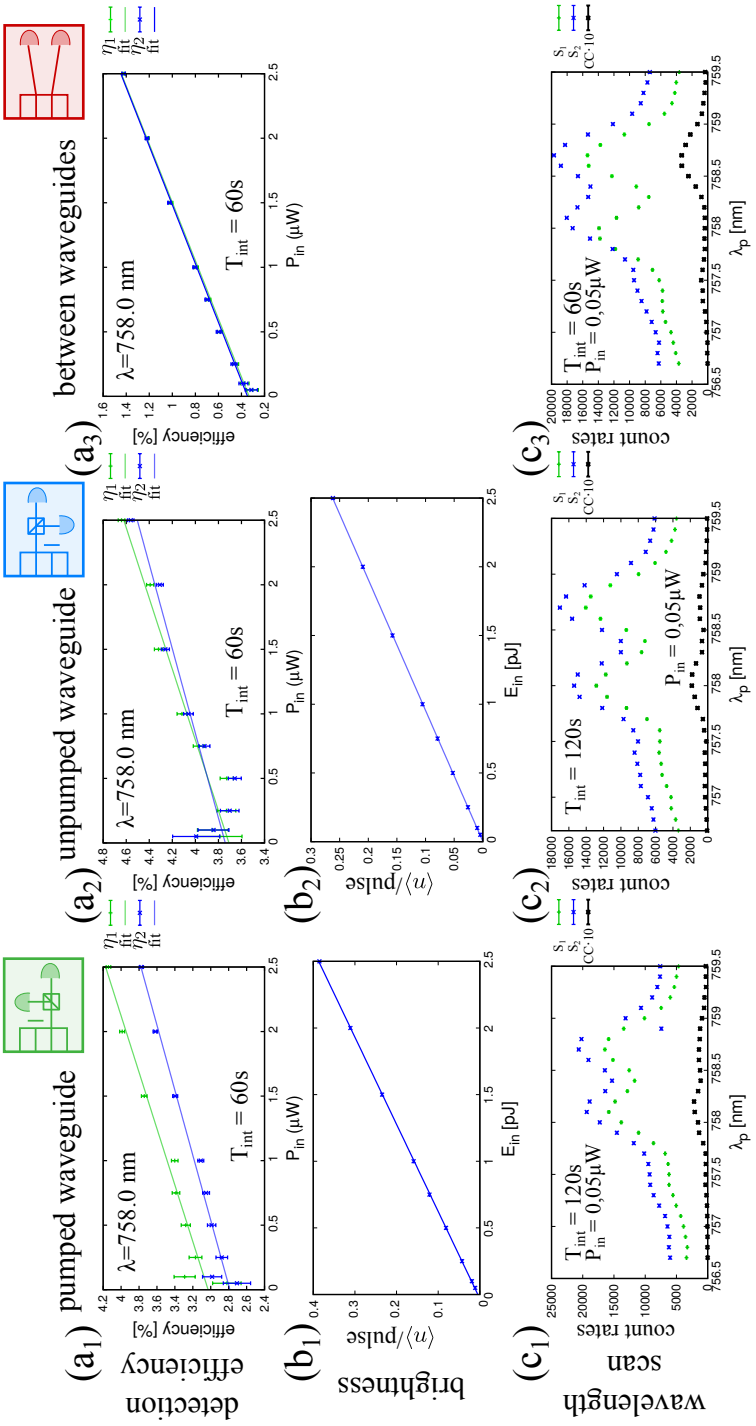

Figure C.2 – Setup characterisation for the different coincidence measurement configurations. Figures (a) show the calibration of the overall detection efficiency, while figures (b) show the corresponding mean photon numbers, from which we extract the brightness by the linear slope. Figures (c) show the raw data for the single S and coincidence counts CC for the wavelength scan of figure 2.10(b).

phase-stable single-mode squeezed states (and therefore two independent PDC sources), compare section 2.5, we can use the coincidence measurements of the pumped and the unpumped waveguide to obtain a measure for the detection efficiency. However, the Klyshko model does not apply for the case of the cross coincidences, since we do not measure two arms of the same PDC source, but two arms of two independent PDC sources. Especially, when we consider the two-photon regime, we expect the cross coincidences to vanish and the low measured efficiencies make perfect sense. Only the finite state fidelity of $\mathcal{F} = (84.2 \pm 2.6)\,\%$ leads to a finite cross coincidence count rate and therefore to efficiencies > 0. As such, the significance of this measurement is rather limited and we only consider it for completeness.

We can also extract a second figure of merit from our measurements, the brightness of our PDC source. We obtained it from the single rates in the two detectors and the corresponding detection efficiencies via

$$\langle n \rangle = \left(\frac{S_1}{\eta_1} + \frac{S_2}{\eta_2} \right) \frac{1}{T_{\text{int}} \cdot R_{\text{Rep}}} \,. \tag{C.2}$$

Accordingly, we plot the measured mean photon numbers in figures C.2($b_{1,2}$), with error bars by error propagation from the count rates and the efficiency errors. However, the error bars are so small that they are within the size of the data points. We extracted the brightness of our PDC source from the line slope of figure C.2(b_1) with $\mathcal{B} \approx 1.5 \cdot 10^5 \frac{\text{pairs}}{s \times \mu W}$.

Finally, in figures C.2(c_{1-3}), we depict the raw single and coincidence counts for figure 2.10(b), where error bars in all cases were estimated with the square-root-error of the count rate. However, they are so small that they vanish in the size of the data points. To obtain 2.10(b) from these numbers, we used the depicted coincidence rates for all three configurations and normalised them to the respective detection efficiencies for the pumped and unpumped arm

$$\begin{aligned} CC_{\text{norm}}^{\text{pumped}} &= 2 \frac{CC_{\text{raw}}^{\text{pumped}}}{\eta_1^{\text{pumped}} \cdot \eta_2^{\text{pumped}} \cdot T_{\text{int}}} \\ CC_{\text{norm}}^{\text{unpumped}} &= 2 \frac{CC_{\text{raw}}^{\text{unpumped}}}{\eta_1^{\text{unpumped}} \cdot \eta_2^{\text{unpumped}} \cdot T_{\text{int}}} \\ CC_{\text{norm}}^{\text{cross}} &= \frac{CC_{\text{raw}}^{\text{cross}}}{(\eta_1^{\text{pump}} + \eta_2^{\text{pump}})/2 \cdot (\eta_1^{\text{unpumped}} + \eta_2^{\text{unpumped}})/2 \cdot T_{\text{int}}} \end{aligned} \tag{C.3}$$

The additional factor of 2 in the pumped and unpumped waveguide measurement is to correct for the 50/50 beam splitter, which reduces the coincidence count rates by a factor of 2. Due to the non-applicability of the Klyshko model in the case of the cross-coincidence measurement, the coincidences between the waveguides were normalised to the product of the mean efficiency in the pumped and unpumped waveguide. To further normalise the count rates to counts per second, all rates were divided by the corresponding integration time T_{int}.